Title
Hierarchical Modeling for Population-Based Heat Exchanger Design

Author
Geb, David

Publication Date
2013

Peer reviewed|Thesis/dissertation

UNIVERSITY OF CALIFORNIA

Los Angeles

Hierarchical Modeling for Population-Based Heat Exchanger Design

A dissertation submitted in partial satisfaction

of the requirements for the degree

Doctor of Philosophy in Mechanical Engineering

by

David Geb

2013

ABSTRACT OF THE DISSERTATION

Hierarchical Modeling for

Population-Based Heat Exchanger Design

by

David Geb

Doctor of Philosophy in Mechanical Engineering
University of California, Los Angeles, 2013
Professor Ivan Catton, Chair

To tackle complex problems, engineers have increasingly looked to natural processes and creatures, as models and metaphors, for inspiration. Darwinian evolution and social group behavior, two instances of optimization mechanisms in nature, have inspired the two main families of nature-inspired intelligent computing algorithms, i.e. evolutionary and swarm algorithms. Although both families of algorithms are generally applied towards search and optimization problems, each has its own distinguishing features. In this dissertation, a genetic algorithm and particle swarm optimizer, instances of each main family of nature-inspired intelligent computing algorithms, are implemented to optimize heat transfer devices such as heat sinks and compact heat exchangers. These optimization methods are ideal for obtaining optimal designs of the constrained, multi-parameter, multi-objective, and multi-model complex optimization problems faced by heat transfer device engineers. However, the primary hurdle facing designers of such

heat transfer devices, which has precluded the use of these optimization methods, is the significant computational costs of performing direct numerical simulations (DNS), i.e. with CFD, of the flow and heat transfer in such heterogeneous (and porous), hierarchical devices with conjugate effects included and flow often in the turbulent regime. This makes device simulations very costly and population-based optimization nearly impossible, which has resulted in most designs being based on ad hoc considerations, resulting in constrained performance, and thus accumulating financial losses for those manufacturing and operating the devices, and troubling environmental effects, i.e. excessive carbon emissions and thermal pollution, due to the accompanying energy losses.

Breakthroughs in the past few decades in the modeling of transport phenomena in heterogeneous media with Volume Averaging Theory (VAT) have allowed engineers to fully simulate flow and heat transfer in thermal devices in mere seconds on a modern laptop, in comparison with the many hours it takes to do so with CFD, paving the way to thorough optimization studies of the multi-parameter devices. VAT is a hierarchical modeling method in which the lower-scale governing equations are the Navier-Stokes and thermal energy equations in the fluid and solid phases, and the upper-scale governing equations are the VAT-based mass, momentum, and fluid and solid thermal energy transport equations. The two sets of equations are rigorously connected by mathematical scaling (i.e. averaging) procedures and the result of such a model allows a nonlocal description of transport phenomena in heterogeneous thermal devices, with the morphology directly incorporated into the field equations and conjugate effects fully

treated.

The upper-scale VAT-based governing equations in hierarchical and heterogeneous media are complicated and at first formidable, yielding additional integral and differential terms when compared to the transport equations in homogeneous media. Understanding these additional terms led to them being directly related to the local transport coefficients, i.e. heat transfer coefficient and drag coefficient, providing a rigorous yet intuitive method of closure to the complicated integro-differential equations, and yielding simple differential equations that are quickly solved with straight forward numerical methods. Closure of the VAT-based equations can be obtained either theoretically, numerically, or experimentally, and past work has focused on numerical methods (i.e. CFD). In this work novel experimental methods for obtaining closure are explored, developed, and then implemented for several surfaces. With the VAT equations closed, rapid simulations can be performed, and thus the nature-inspired optimization methods can be exploited to guide the design to its optimal configuration.

The dissertation of David Geb is approved.

_____

Adrienne Lavine

_____

Laurent Pilon

_____

William W-G. Yeh

_____

Ivan Catton, Committee Chair

University of California, Los Angeles

2013

TABLE OF CONTENTS

1. INTRODUCTION 1

2. HIERARCHICAL TRANSPORT MODEL 6

2.1. Lower-Scale Governing Equations 9

2.2. Upper-Scale Governing Equations 10

2.2.1. Continuity Equation 10

2.2.2. Momentum Equation 11

2.2.3. Turbulent Kinetic Energy Equation 12

2.2.4. Thermal Energy Equations 13

2.3. Transport Coefficients and Closure Statements 15

2.3.1. Friction Factor and Momentum Equation 16

2.3.2. Heat Transfer Coefficient and Thermal Energy Equations 19

2.4. Conclusions 21

3. EXPERIMENTAL CLOSURE OF THE VAT-BASED GOVERNING EQUATIONS 22

3.1. Single-Blow Method for Random Fiber Matrices 25

3.1.1. Background 25

3.1.2. Experimental Method 26

3.1.3. Model and Computational Method 29

3.1.4. Experimental Results 35

3.1.5. Conclusions 46

3.2. Induction Heating Method for Cylinder Arrays 46

3.2.1. Background 47

3.2.2. Experimental Method 49

3.2.3. Model and Computational Method 52

3.2.4. Discussion of Experimental Results 56

3.2.5. Conclusions 64

3.3. Induction Heating Method for Particle Beds 65

3.3.1. Experimental Configuration 65

3.3.2. Model Assumptions and Effective Thermal Conductivity 75

3.3.3. Results and Discussion 77

3.3.4. Conclusions 81

3.4. Conclusions 82

4. OPTIMIZATION WITH VAT-BASED THERMO-FLUID MODELING 84

4.1. Finned-Tube Heat Exchanger Optimization with a Genetically Inspired Algorithm 84

4.1.1. Background 85

4.1.2. VAT Heat Exchanger Model 90

4.1.3. Genetic Algorithm Optimization 97

4.1.4. Results & Discussion 103

4.1.5. Conclusions 111

4.2. Heat Sink Optimization with a Socially Inspired Algorithm 113

4.2.1. Background 114

4.2.2. Heat Sink Transport Model 118
4.2.3. Computational Methods and Solution Procedure 120
4.2.4. Particle Swarm Optimization 123
4.2.5. Results and Discussion 127
4.2.6. Conclusions 144
4.3. Conclusions 145
5. CONCLUSIONS 147
REFERENCES 154
APPENDIX 173
A VAT-Based Length Scale 173
B An Abridged Review of Transient Test Techniques 174
C An Abridged Review of Heat Sink and Heat Exchanger Population-Based Optimization Studies 177
D Experimental Closure Source Code 187
E Finned-Tube Heat Exchanger Subroutine 208

LIST OF FIGURES

Figure 1.1: Dissertation outline..... 2

Figure 1.2: Chapter 2 outline 3

Figure 1.3: Chapter 3 outline 4

Figure 1.4: Chapter 4 outline 5

Figure 2.1: Schematic of a Representative Elementary Volume (REV) 7

Figure 3.1: Test rig schematic..... 27

Figure 3.2: Iteration Procedure 33

Figure 3.3: Heat exchanger core pressure drop. Adapted from Kays and London [30].. 35

Figure 3.4: Nusselt number data and correlation, for air 37

Figure 3.5: Experimental Nusselt number values plotted against the correlation values, for air..... 38

Figure 3.6: Friction factor data and correlation 39

Figure 3.7: Experimental friction factor values plotted against the correlation values 40

Figure 3.8: Nusselt number correlations..... 43

Figure 3.9: Friction factor correlations 44

Figure 3.10: Conceptual illustration of the application of VAT with closure relationships to a) a pin fin heat sink, and b) a tube bank heat exchanger. 49

Figure 3.11: Experimental diagram. 50

Figure 3.12: Test section diagram..... 52

Figure 3.13: Schematic of automated iteration procedure. Each simulation corresponds to a different heat transfer coefficient value. 56

Figure 3.14: The minimum intertube space in a staggered tube bank may occur in the transverse plane, i.e. A_1, or in the diagonal plane, i.e. A_2. Adapted from [61]. . 60

Figure 3.15: Nusselt number data plotted against Reynolds number. 62

Figure 3.16: Experimental heat transfer results obtained in the present study compared to the correlation given by Zukauskas and Ulinskas [57]. 63

Figure 3.17: Experimental flow friction results obtained in the present study compared to the correlation given by Zukauskas and Ulinskas [58]. 64

Figure 3.18: Test section diagram, not shown to scale. Item # 8 in Figure 3.11. 66

Figure 3.19: Near wall void fraction and preferential flow (velocity is scaled with centerline velocity) in a randomly packed bed of uniform spheres (spheres were not heated), Test Section 1, Re = 305. Void fraction distribution taken from the formula given in Eq. (2), where $\varepsilon_C = 0.39$, and $\varepsilon_{min} = 0.23$. 71

Figure 3.20: Modeling the near-wall bypass or channeling effect..... 72

Figure 3.21: Measured ratio of core superficial velocity U to upstream superficial velocity U' for the three test sections over the flow rate ranges in each. U'_{min} and U'_{max} respectively correspond to the minimum and maximum flow rates achieved in the experiment for each of the three test sections. 74

Figure 3.22: Variation of δ_{sim} versus $\hat{t}$ with effective thermal conductivity [W m^{-1} K^{-1}]. Nusselt number is unity, Re = 300. 76

Figure 3.23: Variation of δ_{sim} versus $\hat{t}$ with Nusselt number. $K_{eff} = 20$ W m^{-1} K^{-1}, Re = 300. 77

Figure 3.24: Experimental heat transfer coefficient data. 78
Figure 3.25: Experimental data for Test Sections 1, 2, and 3. Correlations are from Kays and London [30], Whitaker [32], and Nie et al. [31]. 78
Figure 3.26: Internal effective heat transfer coefficient in porous media, reduced based on VAT scale transformations, from experiments by 1, Kar and Dybbs [74] for laminar regime; 2, Rajkumar [75]; 3, Achenbach [68]; 4, Younis and Viskanta [76]; 5, Galitseysky and Moshaev [77]; 6, Kokorev et al. [78]; 7, Gortyshov et al. [79]; 8, Kays and London [30]; 9, Heat Exchangers Design Handbook [80]; 10, Nie et al. [31]; 11, Whitaker [32]; 12, Eq. (38). Adapted from Travkin and Catton [1]. 79
Figure 4.1: VAT-based porous media model of a FTHE. 91
Figure 4.2: Schematic of computational grid and coil circuitry. 93
Figure 4.3: Representative Elementary Volume (REV) for a Finned-Tube Heat Exchanger, [29]. 95
Figure 4.4: Geometrical constraints in (a) $x-y$, and (b) $y-z$ planes. 100
Figure 4.5: Visual outline of the basic GA optimizer. 101
Figure 4.6: Schematic of the genetic operators acting during the breeding process. (a) Two parent individuals are selected and paired for mating. (b) A location on their chromosomes is randomly selected for splitting. (c) The crossover mechanism then occurs. (d) Subsequently, genetic mutations are allowed to take place. ... 101
Figure 4.7: Fitness evolution of the best individual in each generation for five trials. .. 104

Figure 4.8: Optimum heat exchanger body dimensions, L_x, L_y, and L_z, drawn to scale with tube pass and row numbers, N_x and N_y, indicated (tube diameters not drawn to scale) for the five trials. 107

Figure 4.9: Evolution of $\bar{\mathbf{x}}$ for the best individual in each generation for a) Trial 1 and b) Trial 3. 111

Figure 4.10: Illustration of a straight-fin heat sink with tapered, a) smooth and b) scale-roughed surface fins 118

Figure 4.11: Flow chart of the VAT-based heat sink simulation routine 121

Figure 4.12: Flow chart of PSO algorithm 126

Figure 4.13: Evolution of thermal resistance during the a) PSO and b) GA optimizations of a smooth surface straight-fin heat sink. Thin, light colored lines indicate the individual trials while thick, dark colored lines indicate the average of the ten trials 129

Figure 4.14: Evolution of the scaled design parameters during the a) PSO and b) GA optimizations of a smooth surface straight-fin heat sink. Thin, light colored lines indicate the individual trials while thick, dark colored lines indicate the average of the ten trials. 130

Figure 4.15: Evolution of thermal resistance during the a) PSO and b) GA optimizations of a scale-roughened straight-fin heat sink 134

Figure 4.16: Evolution of the scaled design parameters during the a) PSO and b) GA optimizations of a scale-roughened straight-fin heat sink 136

Figure 4.17: Nonlocal fluid (left) and solid (right) temperature fields for the optimal scale-roughened straight-fin heat sink found by the PSO after its a) first, b) fourth, and c) final iteration, along with those for the d) optimal smooth straight-fin heat sink. The fully-developed velocity field profiles and the 90°C contour lines are indicated superimposed on the fluid and solid temperature fields respectively. 139

Figure 5.1: Pareto optimal front for a multiple objective optimization problem..... 152

LIST OF TABLES

Table 3.1: Physical properties of the materials. 28

Table 3.2: Test sample properties, $L = 1.3"$, $D = 1.0"$. 28

Table 3.3: Physical properties of the materials. 51

Table 3.4: Dimensional test section configurations. 51

Table 3.5: Definitions employed by various investigators. 59

Table 3.6: Dimensionless number conversion factors between the conventions of the present VAT-based analysis and those of Zukauskas and Ulinskas. 60

Table 3.7: Test section characteristics from the present study and from Kays and London [30]. 62

Table 3.8: Geometrical characteristics of the test sections. 67

Table 3.9: Induction coil parameters. Copper coil, d_C = 9.5 mm, and P_C = 1.27 cm. The coils are internally cooled with deionized water, flowing in a closed loop, from a water cooler. 67

Table 3.10: Core to upstream superficial velocity ratios, $\pm 7\%$. 74

Table 4.1: Search parameters and their ranges. 99

Table 4.2: Physical and optimization constraints. 99

Table 4.3: Parameter selection and corresponding fitness for the five trials. 105

Table 4.4: Heat exchanger performance at $\mathbf{x} = \mathbf{x}^*$ for the five trials, $\dot{Q}_{max} = 125.58$ kW. 109

Table 4.5: Design parameter ranges for the straight-fin heat sinks 124

Table 4.6: PSO operation settings 127

Table 4.7: GA operation settings 131

Table 4.8: Characteristics of optimized smooth surface straight-fin heat sink for PSO and GA methods 132

Table 4.9: Characteristics of optimized scale-roughened surface straight-fin heat sinks for PSO and GA methods 137

Table 4.10: Characteristics of the heat sinks considered in Figure 4.17..... 140

NOMENCLATURE

A	core cross-sectional area; total heat transfer area, [m^2]
A'	test section cross-sectional area, [m^2]
A_c	minimum free flow area, [m^2]
b	mean turbulent fluctuation energy, $\frac{1}{2}\overline{u_i' u_i'}$, [$m^2$ s^{-2}]
Bi	Biot number, [-]
c_1, c_2	parameters in PSO algorithm, [-]
c_d	drag resistance coefficient, [-]
c_{dp}	form drag resistance coefficient, [-]
c_f'	skin friction coefficient, [-]
c_{fL}	skin friction coefficient over the laminar area of ∂S_w, [-]
$\tilde{c}_d$	skin friction coefficient over the turbulent area of ∂S_w, [-]
c_p	specific heat capacity, [J kg^{-1} K^{-1}]
C_1	constant coefficient in Kolmogorov turbulent exchange correlation, [-]
C_D, C_μ	empirical turbulence exchange coefficients, [-]
d	mean effective sphere or fiber diameter, [m]
d_p	particle or capillary diameter, [m]

D	outer diameter of cylinder, tube, or pin; diameter of test section; scale diameter, [m]
D_c, D_i	tube collar and inner diameter, [m]
d_h	porous media hydraulic diameter, [m]
∂S_w	internal surface area in the REV, [m^2]
ds	interphase differential area in porous medium, [m^2]
$d\omega$	differential volume element in REV, [m^3]
e	scale height, [m]
f	Fanning friction factor, [-]
F	fitness function, [-]
F_p	fin pitch, [m]
$\tilde{g} \equiv \{g\}_f$	intrinsic averaged variable g
$\langle g \rangle_f$	phase averaged variable g
$\hat{g}$	morpho-fluctuation variable g
G	mass flux, from Kays and London, [kg m^{-2} s^{-1}]
h	convective heat transfer coefficient, [W m^2 K^{-1}]
H	height of test section or channel, [m]
H_b	base plate thickness, [m]

H_f	fin height, [m]
k	thermal conductivity, [W m^{-1} K^{-1}]
k_T	turbulent eddy thermal conductivity, [W m^{-1} K^{-1}]
K_c, K_e	contraction and expansion coefficients, [-]
l	turbulence mixing length scale; length of upstream adiabatic flow development section, [m]
L	length; length of test section, [m]
m, $\dot{m}$, $\dot{m}''$	mass, [kg]; mass flow rate, [kg s^{-1}]; mass flux, [kg s^{-1} m^2]
$\langle m \rangle$	locally averaged porosity, [-]
n	number of bounded parameters describing an individual; dimension of the optimization search space, [-]
N_G, N_P	total number of iterations or generations; population size, [-]
N_S	number of individuals in a neighborhood in PSO, [-]
N_x, N_y	columns (x) and rows (y) of tubes, [-]
p	pressure, [Pa]
P	scale or tube pitch, [m]
P_C	crossover probability in GA, [-]; induction coil pitch, [m]
P_M	mutation probability in GA, [-]
PP	pumping power, [W]

Pr	Prandtl number, [-]
$\dot{Q}$	heat transfer rate, [W]
Re	Reynolds number, [-]
R_{th}	heat sink thermal resistance, $R_{\text{th}} = \frac{\Delta T_{\max}}{\dot{Q}}$, [$^{\circ}C/W$]
S	pitch; dimensionless pitch, [m]
S_w	specific surface area of a porous medium, $\partial S_w / \Delta\Omega$, [$m^{-1}$]
S_{wp}	the cross flow projected area per volume, $S_{\perp} / \Delta\Omega$, [m^{-1}]
S_y	dimensionless fin pitch, $= F_p / \delta_{\text{base}}$, [-]
St	Stanton number, Nu/Re/Pr, [-]
t	time, [s]
T	temperature, [K]
u, v, w	x, y, z direction velocity terms, [m s^{-1}]
U	superficial velocity, [m s^{-1}]
V	volume, [m^3]
w	inertia weight in PSO, [-]
W	width of test section, [m]; heat exchanger total mass, [kg]
x, y, z	cartesian coordinates, [m]

$\mathbf{x}$, X	search space vectors, [-]
z	number of tube rows, $= L/S_L$, [-]

Greek

α , β , γ	thermal diffusivity, [m^2 s^{-1}]; governing equation parameters, [-]
δ	dimensionless fluid temperature response between the inlet and exit of the test section, [-]; fin thickness, [m]; thickness, [m]
ΔT_f	characteristic temperature difference, [K]
$\Delta\Omega$	the volume of the REV, [m^3]
ε , ε_{PP} , $\varepsilon_{\Delta T}$	heat exchanger effectivenesses, $\varepsilon = \dot{Q}_1 / \dot{Q}_{\max}$, [-]; $\varepsilon_{PP} = \dot{Q}_1 / PP_{\mathrm{T}}$, [-]; $\varepsilon_{\Delta T} = \varepsilon_{PP} / \left(T_{2,\mathrm{in}} - T_{1,\mathrm{in}}\right)$, [$K^{-1}$]
μ	dynamic viscosity, [kg m^{-1} s^{-1}]
μ_r	relative magnetic permeability of the test section, [-]
ν	kinematic viscosity, [m^2 s^{-1}]
ν_T	turbulent eddy viscosity, [m^2 s^{-1}]
ρ	density, [kg m^{-3}]
ρ_R	electrical resistivity of the test section material, [Ω m]
σ	free-flow to frontal area ratio, [-]
σ_b	turbulent coefficient exchange ratio, [-]

τ	characteristic time scale, [s]; shear stress, [N m^{-2}]
υ	specific volume, [m^3 kg^{-1}]
χ	hydraulic diameter to length ratio; dimensionless pitch, [-]

Subscripts and Superscripts

~	phase averaged value
–	mean turbulent quantity
'	turbulent fluctuation value; upstream; overall; or reference
^	fluctuation of a value; dimensionless value
*	nondimensional value; optimum
0	evaluated at the wall or surface
1	upstream value; air/fin side
2	downstream value; water/tube side
amb	ambient
avg	average
b	evaluated at the bulk temperature or base
base/top	fin base/top

C	coil
d	tube wall
D	diagonal
eff	effective
exp	experimental
f	a value in the fluid phase; fin
i	index
in/out	inlet (or initial)/outlet condition
K&L	conventions of Kays and London, 1985
L	laminar; longitudinal
lim	limiting
max	maximum value
min	minimum value
s	a value in the solid phase
sim	simulated
T	turbulent; transverse
tot	total

VAT	conventions of the present analysis
w	wall
W	conventions of Whitaker, 1972
x, y, z	x, y, z coordinate directions
Z&U	conventions of Zukauskas, 1988

ACKNOWLEDGEMENTS

My Fiancé, Parents, and Family for their support.

Professor Catton, for providing priceless intellectual and professional guidance during my time as a graduate student.

My Committee members, Professors Lavine, Pilon, and Yeh, for supporting and helpfully guiding me academically, professionally, and personally. Also, there are a number of other UCLA MAE faculty members who have made significant contributions towards cultivating my academic development during my ten years at the school.

Chris Woods, Malik Evangelatos, and Mike Ahn, for their friendships during my time as a graduate student. I have greatly valued their friendships and have appreciated the accommodations they've made for me as I've pursued a Ph.D.

My mentor for two years at Los Alamos National Laboratory, Dr. Torsten Staab, for instilling in me a strong sense of technical ability and confidence, and encouraging me to pursue a Ph.D.

My high school teacher Ms. Lynell Hankins who sacrificed much of her time to allow me to pursue Mathematics. Without her substantial contributions I would have been unable to pursue Mathematics and Science at the university level.

Fellow students with whom I worked for their friendship and academic support. In particular, Feng Zhou, George DeMoulin, Krsto Sbutega, Sean Reilly, Jonathan Chu, Angelo Lerro, Michael Ge, and Param Sunny Sangha. Also, the staff in the Mechanical and Aerospace Engineering Department for their friendliness and support.

Ron Olan of Infinia Corporation, for his benevolence towards me during my time as a graduate student.

Lastly, the support of the DARPA MACE program Grant No. W31P4Q-09-1-0005 is gratefully acknowledged.

VITA

2007-2008	Mechanical Engineer Internship (DOE SULI Fellowship) Los Alamos National Laboratory
2008	B.S., Mechanical Engineering University of California, Los Angeles
2008-2013	Graduate Student Researcher and Teaching Assistant Department of Mechanical and Aerospace Engineering University of California, Los Angeles
2011	M.S., Mechanical Engineering University of California, Los Angeles

PUBLICATIONS

JOURNAL PUBLICATIONS

1. **Geb, D.**, Zhou, F., DeMoulin, G., and Catton, I., 2013, "Genetic Algorithm Optimization of a Finned-Tube Heat Exchanger Modeled with Volume Averaging Theory," Journal of Heat Transfer, In Production.

2. **Geb, D.**, Ge, M., Chu, J., and Catton, I., 2013, "Measuring Transport Coefficients in Heterogeneous and Hierarchical Heat Transfer Devices," Journal of Heat Transfer, In Production.

3. **Geb, D.**, Lerro, A., Sbutega, K., and Catton, I., 2013, "Internal Transport Coefficient Measurements in Random Fiber Matrix Heat Exchangers," Thermal Science and Engineering Applications, In Production.

4. **Geb, D.**, Zhou, F., and Catton, I., 2012, "Internal Heat Transfer Coefficient Determination in a Packed Bed from the Transient Response Due to Solid Phase Induction Heating," Journal of Heat Transfer, 134(4): 042604.

5. **Geb, D.** and Catton, I., 2013, "Nonlocal Modeling and Swarm-Based Design of Heat Sinks," Journal of Heat Transfer, Under Revision.

6. Zhou, F., DeMoulin, G.W., **Geb, D.**, and Catton, I., 2012, “Closure for a Plane Fin Heat Sink with Scale-Roughened Surfaces for Volume Averaging Theory (VAT) Based Modeling,” International Journal of Heat and Mass Transfer 55(25-26): 7677-7685.

7. Zhou, F., Hansen, N., **Geb, D.**, and Catton, I., 2011, "Obtaining Closure for Fin-And-Tube Heat Exchanger Modeling Based on Volume Averaging Theory (VAT)," Journal of Heat Transfer, 133(11): 111802.

8. Zhou, F., Hansen, N., **Geb, D.**, and Catton, I., 2011, "Determination of the Number of Tube Rows to Obtain Closure for Volume Averaging Theory Based Model of Fin-And-Tube Heat Exchangers," Journal of Heat Transfer, 133(12): 121801.

CONFERENCE PROCEEDINGS

1. **Geb, D.**, Demoulin, G., and Catton, I., 2013, “Population-Based Optimization for Heat Sink Design in Electronics Cooling Applications,” Proc. Semiconductor Thermal Measurement and Management Symposium (SEMI-THERM), 29th Annual IEEE.

2. **Geb, D.**, Zhou, F., DeMoulin, G., and Catton, I., 2012, “Genetic Algorithm Optimization of a Compact Heat Exchanger Modeled Using Volume Averaging Theory,” HT2012-58067, Proceedings of the 2012 ASME Summer Heat Transfer Conference, San Juan, Puerto Rico, USA.

3. **Geb, D.**, Sbutega, K., and Catton, I., 2012, “A New Technique for Measuring Convective Heat Transfer Coefficients in Solid Matrices for Compact Heat Exchanger Design.” HT2012-58071, Proceedings of the 2012 ASME Summer Heat Transfer Conference, San Juan, Puerto Rico, USA.

4. **Geb, D.**, Chu, J., Zhou, F., and Catton, I., 2011, “Obtaining Experimental Closure for the VAT-Based Energy Equations Modeling a Heat Sink as a Porous Medium,” in the Proceedings of the ASME 2011 International Mechanical Engineering Congress and Exposition: IMECE2011-62638, Denver, Colorado, USA.

5. **Geb, D.** and Catton, I., 2010, "Non-Intrusive Heat Transfer Coefficient Determination in a Packed Bed of Spheres," ASME Conference Proceedings 2010(49415): 901-910.

6. Lerro, A., **Geb, D.**, Sbutega, K., and Catton, I., 2012, “A Single-Blow Transient Test Technique with Volume Averaging Theory Modeling for Random Fiber Matrices,” HT2012-58358, Proceedings of the 2012 ASME Summer Heat Transfer Conference, San Juan, Puerto Rico, USA.

7. Zhou, F., DeMoulin, G.W., **Geb, D.**, and Catton, I., 2012, "Hierarchical modeling and closure evaluation for fin-and-tube heat exchangers using 3-D numerical simulation,"

Proc. ASME 2012 Summer Heat Transfer Conference: HT2012-58018, Rio Grande, Puerto Rico, USA.

8. Zhou, F., DeMoulin, G.W., **Geb, D.**, and Catton, I., 2012, "Closure for a Plane Fin Heat Sink with Scale-Roughened Surfaces for Volume Averaging Theory (VAT) Based Modeling," Proc. GOMACTech 2012: 31-1, Las Vegas, Nevada, USA.

9. Zhou, F., **Geb, D.**, and Catton, I., "Numerical Investigation on Air Side Performance of Fin-And-Tube Heat Exchangers with Large Diameter Tubes and Large Number of Tube Rows," in the Proceedings of the ASME 2011 International Mechanical Engineering Congress and Exposition: IMECE2011-62302, Denver, Colorado, USA.

10. Zhou, F., Vasquez, D.A., DeMoulin, G.W., **Geb, D.**, and Catton, I., "Volume Averaging Theory (VAT) based modeling and closure evaluation of scale-roughened plane fin heat sink," Proc. Semiconductor Thermal Measurement and Management Symposium (SEMI-THERM), 2012 28th Annual IEEE, pp. 260-268.

11. Zhou, F., **Geb, D.**, and Catton, I., 2011, "Cooling Performance Comparisons of Five Different Plate-Pin Compound Heat Sinks Based on Two Different Length Scale," ASME Conference Proceedings 2011(44625): 47-57.

12. Zhou, F., DeMoulin, G.W., **Geb, D.**, and Catton, I., "Modeling of pin fin heat sinks based on Volume Averaging Theory," Proc. ASME-JSME-KSME Joint Fluids Engineering Conference 2011, AJK2011-FED, Hamamatsu, Shizuoka, JAPAN, AJK2011- 03035.

1. INTRODUCTION

Travkin and Catton [1] note that modeling transport phenomena in heterogeneous porous media presents significant challenges, even when subject to simplifications, e.g. the specification of medium periodicity or regularity. They point out that employing linear or linearized models fails to intrinsically account for transport phenomena, "requiring dynamic coefficient models to correct for short-comings in the governing models," and observe that "this problem has been treated by procedures that are mostly heuristic in nature" in the past [1]. Travkin and Catton [1-7] developed Volume Averaging Theory (VAT) for nonlinear and turbulent transport in heterogeneous and hierarchical media in a series of articles from the early 1990s to the early 2000s, the result of which includes a well-accepted hierarchical transport model and its associated closure theory, overcoming many of the short-comings present in existing models. The VAT model for nonlinear and turbulent transport, although developed, has not been ambitiously exploited for optimization and design, and the closure theory has not been addressed experimentally, leaving significant gaps in the continuation of VAT's development.

The aim of this dissertation is to fill these gaps by

1. developing, implementing, and validating experimental techniques for VAT closure evaluation; and
2. exploiting the resulting closed VAT-based equations with intelligent design techniques, and applying them to important thermal engineering problems.

Realizing these goals results in a design tool with capabilities that far exceed those currently in practice in the field, i.e. those employing CFD and other porous media models. Moreover, such a tool possesses far-reaching applicability to a vast array of engineering problems involving transport phenomena in heterogeneous media with significant scientific and social implications.

After this introductory chapter, Chapter 1, the dissertation consists of three core chapters. Chapter 2 concisely presents the VAT-based hierarchical physical model for nonlinear and turbulent transport, Chapter 3 addresses closure of the VAT model, and Chapter 4 describes population-based design efforts, the foundation of which is the closed VAT-based model. Chapter 5 then offers conclusions. The intuitive and concise outline of the dissertation is presented in Figure 1.1, and emphasizes the method behind *Hierarchical Physical Modeling for Population-Based Heat Exchanger Design*, which boils down to a three-step process.

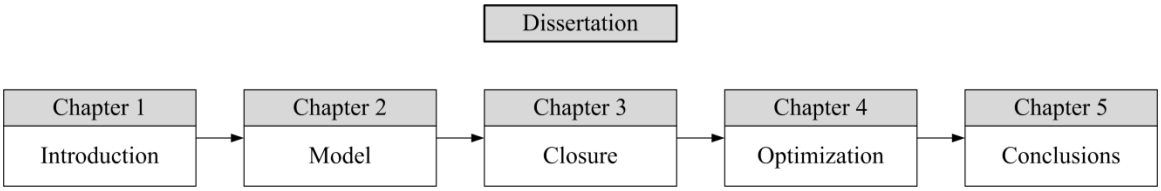

Figure 1.1: Dissertation outline

The first step, i.e. formulating the physical model, is presented in Chapter 2, the outline of which is exhibited in Figure 1.2. Chapter 2 presents the VAT-based governing equations employed to model transport phenomena in hierarchical and heterogeneous

porous media, e.g. heat exchangers and heat sinks. These equations have been previously derived from fundamental equations using rigorous mathematical averaging techniques and are theoretically correct. Their form however is complicated and not conducive to convenient numerical solution until closed. The closure theory developed by Travkin and Catton, and summarized in [1], is then presented, so that it may be addressed in Chapter 3. Then, using the closure statements, the closed VAT-based governing equations are presented so that they may be employed for population-based design of heat exchangers and heat sinks in Chapter 4.

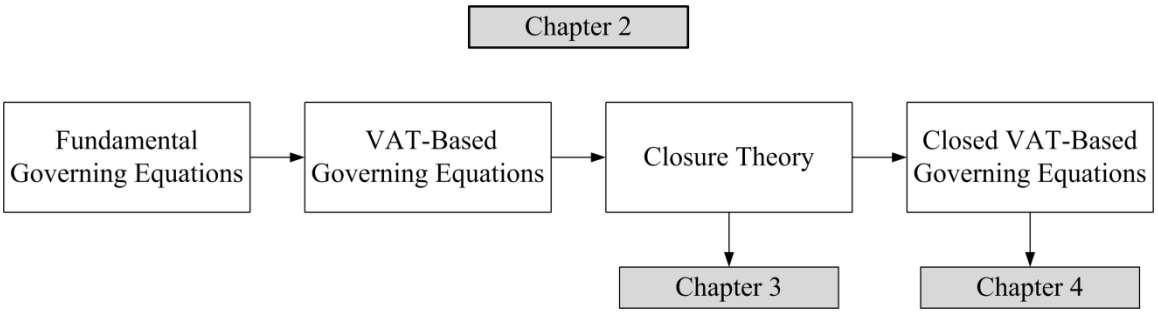

Figure 1.2: Chapter 2 outline

The next step in *Hierarchical Physical Modeling for Population-Based Heat Exchanger Design*, after the VAT-based transport model is presented, is to address the problem of closure. Chapter 3, the outline of which is illustrated in Figure 1.3, addresses the closure problem using experimental techniques. Based on the closure statements presented in Chapter 2, two novel experimental methods are devised to close the VAT-based governing equations. These methods are then implemented for a series of surfaces in order to obtain new closure correlations and validation of the new methods.

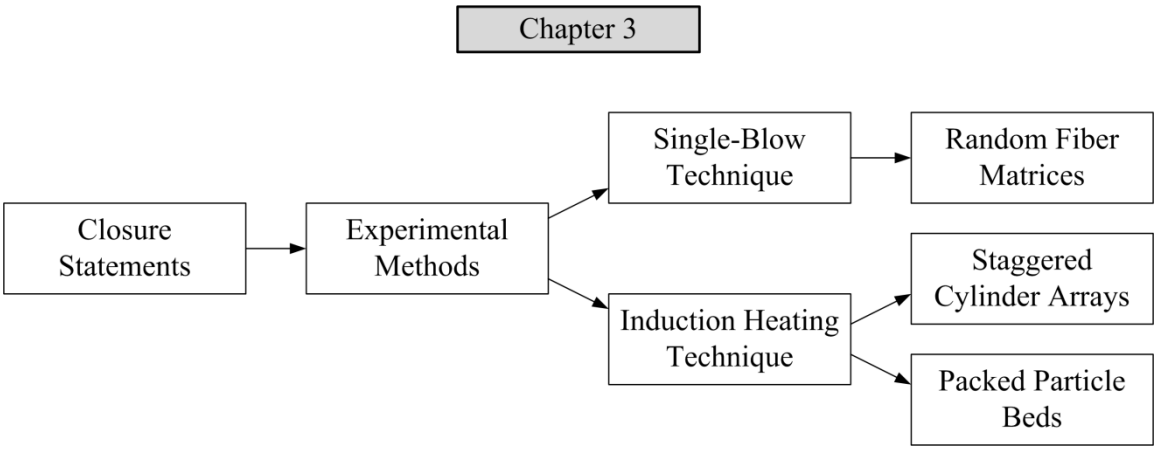

Figure 1.3: Chapter 3 outline

With solutions to the closure problem addressed, the final step in *Hierarchical Physical Modeling for Population-Based Heat Exchanger Design*, is to develop and implement the design methods. Chapter 4, the outline of which is shown in Figure 1.4, details population-based design of a heat exchanger and a heat sink modeled with VAT. Starting with the closed VAT-based governing equations, two population-based optimization algorithms are presented and applied to the VAT-based solution routines for a heat exchanger and a heat sink. The results presented in this chapter demonstrate the power, and significant advantages, of *Hierarchical Physical Modeling for Population-Based Heat Exchanger Design*, and highlight the capabilities of this method that are unmatched by existing tools, i.e. CFD and empirically-based porous media models.

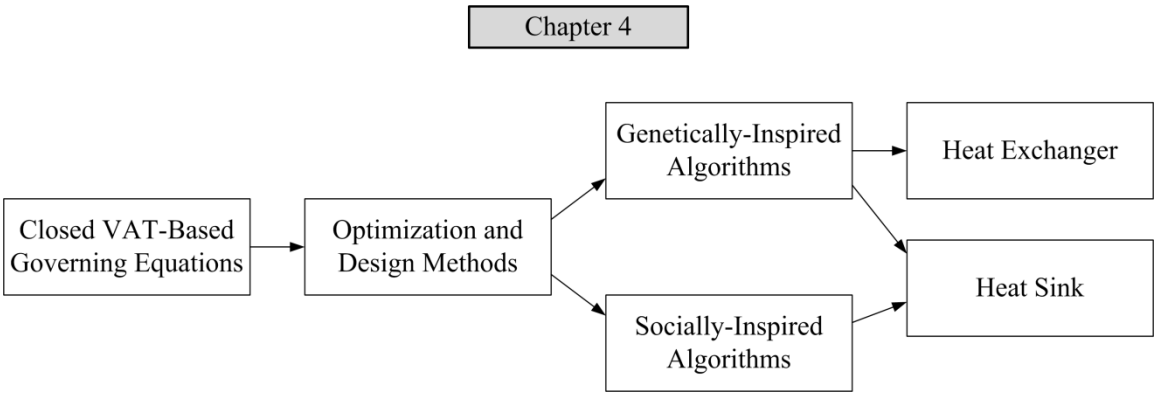

Figure 1.4: Chapter 4 outline

Chapter 5 proceeds to offer conclusions to the dissertation, contemplate the application of VAT-based modeling combined with population-based design to a multitude of new and important problems involving transport phenomena in heterogeneous porous media, survey existing challenges with VAT modeling that need to be addressed, and propose the incorporation of additional optimization strategies that exhibit promise as design methodologies. Appendices including selected source codes are attached to the end of the dissertation. A common theme throughout the dissertation is the flexibility and ready application of VAT to problems involving hierarchical transport phenomena in heterogeneous porous media. This theme is made evident through the generality of the model presented in Chapter 2, the variety of surfaces examined in Chapter 3, the different problems considered in Chapter 4, and the discussions on future work in Chapter 5. This aspect of VAT is perhaps its most significant, and the landscape of this dissertation is meant to exhibit and emphasize this.

2. HIERARCHICAL TRANSPORT MODEL

The Volume Averaging Theory (VAT)-based fluid mechanics and thermal energy equations modeling fluid flow and heat transport within a heterogeneous porous medium are derived from the fundamental Navier-Stokes and thermal energy equations, which are the basis for studying fluid flow and thermal phenomena in porous media [7]. Work on VAT began in the 1960s with contributions by Anderson and Jackson [8], Slattery [9], Marle [10], Whitaker [11], and Zolotarev and Radushkevich [12], and continued with contributions by Slattery [13], Kaviany [14], Gray et al. [15], Whitaker [16, 17], Kheifets and Neimark [18], Dullien, [19] and Adler [20]. Travkin, Catton and coauthors [2-6] extended its application to nonlinear and turbulent transport in porous media and recently Nakayama and coauthors [21-24] have contributed to continuing VAT's development. The following provides a discussion on the nature of VAT modeling that is based on discussions found in [1, 7].

The VAT method has become "a well-substantiated mathematical theory that addresses linear, non-linear, laminar and turbulent hierarchical transport in non-isotropic heterogeneous media, accounting for modeling level, interphase exchange and micro-roughness" [1]. Models were developed for transport in porous media using an advanced averaging technique, a hierarchical modeling methodology, and fully turbulent models with Reynolds stresses and fluxes in every pore space [1-7]. The transport equations obtained using VAT involve additional terms that quantify the influence of the medium morphology, and the description of the porous medium structural morphology determines the importance of these terms and the range of application of closure schemes [1-7].

The VAT-based equations are derived by averaging the Navier-Stokes and thermal energy equations over a specified Representative Elementary Volume (REV), as shown in Figure 2.1. Due to the averaging process, the VAT-based governing equations yield additional integral and differential terms when compared to the homogenized or classical continuum mechanics equations. Surmounting problems associated with a lack of understanding of these new, advanced integral-differential equations and an insufficient development of closure theory has posed a significant challenge. Travkin and Catton [1] however made an effort to develop the closure theory and relate these additional terms to the local transport coefficients. Once these additional terms are closed, the resulting equation set is relatively simple and its solution can be obtained using simple numerical methods that are quick enough to realize multiple-parameter optimization on the system level.

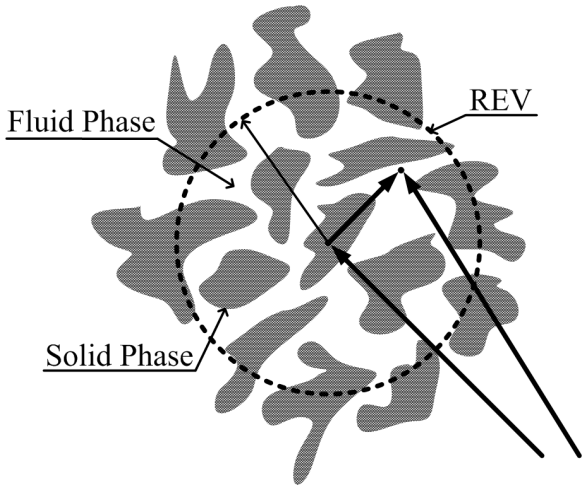

Figure 2.1: Schematic of a Representative Elementary Volume (REV)

The application of VAT yields many desirable features as a tool to characterize the physical processes taking place in heterogeneous and multi-scale media. VAT allows one to consider specific medium types and morphologies, and incorporates the morphology description directly into the governing field equations. In addition to allowing the effects of interfaces to be included in the modeling, VAT allows separate and combined fields and their interactions to be described exactly (i.e. no assumptions about effective coefficients are required), and provides for the consideration of lower-scale fluctuations of variables, cross-effects of different variable fluctuations, and interface variable fluctuation effects [1-7]. Independent treatment of convective turbulent energy transport in the fluid phase and diffusive energy transport in the solid phase, connected through the solid-fluid interface allows for more accurate modeling of the heat transfer mechanisms between the heterogeneous and porous solid structure and the fluid phases. Moreover, the hierarchical physical description provided by the VAT governing equations connects properties and morphological characteristics to component features. Perhaps most importantly, the mathematically rigorous non-local description of hierarchical, multi-scale processes resulting from the application of VAT, provides the capability to perform a purposeful search for the optimal designs of spatially heterogeneous transport structures.

In this chapter the governing equations are presented, starting with the fundamental lower-scale equations, and followed by the upper-scale VAT-based equations. Details of the derivation of the VAT-based nonlinear equations are well documented and can be found in [1-7, 25, 26], so they are not presented here. After the

VAT-based equations are presented, the closure statements are presented that mathematically connect the lower-scale phenomena to the upper-scale phenomena.

2.1. Lower-Scale Governing Equations

The Navier-Stokes and thermal energy equations in both the fluid and solid phases are the starting point and basis for studying flow and heat transfer in porous and heterogeneous media. These equations constitute the lower-scale governing equations on which the VAT method is based.

The lower-scale governing transport equations for steady-state turbulent flow follow. The laminar flow statements are easily obtained from the turbulent flow statements. In the fluid phase, the transport equations are

$$\frac{\partial \overline{u}_j}{\partial x_j} = 0\,, \tag{2.1}$$

$$\overline{u}_j \frac{\partial \overline{u}_i}{\partial x_j} = -\frac{1}{\rho_f}\frac{\partial \overline{p}}{\partial x_i} + \frac{\partial}{\partial x_j}\left(\nu \frac{\partial \overline{u}_i}{\partial x_j} - \overline{u_i' u_j'} \right), \tag{2.2}$$

$$\rho_f c_{pf} \overline{u}_j \frac{\partial \overline{T}_f}{\partial x_j} = \frac{\partial}{\partial x_j}\left(k_f \frac{\partial \overline{T}_f}{\partial x_j} - \overline{T_f' u_j'} \right). \tag{2.3}$$

In the solid phase, without heat generation, the transport equation is

$$0 = \frac{\partial}{\partial x_j}\left(k_s \frac{\partial T_s}{\partial x_j} \right). \tag{2.4}$$

2.2. Upper-Scale Governing Equations

The VAT-based governing equations accounting for turbulent transport in heterogeneous porous media follow. They constitute the upper-scale governing equations on which the work of this dissertation is focused. The laminar flow statements are easily obtained from the turbulent flow statements. These equations are derived from the lower-scale governing equations using rigorous mathematical averaging techniques, the details of which are well documented [1, 7, 25-27].

2.2.1. Continuity Equation

For incompressible, turbulent flow, the Reynolds averaged continuity equation is given in Equation (2.1). Applying the volume averaging method, the averaged continuity equation in the fluid phase of the porous medium is written as

$$\frac{\partial}{\partial x_i}\left\langle \overline{u}_i \right\rangle_f + \frac{1}{\Delta\Omega}\int_{\partial S_w} \overline{u}_i \cdot d\vec{s} = 0. \tag{2.5}$$

For no flow penetration through the interphase surfaces the continuity equation reduces to

$$\frac{\partial}{\partial x_i}\left\langle \overline{u}_i \right\rangle_f = 0. \tag{2.6}$$

2.2.2. Momentum Equation

The Reynolds averaged momentum equation is given in Equation (2.2) for steady flow conditions. Applying the volume averaging method, the averaged turbulent flow momentum equation in the fluid phase of the porous medium is

$$\begin{aligned}
&\langle m\rangle \tilde{\bar{u}}_j \frac{\partial \tilde{\bar{u}}_i}{\partial x_j} - \tilde{\bar{u}}_i \frac{1}{\Delta\Omega}\int_{\partial S_w} \bar{u}_j \cdot d\vec{s} + \frac{\partial}{\partial x_j}\left\langle \hat{\bar{u}}_i \hat{\bar{u}}_j \right\rangle_f + \frac{1}{\Delta\Omega}\int_{\partial S_w} \bar{u}_j \bar{u}_i \cdot d\vec{s} = \\
&-\frac{1}{\rho_f}\frac{\partial}{\partial x_i}\left(\langle m\rangle \tilde{\bar{p}}\right) - \frac{1}{\rho_f}\frac{1}{\Delta\Omega}\int_{\partial S_w} \bar{p} d\vec{s} + \frac{\partial}{\partial x_j}\left(\langle m\rangle \nu \frac{\partial \tilde{\bar{u}}_i}{\partial x_j}\right) + \frac{1}{\Delta\Omega}\int_{\partial S_{wL}} \nu \frac{\partial \bar{u}_i}{\partial x_j} \cdot d\vec{s} + \\
&\frac{\partial}{\partial x_j}\left\langle -\overline{u'_i u'_j} \right\rangle_f - \frac{1}{\Delta\Omega}\int_{\partial S_w} \overline{u'_i u'_j} \cdot d\vec{s}
\end{aligned} \tag{2.7}$$

In analogy to the viscous stresses in laminar flows, the turbulent stresses can be assumed to be proportional to the mean-velocity gradients. For general flow situations the Reynolds stress can be expressed as

$$-\overline{u'_i u'_j} = \nu_T \left(\frac{\partial \bar{u}_i}{\partial x_j} + \frac{\partial \bar{u}_j}{\partial x_i} \right), \tag{2.8}$$

where ν_T is the mean eddy viscosity. Further, assuming no flow penetration through the interphase surfaces, the momentum equation is reduced to

$$\langle m\rangle \tilde{\bar{u}}_j \frac{\partial \tilde{\bar{u}}_i}{\partial x_j} + \frac{\partial}{\partial x_j}\left\langle \hat{\bar{u}}_i \hat{\bar{u}}_j \right\rangle_f = -\frac{1}{\rho_f}\frac{\partial \langle \bar{p}\rangle_f}{\partial x_i} + \frac{\partial}{\partial x_j}\left(\langle m\rangle (\nu + \nu_T)\frac{\partial \tilde{\bar{u}}_i}{\partial x_j} \right) - \frac{1}{\rho_f}\frac{1}{\Delta\Omega}\int_{\partial S_w} \bar{p}\, d\vec{s} + \frac{1}{\Delta\Omega}\int_{\partial S_w} (\nu + \nu_T)\frac{\partial \bar{u}_i}{\partial x_j}\cdot d\vec{s} \tag{2.9}$$

The mean eddy viscosity ν_T is determined using Prandtl's mixing length theory, with

$$\nu_T = C_\mu l(z)\sqrt{b}\,, \tag{2.10}$$

where C_μ is a constant, $l(z)$ is the mixing length scale function defined by the assumed porous medium structure, and $\sqrt{b}$ is the velocity scale [1, 7, 25, 26]. The turbulent kinetic energy b is expressed as

$$b = \frac{1}{2}\left(\overline{u'^2} + \overline{v'^2} + \overline{w'^2}\right). \tag{2.11}$$

In order to determine ν_T, an equation for the turbulent kinetic energy b must be introduced and solved.

2.2.3. Turbulent Kinetic Energy Equation

According to Rodi [28], the equation for the mean turbulent fluctuation energy $b(z)$ can be written as

$$C_D C_\mu \frac{b^2}{\nu_T} = \nu_T \left(\frac{\partial \tilde{\bar{u}}}{\partial z} \right)^2 + \frac{d}{dz}\left[\left(\frac{\nu_T}{\sigma_b} + \nu \right) \frac{db}{dz} \right] + \overline{X'u'} + 2\nu \left(\frac{db^{1/2}}{dz} \right)^2 - \frac{g}{T\sigma_b}\left(\nu_T \frac{d\tilde{\bar{T}}}{dz} \right) \tag{2.12}$$

where C_D, C_μ, and σ_b are empirical coefficients. $C_D C_\mu \approx 0.08$ and $\sigma_b = 1$ appear to be reasonable values of the empirical constants [1, 7, 25, 26]. It can be concluded [1, 7, 25, 26] that

$$\overline{X'u'} = c_d S_w \tilde{\bar{u}}^3 . \tag{2.13}$$

It then follows that the equation for $b(z)$ can be written as

$$C_D C_\mu \frac{b^2}{\nu_T} = \nu_T \left(\frac{\partial \tilde{\bar{u}}}{\partial z} \right)^2 + \frac{d}{dz}\left[\left(\frac{\nu_T}{\sigma_b} + \nu \right) \frac{db}{dz} \right] + c_d S_w \tilde{\bar{u}}^3 + 2\nu \left(\frac{db^{1/2}}{dz} \right)^2 - \frac{g}{T\sigma_b}\left(\nu_T \frac{d\tilde{\bar{T}}}{dz} \right) \tag{2.14}$$

2.2.4. Thermal Energy Equations

2.2.4.1. Fluid Phase

The steady-state turbulent thermal energy transport equation in the fluid phase is given in Equation (2.3). Applying the VAT method, the averaged thermal energy

equation in the fluid phase of the porous medium for turbulent flow is

$$\rho_f c_{pf}\left[\langle m\rangle\tilde{\bar{u}}_j\frac{\partial\tilde{\bar{T}}_f}{\partial x_j}-\tilde{\bar{T}}_f\frac{1}{\Delta\Omega}\int_{\partial S_w}\bar{u}_j\cdot d\vec{s}\right]+\rho_f c_{pf}\left(\frac{\partial}{\partial x_j}\left\langle\hat{\bar{T}}_f\hat{\bar{u}}_j\right\rangle_f+\frac{1}{\Delta\Omega}\int_{\partial S_w}\bar{u}_j\bar{T}_f\cdot d\vec{s}\right)=$$
$$\frac{\partial}{\partial x_j}\left(\langle m\rangle k_f\frac{\partial\tilde{\bar{T}}_f}{\partial x_j}\right)+\frac{1}{\Delta\Omega}\int_{\partial S_{wL}}k_f\frac{\partial\bar{T}_f}{\partial x_j}\cdot d\vec{s}+\frac{\partial}{\partial x_j}\left(\frac{k_f}{\Delta\Omega}\int_{\partial S_w}\bar{T}_f ds\right) \tag{2.15}$$
$$-\frac{\partial}{\partial x_j}\left\langle\overline{T_f{}'u_j{}'}\right\rangle_f-\frac{1}{\Delta\Omega}\int_{\partial S_w}\overline{T_f{}'u_j{}'}\cdot d\vec{s}$$

In analogy to the concept of eddy viscosity, the turbulent fluctuation terms in Equation (2.15) are taken as proportional to the mean temperature gradients. Further, assuming no flow penetration through the interphase surface, the thermal energy equation in the fluid phase is reduced to

$$\rho_f c_{pf}\langle m\rangle\tilde{\bar{u}}_j\frac{\partial\tilde{\bar{T}}_f}{\partial x_j}+\rho_f c_{pf}\frac{\partial}{\partial x_j}\left\langle\hat{\bar{T}}_f\hat{\bar{u}}_j\right\rangle_f=\frac{\partial}{\partial x_j}\left[\langle m\rangle\left(k_T+k_f\right)\frac{\partial\tilde{\bar{T}}_f}{\partial x_j}\right]$$
$$+\frac{1}{\Delta\Omega}\int_{\partial S_w}\left(k_T+k_f\right)\frac{\partial\bar{T}_f}{\partial x_i}\cdot d\vec{s}+\frac{\partial}{\partial x_j}\left(\frac{k_f}{\Delta\Omega}\int_{\partial S_w}\bar{T}_f ds\right) \tag{2.16}$$

where k_T is the turbulent heat conductivity.

2.2.4.2. Solid Phase

The steady-state thermal energy transport equation in the solid phase is given in Equation (2.4). Applying the VAT method, the averaged thermal energy equation in the solid phase of the porous medium is

$$\frac{\partial}{\partial x_j}\left[\left(1-\langle m\rangle\right)k_s\frac{\partial \tilde{T}_s}{\partial x_j}\right]+\frac{\partial}{\partial x_i}\left(\frac{k_s}{\Delta\Omega}\int\limits_{\partial S_w}T_s ds\right)+\frac{1}{\Delta\Omega}\int\limits_{\partial S_w}k_s\frac{\partial T_s}{\partial x_i}\cdot d\vec{s}_1=0\,, \tag{2.17}$$

where

$$d\vec{s}_1=-d\vec{s}\,. \tag{2.18}$$

2.3. Transport Coefficients and Closure Statements

Nonlinear equations accounting for turbulent transport developed from VAT were presented in Equations (2.6), (2.9), (2.16), and (2.17). To be closed, these equations require the evaluation of transport coefficient models. The coefficients in the equations, as well as the form of the equations themselves, must be consistent to accurately model the processes and morphology of the porous medium [1-7]. The integral terms in the equations must be dropped or transformed in a rigorous fashion consistent with physical arguments regarding the porous medium structure, and flow and heat transfer regimes [1-7]. Coefficient models used must be strictly connected to the porous medium morphology models, meaning that the coefficient values are determined in a manner consistent with the selected geometry [1-7].

It is apparent that the VAT-based transport equations have more integral and differential terms than the homogenized or classical continuum mechanics equations, e.g. Equations (2.1) - (2.4). The description of the porous media structural morphology

determines the importance of these terms and the range of application of the closure schemes. The natural way to close the integral terms in the transfer equations is to attempt to find the integrals over the interphase surface, or over outlined areas of this surface [1-7]. Closure models allow one to find connections between experimental correlations for bulk processes and the simulation representation, and then incorporate them into numerical procedures [1-7].

2.3.1. Friction Factor and Momentum Equation

The VAT-based momentum equation, for turbulent steady-state flow and no flow penetration through the interphase surfaces, is given by Equation (2.9). From a physical point of view, the integral terms represent momentum loss due to the friction resistance and form drag over the interphase surfaces. The skin friction coefficient c_f is defined by, and conveniently decomposed as

$$c_f \equiv \frac{\int_{\partial S_w} \vec{\tau}_w \cdot d\vec{s}}{\frac{1}{2}\rho_f A_w \tilde{\bar{u}}^2} = \frac{\int_{\partial S_{wL}} \vec{\tau}_{wL} \cdot d\vec{s} + \int_{\partial S_{wT}} \vec{\tau}_{wT} \cdot d\vec{s}}{\frac{1}{2}\rho_f A_w \tilde{\bar{u}}^2} \equiv c_{fL} + \tilde{c}_d \,, \tag{2.19}$$

where τ_w is the wall shear stress, τ_{wL} and τ_{wT} are the decomposed wall shear stresses for the laminar and turbulent regions respectively, and c_{fL} and $\tilde{c}_d$ are the respective decomposed skin friction coefficients. The form drag coefficient c_{dp} for flow over an obstacle is defined as

$$c_{dp} \equiv \frac{-\int_{\partial S_w} \overline{p} ds}{\frac{1}{2}\rho_f A_{wp} \tilde{\tilde{u}}^2}, \tag{2.20}$$

where A_{wp} is the cross-flow projected area. It will prove convenient to group these drag coefficients into an overall drag coefficient c_d. Vadnjal [26] and Catton [7] wrote a general expression for c_d, incorporating additional terms, as

$$c_d = c_{dp}\left(\frac{S_{wp}}{S_w}\right) + c_{fL} + \tilde{c}_d - \frac{\frac{\partial}{\partial x_j}\left\langle \hat{\tilde{u}}_i \hat{\tilde{u}}_j \right\rangle_f}{\frac{1}{2}\rho_f \tilde{\tilde{u}}^2} + \frac{\frac{\partial}{\partial x_j}\left(\left\langle \nu_T \frac{\partial \tilde{\tilde{u}}_i}{\partial x_j} \right\rangle_f\right)}{\frac{1}{2}\rho_f \tilde{\tilde{u}}^2}, \tag{2.21}$$

where in [7, 26] it was explained that the first term is the form drag, the second term is the laminar contribution to skin friction, the third term is the turbulent contribution to skin friction, and the fourth term represents spatial flow oscillations which are a function of the porous medium's morphology and tells one how the flow is being deviated from some mean value over the REV. There are two possibilities of flow deviations in this term: one is solely due to flow time and space dependent oscillations, and the other is solely due to morphology variations in the direction of the flow. Vadnjal and Catton [7, 26] also wrote down a fifth term that they explained represents flow oscillations that are due to the Reynolds stresses and is a function of the porous medium's morphology and its time averaged flow oscillations. The closed momentum equation is then simply written

as

$$\langle m\rangle \tilde{\bar{u}}_j \frac{\partial \tilde{\bar{u}}_i}{\partial x_j} = -\frac{1}{\rho_f}\frac{\partial \langle \bar{p}\rangle_f}{\partial x_i} + \frac{\partial}{\partial x_j}\left(\langle m\rangle(\nu + \nu_T)\frac{\partial \tilde{\bar{u}}_i}{\partial x_j}\right) + \frac{1}{2}c_d S_w \tilde{\bar{u}}_i^2 . \tag{2.22}$$

For constant morphological characteristics and flow field properties, and fully developed flow, Travkin and Catton [1] showed that the friction factor f is directly related to the drag coefficient, and correlated, as

$$c_d = f \equiv \frac{d_h}{2\rho_f \tilde{\bar{u}}^2}\frac{\Delta p}{L} = \frac{\mathrm{A}}{\mathrm{Re}} + \mathrm{B}, \tag{2.23}$$

where A and B are constants corresponding to the morphology of the porous media, the Reynolds number is defined as

$$\mathrm{Re} = \frac{\tilde{\bar{u}} d_h}{\nu}, \tag{2.24}$$

and the porous media length scale is

$$d_h = \frac{4\langle m\rangle}{S_w}. \tag{2.25}$$

Past work [1, 7, 26, 29] was able to show that choosing the above form of f, in Equation (2.23), allows one to collapse capillary flow and flow in a bed of spheres, spanning the

physical description from globular to capillary geometry with a single length scale, i.e. d_h. See Appendix A for a discussion on the basis for using the length scale given in Equation (2.25). The friction factor presented above has two distinctive terms, each corresponding to different pressure drop mechanisms. One is attributed to the viscous flow, that is linearly proportional to velocity and the other term is due to convection of the fluid momentum that is proportional to the velocity squared.

2.3.2. Heat Transfer Coefficient and Thermal Energy Equations

2.3.2.1. Fluid Phase Equation

The VAT-based fluid phase energy equation is given by Equation (2.16). The nature of the equation shows that the energy transferred from the surface is integrated over an area and then divided by an REV volume. Therefore, the heat transfer coefficient is defined in terms of the porous medium's morphology, usually described by the specific surface area and the porosity. The number and the nature of the closure terms in the VAT-based governing equations were rigorously derived from the lower-scale governing equations and they are clearly defined. The heat transfer coefficient definition is written as

$$h = \frac{\frac{1}{\Delta\Omega}\int_{\partial S_w}\left(k_f + k_T\right)\frac{\partial \overline{T}_f}{\partial x_i}\cdot d\vec{s} - \rho_f c_{pf}\frac{\partial}{\partial x_j}\left\langle \hat{\tilde{T}}_f \hat{\tilde{u}}_j \right\rangle_f + \frac{\partial}{\partial x_j}\left(\frac{k_f}{\Delta\Omega}\int_{\partial S_w}\overline{T}_f ds\right)}{S_w\left(\tilde{T}_s - \tilde{\overline{T}}_f\right)}. \quad (2.26)$$

The first term represents smaller scale inter-phase heat transfer, the second term

represents spatial velocity and temperature fluctuations, and the third term represents larger scale heat transfer. The second and third terms in Equation (2.26) can be neglected by assuming fully developed flow and using scaling arguments [26], respectively, significantly simplifying the scope of the closure problem. The VAT-based fluid phase energy equation can now be closed and written simply as

$$\rho_f c_{pf} \langle m \rangle \tilde{\bar{u}}_j \frac{\partial \tilde{\bar{T}}_f}{\partial x_j} = \frac{\partial}{\partial x_j}\left[\langle m \rangle \left(k_f + k_T \right) \frac{\partial \tilde{\bar{T}}_f}{\partial x_j} \right] + hS_w \left(\tilde{T}_s - \tilde{\bar{T}}_f \right). \tag{2.27}$$

The heat transfer coefficient is correlated in terms of the Nusselt number as

$$\mathrm{Nu} \equiv \frac{hd_h}{k_f} = \mathrm{C}\,\mathrm{Re}^{\mathrm{D}}\,\mathrm{Pr}^{1/3}, \tag{2.28}$$

where C and D correspond to the type of porous media morphology. A $\mathrm{Pr}^{1/3}$ dependence is precedent for gas flows [30-32], which are prevalent in this dissertation, however this assumption should not be made for liquid flows.

2.3.2.2. Solid Phase Equation

The VAT-based energy equation for the solid phase is given by Equation (2.17). On the fluid side, the energy equation closure for the heat exchange integral terms is naturally described as heat flux transferred from the surface and is embodied in the heat transfer coefficient. By performing an energy balance at the interface between the solid and fluid, see [26], one can see that the heat exchange from solid phase to fluid phase is

of equal magnitude, but with opposite sign to the heat exchange from fluid phase to solid phase and it is evident that the heat transfer coefficient is the connection between the two phases at the upper scale. In the fluid, the energy transport is due to the laminar or the turbulent convective heat transport, depending on the flow regime, while on the solid side energy is transferred by conduction only. From the interface energy balance, the VAT-based solid phase energy equation can now be closed as

$$\frac{\partial}{\partial x_j}\left[\left(1-\langle m\rangle\right)k_s\frac{\partial \tilde{T}_s}{\partial x_j}\right]-hS_w\left(\tilde{T}_s-\tilde{\tilde{T}}_f\right)=0\,. \tag{2.29}$$

2.4. Conclusions

Applying the method of volume averaging to the lower-scale governing equations, Equations (2.1) - (2.4), has resulted in simple upper-scale field equations, Equations (2.6), (2.22), (2.27) and (2.29), with explicitly defined transport coefficients, Equations (2.21) and (2.26). These simple upper-scale equations offer significant advantages, particularly for design and optimization efforts. However, before the simple equations are obtained, the closure problem must be addressed by evaluating the explicitly defined transport coefficients. Chapter 3 will explore experimental techniques to evaluate these transport coefficients, paving the way towards the simple VAT-based equations given in this chapter and allowing for intelligent design algorithms to operate on the hierarchical physical model.

3. EXPERIMENTAL CLOSURE OF THE VAT-BASED GOVERNING EQUATIONS

In Chapter 2 a correct physical-mathematical representation of transport phenomena in heterogeneous hierarchical structures for which full conjugate effects are accounted is accurately formulated in the VAT-based governing equations, providing a fundamental understanding of the problem. However, as was explained, the numerical tools available are not sufficient for the mathematical complexities present in solving the integro-differential VAT-based equations, i.e. Equations (2.9), (2.16), and (2.17), that represent the physical phenomena. Therefore, evaluation of the lower-scale phenomena, through either numerical or experimental techniques, is relied upon to provide closure to the general upper-scale VAT-based equations and yield manageable equations that are simple enough to be readily solved yet rigorously formulated.

Closure theories for transport equations in heterogeneous media have been the primary measure of advancement and for measuring success in research on transport in porous media [1]. It is believed that the only way to achieve substantial gains is to maintain the connection between porous medium morphology and the rigorous formulation of mathematical equations for transport [1]. As was explained in Chapter 1, Travkin and Catton related the complex closure statements directly to the local transport coefficients. In general, there are different methods for obtaining closure to the VAT-based governing equations describing transport phenomena within a heterogeneous structure. For previously studied structures one can refer to published experimentally or

numerically derived correlations that are provided for fully-developed conditions provided that conjugate effects are properly taken into account, see Zhou et al. [29, 33]. However, for a new surface that may hold promise for heat transfer augmentation that has not been studied in the past closure must be obtained anew, and it can be done through either conducting lower-scale numerical simulations (e.g. with CFD) and/or an appropriate experimental study.

Recently Zhou et al. [33, 34], and in the past, Horvat and Mavko [35] and Vadnjal [36], have demonstrated the usefulness of commercial CFD packages in resolving the lower-scale and allowing direct calculations of the closure terms in the VAT-based governing equations to be made. CFD software allows the user to close the integral terms in the transport equations in a natural way, that is, by integrating over the inter-phase surface, or of some other outlined areas. Although CFD provides a convenient tool to obtain closure to the VAT-based equations, it has not replaced the value of experimental measurements in porous media studies and is incapable of accommodating many geometries. Moreover, one typically needs experimental validation for numerical studies.

Experimental results in porous media studies are indispensable. However, obtaining them, particularly the internal heat transfer coefficient, can be quite challenging for complicated and intricate morphologies. Because of the character of such structures a transient test technique is virtually mandatory to obtain the convective heat transfer data, and numerous researchers have employed variations of such a technique, see Appendix B. Typically, in such transient tests a single fluid stream, under steady flow conditions, is subjected to an inlet fluid temperature perturbation. The temperature perturbation could

be a step change or an oscillatory function. The inlet and outlet stream temperatures are measured continuously over an interval of time and compared to the predictions of a model in order to determine the desired heat transfer information. This so-called "single-blow" method, and its variations, along with various other transient techniques have been investigated, to some degree, for nearly a century, as explained in a recent review on the subject [37].

It appears that none of the existing methods have taken advantage of the theoretically rigorous modeling approach to transport in heterogeneous porous media provided by the developments in Volume Averaging Theory (VAT). VAT provides a correct description of experiments in heterogeneous media and yields clear expressions for local transport coefficients in porous media that are derived from fundamental equations using rigorous mathematical techniques, see Chapter 1. In many of the existing studies, the homogeneous presentation of medium properties is used and explanation of experiments is done via bulk features. Those bulk features describe the field as by classical homogeneous medium differential equations and the description of transport is not based on a theoretically correct development [1].

In this chapter two novel inverse experimental techniques are presented for evaluating the closure statements, i.e. Equations (2.21) and (2.26). Measurements of the closure statements are made for flow through random fiber matrices, staggered cylinder arrays, and packed particle beds. Correlations are then obtained for the convective heat transfer and flow resistance, allowing the VAT-based equations modeling flow and heat transfer in heterogeneous porous media, Equations (2.9), (2.16) and (2.17), to be closed

and conveniently subjected to optimization and design efforts, as demonstrated in Chapter 4.

3.1. Single-Blow Method for Random Fiber Matrices

This section presents a new single-blow treatment that is based on the VAT model and applies it to regenerative random fiber matrix samples. The goal is to (1) present a new general treatment of the experimental determination of heat exchanger design data, to (2) provide simple correlations for high porosity random fiber matrices for broad design applications, and to (3) illustrate how such measurements close the VAT-based equations governing transport phenomena in heterogeneous porous media. The combined experimental and computational inverse method employed here for determining the internal heat transfer coefficient in the heterogeneous porous structure combines with simple pressure drop measurements to yield the relevant design data for eight different high porosity random fiber samples. The design data is correlated based on the porous media length scale, Equation (2.25), and the transport coefficient correlations obtained are valid for gas flows over a Reynolds number range between 5 and 70. Finally, the correlations are related to the closure statements, Equations (2.21) and (2.26).

3.1.1. Background

In this section, Chapter 3.1, measurements of the internal heat transfer coefficient and friction factor for flow through high porosity random fiber matrices used as

regenerators are made that experimentally close the VAT-based equations governing transport phenomena in the porous media. Many kinds of regenerators exist in practice, and they differ from each other in the layout of their internal structures, however they are typically characterized by a high porosity (>70%) core, in order to maintain lower friction factors. Indeed, the main purpose of regenerators is to act as heat storage devices, while minimizing the amount of pumping power requirements. In the field of transport in porous media, early investigations were performed for lower porosity media, ranging from 30% to 60%, because of the wide presence of natural porous materials, well documented by Kaviany [14]. Interest in high porosity random fiber matrices [38, 39] has grown in the recent decades due to the need to improve heat exchange in several engineering applications, such as regenerators for Stirling engines [40-48], and transfer media for Phase Change Materials (PCM) used for heat storage [49]. The use of random fiber matrices is highly favorable in some applications, such as in electronic cooling systems and solar collectors. Some advanced structures have been built and tested by Knowels [50], for NASA Stirling engine applications, that were composed of several layers of different materials in order to optimize the overall performance. High porosity random fiber structures such as those considered here present an important structure whose corresponding transport properties must be carefully considered.

3.1.2. Experimental Method

To measure the internal heat transfer coefficient, steady-state flow through the fiber matrix samples is achieved. The inlet fluid temperature is then subjected to a step

change in temperature via an upstream heater and a spring-loaded shuttle mechanism. The transient air exit temperature response is measured until steady state thermal conditions are realized. A schematic of the experimental configuration is illustrated in Figure 3.1. The samples are held within the shuttle and insulated with 2 mm thick ceramic tape enclosed in 6 mm thick closed-cell foam. The stainless steel regenerator holder, or shuttle, slides vertically over a lubricated closed-cell foam strip, which insulates the shuttle mechanism from the stainless steel structure, and two lubricated side teflon walls. The entire test rig is placed on a wooden surface.

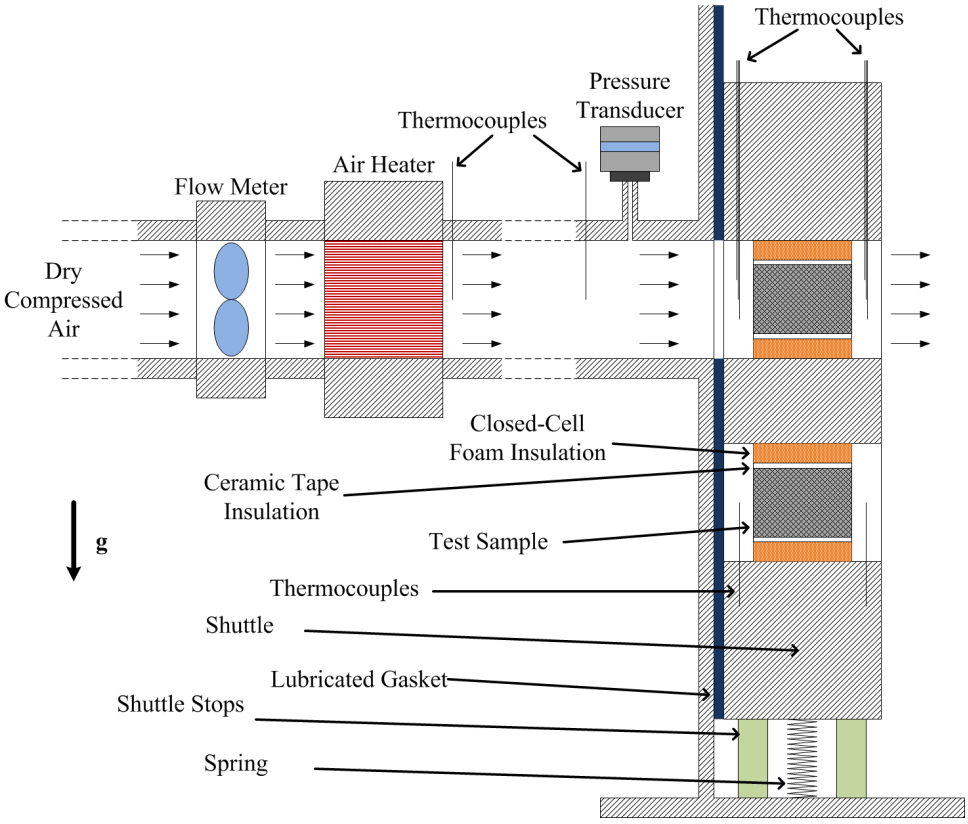

Figure 3.1: Test rig schematic.

Eight different test sections, fabricated by five different manufacturers, are considered. Their physical properties can be collected into two main groups as shown in Table 3.1. Samples A-F are made of stainless steel fibers, while samples G, and H are made of FrCr alloy. The morphological characteristics of the samples are indicated in Table 3.2.

		Sample (A,B,C,D,E,F)	Sample (G,H)	Fluid Phase (air, at 60 °C)	Insulation
Mechanical	ρ [kg m^{-3}]	7.90×10^{3}	7.20×10^{3}	1.070	40
	μ [kg m^{-1} s^{-1}]	/	/	1.99×10^{-5}	/
Thermal	k [W m^{-1} K^{-1}]	16.3	23.0	2.79×10^{-2}	0.037
	c_p [J kg^{-1} K^{-1}]	0.50×10^{3}	0.46×10^{3}	1.006×10^{3}	1.030

Table 3.1: Physical properties of the materials.

Case	d [μm]	$\langle m \rangle$	S_w [m^{-1}]
A	80	0.829	8,556.33
B	22	0.865	24,484.76
C	88	0.811	8,588.24
D	22	0.935	11,780.20
E	30	0.902	13,047.99
F	25	0.906	15,054.77
G	35	0.916	9,574.20
H	30	0.905	12,720.53

Table 3.2: Test sample properties, $L = 1.3"$, $D = 1.0"$.

Sets of thermocouples positioned upstream and downstream of the test section, as shown in Figure 3.1, measure the transient air temperature response. A flowmeter measures the air flow rate, and an air velocity transducer measures the air velocity

distribution at the inlet and outlet (under non-heating conditions). An air heater heats the upstream air.

Independent of the thermal measurements, cold-core pressure drop measurements are made. A differential pressure transducer records the pressure drop across each of the test sections for the same range of flow rates considered in the thermal tests.

3.1.3. Model and Computational Method

3.1.3.1. Internal Heat Transfer Coefficient

To determine the internal heat transfer coefficient in the fiber matrices a simulation of the transient experimental process, based on the VAT equations, is carried out. The only unknown in the simulation is the heat transfer coefficient. By matching the simulation's results to those of the experiment the heat transfer coefficient can be deduced.

To develop the model on which the simulation is based the following assumptions are made:

1. Flow and heat transfer are one-dimensional
2. Flow is incompressible and uniform
3. Properties are constant (sufficiently low temperature differences are maintained)
4. Fluid phase diffusion is negligible
5. Natural convection processes are negligible
6. Fibers are of circular cross-section
7. Porosity $\langle m \rangle$ is uniform

8. Specific surface area S_w is uniform and given by the relationship

$$S_w = 4\frac{\left(1-\langle m\rangle\right)}{d}. \tag{3.1}$$

9. Effective thermal conductivity K_{eff} is constant and determined from [51]

Therefore, the transient VAT-based thermal energy governing equations for the fluid and solid phases are

$$c_{pf}\rho_f \langle m\rangle \frac{\partial \tilde{\bar{T}}_f}{\partial t} + c_{pf}\rho_f \langle m\rangle \tilde{\bar{u}} \frac{\partial \tilde{\bar{T}}_f}{\partial x} = hS_w\left(\tilde{T}_s - \tilde{\bar{T}}_f\right), \tag{3.2}$$

and

$$\rho_s c_{ps}\left(1-\langle m\rangle\right)\frac{\partial \tilde{T}_s}{\partial t} = K_{\text{eff}}\frac{\partial^2 \tilde{T}_s}{\partial x^2} + hS_w\left(\tilde{\bar{T}}_f - \tilde{T}_s\right), \tag{3.3}$$

respectively. Here, it is worth noting that the effective thermal conductivity K_{eff} has been defined over the entire cross-sectional area of the medium, rather than over the area of the solid phase. This convention is simply for convenience.

The fluid and solid phase temperatures are written in dimensionless form as

$$\theta_{\text{f}} = \frac{\tilde{\bar{T}}_{\text{f}} - T_{\text{amb}}}{T_{\text{in}} - T_{\text{amb}}},\ \theta_{\text{s}} = \frac{\tilde{T}_{\text{s}} - T_{\text{amb}}}{T_{\text{in}} - T_{\text{amb}}}. \tag{3.4}$$

The spatial and temporal coordinates are expressed in dimensionless form as

$$x^* = \frac{x}{L}, t^* = \frac{t}{\tau}, \tag{3.5}$$

where

$$\tau = \frac{L}{\tilde{\bar{u}}}. \tag{3.6}$$

The fluid velocity is nondimensionalized as

$$u^* = \frac{\tilde{\bar{u}}}{U/\langle m \rangle}, \tag{3.7}$$

and $u^* = 1$ from the uniform flow assumption.

In writing the dimensionless VAT-based governing equations it is useful to use the following dimensionless parameters:

$$\alpha = \frac{4\mathrm{Nu}}{\chi \,\mathrm{Re}\,\mathrm{Pr}}, \ \beta = \frac{\langle m \rangle}{1-\langle m \rangle}\frac{\rho_{\mathrm{f}} c_{\mathrm{p_f}}}{\rho_{\mathrm{s}} c_{\mathrm{p_s}}}, \ \gamma = \frac{K_{\mathrm{eff}}}{k_{\mathrm{f}}}\frac{\chi}{\langle m \rangle \,\mathrm{Re}\,\mathrm{Pr}}, \tag{3.8}$$

and

$$\chi = \frac{d_h}{L} = \frac{4\langle m \rangle}{S_w L}. \tag{3.9}$$

With the above development, the governing fluid and solid phase temperature equations can be simply expressed in dimensionless form as

$$\frac{\partial \theta_{\mathrm{f}}}{\partial t^*} + \frac{\partial \theta_{\mathrm{f}}}{\partial x^*} = \alpha \left(\theta_{\mathrm{s}} - \theta_{\mathrm{f}} \right), \tag{3.10}$$

and

$$\frac{\partial \theta_{\mathrm{s}}}{\partial t^*} = \alpha\beta \left(\theta_{\mathrm{f}} - \theta_{\mathrm{s}} \right) + \beta\gamma \frac{\partial^2 \theta_{\mathrm{s}}}{\partial x^{*2}}, \tag{3.11}$$

respectively.

The initial conditions corresponding to the experimental method are

$$\theta_{\mathrm{s}} \left(x^*, 0 \right) = \theta_{\mathrm{f}} \left(x^*, 0 \right) = 0, \tag{3.12}$$

and the boundary conditions are

$$\theta_{\mathrm{f}} \left(0, t^* \right) = 1 \text{ and } \left. \frac{\partial \theta_{\mathrm{s}} \left(x^*, t^* \right)}{\partial x^*} \right|_{x^* = 0} = \left. \frac{\partial \theta_{\mathrm{s}} \left(x^*, t^* \right)}{\partial x^*} \right|_{x^* = 1} = 0. \tag{3.13}$$

With this physical model describing the thermal phenomena of the system a

numerical simulation can be performed provided that the heat transfer coefficient is known. A computational method has been developed that allows one to deduce the heat transfer coefficient from this model and the experimental data with an iterative procedure. The simulation is performed for a series of heat transfer coefficient values until the temperature response predicted by the simulation matches that obtained from the experiment. This iteration procedure is illustrated in Figure 3.2. Upon agreement of the simulation (with assumed h) and experiment, the heat transfer coefficient is known.

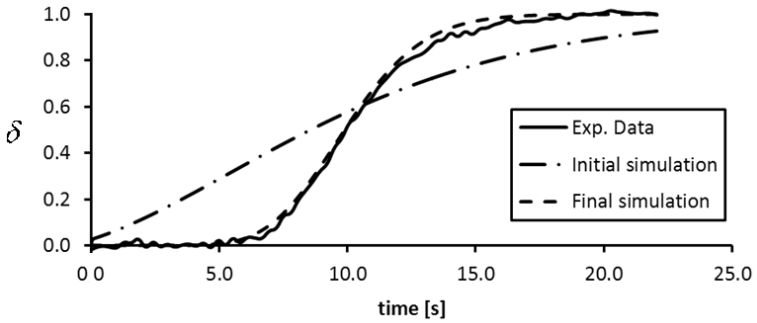

Figure 3.2: Iteration Procedure

3.1.3.2. Friction Factor

Measuring the pressure drop and friction factor in a heterogeneous porous heat transfer device, such as the compact regenerator matrix considered here, is relatively straight forward. In the typical installation of a compact heat exchanger there is a flow contraction and expansion at the exchanger entrance and exit, respectively, which can introduce additional flow-stream pressure drops and rises that the designer must consider.

As per Kays and London [30], the entrance pressure drop is attributed to that which would occur due to flow area change alone, without friction, and to that due to the irreversible free expansion and momentum changes following the abrupt contraction. Similarly, the exit pressure rise is attributed to that which would occur due to flow area change alone, without friction, and takes into account the pressure loss due to the irreversible free expansion and momentum changes following an abrupt expansion. In general, for a one-dimensional flow through a porous heat transfer device, Figure 3.3, an expression for the pressure drop is obtained by integrating the momentum equation. Kays and London [30] wrote the expression for total pressure drop through a compact heat exchanger as

$$\Delta P_{\text{tot}} = \frac{1}{2} G^2 \upsilon_1 \left[\left(K_c + 1 - \sigma^2 \right) + 2 \left(\frac{\upsilon_2}{\upsilon_1} - 1 \right) + f_{\text{K\&L}} \frac{A}{A_c} \frac{\upsilon_m}{\upsilon_1} - \left(1 - \sigma^2 - K_e \right) \frac{\upsilon_2}{\upsilon_1} \right]. \quad (3.14)$$

The conventions employed in this expression are those of Kays and London [30]. To obtain the core friction factor one must separate contraction, expansion, and acceleration effects from the core losses. The pressure drop through the core is then substituted into Equation (2.23) to obtain the desired friction factor f.

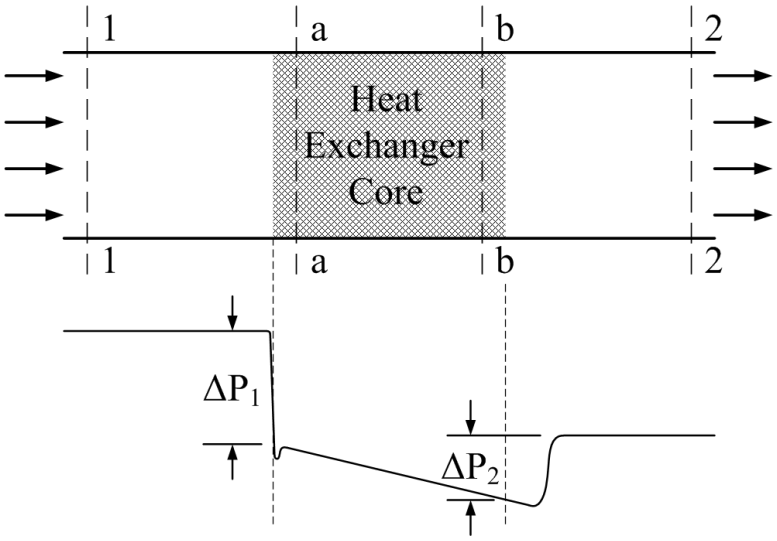

Figure 3.3: Heat exchanger core pressure drop. Adapted from Kays and London [30].

For flow through fiber matrix configurations similar contractions and expansions occur throughout the matrix as at the entrance and exit. Therefore, the entrance and exit contraction and expansion behavior is accounted for in the core friction factor and does not need separate treatment. The cold-core pressure drop expression for fiber matrices is then simply

$$\Delta P_{\text{tot}} = 2\rho\tilde{\bar{u}}^2 f \frac{L}{d_h}, \tag{3.15}$$

directly relating the measured pressure drop between the inlet and outlet to the friction factor.

3.1.4. Experimental Results

The following presents and discusses the experimental results obtained for the

random fiber matrices. First the data obtained is considered and correlations are suggested. Next the results obtained here are compared to those of other investigators. Finally, comments on the applicability of the correlations presented here are provided.

3.1.4.1. Experimental Data and Correlations

The method for obtaining the uncertainty associated with the thermal measurements in this study was outlined in [52] and involves propagating the uncertainties associated with the instrumentation through the numerical solution routine. The uncertainty associated with the thermal measurements obtained here is $\pm 8\%$, and that associated with the flow friction measurements is $\pm 5\%$.

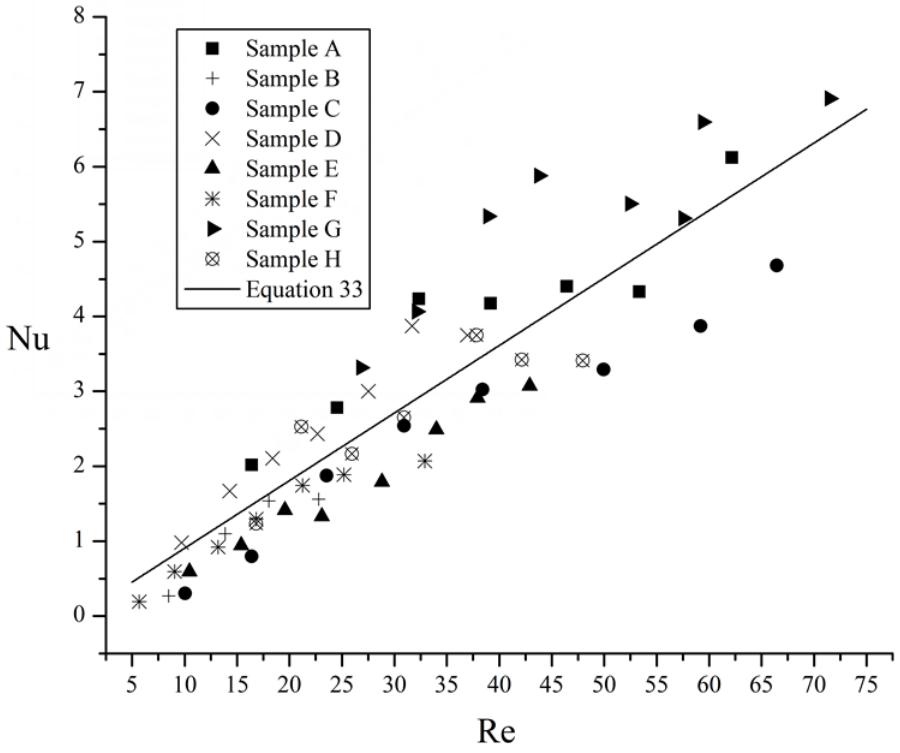

Figure 3.4: Nusselt number data and correlation, for air

The heat transfer data is presented in Figure 3.4 in terms of the Nusselt number and is correlated in the form of Equation (2.28) as

$$\mathrm{Nu} = 0.103\,\mathrm{Re}_{\mathrm{VAT}}^{0.998}\,\mathrm{Pr}^{1/3}, \tag{3.16}$$

where C = 0.103 and D = 0.998. This correlation predicts 71% of the data within 30% and is included in Figure 3.4. A comparison of the experimental data with the correlation is shown in Figure 3.5.

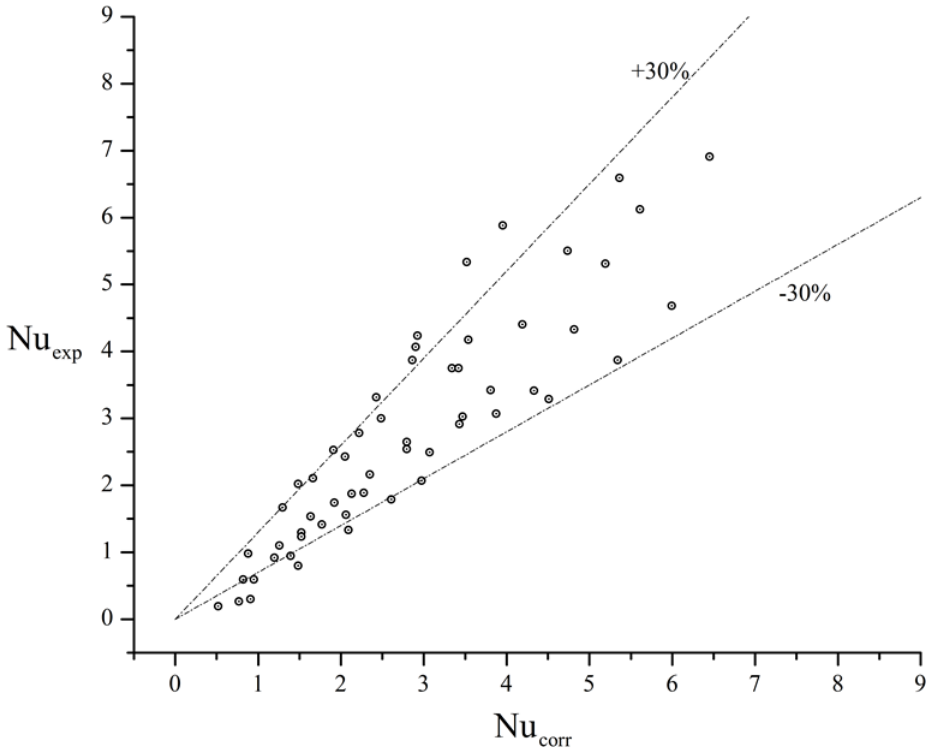

Figure 3.5: Experimental Nusselt number values plotted against the correlation values, for air

Similarly, the flow friction data is presented in Figure 3.6 in terms of the Fanning friction factor and is correlated in the form of Equation (2.23) as

$$f = \frac{36.26}{\mathrm{Re}} + 1.98, \tag{3.17}$$

where A = 36.26 and B = 1.98. This correlation predicts 78% of the data within 30% and is included in Figure 3.6. A comparison of the experimental data with the correlation is shown in Figure 3.7.

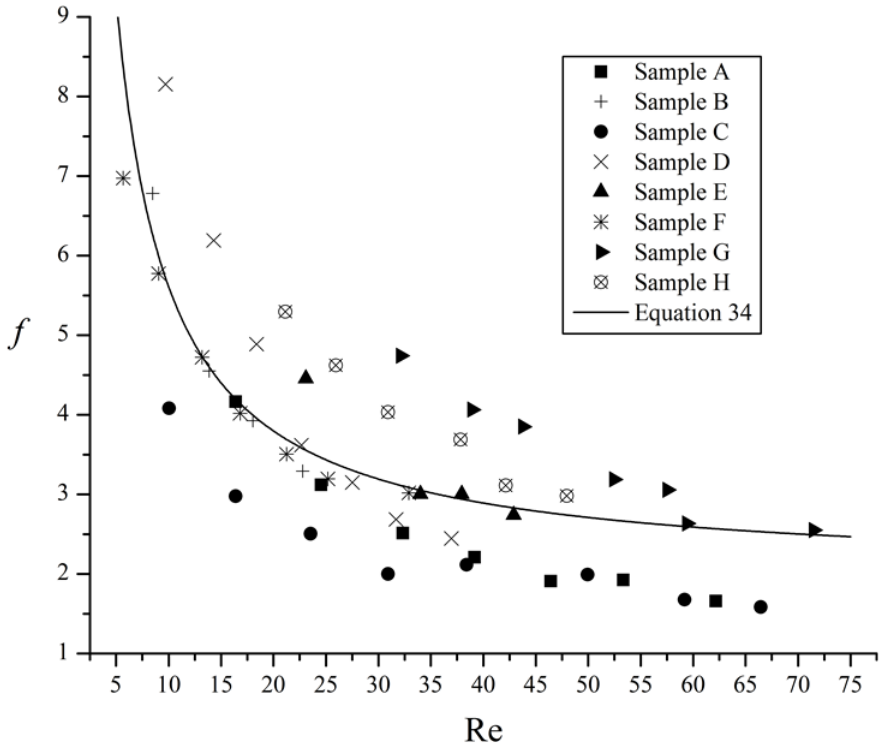

Figure 3.6: Friction factor data and correlation

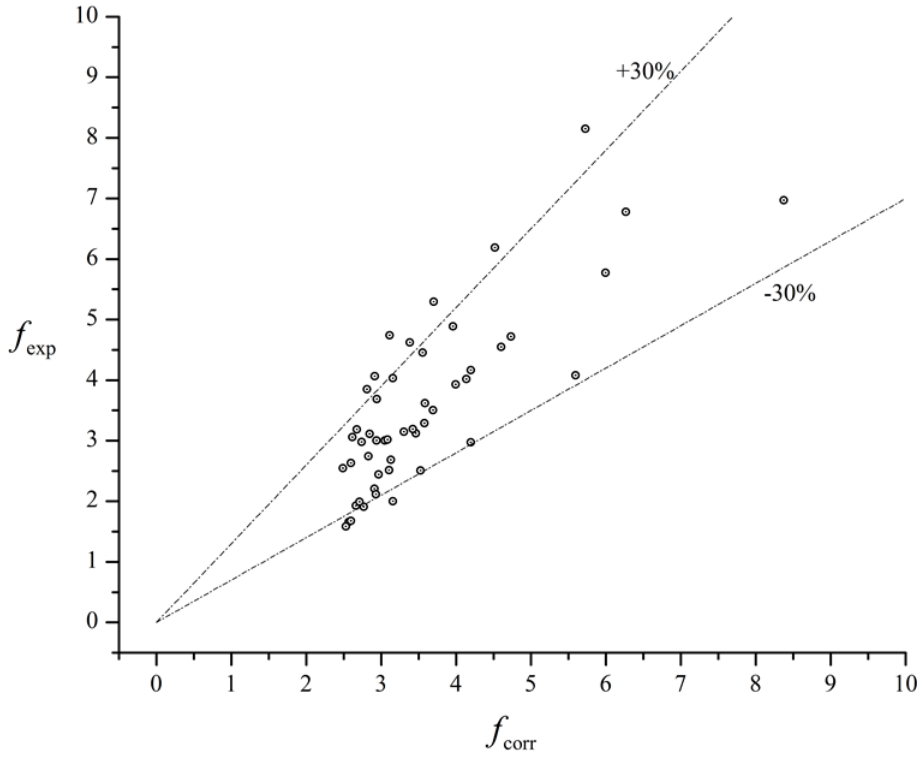

Figure 3.7: Experimental friction factor values plotted against the correlation values

The VAT-based length scale defined in Equation (2.25) achieved reasonable success in collapsing the experimental flow friction and heat transfer data from the various samples to very simple correlations. However, it is apparent that the correlations only serve as rough approximations for some of the data points. It is suspected that the primary reason for the spread of data around the correlation predictions is due to internal morphology characteristic differences due to different fabrication methods among the different manufacturers and samples not correlated with d_h. An investigation into how sample fabrication methods affect internal morphology characteristics not characterized

by d_h along with the transport coefficients in high porosity random fiber matrices should be explored in future studies.

One other observation is that the data obtained in this study was collected over a Reynolds number range of about 5 to 70. Due to the very high specific surface areas of the samples (~10^4 m^{-1}) the Reynolds numbers considered are relatively small, however the flow velocities in these tests were more moderate, ranging from about 0.5 to 3.0 m s^{-1}.

3.1.4.2. Comparisons to Existing Correlations

Data and correlations from several sources are employed for comparisons to the correlations obtained in this study. One such source, Kays and London [30], presented flow and heat transfer characteristics of several matrix surfaces (e.g. randomly stacked woven screens and spheres, along with plate-fin and glass ceramic matrices), some of which have found applications in regenerative heat exchangers. The data of Kays and London was obtained by implementing a single-blow transient test technique similar to the one employed in the present study, whereby a step change in the inlet air temperature produced a transient outlet temperature response profile whose maximum slope allowed the heat transfer coefficient to be deduced from an analysis. The major difference between their method and the present one is the transport modeling methodology used. The analysis they used was based on the early Anzelius and Schumann analysis of heat transfer to an idealized porous body [53, 54].

Gedeon and Wood [43] considered several wire mesh ($\langle m \rangle = 0.6232 - 0.7810$) and metal felt ($\langle m \rangle = 0.688 - 0.8405$) test samples typically employed in Stirling cycle

regenerators, and presented generic flow friction and heat transfer correlations for them. They obtained their data using an oscillating-flow test rig, rather than steady-flow tests. However, their previous work showed that their results are valid for both types of flows (provided the Valensi number, a dimensionless number that characterizes angular frequency, is not too large, i.e. greater than 20). To measure pressure drop the cycle mean sample pumping dissipation was inferred from the PV work done by the piston, and to measure heat transfer characteristics the cycle average net heat flux down the regenerator was inferred from cooler heat rejection less PV power and heat leaks. They expected their correlations to predict pressure drop to within about $\pm 10\%$ and $\pm 27\%$ for screens and felts respectively. Moreover, while they expected their correlations to predict overall regenerator energy flux to within $\pm 10\%$ at high Reynolds numbers around 1000, the accuracy decreased considerably at lower Reynolds numbers, due to thermal noise, to $\pm 50\%$ below a Reynolds number of about 5.

In Gedeon's Sage software user manual [55] correlations for several surfaces, including random fiber matrices are collected. The correlations for random fiber matrices presented in [55] were obtained from data gathered from tests on eight different samples (that were funded from multiple sources), the details of which are reported in personal memorandums that are cited in [55]. The data on which the random fiber matrix correlations are based was gathered using the experimental method described by Gedeon and Wood [43], discussed above.

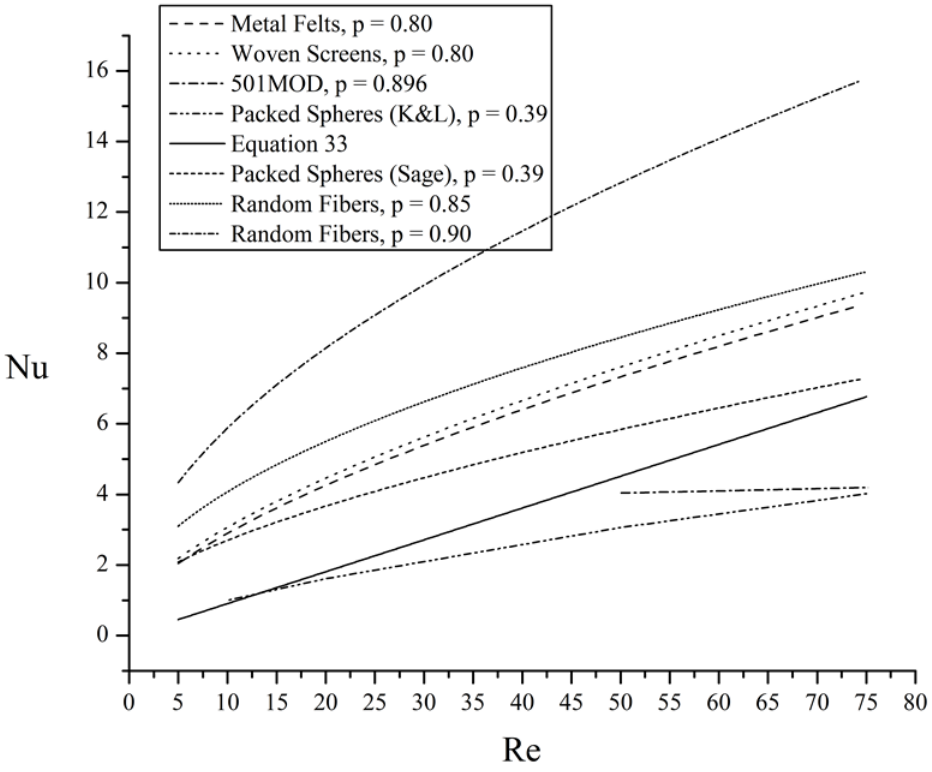

Figure 3.8: Nusselt number correlations

It is these correlations, discussed above, against which we wish to compare Equations (3.16) and (3.17). In Figure 3.8 and Figure 3.9 the correlations obtained here for Nusselt number and friction factor respectively are plotted with correlations and data from the other studies that considered, in addition to random fiber matrices, packed sphere beds, woven meshes, metal felts, and plate-fin packings. The metal felt and woven screen plots shown in Figure 3.8 and Figure 3.9 are taken from [43], and a porosity of 0.80 is taken in both correlations as the samples tested on which the correlations are based did not possess porosities much higher than this. The two plots

from [30], "501MOD" and packed spheres, are actually each based on only a single sample, the full properties of which are divulged in [30] (though the porosities of each are indicated in the figures). The second plot for packed spheres along with the two plots for random fiber matrices are taken from [55] (it is noted in [55] that the correlation for packed spheres is based on unpublished data). The two different random fiber matrix plots in each figure correspond to porosities of 0.85 and 0.90.

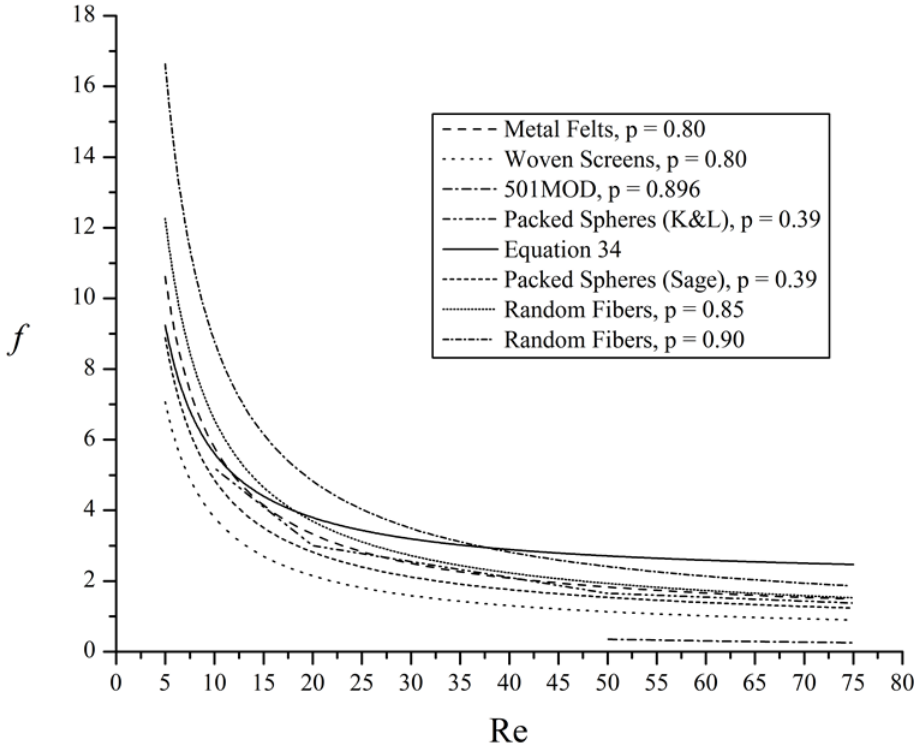

Figure 3.9: Friction factor correlations

Evident from Figure 3.8 and Figure 3.9 is that the present correlations are distinct

from the existing random fiber matrix correlations [55] in the Reynolds number range under consideration. In particular, the Nusselt number correlation produced in this study predicts significantly more conservative heat transfer characteristics than that given in [55]. Such a difference may be due to the low accuracy, due to thermal noise, of the correlations obtained using the experimental method described in [43] at the lower Reynolds numbers considered here. Alternatively, it may be due to differences in axial conduction models employed. Moreover, the friction factor correlation produced in this study predicts lower values of the friction factor at lower Reynolds numbers and higher values of the friction factor at higher Reynolds numbers compared to the correlation given in [55]. The difference in friction factor correlations is less clear.

3.1.4.3. Correlation Applications

Equations (3.16) and (3.17), correlating heat transfer and flow friction losses, respectively, in high porosity random fiber matrices, from tests on eight distinct samples, are applicable to the Reynolds number range considered, Prandtl numbers in the gas range, and both steady and oscillatory flows [43]. The data gathered here indicates that the equations correlate 78% of the friction factor data and 71% of the Nusselt number data to within 30%. While it is expected that the reliability of the correlations is decreased due to differences in internal characteristics across different manufacturers and samples not correlated with d_h, single and simple correlations for both friction factor and Nusselt number for all the samples considered are proposed.

3.1.5. Conclusions

In this section an inverse method for experimentally determining effective local transport coefficients in heterogeneous porous media based on a rigorously derived, hierarchical modeling methodology was outlined and implemented for a selection of high porosity random fiber matrix samples. New design correlations for the Nusselt number and friction factor were obtained that may be used for regenerator design applications. With the illustration of this new experimental tool, and the production of new simple design correlations for high porosity random fiber matrices for regenerative heat transfer applications, within the context of the hierarchical VAT model, future VAT-based simulation studies of such devices may be pursued.

3.2. Induction Heating Method for Cylinder Arrays

In this section a unique treatment of the experimental determination of heat exchanger design data is considered that, although analogous to the method considered in Chapter 3.1, possesses some unique advantages over that and existing techniques. This method was initially explored by Jones and Catton [56]. Here, in order to experimentally obtain the internal heat transfer coefficient, rather than implementing a fluid phase thermal perturbation, the solid phase is subjected to a step change in heat generation rate via induction heating, while the fluid flows through under steady flow conditions. Then, as before, the transient fluid phase temperature response is measured and the heat transfer coefficient is determined by comparing the results of another numerical simulation based on the VAT model with the experimental results. The friction factor is determined

through pressure drop measurements, as was done in the previous section. Several configurations of staggered cylinders in cross flow were selected for this study. Results for the heat transfer coefficient and friction factor are compared to widely accepted correlations and agreement is observed, lending validation to this new experimental method and analysis procedure.

3.2.1. Background

Many of the previously developed transient testing methods used to measure convective heat transfer characteristics of complicated surfaces, including the method considered in the previous section, suffer from difficulties with the experimental implementation of the inlet fluid stream temperature perturbation. In particular, this perturbation is often not ideal as represented in the corresponding model (e.g. a "step change" in fluid temperature is often not exactly that). In this section a method is implemented that seeks to alleviate many of the inherent experimental inconveniences associated with other transient methods, and that still rigorously models the transport phenomena within the heterogeneous and hierarchical media with VAT. Measurements of the internal heat transfer coefficient and friction factor for cross flow over staggered cylinders, i.e. tube banks or pin fins, are made, using this new method, that close the VAT-based equations governing transport phenomena in the porous medium. Applications of heat transfer to or from a bank of tubes or pin fins in cross flow include steam generation in a boiler, air cooling in the coil of an air conditioner, and heat sinking in electronics, to name just a few.

Once the VAT-based equations are closed, using the methods presented here, heterogeneous and hierarchical heat transfer devices such as the tube bank heat exchanger or pin fin heat sink, Figure 3.10, may be idealized simply as "homogeneous media" with two phases. However, strictly speaking, VAT does not homogenize the porous media. The difference between homogenization and the use of VAT is in the closure. As a result the equations look similar, but the VAT equations are rigorous when the closure is treated correctly, as is done here.

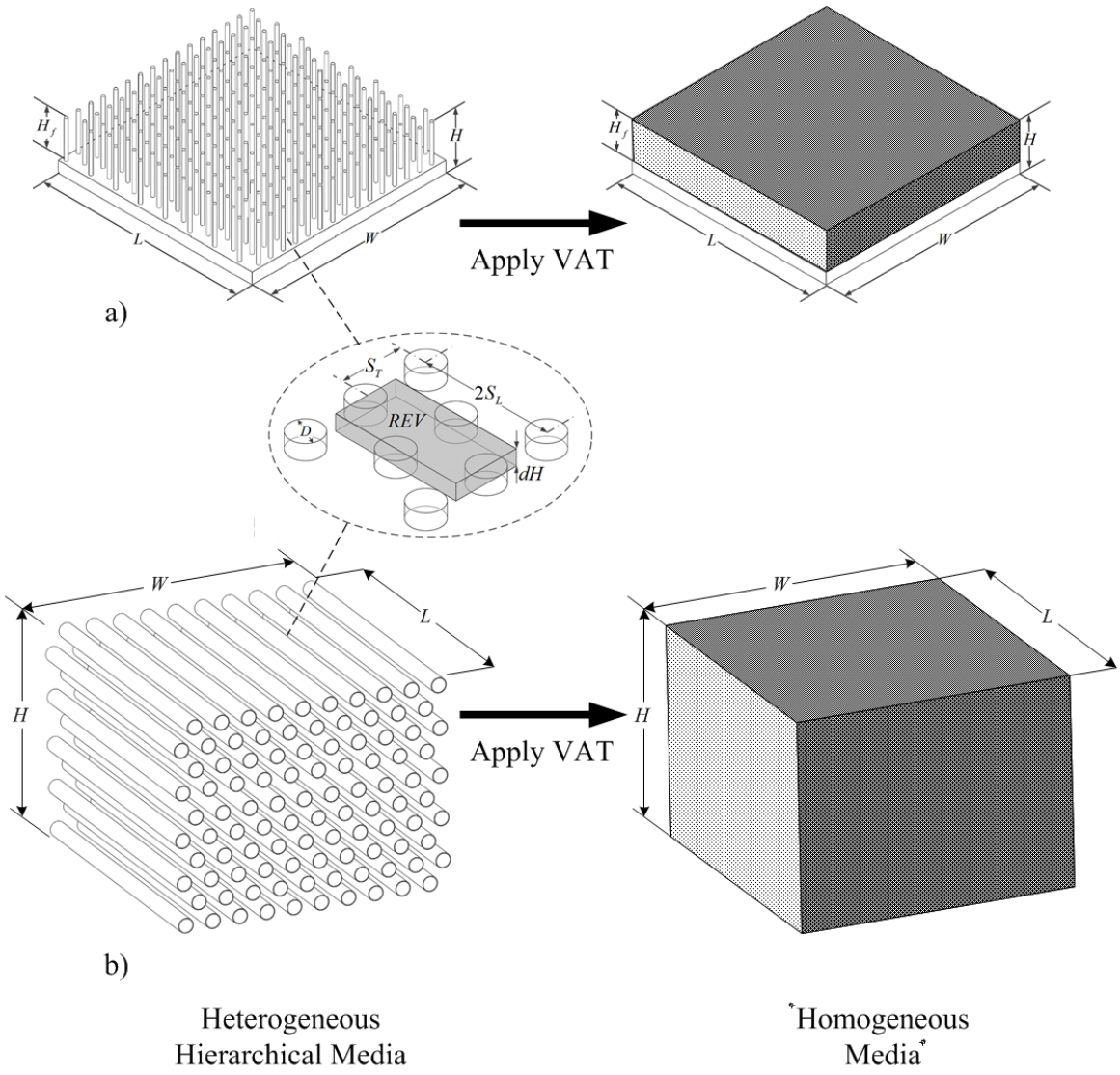

Figure 3.10: Conceptual illustration of the application of VAT with closure relationships to a) a pin fin heat sink, and b) a tube bank heat exchanger.

3.2.2. Experimental Method

To measure the internal heat transfer coefficient, in a staggered bank of cylinders using this new technique, steady-state flow across the bank is achieved. The cylinders are then subjected to a step change in heat generation rate via induction heating. The

transient air exit temperature response is measured until steady state thermal conditions are realized. It is evident that this process is analogous to that presented in the previous section. A schematic of the experimental configuration is illustrated in Figure 3.11.

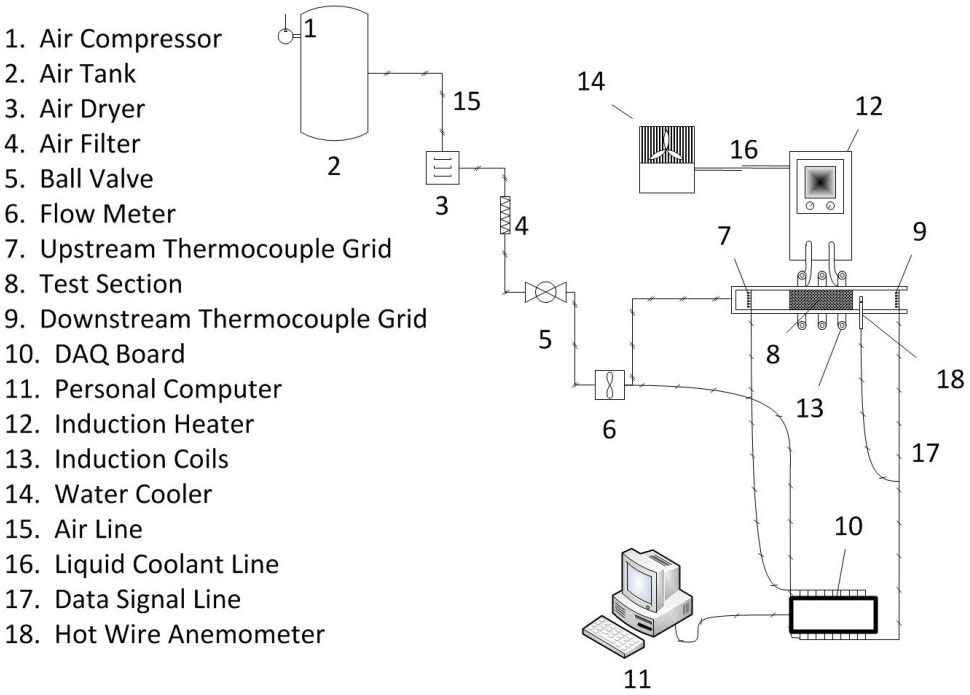

Figure 3.11: Experimental diagram.

The cylinders are plain steel. The rectangular channel in which the staggered cylinder test sections are contained is a thermoplastic, and is well insulated. The physical properties of the materials are tabulated in Table 3.3.

		Solid Phase (steel, at 100 °C)	Fluid Phase (air, at 60 °C)	Wall (PVC, at 20 °C)
Mechanical	ρ [kg m^{-3}]	7.87×10^{3}	1.070	1.4×10^{3}
	μ [kg m^{-1} s^{-1}]		1.99×10^{-5}	
Thermal	k [W m^{-1} K^{-1}]	6.03×10^{1}	2.79×10^{-2}	1.7×10^{-1}
	c_p [J kg^{-1} K^{-1}]	4.82×10^{2}	1.006×10^{3}	1.05×10^{3}
Electrical and Magnetic†	ρ_R [Ω m]	1.78×10^{-7}		
	μ_r [-] ††	5×10^{1}		

† The Curie temperature, T_C, of the steel is 770 °C. †† Approximate value.

Table 3.3: Physical properties of the materials.

Four different test sections are examined. Their morphological characteristics are tabulated in Table 3.4.

Test Section	S_T [mm]	S_L [mm]	S_D [mm]	D [mm]	H, W, L [cm]
1	4.242	4.623	5.086	1.702	4.445, 4.763, 4.623
2	4.394	4.394	4.913	1.994	4.153, 4.864, 4.394
3	5.240	5.041	5.681	3.175	5.237, 5.250, 5.041
4	8.103	7.820	8.807	6.352	7.823, 8.382, 7.820

Table 3.4: Dimensional test section configurations.

Two thermocouple grids positioned upstream and downstream of the test section, as shown in Figure 3.12, measure the transient air temperature response. A flowmeter measures the air flow rate, and an air velocity transducer measures the air velocity distribution at the inlet and outlet (under non-heating conditions).

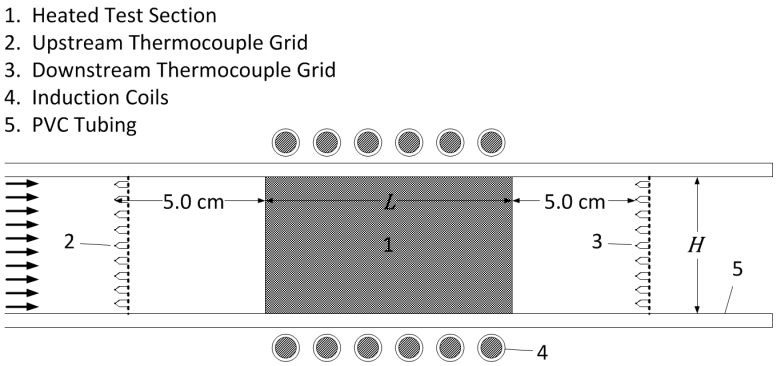

Figure 3.12: Test section diagram.

The cylinders are heated via high frequency (on the order of 10^2 kHz) induction heating. The induction coil used was of the basic solenoidal type. Spatially uniform heating of the test section was observed, with thermocouples attached to the ends of the cylinders, and carefully maintained throughout the tests.

Independent of the thermal measurements, cold-core pressure drop measurements are made. A differential pressure transducer records the pressure drop across each of the test sections for the same range of flow rates considered in the thermal tests.

3.2.3. Model and Computational Method

3.2.3.1. Internal Heat Transfer Coefficient

Heat transfer in a staggered bank of cylinders is governed mainly by flow velocity, geometry, fluid physical properties, and thermal load [57]. To determine the internal heat transfer coefficient in the staggered cylinder banks a simulation of the experimental process, based on the VAT equations, is carried out, as was done in the previous section. The only unknown in the simulation is again the heat transfer

coefficient. By matching the simulation's results to those of the experiment the heat transfer coefficient can be deduced.

To develop the model on which the simulation is based, in addition to assumptions 1 – 5 of Chapter 3.1, the following assumptions are made:

6. Heat is only generated in the cylinders
7. Porosity $\langle m \rangle$ is uniform and given by

$$\langle m \rangle = 1 - \frac{\pi}{4\chi_T \chi_L} \tag{3.18}$$

8. Specific surface area S_w is uniform and given by

$$S_w = \frac{\pi}{D\chi_T \chi_L} \tag{3.19}$$

9. Effective thermal conductivity K_{eff} is constant.

Therefore, the thermal energy governing equation for the fluid phase is given again by Equation (3.2) and that for the solid phase is given as

$$\rho_s c_{ps} \left(1 - \langle m \rangle\right) \frac{\partial \tilde{T}_s}{\partial t} = K_{\text{eff}} \frac{\partial^2 \tilde{T}_s}{\partial^2 x} + hS_w \left(\tilde{\bar{T}}_f - \tilde{T}_s\right) + \dot{Q}'''\left(1 - \langle m \rangle\right). \tag{3.20}$$

At steady-state, all energy generated by inductive heating is transferred to the gas

phase, assuming minimal lateral losses (due to radiation or natural convection, for example). Therefore, one may use a characteristic temperature difference to scale both the solid and fluid temperatures that is defined as the fluid temperature response across the porous medium at steady state. Performing an energy balance on the porous medium gives

$$\dot{Q}''' V_{\mathrm{s}} = \dot{m}_{\mathrm{f}}'' c_{\mathrm{p_f}} A_{\mathrm{s+f}} \Delta T_{\mathrm{f}} . \tag{3.21}$$

Here we have defined the mass flux in terms of the solid *and* fluid cross-sectional areas (as we did for the effective thermal conductivity). Solving the energy balance for the characteristic temperature difference ΔT_{f} gives

$$\Delta T_{\mathrm{f}} = \frac{\dot{Q}''' V_{\mathrm{s}}}{\dot{m}_{\mathrm{f}}'' c_{\mathrm{p_f}} A_{\mathrm{s+f}}} = \frac{\dot{Q}''' L \left(1 - \langle m \rangle\right)}{\dot{m}_{\mathrm{f}}'' c_{\mathrm{p_f}}}, \tag{3.22}$$

where geometrical considerations have been employed. The dimensionless fluid and solid phase temperatures are then written as

$$\theta_{\mathrm{f}} = \frac{\tilde{\tilde{T}}_{\mathrm{f}} - T_{\mathrm{in}}}{\Delta T_{\mathrm{f}}}, \; \theta_{\mathrm{s}} = \frac{\tilde{T}_{\mathrm{s}} - T_{\mathrm{in}}}{\Delta T_{\mathrm{f}}} . \tag{3.23}$$

This definition of dimensionless temperatures is particularly advantageous since it allows $\dot{Q}'''$ to drop out of the solid phase energy equation. The spatial and temporal

coordinates are expressed in dimensionless form again as given by Equation (3.5), the fluid velocity is nondimensionalized as given by Equation (3.7), and so $u^* = 1$ from the uniform flow assumption. Again it is useful to use the dimensionless parameters given by Equations (3.8) and (3.9).

With the above development, the governing fluid phase temperature in dimensionless form is again given by Equation (3.10) and the solid phase temperature equation is expressed in dimensionless form this time as

$$\frac{\partial \theta_s}{\partial t^*} = \alpha\beta\left(\theta_f - \theta_s\right) + \beta + \beta\gamma \frac{\partial^2 \theta_s}{\partial x^{*2}}. \tag{3.24}$$

The initial conditions corresponding to this experimental method are given by Equation (3.12) and the boundary conditions this time are

$$\theta_f\left(0, t^*\right) = \left.\frac{\partial \theta_s\left(x^*, t^*\right)}{\partial x^*}\right|_{x^*=0} = \left.\frac{\partial \theta_s\left(x^*, t^*\right)}{\partial x^*}\right|_{x^*=1} = 0. \tag{3.25}$$

A computational method has been developed, like the one described in the previous section, that allows one to deduce the heat transfer coefficient from this model and the experimental data with an iterative procedure, see Appendix D. This new iteration procedure is illustrated in Figure 3.13. Again, upon agreement of the simulation (with assumed h) and experiment, the heat transfer coefficient is known.

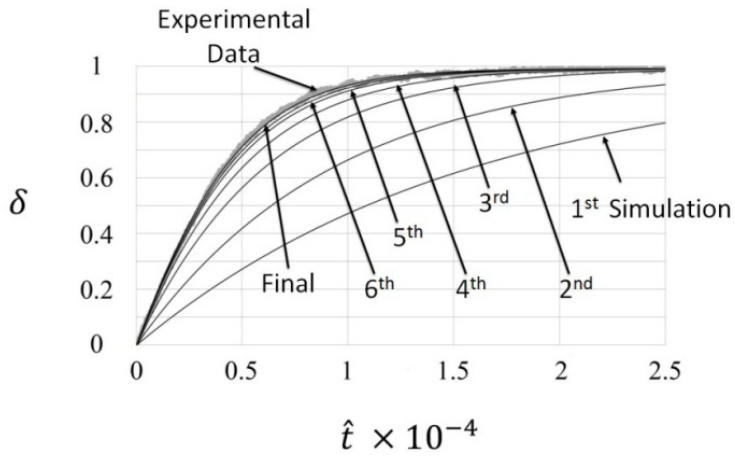

Figure 3.13: Schematic of automated iteration procedure. Each simulation corresponds to a different heat transfer coefficient value.

3.2.3.2. Friction Factor

Pressure drop across banks of staggered cylinders is governed by the flow dynamics between the cylinders and depends on the Reynolds number, geometry, and the number of transverse cylinder rows z [57, 58]. For flow normal to banks of staggered cylinders, each row consists of similar contractions and expansions. Therefore, the entrance and exit contraction and expansion behavior is accounted for in the core friction factor and does not need separate treatment, as was the case in the previous section for random fiber matrices. The cold-core pressure drop expression for staggered banks of cylinders is then simply given by Equation (3.15).

3.2.4. Discussion of Experimental Results

In 1972 Whitaker [32] obtained a correlation for convective heat transfer in cross flow over staggered tube bundles by collecting previously obtained data from a number

of investigators and rescaling it based upon a length scale similar to Equation (2.25), differing by only a constant. He found the correlation to be valid for tube bundles and, additionally, packed particle beds. Whitaker's heat transfer correlation, however, has a high uncertainty, $\pm 25\%$, and is not valid for $\langle m \rangle \geq 0.65$, which precludes its use for some of the test sections considered here.

Kays and London [30] present a relatively modest, yet still thorough, collection of their own heat transfer and flow friction design data for staggered tube bundles in cross flow in their widely cited 1985 monograph. Kays and London tested seven staggered tube bank surfaces using a transient test technique particularly well suited – but limited – to cylinders in cross flow, and made some relatively modest efforts in correlating the data. However, Kays and London stopped short of appreciably varying the geometric parameters and testing fluids other than air, and didn't devote extensive effort towards correlating their data as these objectives were not within the scope of their work.

Zukauskas and Ulinskas [57-60] established their correlations for convective heat transfer and flow friction losses based upon experiments in which they tested over 150 tube banks of different pitches and diameters while varying the flow conditions and fluid physical properties. The comprehensive correlations obtained by Zukauskas and Ulinskas for heat transfer and flow friction losses for cross flow over staggered tube banks are the most widely cited and trusted for this configuration. The uncertainty in the correlation for the average heat transfer of a tube in an inner row of a staggered bank of smooth tubes provided by the Zukauskas and Ulinskas correlation is $\pm 15\%$, however that for the friction factor does not seem to be reported. It is apparent that the data

collected here should primarily be compared to the results of Zukauskas and Ulinskas in order to gauge the present method's validity.

It is well known that the tubes in the first few rows of a tube bank serve as turbulence generators, impacting the transport phenomena occurring in subsequent rows. Transport coefficients associated with the first few rows can be significantly different from those associated with inner rows. Most investigators introduce a correction factor to account for this behavior, however different investigators report different row numbers required in order for flow and thermal conditions to stabilize. Zukauskas and Ulinskas report the relationship between the friction factor and heat transfer coefficient in a bank of staggered cylinders with a finite number of rows, f_Z^{finite} and h^{finite}, and one with an infinite number of rows, f_Z and h, respectively. For a staggered tube bank with ten rows, from Zukauskas and Ulinskas [59],

$$\frac{f_Z^{\text{finite}}}{f_Z} \approx 0.93 \text{ and } \frac{h^{\text{finite}}}{h} \approx 0.97, \tag{3.26}$$

and these ratios are used below in plotting the results.

	VAT	K&L	Z&U	W
Length Scale	$D_{\mathrm{VAT}} = 4\dfrac{\langle m \rangle}{S_w}$	$D_{\mathrm{K\&L}} = 4\dfrac{A_c L}{A}$	$D_{\mathrm{Z\&U}} = D$	$D_{\mathrm{W}} = 6\dfrac{\langle m \rangle}{S_w}$
Velocity Scale	$\tilde{\bar{u}}$	$V_{\max}$	$V_{\max}$	$\tilde{\bar{u}}$
Reynolds Number	$\dfrac{\rho \tilde{\bar{u}} D_{\mathrm{VAT}}}{\mu}$	$\dfrac{\rho V_{\max} D_{\mathrm{K\&L}}}{\mu}$	$\dfrac{\rho V_{\max} D}{\mu}$	$\dfrac{\rho \tilde{\bar{u}} D_{\mathrm{W}}}{\mu}$
Friction Factor	$\dfrac{\Delta p}{2\rho \tilde{\bar{u}}^2}\dfrac{D_{\mathrm{VAT}}}{L}$	$\dfrac{\Delta p}{2\rho V_{\max}^2}\dfrac{D_{\mathrm{K\&L}}}{L}$	$\dfrac{\Delta p}{2\rho V_{\max}^2}\dfrac{1}{z}$	
Nusselt Number	$\dfrac{h D_{\mathrm{VAT}}}{k_f}$	$\dfrac{h D_{\mathrm{K\&L}}}{k_f}$	$\dfrac{hD}{k_f}$	$\dfrac{h D_{\mathrm{W}}}{k_f}$

Table 3.5: Definitions employed by various investigators.

The conventions used in the present VAT-based analysis, and those used by Kays and London, Zukauskas and Ulinskas, and Whitaker are summarized in Table 3.5. In particular, we are presently interested in comparing the present experimental results with those of Zukauskas and Ulinskas. Explicit conversion relationships between the VAT and Zukauskas and Ulinskas dimensionless numbers are given as

$$\mathrm{Re}_{\mathrm{VAT}} = C_{\mathrm{Re}}\,\mathrm{Re}_{\mathrm{Z\&U}}, \tag{3.27}$$

$$f_{\mathrm{VAT}} = C_f f_{\mathrm{Z\&U}}, \tag{3.28}$$

and

$$\mathrm{Nu}_{\mathrm{VAT}} = C_{\mathrm{Nu}}\mathrm{Nu}_{\mathrm{Z\&U}}, \tag{3.29}$$

where the conversion factors are tabulated in Table 3.6, and depend on the test section

geometry since $V_{\max}$ may occur in either the transverse or diagonal plane, Figure 3.14. With these conversion relations the results of the present study may be directly compared to those of Zukauskas and Ulinskas.

	$\frac{\chi_T+1}{\sqrt{4\chi_L^2+\chi_T^2}}>1$	$\frac{\chi_T+1}{\sqrt{4\chi_L^2+\chi_T^2}}\le 1$
C_{Re}	$\frac{(4\chi_T\chi_L-\pi)\left(\sqrt{4\chi_L^2+\chi_T^2}-2\right)}{\chi_T\langle m\rangle\pi}$	$\frac{(4\chi_T\chi_L-\pi)(\chi_T-1)}{\chi_T\langle m\rangle\pi}$
C_f	$\left(\frac{\chi_T\langle m\rangle}{\sqrt{4\chi_L^2+\chi_T^2}-2}\right)^2\left(\frac{4\chi_T\chi_L-\pi}{\chi_L\pi}\right)$	$\left(\frac{\chi_T\langle m\rangle}{\chi_T-1}\right)^2\left(\frac{4\chi_T\chi_L-\pi}{\chi_L\pi}\right)$
C_{Nu}	$\frac{4\chi_T\chi_L-\pi}{\pi}$	

Table 3.6: Dimensionless number conversion factors between the conventions of the present VAT-based analysis and those of Zukauskas and Ulinskas.

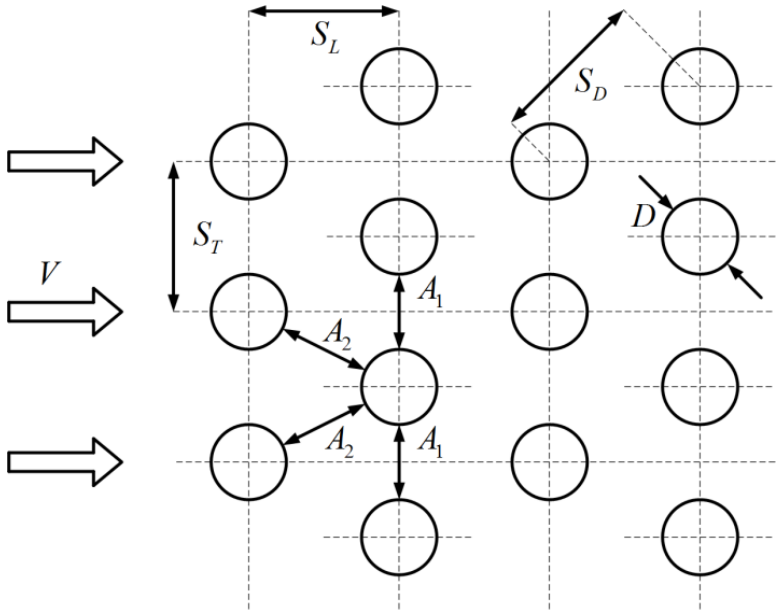

Figure 3.14: The minimum intertube space in a staggered tube bank may occur in the transverse plane, i.e. A_1, or in the diagonal plane, i.e. A_2. Adapted from [61].

In Figure 3.15 experimental results for the heat transfer coefficient measured in this study, using the novel combined experimental and numerical technique described above, for the four test sections considered, are plotted in terms of Nusselt number and Reynolds number, following Zukauskas and Ulinskas' conventions. Also plotted in this graph for comparison purposes are heat transfer data collected by Kays and London, following Zukauskas and Ulinskas' conventions, superimposed upon Zukauskas and Ulinskas' heat transfer correlation with its stated uncertainty indicated. In Table 3.7 the test section characteristics from Kays and London [30] are tabulated for easy reference and compared to those of the present study. Evident from the graph in Figure 3.15 are the Reynolds number ranges considered for each test section. To provide a more clear comparison between the experimental heat transfer data collected here and the heat transfer correlation of Zukauskas and Ulinskas, Figure 3.16 was prepared. In this figure it is clearly indicated that the present experimental heat transfer results match well with the predictions of Zukaskas and Ulinskas. In a similar fashion, Figure 3.17 was prepared to provide a clear comparison between the experimental flow friction data collected here and the flow friction correlation of Zukauskas and Ulinskas. Like Figure 3.16, Figure 3.17 clearly indicates that the present experimental flow friction results match with the predictions of Zukauskas and Ulinskas.

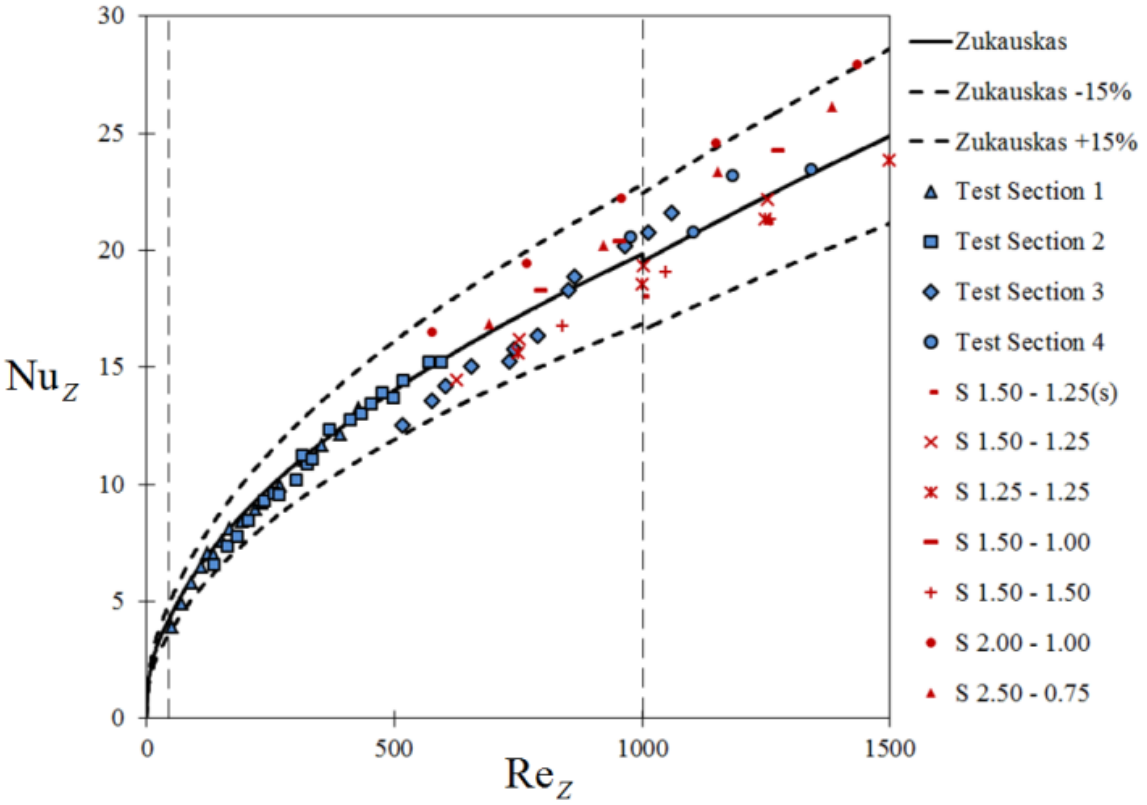

Figure 3.15: Nusselt number data plotted against Reynolds number.

Test Section	χ_T [-]	χ_L [-]	D [mm]	$\langle m \rangle$ [-]	S_w [m^{-1}]	D_{VAT} [mm]
1	2.49	2.72	1.702	0.884	272.649	12.969
2	2.20	2.20	1.994	0.838	324.410	10.333
3	1.65	1.59	3.175	0.700	377.687	7.414
4	1.28	1.23	6.352	0.500	314.943	6.350
S 1.50 - 1.25(s)	1.50	1.25	6.350	0.581	263.861	8.810
S 1.50 - 1.25	1.50	1.25	9.525	0.581	175.907	13.214
S 1.25 - 1.25	1.25	1.25	9.525	0.497	211.089	9.424
S 1.50 - 1.00	1.50	1.00	9.525	0.476	219.884	8.666
S 1.50 - 1.50	1.50	1.50	9.525	0.651	146.589	17.762
S 2.00 - 1.00	2.00	1.00	9.525	0.607	164.913	14.730
S 2.50 - 0.75	2.50	0.75	9.525	0.581	175.907	13.214

Table 3.7: Test section characteristics from the present study and from Kays and London [30].

The method for obtaining the uncertainty associated with the thermal measurements was outlined in [52] and involves propagating the uncertainties associated with the instrumentation through the numerical solution routine. The uncertainty associated with the thermal measurements obtained here is ± 8%, and that associated with the flow friction measurements is ± 5%.

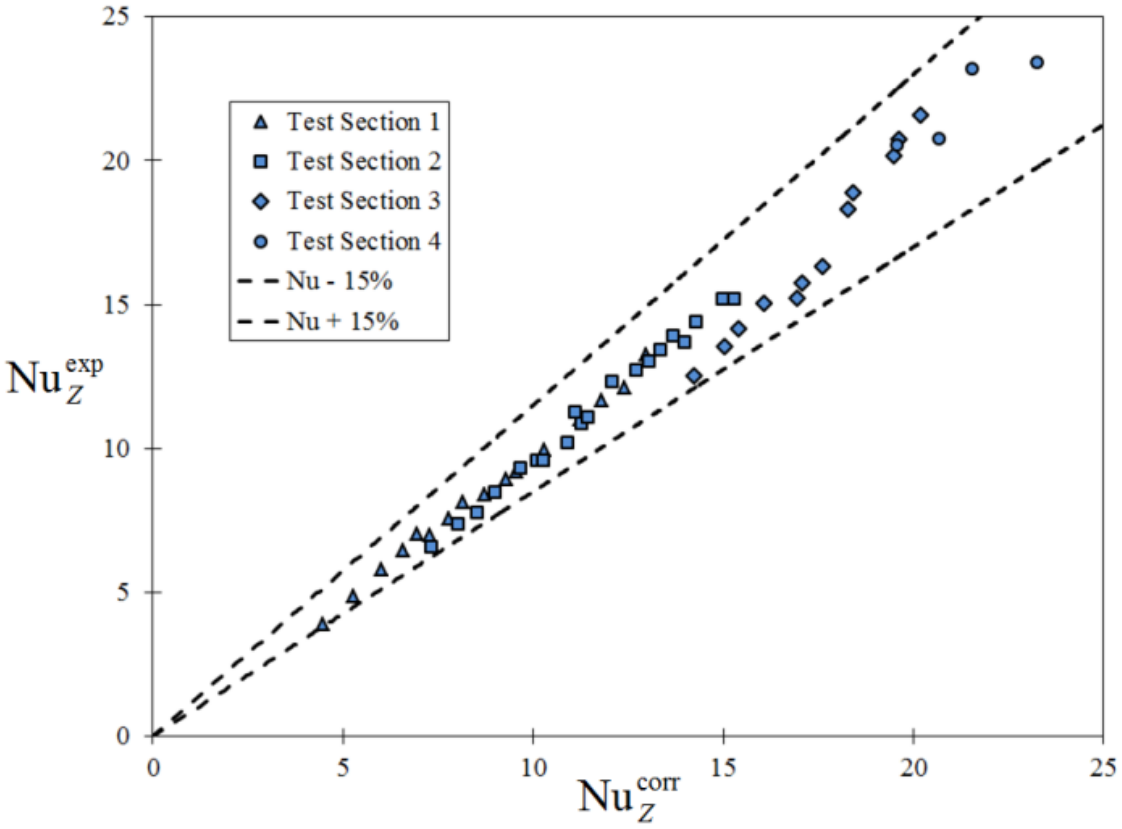

Figure 3.16: Experimental heat transfer results obtained in the present study compared to the correlation given by Zukauskas and Ulinskas [57].

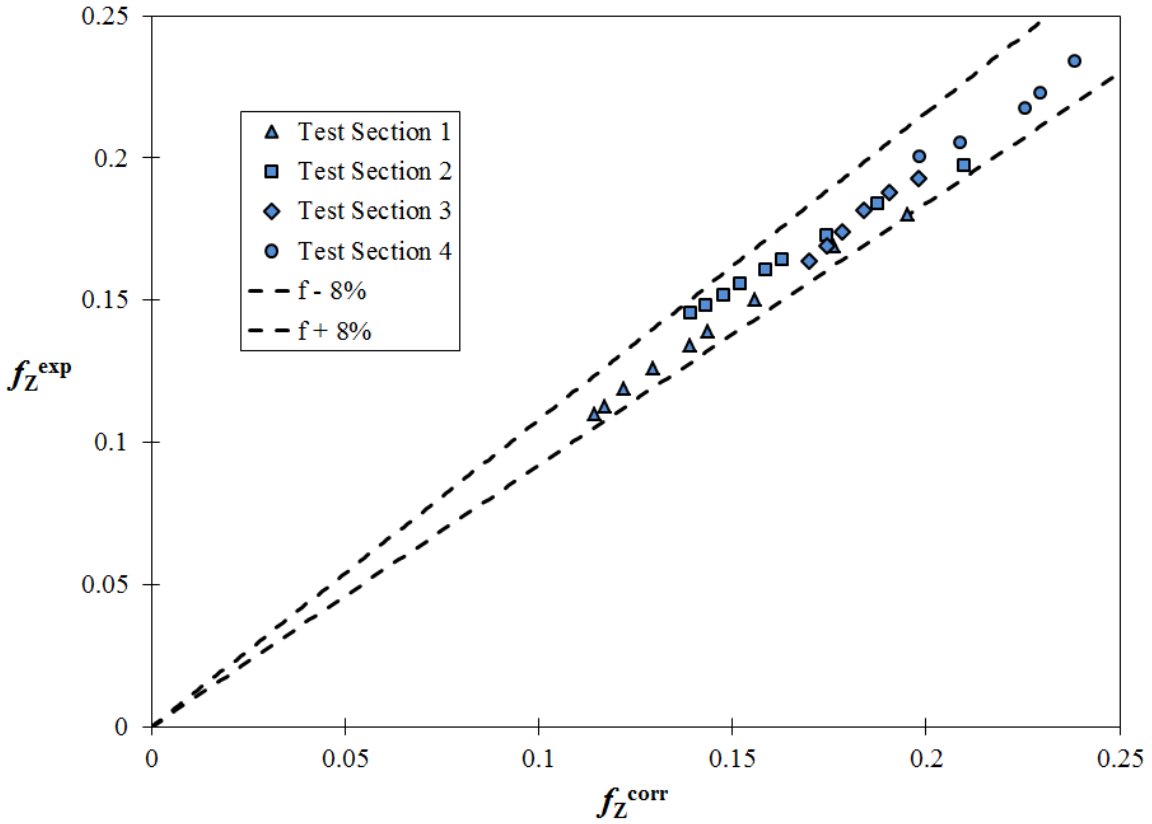

Figure 3.17: Experimental flow friction results obtained in the present study compared to the correlation given by Zukauskas and Ulinskas [58].

3.2.5. Conclusions

In this section a new method for experimentally determining effective local transport coefficients in heterogeneous and hierarchical heat transfer devices was outlined and implemented for the simple case of cross flow over staggered cylinders, which is commonly implemented in heat sinking and compact heat exchanger devices. It is expected that a more convenient and accurate tool for experimental closure of the VAT-based equations modeling transport in heterogeneous and hierarchical media, which comes down to measuring the transport coefficients, will allow for easier modeling and

subsequent optimization of high performance compact heat exchangers and heat sinks for which design data does not already exist. As was the case for the method considered in the previous section, the only information needed to determine the heat transfer coefficient is the basic material and geometric properties of the sample, the flow rate, and the transient fluid temperature response data. The computational procedure alleviates the need for solid and fluid phase temperature measurements within the porous medium. In the next section this same method is applied to measure the internal heat transfer coefficient in packed particle beds.

3.3. Induction Heating Method for Particle Beds

In this section, the non-intrusive induction heating transient testing method presented in Chapter 3.2 is applied to packed particle beds, like the ones used in heat and mass exchangers and in thermal storage applications. Measured internal heat transfer coefficients in the core of randomly packed beds of uniform spherical particles are reported, and correlated in terms of the Nusselt number, over a Reynolds number range of 20 to 500.

3.3.1. Experimental Configuration

The experimental configuration and procedure is nearly identical to that described in Chapter 3.2. Here, randomly packed beds of uniform steel spheres through which air flows are considered. The tube in which the packed bed is contained is a polyvinyl chloride (PVC) that is well insulated. The physical properties of the materials for this

study are identical to those in the previous section, see Table 3.3. A packed bed of identically sized polypropylene spheres is in contact with, and immediately upstream and downstream of, the heated test section, as illustrated in Figure 3.18. The two packed bed segments of plastic spheres are of length l, where it was ensured that $l > 10d$ and $l > D$, and serve to eliminate fluid flow inlet and outlet effects, allowing a hydrodynamically fully developed flow to enter the heated test section. Additionally, the two packed bed segments of plastic spheres ensure a uniform axial porosity in the heated section.

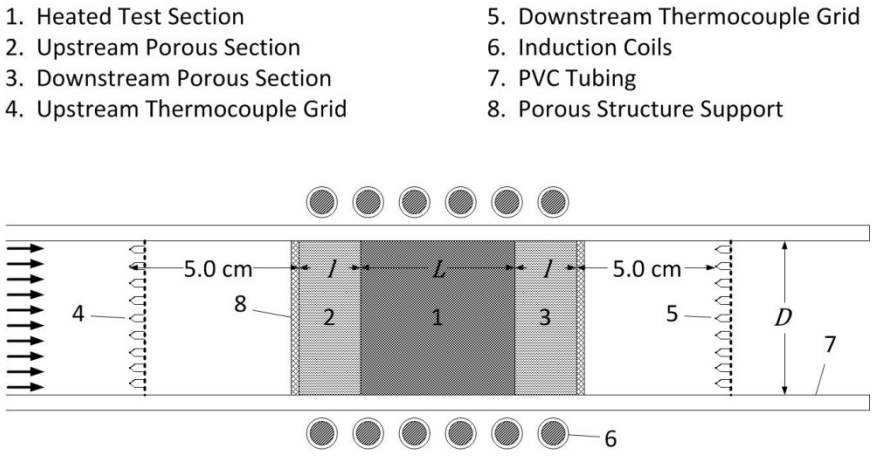

Figure 3.18: Test section diagram, not shown to scale. Item # 8 in Figure 3.11.

Three different test sections were examined. Their geometrical characteristics are tabulated in Table 3.8.

Test Section	$d \times 10^3$ [m]	$D \times 10^2$ [m]	$L \times 10^2$ [m]	$l \times 10^2$ [m]
1	1.59	6.731	1.778	6.858
2	3.18	6.731	3.226	7.163
3	4.76	6.731	4.826	6.985

Table 3.8: Geometrical characteristics of the test sections.

Two thermocouple grids are positioned upstream and downstream of the porous medium to measure the transient gas phase temperature response, see Figure 3.18. A rotameter measures the gas flow rate, and an air velocity transducer measures the gas velocity distribution at the outlet (under non-heating conditions).

3.3.1.1. Inductively Heating a Packed Bed of Spheres

The particle bed is heated via high frequency (on the order of 10^2 kHz) induction heating. The induction coil used was of the basic solenoidal type and its geometric parameters, for each test section, are indicated in Table 3.9, where d_C and P_C are the diameter and pitch of the induction coil, and D_C is the solenoid diameter. The spatial uniformity of induction heating in a packed particle bed is not at first evident.

Test Section	# of coil turns	D_C (cm)
1	2	16.51
2	3	16.51
3	4	13.97

Table 3.9: Induction coil parameters. Copper coil, d_C = 9.5 mm, and P_C = 1.27 cm. The coils are internally cooled with deionized water, flowing in a closed loop, from a water cooler.

Rhee [62] examined the internal heat generation distribution in a randomly

packed bed of stainless steel spherical particles subjected to a high frequency induction heat source. The particle bed was centered in a solenoidal work coil whose diameter, D_C, was approximately twice the diameter of the bed D. The particle bed Rhee examined was dimensionally similar to those considered in the present study (i.e., d = 6.35 mm, D = 104 mm, and L = 26 or 52 mm). Twenty thermocouples encased in thin glass tubes were distributed at various radial and axial locations in the bed. The heat generation was determined from the transient temperature response during heating. It was found that the difference between the mean value of the heat generation measurements and a single local value is less than 5%, indicating that the heat generation in the packed bed is nearly volumetrically uniform.

Somerton [63] conducted a similar experiment in which he also used high frequency induction heating to heat a packed particle bed. The primary difference between Somerton's and Rhee's experiments is that Somerton's solenoidal copper work coil was tightly wrapped around the particle bed (i.e. $D_C \approx D$). Somerton presented plots of the radial and axial heat generation distribution for a typical case. It was found that the heat generation varied by about 7% in the radial direction. In the axial direction it was observed that the heat generation "profile is very flat with a slight tapering off of the power at the ends." Cherng [64] conducted similar experiments on the uniformity of induction heating in a packed bed and came to a similar conclusion that the heat generation is essentially volumetrically uniform. Additionally, we conducted measurements for our particular experimental setup using Rhee's method [62] and observed essentially uniform heating. It is therefore evident that an assumption of

spatially uniform heat generation in the packed bed is appropriate for the purposes of this study.

Additionally, for each individual particle, the lumped thermal capacity model is valid provided that the sphere's internal resistance to heat transfer (i.e. conduction) is small compared to its external resistance (i.e. convection). The Biot number, Bi, characterizes the relative influence of internal and external resistances to heat transfer. For a sphere, Bi < 0.1 is a suitable criterion for assuming that the particle has a spatially uniform temperature [61, 65]. For the experiments considered here, the largest Biot number encountered $\mathrm{Bi}_{\max}$, neglecting conduction between particles, may be calculated, from Test Section 3 at Re = 500 (see Results section), as

$$\mathrm{Bi}_{\max} = \frac{h(d/6)}{k_s} = \frac{\left(307\ \mathrm{Wm^{-2}K^{-1}}\right)\left(4.76\times10^{-3}\ \mathrm{m}\right)}{6\left(65.2\ \mathrm{Wm^{-1}K^{-1}}\right)} = 3.7\times10^{-3} < 0.1, \tag{3.30}$$

where the characteristic length is the ratio of the particle's volume to its surface area. The lumped thermal capacity model is therefore applicable to each spherical particle in the bed for these experiments, indicating that a uniform temperature profile exists in each particle as it undergoes its transient thermal response.

3.3.1.2. Distinguishing the Near-Wall and Core Regions in a Packed Bed of Spheres

It is known that there exists a radial variation in void fraction within a randomly packed bed of uniform spheres. In particular, Benenati and Brosilow [66] demonstrated

that void fraction is unity at the wall and follows a damped oscillatory function to an essentially constant value of 0.39 in the core of the bed, about four to five sphere diameters in from the wall. This void fraction profile is due to the point contact between the spheres and the container wall, the highly ordered structure they attain near the wall, and the gradual influence of the random packing as the bed's core is approached from the wall. Martin [67] presented an algebraic expression for the void fraction profile. Investigators such as Achenbach [68] and Ziółkowska and Ziółkowski [69] have noted that this voidage profile leads to a bypass or channeling effect, that is, preferential flow near the wall of the packed bed, since pressure drop is strongly dependent upon porosity, and in particular, when the bed is heated, leads to a cold flow bypass in the near-wall region. The effect of a cold flow bypass in our experiment, if not accounted for, is to decrease the measured value of the heat transfer coefficient. Some researchers, such as Kays and London [30], specify that they are looking at an "infinite" packed bed, in which the wall effects are negligible. Ziółkowska and Ziółkowski [69] give a criterion for determining the ratio of tube to particle diameter, D/d, at which wall effects are negligible, namely, $D/d \geq 120$. Such a criterion is not realized for some test rigs and for some experimental methods. Moreover, many examples of packed beds used in industrial processes do not meet this requirement, preventing them from being modeled by a uniform radial porosity.

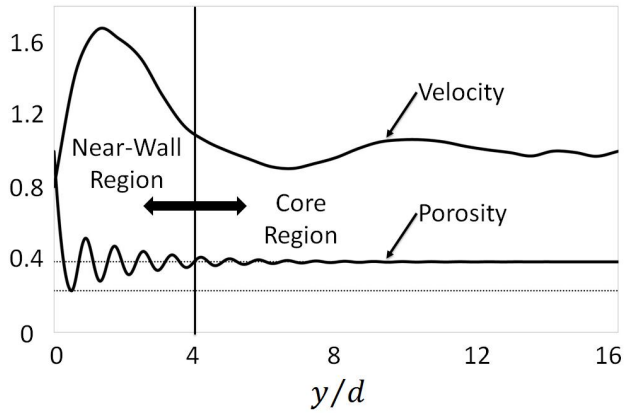

Figure 3.19: Near wall void fraction and preferential flow (velocity is scaled with centerline velocity) in a randomly packed bed of uniform spheres (spheres were not heated), Test Section 1, Re = 305. Void fraction distribution taken from the formula given in Eq. (2), where $\varepsilon_C = 0.39$, and $\varepsilon_{min} = 0.23$.

Measurements of the velocity profile in a randomly packed bed of uniform spherical particles were obtained and are presented, along with the void fraction profile, in Figure 3.19. Note that this void fraction is not the same as the volume averaged porosity, $\langle m \rangle$. Schlünder [70] proposed that for a packed bed, which is finite in the radial direction, one may divide the area perpendicular to the flow direction into a near-wall region and a core region. One then assumes uniform voidage and flow in each section. Schlünder's success, and that of others ([71], for example), with this method has led us to consider analyzing the core of our packed bed as separate from the near wall region. Schlünder defined the near-wall region to be within a distance of $0.5d$ from the wall, because the average void fraction remains practically constant at 0.39 beyond this point, and is equal to 0.50 within. From Figure 3.19 it is apparent that one may define a so called "near-wall region" within 4 sphere diameters from the wall, and a "core region"

beyond the near wall region. Unlike Schlünder's definition which is based on void fraction distribution considerations, the near-wall region definition used in this study is based on measured velocity profiles for the cases under consideration. This definition of the near-wall and core regions will be taken in our analysis and is illustrated schematically in Figure 3.20.

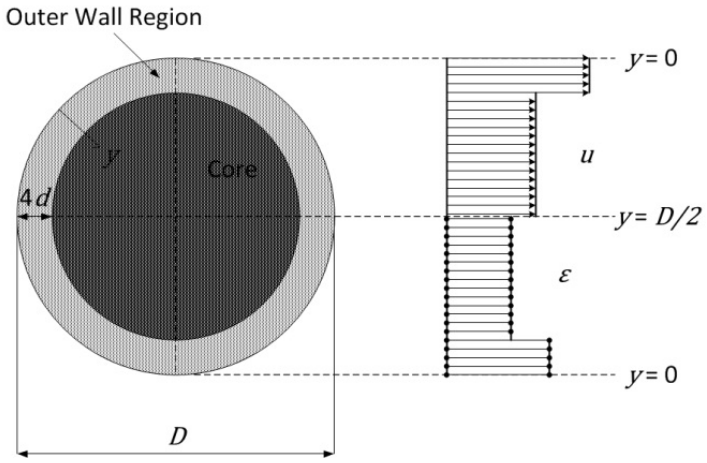

Figure 3.20: Modeling the near-wall bypass or channeling effect.

Measurements of the velocity profile in our three test sections were made at several flow rates for each test section. A calibrated air velocity transducer was used and 10^3 measurements were made for each test section and each flow rate at various radial and circumferential locations 1.50 cm above the packed bed outlet. The Dupuit-Forchheimer hypothesis [72] relates the interstitial velocity $\tilde{\bar{u}}$ to the superficial or apparent velocity U, measured by the air velocity transducer, and the bed porosity, $\tilde{\bar{u}} = U/\langle m \rangle$. From these measurements we can determine the dependence of core

velocity on the overall measured flow rate for each test section. Figure 3.21 plots the ratio of core superficial velocity U to upstream superficial velocity U' for our three test sections over the flow rate ranges considered for each test section. The upstream superficial velocity is related to the overall flow rate through the test section $\dot{m}'$, measured by the rotameter, by

$$U' = \frac{\dot{m}'}{\rho A'}, \tag{3.31}$$

where A' is the cross-sectional area of the test section. The core superficial velocity may be expressed, similarly, as

$$U = \frac{\dot{m}}{\rho A} = \frac{\dot{m}''}{\rho}, \tag{3.32}$$

where $\dot{m}$ is the mass flow rate through the core of the test section, $\dot{m}''$ is the mass flux through the core of the test section, and A is the cross sectional area of the core of the test section. The ratio of core to upstream superficial velocities may be expressed as

$$\frac{U}{U'} = \frac{\dot{m}''}{\left(\dot{m}'/A'\right)}, \tag{3.33}$$

where $\left(\dot{m}'/A'\right)$ is the overall mass flux through the test section. It is apparent from our measurements that while the bypass effect is highly dependent upon the ratio of particle

to tube diameter, it depends little upon the flow rate. In Table 3.10 the core to upstream superficial velocity ratio used to correct the rotameter readings for each flow rate is stated for each test section along with the uncertainty in its value.

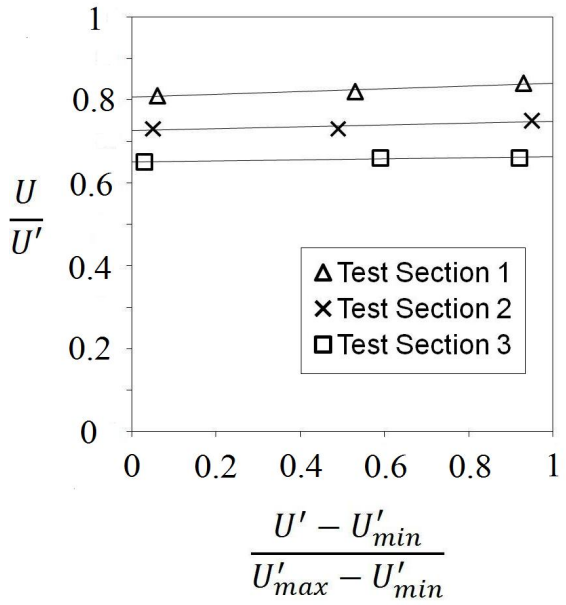

Figure 3.21: Measured ratio of core superficial velocity U to upstream superficial velocity U' for the three test sections over the flow rate ranges in each. U'_{min} and U'_{max} respectively correspond to the minimum and maximum flow rates achieved in the experiment for each of the three test sections.

	Test Section 1	Test Section 2	Test Section 3
U/U'	0.83	0.74	0.66

Table 3.10: Core to upstream superficial velocity ratios, $\pm 7\%$.

Just as the velocity is taken at the core of the packed bed for our analysis, the fluid temperature response is also taken at the outlet of the core of the packed bed. The

thermocouple grid at the outlet allows several transient fluid temperature response measurements to be made across the packed bed core for each experimental run. The average of these core flow temperature measurements are input into the solution algorithm. The spread in their values is used in assessing uncertainty in the solution.

Although turbulent flow within a packed bed on the lower scale is three-dimensional and chaotic, dividing the packed bed into a near-wall and a core region has precedent as a successful strategy (as demonstrated in [70, 71]), and thus we have decided to adopt it.

3.3.2. Model Assumptions and Effective Thermal Conductivity

Assumptions 1 – 5 of Chapter 3.1 are adopted, along with the following assumptions:

6. Heat is only generated in the steel spheres
7. Porosity $\langle m \rangle$ is uniform in the core with a value of 0.39, see [66].
8. Specific surface area S_w is uniform and given by

$$S_w = \frac{6\left(1-\langle m \rangle\right)}{d} \tag{3.34}$$

9. Effective thermal conductivity K_{eff} is constant at 20 W m^{-1} K^{-1}, see [73].

While only an approximate value of K_{eff} is taken in assumption 9, it can be observed that the particular value of the effective thermal conductivity has negligible

influence on the determination of the internal heat transfer coefficient. This can be observed in Figure 3.22, where the value of the effective thermal conductivity is varied over a wide range, yet the transient fluid temperature response profile is hardly affected by this variation. Travkin and Catton [1] show this using fundamental arguments. Figure 3.22 can be compared to Figure 3.23, where the value of h is varied over a considerably smaller range yet the temperature profiles are clearly distinguishable provided that h is not too high. For a high enough h the two temperature model will break down, and this experimental method is not viable unless the surface area of the porous structure is decreased by decreasing L, or the product $\dot{m}c_p$ is increased by changing the working fluid. Additionally, a scaling analysis shows that in the solid phase energy equation the conduction term is two orders of magnitude less than the transport and generation terms, for our experiments, and thus plays a small role in the solution.

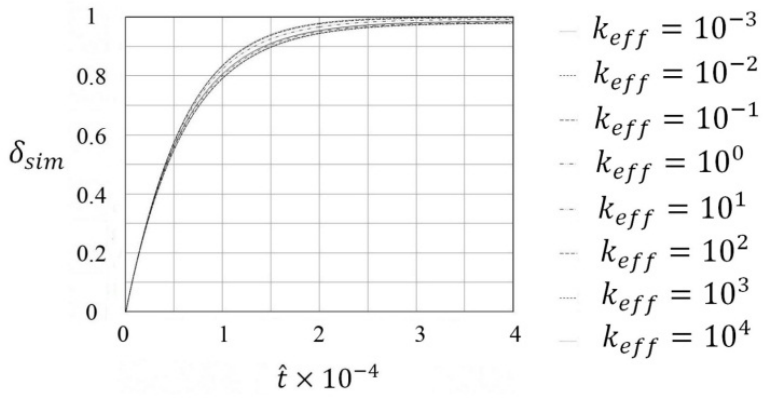

Figure 3.22: Variation of δ_{sim} versus $\hat{t}$ with effective thermal conductivity [W m^{-1} K^{-1}]. Nusselt number is unity, Re = 300.

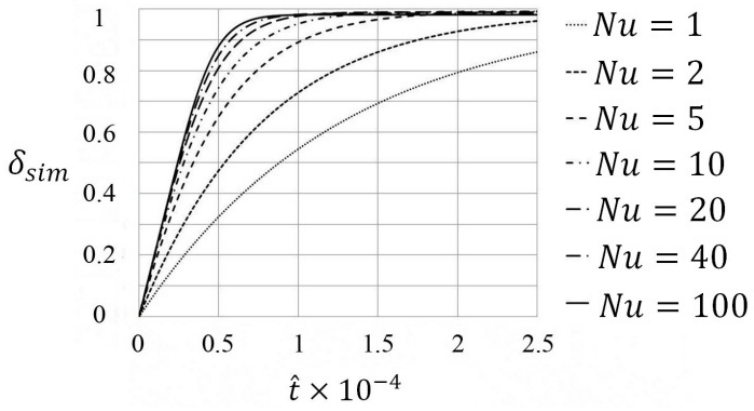

Figure 3.23: Variation of δ_{sim} versus $\hat{t}$ with Nusselt number. $K_{\text{eff}} = 20\ \text{W m}^{-1}\ \text{K}^{-1}$, Re = 300.

3.3.3. Results and Discussion

The experimental heat transfer coefficient results for Test Sections 1, 2 and 3 are plotted in Figure 3.24. In Figure 3.25 the Nusselt number data is presented along with the well-known correlations for packed beds of spheres of Kays and London [30] and Whitaker [32], and the correlation of Nie et al. [31], all of which have been expressed in terms of the VAT conventions. From our experimental data, we obtain the following new correlation for the Nusselt number as a function of the Reynolds and Prandtl numbers.

$$\text{Nu} = 0.057\,\text{Re}^{0.96}\,\text{Pr}^{1/3}. \tag{3.35}$$

This correlation is valid for Reynolds numbers between 20 and 500 and is expected to be valid at reasonable limits beyond this. In Figure 3.26 this correlation is superimposed on

a graph of a multitude of porous media convective heat transfer correlations obtained from Travkin and Catton [1].

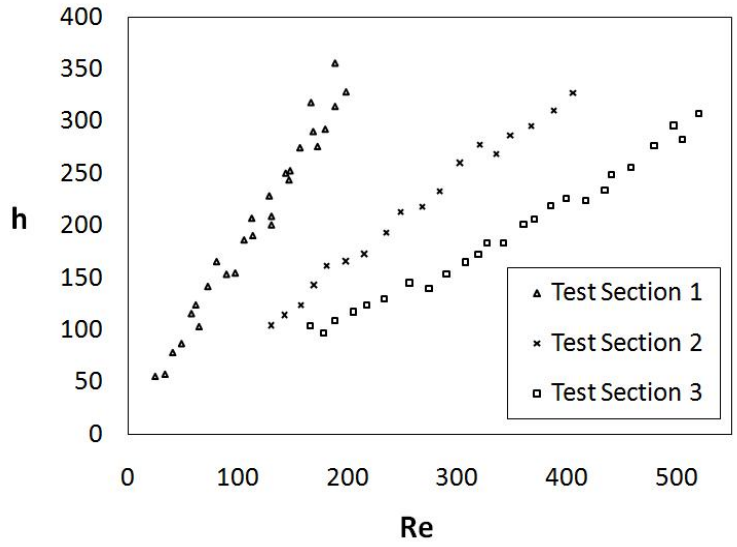

Figure 3.24: Experimental heat transfer coefficient data.

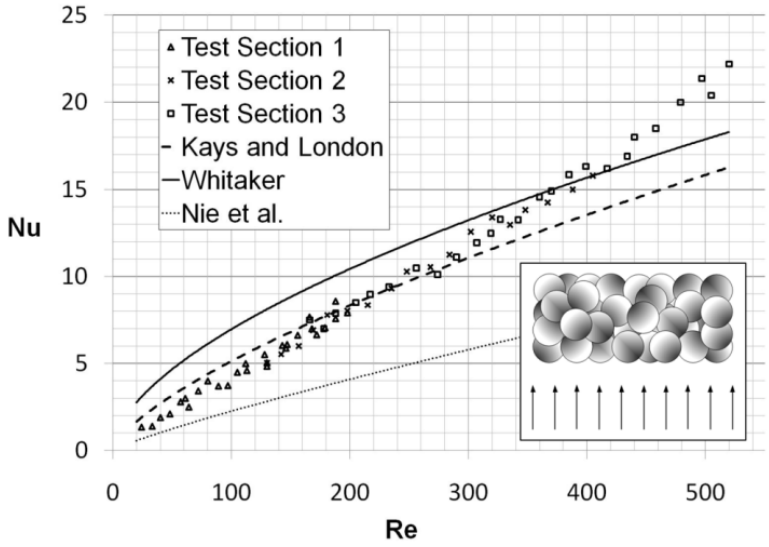

Figure 3.25: Experimental data for Test Sections 1, 2, and 3. Correlations are from Kays and London [30], Whitaker [32], and Nie et al. [31].

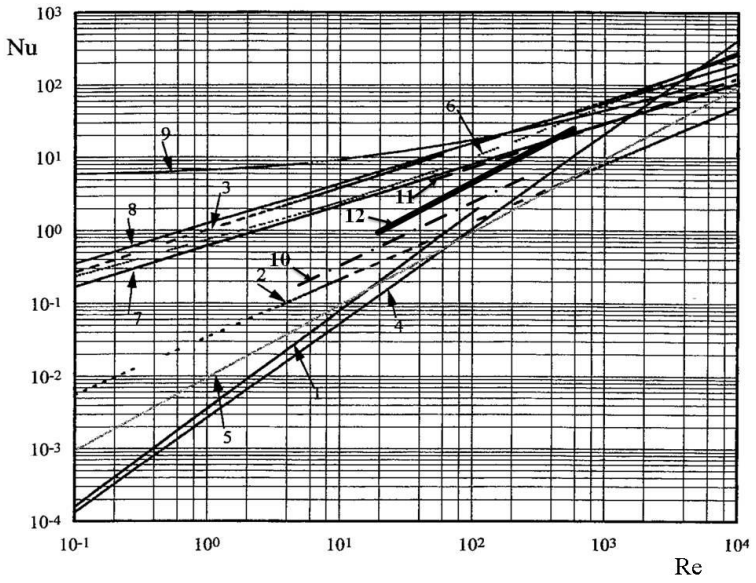

Figure 3.26: Internal effective heat transfer coefficient in porous media, reduced based on VAT scale transformations, from experiments by 1, Kar and Dybbs [74] for laminar regime; 2, Rajkumar [75]; 3, Achenbach [68]; 4, Younis and Viskanta [76]; 5, Galitseysky and Moshaev [77]; 6, Kokorev et al. [78]; 7, Gortyshov et al. [79]; 8, Kays and London [30]; 9, Heat Exchangers Design Handbook [80]; 10, Nie et al. [31]; 11, Whitaker [32]; 12, Eq. (38). Adapted from Travkin and Catton [1].

The uncertainties in the temperature and flow rate measurements were propagated using the code, and uncertainties in Nusselt number were obtained for various Reynolds numbers. From this analysis, it is seen that the correlation, Equation (3.35), is accurate to within 15% for the range of Reynolds numbers under consideration.

From Figure 3.25 it is apparent that the experimental results obtained in this study compare in magnitude reasonably with the established correlations for the internal heat transfer coefficient in packed beds of spheres. The exponent in the Reynolds number obtained here, however, is higher than that in the established correlations. Let us discuss

these correlations and how they compare with the present results in more detail.

Whitaker's correlation [32], reduced based on the VAT scale definitions,

$$\mathrm{Nu} = \left[\frac{1}{3}\left(\frac{3}{2}\mathrm{Re}\right)^{1/2} + \frac{2}{15}\left(\frac{3}{2}\mathrm{Re}\right)^{2/3} \right] \mathrm{Pr}^{1/3}, \tag{3.36}$$

was obtained from correlating a large amount of data for various packings from a wide range of researchers. It has been used successfully as an approximation but is not intended to be the most accurate correlation for packed beds. Our correlation sees good agreement with Whitaker's, particularly at higher flow rates.

Kays and London's correlation [30],

$$\mathrm{Nu} = 0.23\,\mathrm{Re}^{0.7}\,\mathrm{Pr}^{1/3}, \tag{3.37}$$

written based on the definitions used in this paper, was obtained by implementing a standard single-blow transient testing technique to an "infinite" packed bed of spheres, whereby a step change in the inlet air temperature produced a transient outlet temperature profile whose maximum slope allowed h to be deduced from an analysis. The analysis used was based on the early Anzelius and Schumann analysis of heat transfer to an idealized porous body [53, 54]. This correlation sees reasonable agreement with Equation (3.35), particularly at lower flow rates.

The results obtained in this study lie above those more recently obtained by Nie et al. [31] for a packed bed of spheres. Their correlation for the Nusselt number is written,

based on the VAT definitions, as

$$\mathrm{Nu} = 0.0491\,\mathrm{Re}^{0.8572}\,\mathrm{Pr}^{1/3}\,. \tag{3.38}$$

Like the test sections examined in this study, they looked at packed beds for which near wall preferential flow was present ($16 \le D/d \le 51$). Our correcting for the bypass effect played a role in Equation (3.35) being higher than their correlation.

It can also be observed from Figure 3.25 that the results are independent of the size of the spheres. This is evident in the considerable overlap of the results for each test section, seen over the Reynolds number range of about 100 to 400, and the application of a single correlation for all three test sections. This observation allows broad application of Equation (3.35).

3.3.4. Conclusions

In this section the novel transient method discussed in Chapter 3.2 for determining the internal heat transfer coefficient in porous media was applied to a randomly packed bed of uniform spherical particles. Near-wall preferential flow in a packed bed was experimentally observed and accounted for in the analysis by adopting methods that have previously shown success. Experimental results for the Nusselt number over a Reynolds number range of 20 to 500 were obtained for the core of three different randomly packed beds of spheres, and a new correlation was presented. This correlation is seen to be in reasonably good agreement with the results of other investigators.

It was observed here that the internal heat transfer coefficient is essentially independent of the effective thermal conductivity. This observation allows the initial two parameter problem, i.e. h and K_{eff}, to be approached as a one parameter problem, greatly simplifying the task.

The presence of near-wall preferential flow in packed beds was noted. It is suspected that this phenomenon may contribute to the smaller measured Nusselt number values in finite packeds beds compared to those in "infinite" packed beds. A method was implemented to account for such near-wall preferential flow by looking solely at the core of the packed bed, as the core of a finite packed bed resembles an infinite packed bed in its structure.

Additionally we observed the independence of the packed bed's sphere diameters in our results. This was also noticed by Nie et al. [31].

3.4. Conclusions

Measurements obtained using the methods presented in this chapter allow for thermal-fluid modeling of heterogeneous and hierarchical heat transfer devices by closing the theoretically correct VAT-based governing integro-differential equations describing transport phenomena in porous media, i.e. Equations (2.9), (2.16), and (2.17). Closure of the VAT-based equations has previously been directly related to the local transport coefficients [1-7], providing explicit and rigorously derived expressions for c_d and h, i.e. Equations (2.21) and (2.26), respectively . It is these coefficients that are measured in this chapter, using two distinct and unique techniques, for random fiber matrices,

staggered cylinder arrays, and packed particle beds. It is suggested that the experimental methods outlined here be used in the future to consistently obtain data and correlations for new and advanced high performance compact heat exchanger and heat sink surfaces whose geometries preclude direct internal measurements.

Such experimental methods for convenient and accurate measurements of transport coefficients in heterogeneous and hierarchical devices that are based on a unified and theoretically correct model that starts with the Navier-Stokes and thermal energy equations for both the fluid and solid phases, allows for modeling and subsequent optimization of heat transfer devices, based on rigorously derived governing field equations, for which appropriate design data does not already exist. With transport coefficient correlations obtained, VAT-based modeling and subsequent optimization based on the rigorously derived governing field equations may proceed, free of the burdening constraints inherent in CFD approaches or the modeling insufficiencies of others. The following chapter addresses optimization based on the closed VAT equations.

4. OPTIMIZATION WITH VAT-BASED THERMO-FLUID MODELING

In Chapter 3 experimental closure of the VAT-based governing equations, which were presented in Chapter 2, was addressed. In this chapter the closed VAT-based governing equations are exploited to perform multi-parameter optimization and design of heat exchangers. Population-based optimization routines are coupled to VAT-based numerical solvers to perform design. Chapter 4.1 considers a two-stream heat exchanger modeled with VAT and optimized with a Genetic Algorithm (GA). Chapter 4.2 considers a heat sink modeled with VAT and utilizes a Particle Swarm Optimizer (PSO) to carry out the design.

4.1. Finned-Tube Heat Exchanger Optimization with a Genetically Inspired Algorithm

This chapter presents a new methodology for optimizing Finned-Tube Heat Exchangers (FTHEs) using a hierarchical physical model, i.e. VAT, and a Genetic Algorithm (GA) numerical optimizer. This method allows for multiple-parameter constrained optimization of FTHEs by design of their basic morphological structures. A consistent model is used to describe transport phenomena in a FTHE based on VAT, which allows for the volume averaged conservation of mass, momentum, and energy equations to be solved point by point, with the morphology of the structure directly incorporated into the field equations and full conjugate effects included. The VAT-based

FTHE solution algorithm is extremely fast running compared to CFD, but still able to present a detailed picture of the temperature fields in *both* of the fluid flows as well as in the solid structure of the heat exchanger. A GA is integrated with the VAT-based solver to carry out the FTHE numerical optimization, which is a ten parameter problem, and the FTHE is optimized subject to imposed constraints.

4.1.1. Background

Despite the crucial role of heat exchangers in industrial installations, there is still a great deal of empiricism in their design. Although current guidelines provide an ad-hoc solution, a unified design approach based on simultaneous modeling of the thermal-hydraulics and thermal-structural behavior has not been proposed beyond direct numerical simulation-based methods, which at this point are too computationally costly for designers. As a consequence, designs are often overly constrained with a resulting economic penalty. It is apparent that a more scientific procedure for the design and optimization of heat exchangers is needed.

Past work, while using GAs for multi-parameter optimization, has relied upon traditional methods of heat exchanger thermal modeling. In one such study, Ozkol and Komurgoz [81] optimized the size of a heat exchanger for a given surface with the help of a GA. They used the ε-NTU method and sought to minimize cost. Similarly, Xie, Wang, and Sunden [82] applied a GA to optimize FTHEs using the Log-Mean Temperature Difference (LMTD) method for the thermal design, and imposed pressure drop constraints. Experimental transfer coefficient correlations were employed for both

the air and water sides, and the total weight and annual cost of the FTHE were minimized separately. In a more detailed study, Domanski [83] describes a public-domain FTHE simulation software tool, EVAP-COND, a study continued in [84], and discusses its integration with an optimization routine in [85]. The heat exchanger performance is determined using a tube-by-tube segmented LMTD approach with empirical correlations employed for the heat transfer coefficients and pressure drops. Similarly, Jiang, Aute, and Radermacher [86] describe a flexible design tool, CoilDesigner, that can also be integrated with optimization procedures [87], adopts a network viewpoint, and takes a segmented modeling approach using the ε-NTU method.

Other investigators have employed direct numerical simulation-based methods coupled with GAs. Mousavi, Hooman, and Mousavi [88] for example used a GA to optimize the structure of a finned channel, for a fixed flow rate, in terms of the location and size of the fins with the aim of minimizing pressure drop and maximizing heat transfer. The fluid flow and temperature fields were obtained using the finite volume method, assuming two-dimensional, laminar, steady state flow with constant properties [89]. The GA found an optimum configuration, however, in this study the fins were considered perfectly conductive and of negligible thickness, so the solid side was not treated, and the conjugate problem was not solved.

Although not employing a GA, Matos et al. [90] demonstrated what they labeled as "numerical and experimental double optimization" on the geometry of staggered circular and elliptical finned tubes. Their objective was to find the optimal geometry in terms of tube-to-tube spacing, tube eccentricity, and fin-to-fin spacing, such that the

volumetric heat transfer density was maximized, subject to a volume constraint. Assuming incompressible, steady state, laminar flow with constant properties, three-dimensional direct numerical calculations of the flow and temperature were performed using the finite element method. The numerical calculations were experimentally validated and used to perform the parametric optimization. Unfortunately, it is apparent that the cost of the direct numerical simulations and/or experimental trials prevented the possibility of a more thorough search of the domain, and only four eccentricities, four tube pitches, and two flow rates were considered (the number of fin-to-fin spacings considered was not reported).

In a good example of properly accounting for the conjugate effects, Fabbri [91] considered heat transfer into a channel flow through a wall with a corrugated surface whose profile is periodic and described by a fifth order polynomial. A finite element model solved the conjugate heat transfer problem assuming two-dimensional, laminar, steady-state, fully developed, incompressible flow with uniform properties. Optimal corrugation profiles were obtained with a GA by maximizing the heat transfer for a given channel pressure drop and wall volume for two distinct Reynolds and Prandtl numbers. However, although the number of simulations was not reported, it is expected that the computational costs significantly limited the search ability of the GA.

Foli et al. [92] used a multi-objective GA to optimize the performance of a micro heat exchanger by considering the shape of its channels. They simultaneously maximized the heat transfer and minimized the pressure drop by searching for the optimal shape of the separator between the fluids, which was represented by two Non-

Uniform Rational B-Splines (NURBS) with ten control points. The governing flow and heat transfer equations were solved with commercially available CFD software and conjugate heat transfer effects between the solid and fluid were taken into account. A Pareto Optimal Front (i.e. the set of all non-dominated solutions) was obtained, however, it was reported that a month of calculations were necessary to do so.

In yet another example of the significant costs of using CFD for heat exchanger optimization, a multi-objective GA optimization on the tube shape in a tube bank heat exchanger using direct numerical simulation was detailed by Hilbert et al. [93]. A steady, two-dimensional, laminar flow model was employed, and the tube-side flow and heat transfer were ignored. The tube shape was varied by adjusting four parameters that described it. The objectives were to simultaneously maximize the heat transfer while minimizing the pressure loss. A fully automatic optimization computer package would repeatedly call special software to generate both the tube geometry from input parameters and the appropriate simulation mesh, and the CFD program to perform the numerical simulation over the mesh. Post-processing of the CFD results to obtain the objective function values was done with an in-house interfacing code. The simulations were performed in parallel on a multi-node Linux PC cluster with 15 worker PCs, and the population of the GA was 30 and it operated for 20 generations. Solution times on the order of 10 minutes and a Pareto optimal front were reported.

Although they did not consider optimization, Hooman and Gurgenci [94] adopted a porous medium approach to *turbulent* transport in air flow over a finned tube bundle, and considered the effects of fin height and number density variations. Using a

commercial CFD package that solves porous media turbulent transport equations given the porosity, permeability, and a form drag coefficient, they considered two dimensional, steady state, turbulent transport over the finned-tube bundle represented as a porous medium. Once the porous media model was calibrated against experimental data it yielded reliable thermal predictions. The governing equations used in [94] however were developed from ad hoc considerations and not a rigorous mathematical formulation, and the heterogeneous structure of the finned tube bundle was homogenized.

The VAT model that is used in this section to optimize the thermal-hydraulic characteristics of FTHEs addresses many of the undesirable characteristics of the methods discussed above. Its ability to directly incorporate the morphology description and quickly yield a non-local description of the temperature and flow fields in the FTHE, with full conjugate effects and turbulence modeling included, makes it an ideal tool for heat exchanger optimization. The ten-parameter Genetic Algorithm (GA) optimization starts with the developed VAT transport model for FTHEs. This model is the basis for an optimization method that enables full exploitation of the possible parameter variations that are known to be beneficial to the heat exchanger performance. With the use of VAT, heat exchanger modeling and optimization are based on theoretically correct governing field equations rather than the usual balance equations or the semi-empirical porous media models. Before initiating the optimization procedure, what is to be optimized must be determined and the constraints must be set from physical and specified limitations. Presently, in this section, this is done somewhat arbitrarily due to the fact that different designers will have different objectives, so the present case study is meant to serve as a

demonstration. Nonetheless, the method presented is general and may be easily adapted to the particular needs of individual designers.

4.1.2. VAT Heat Exchanger Model

Previous work has shown that flow and heat transfer in heat exchangers can be treated as phenomena in highly heterogeneous structures and that their behavior can be properly predicted with porous media modeling through applying the method of volume averaging to the Navier-Stokes and thermal energy equations for both the fluid and solid phases [1, 7]. Such VAT-based modeling directly incorporates the medium morphology characteristics into the governing field equations. Using different flow regime transport models and second order turbulence models, equation sets have been obtained for turbulent momentum transport and *three*-temperature heat transport in heterogeneous heat exchanger media while accounting for inter-phase exchange. Independent treatment of turbulent convective energy transport in the fluid phases and conductive energy transport in the solid phase, connected through the interfacial surfaces allows for more accurate modeling of the heat transfer mechanisms between heterogeneous structures and the fluid phases, and if one is to perform a geometric optimization, one must separate convection effects from conduction effects and solve a conjugate problem as is done in the present VAT model.

The VAT-based model for transport in hierarchical and heterogeneous media that is presented allows for the representation of a Finned-Tube Heat Exchanger (FTHE), Figure 4.1. VAT allows a FTHE to be analyzed as a multi-level device and results in a

non-local description of its hierarchical, multi-scaled transport processes. The lowest level is the fluid-solid interface where the transport coefficients are determined. The next level up in the hierarchy is the local fluid-solid interaction which is a conjugate problem with the heat transfer and drag coefficients acting as the connections between the solid and fluid. The uppermost level concerns the overall behavior of the device, on which the GA optimization study operates. The VAT model lends itself to an analysis of a FTHE in a rigorous way, allowing the effect of the lowest level, the inner passage way surfaces, to impact the uppermost scale, the overall heat exchanger performance, all while including the full conjugate effects. Its unique ability to allow a combination of direct general physical and mathematical statements with the convenience of segmented analysis, whereby overall physical processes or groups of phenomena are divided into selected sub-processes or phenomena that are interconnected, each to the others, by an adopted chain or set of dependencies, usually employed in heat exchanger design makes it an attractive tool.

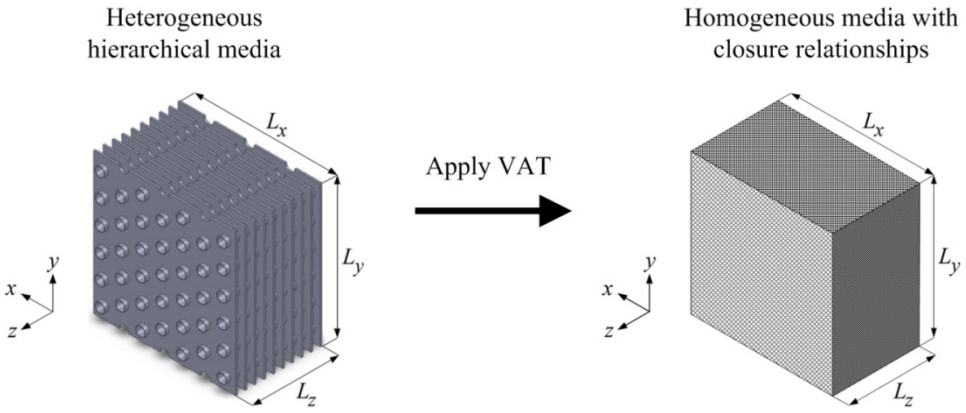

Figure 4.1: VAT-based porous media model of a FTHE.

In the present model, both the fin-side and tube-side flows are considered as separate "porous flows." Air is the fin-side gas, water is the tube-side liquid, and the exchanger is steel. From Equation (2.22), the VAT-based momentum equation for the fin side is

$$-\frac{1}{\rho_1}\frac{\partial\langle\overline{p}_1\rangle_f}{\partial x}+\frac{\partial}{\partial z}\left(\langle m_1\rangle\left(\nu_1+\nu_{T_1}\right)\frac{\partial\tilde{\overline{u}}_1}{\partial z}\right)+\frac{1}{2}c_{d_1}S_{w_1}\tilde{\overline{u}}_1^{\,2}=0\,, \tag{4.1}$$

and, similarly, that for the tube side is

$$-\frac{1}{\rho_2}\frac{\partial\langle\overline{p}_2\rangle_f}{\partial z}+\frac{\partial}{\partial x}\left(\langle m_2\rangle\left(\nu_2+\nu_{T_2}\right)\frac{\partial\tilde{\overline{w}}_2}{\partial x}\right)+\frac{1}{2}c_{d_2}S_{w_2}\tilde{\overline{w}}_2^{2}=0\,. \tag{4.2}$$

While the air flows straight through the exchanger in the positive x- direction, the water follows an oscillatory path through the exchanger, Figure 4.2. Such an oscillatory flow path is modeled as N_x porous channel flows, of cross-stream width L_x/N_x, alternating in the positive and negative z - directions. As the water exits the exchanger on one side it adiabatically returns through the tube bend with pressure drop neglected in the tube bend here for simplicity.

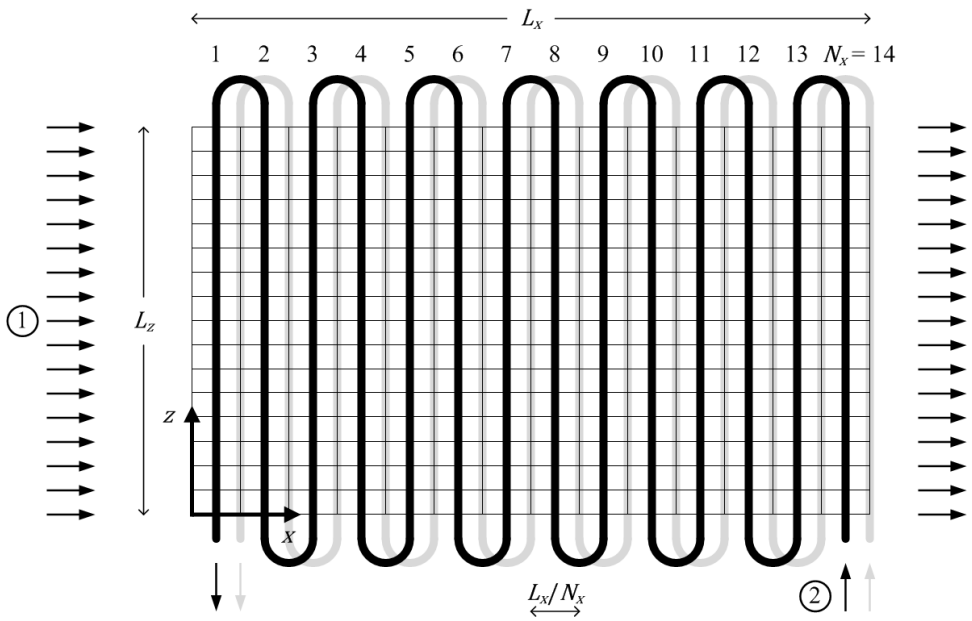

Figure 4.2: Schematic of computational grid and coil circuitry.

Because we are dealing with a conjugate heat transfer problem, the thermal energy equations for the solid and *both* fluid phases are required. From Equation (2.27), for the fin-side fluid the VAT-based thermal energy equation is written as

$$\rho_1 c_{p_1} \langle m_1 \rangle \tilde{\tilde{u}}_1 \frac{\partial \tilde{\tilde{T}}_1}{\partial x} = h_1 S_{w_1} \left(\tilde{T}_s - \tilde{\tilde{T}}_1 \right), \tag{4.3}$$

and, similarly, for the tube-side fluid it is written as

$$\rho_2 c_{p_2} \langle m_2 \rangle \tilde{\tilde{w}}_2 \frac{\partial \tilde{\tilde{T}}_2}{\partial z} = h_2 S_{w_2} \left(\tilde{T}_s - \tilde{\tilde{T}}_2 \right). \tag{4.4}$$

From Equation (2.29), for the solid phase the VAT-based thermal energy equation is

written as

$$\frac{\partial}{\partial x}\left[\left(1-\langle m_1\rangle-\langle m_2\rangle\right)k_s\frac{\partial\tilde{T}_s}{\partial x}\right]+\frac{\partial}{\partial z}\left[\left(1-\langle m_1\rangle-\langle m_2\rangle\right)k_s\frac{\partial\tilde{T}_s}{\partial z}\right] = h_1 S_{w_1}\left(\tilde{T}_s-\tilde{\tilde{T}}_1\right)+h_2 S_{w_2}\left(\tilde{T}_s-\tilde{\tilde{T}}_2\right) \tag{4.5}$$

As discussed in Chapter 2, closure of the general VAT-based integro-differential equations relies on the determination of four terms. These terms are locally averaged over each REV in the domain, and are the specific surface area of the fluid-solid interface, S_w, the porosity, or the volume of the fluid divided by the total volume, $\langle m\rangle$, and the momentum and heat transport coefficients, c_d and h, respectively.

The local porosity and specific surface area are determined directly by the specified morphology of the engineered porous media structure. The Representative Elementary Volume (REV) over which they are defined for the case of a FTHE is depicted in Figure 4.3. From Zhou et al. [29], the porosity for the fin-side of the FTHE is written as

$$\langle m_1\rangle = 1-\frac{\delta_f}{F_p}-\frac{\pi D_c^2\left(F_p-\delta_f\right)}{4P_xP_yF_p}, \tag{4.6}$$

and that for the tube-side is written as

$$\langle m_2 \rangle = \frac{\pi D_i^2}{4 P_x P_y}. \tag{4.7}$$

The specific surface area for the fin-side is given by

$$S_{w_1} = \frac{2 P_x P_y - 2\pi \left(\frac{D_c}{2} \right)^2 + \pi D_c \left(F_p - \delta_f \right)}{P_x P_y F_p}, \tag{4.8}$$

and that for the tube-side is given by

$$S_{w_2} = \frac{\pi D_i}{P_x P_y}. \tag{4.9}$$

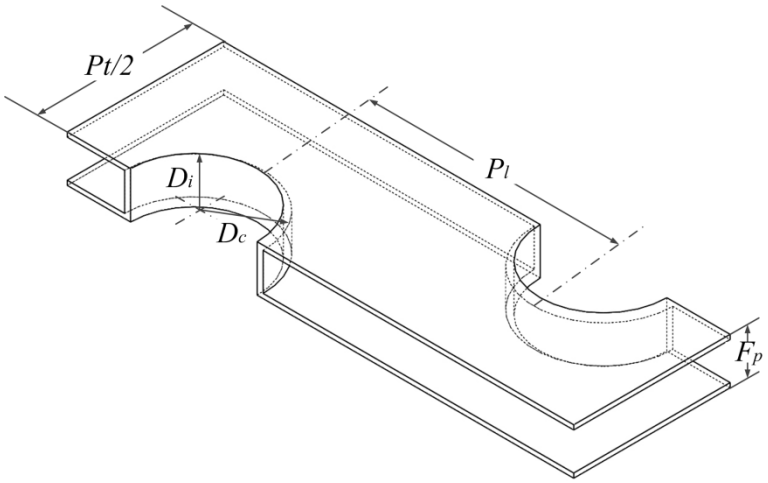

Figure 4.3: Representative Elementary Volume (REV) for a Finned-Tube Heat Exchanger, [29].

The local interfacial transport coefficients, c_d and h, are also needed to close the VAT-based governing equations, and clear definitions of these terms are given by

Equations (2.21) and (2.26), respectively. Collecting published experimental measurements of friction factor and heat transfer performance for the fin-side of FTHEs from Wang et al. [95], Zhou et al. [29] rescaled the data using the length scale given by Equation (2.25) and obtained simple correlations for the fin-side drag and heat transfer coefficients. The drag coefficient, Equation (2.21), is related to the friction factor, see Equation (2.23), and for the fin-side is

$$c_{d_1} \approx f_1 = \frac{112.4}{\mathrm{Re}_1} + 0.252 . \tag{4.10}$$

Similarly, the Nusselt number on the fin-side is expressed as

$$\mathrm{Nu}_1 = 0.24 \mathrm{Re}_1^{0.6} \mathrm{Pr}^{1/3} . \tag{4.11}$$

For closure of the tube-side, all the scaling factors are equal to one (i.e. $D_{h_2} = D_i$) and the friction factor and Nusselt number correlations for fully-developed flow in a pipe are applicable for closure of the tube side VAT equations [29]. Techo et al. [96] correlated the friction factor for turbulent pipe flow as

$$c_{d_2} \approx f_2 = \left\{ 1.7372 \ln \left[\frac{\mathrm{Re}_2}{1.964 \ln\left(\mathrm{Re}_2\right) - 3.8215} \right] \right\}^{-2} . \tag{4.12}$$

As for the heat transfer coefficient, h_2, Whitaker [97] showed that the experimental data

for Nusselt number from a number of investigators for turbulent pipe flow is nicely correlated by the expression

$$\mathrm{Nu}_2 = 0.015\mathrm{Re}_2^{0.83}\mathrm{Pr}^{0.42}. \tag{4.13}$$

At this point in the analysis the VAT-based model of FTHEs, Equations (4.1) – (4.5), is fully closed by Equations (4.6) – (4.13). With the closure expressions determined, the governing equation set is relatively simple and is numerically solved on a contemporary laptop in just seconds to yield a non-local description of the physical fields, thus opening the door to thorough optimization studies based on full simulations. The details of the computational procedure used to solve the VAT-based governing equations were provided in [7] and constant physical properties are assumed in this study. The proper grid size needed to obtain grid independent results with a uniform grid for several selected cases was established and then dynamically adjusted in proportion to the domain size (i.e. L_x and L_z) throughout the optimization procedure. Moreover, only one row of tubes in the y- direction was considered for this case as symmetry allows the heat exchanger capability to be increased by increasing the number of rows in the y- direction.

4.1.3. Genetic Algorithm Optimization

A basic Genetic Algorithm (GA) is employed to perform the multiple (10) parameter constrained optimization on a plain Finned-Tube Heat Exchanger (FTHE).

The fitness function associated with the FTHE, $F(\mathbf{x})$, is chosen to be

$$F(\mathbf{x}) = \varepsilon = \dot{Q}_1 / \dot{Q}_{\max}\,, \tag{4.14}$$

i.e. the heat exchanger effectiveness. This fitness function is to be maximized over the bounded $n = 10$-dimensional search space,

$$\mathbf{x} \equiv \left(D, \delta_d, S_x, S_y, N_x, N_y, \delta_f, S_z, L_z, \dot{m}_1\right), \tag{4.15}$$

where the parameters are bounded between minimum and maximum values, $\mathbf{x}_{\min}$ and $\mathbf{x}_{\max}$ respectively, as shown in Table 4.1. Although designers often find themselves selecting some of these parameters (e.g. D, δ_d, δ_f) discretely from standard tables found in handbooks or production manuals, we have chosen to consider them as continuous variables so as not to restrict the study to a particular set of possible values. If one wants to consider a discrete set of possible values for these variables it is simple to adapt the present method to do so. The mass flow rate of the hot water, $\dot{m}_2$, along with the inlet temperatures of the air, $\tilde{\tilde{T}}_{1,\text{in}}$, and water, $\tilde{\tilde{T}}_{2,\text{in}}$, are taken to be set values in this study at

$$\dot{m}_2 = 1.0 \text{ kg s}^{-1},\ \tilde{\tilde{T}}_{1,\text{in}} = 30\ ^\circ\text{C},\ \text{ and }\ \tilde{\tilde{T}}_{2,\text{in}} = 60\ ^\circ\text{C}\,. \tag{4.16}$$

$\mathbf{x}$	$\mathbf{x}_{\min}$	$\mathbf{x}_{\max}$
D (mm)	5.00	20.00
δ_d (mm)	1.00	5.00
S_x	1.00	5.00
S_y	0.50	2.50
N_x	1	50
N_y	1	50
δ_f (mm)	0.50	10.00
S_z	1.00	10.00
L_z (mm)	50.00	1,500.00
$\dot{m}_1$ (kg s^{-1})	1.00	40.00

Table 4.1: Search parameters and their ranges.

It is obvious that physical constraints on the search space should be implemented when performing the numerical optimization. The physical constraints used here are tabulated in Table 4.2 and can be visualized in Figure 4.4. Additionally, several optimization constraints are chosen to be implemented. These constraints are also tabulated in Table 4.2, and in general are selected by the designer for a given objective.

Physical Constraints	
$D - 2\delta_d \geq 1\text{mm}$	(4.17)
$\sqrt{P_x^2/4 + P_y^2} - D \geq 1\text{mm}$	(4.18)
$P_x - D \geq 1\text{mm}$	(4.19)
$2P_y - D \geq 1\text{mm}$	(4.20)
$F_p - \delta_f \geq 1\text{mm}$	(4.21)
Optimization Constraints	
$PP_T \leq 60$ kW	(4.22)
$W \leq 300$ kg	(4.23)

Table 4.2: Physical and optimization constraints.

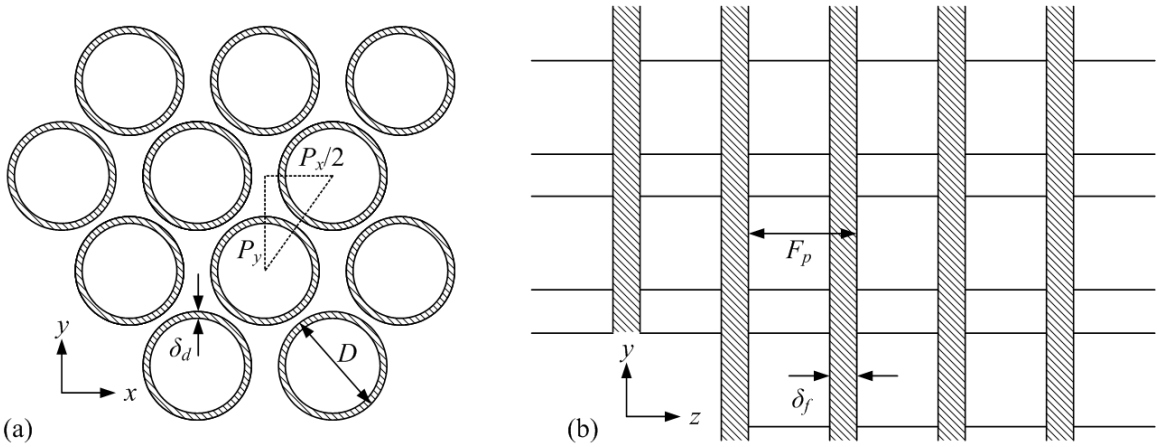

Figure 4.4: Geometrical constraints in (a) $x-y$, and (b) $y-z$ planes.

As the GA optimization routine commences, an initial population of FTHEs is generated by creating N_P individuals with randomly chosen values for each of their bounded n parameters. The fitness of each of these individuals is then determined and the evolutionary process may begin. The population size N_P remains fixed throughout the evolutionary process spanning N_G generations. During each generation, offspring are produced and stored until N_P children have been created. Subsequently, the parent population is exterminated and replaced by the child population. Elitism is enforced so that the fittest individual in the population will survive and be passed into the next generation.

The reproductive cycle loop is nested within the generational cycle loop, see Figure 4.5. A single iteration of the reproductive cycle consists of (1) selecting two parent heat exchangers, (2) constructing their respective chromosomes, (3) mating the parents together by combining their genetic material to produce two offspring chromosomes, allowing mutations on the offspring chromosomes to occur, and (4)

developing the offspring heat exchangers from their genetic make-up.

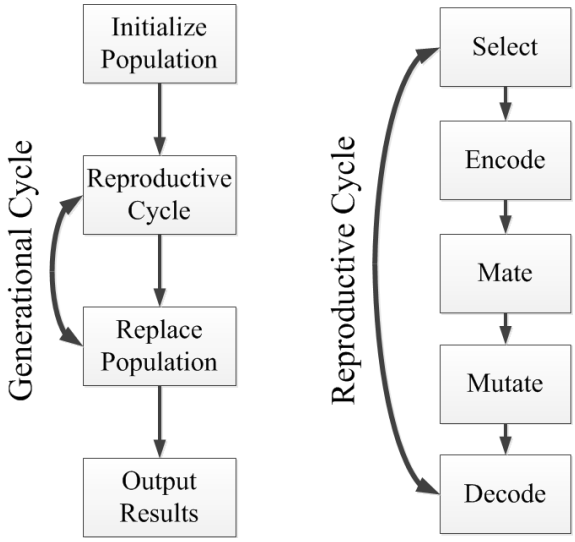

Figure 4.5: Visual outline of the basic GA optimizer.

Parent heat exchangers are selected for breeding stochastically using the commonly employed Roulette Wheel Algorithm (RWA) discussed by Goldberg [98] in which the probability of a parent being selected is proportional to its calculated fitness.

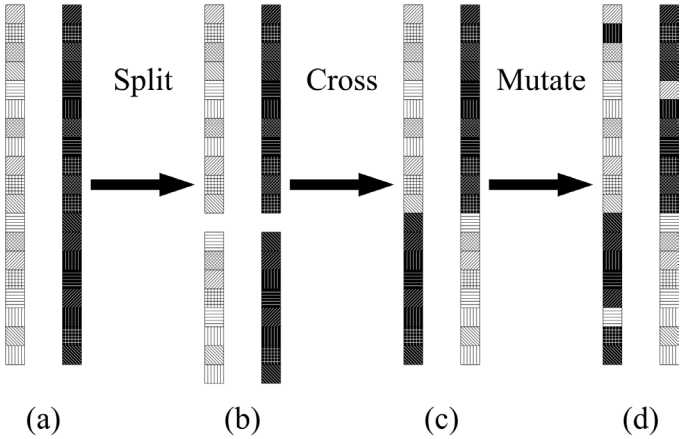

Figure 4.6: Schematic of the genetic operators acting during the breeding process. (a) Two parent individuals are selected and paired for mating. (b) A location on

their chromosomes is randomly selected for splitting. (c) The crossover mechanism then occurs. (d) Subsequently, genetic mutations are allowed to take place.

A single individual heat exchanger can be deconstructed into a chromosome-like structure (genotype), defining that individual's physically observable parameters (phenotype), that will subsequently be subjected to the actions of several genetically inspired operators during the computational breeding process. The complementary process of reconstructing an individual heat exchanger (obtaining its phenotype) from its defining genetic material (its genotype) allows the individual's fitness to then be computed. An individual heat exchanger's chromosome is constructed by coding each of its n defining parameters into a sequence of integers and joining together the n sequences to form a one-dimensional array, see Figure 4.6a. Each element of this chromosomal array may be thought of as a gene having several possible alleles.

Two parent heat exchangers are bred together by first performing a crossover operation on their chromosomes. This operation produces two corresponding offspring chromosomes. To perform the one-point crossover operation a single cutting point is randomly selected along the chromosomes and both parent chromosomes are split here, Figure 4.6b. The chromosomal fragments on one side of the cutting point are interchanged and concatenated to the fragments on the other side, Figure 4.6c, resulting in two offspring chromosomes whose phenotypes can then be constructed. The crossover operation does not always occur during breeding, occurring at a rate P_C.

Before an offspring chromosome is reconstructed into its corresponding phenotype however, each gene in the chromosome is subjected to mutation at the rate of

P_M. A gene affected by a mutation is replaced by a randomly selected value. Although mutation can destroy a superior offspring, it is necessary to implement in order to preserve variability in the population, and to provide a mechanism to overcome premature convergence on secondary maxima in the search space.

In this study the GA operation parameters are $N_P = 100$, $N_G = 500$, $P_C = 0.90$, and $P_M = 0.05$. A detailed search for the optimal GA operation parameters was not carried out; however, the chosen values are typical, falling within the range typically employed, and perform satisfactorily. Upon completion the GA optimizer yields $\mathbf{x}^*$ and $F^* = F\left(\mathbf{x}^*\right)$, the best solution and its corresponding fitness, respectively.

4.1.4. Results & Discussion

The evolution of the best individual's fitness in each generation is plotted in Figure 4.7 for five different trials along with the average of the trials. From this figure it can be observed that as generations pass the computational implementation of natural selection leads to improved heat exchanger designs, as judged by the value of the fitness function. Finally, after N_G generations the evolution ceases, and an optimal, or near-optimal, FTHE is obtained. Running on a 2.20 GHz Intel Core i7-2720QM CPU, the average time for the compiled Fortran GA optimization code (with $N_P = 100$ and $N_G = 500$), over the five trials, was 15.563 hours.

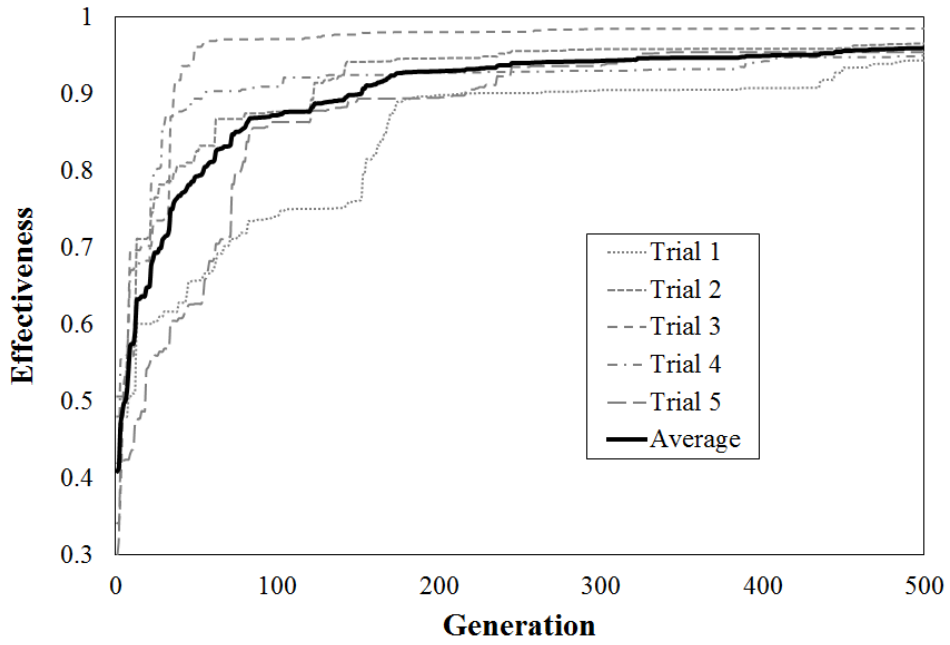

Figure 4.7: Fitness evolution of the best individual in each generation for five trials.

The best solutions $\mathbf{x}^*$ and their corresponding fitness functions $F^* = F\left(\mathbf{x}^*\right)$ for the five trials are tabulated in Table 4.3. As shown in the table, the final fitness functions F^* in the present constrained optimization problem varied only slightly among the five trials, reaching within 6 % of the theoretical optimum. However, some of the search parameters $\mathbf{x}^*$ varied quite significantly due to the absence of additional constraints that would decrease the size of the search space. That is, among the five trials, the GA identified nearly-equivalent optimums in different regions of the search domain.

		Trial 1	Trial 2	Trial 3	Trial 4	Trial 5
$\mathbf{x}^*$	D (mm)	8.41	7.56	7.34	7.36	8.12
	δ_d (mm)	1.02	3.20	2.95	3.02	1.41
	S_x	1.72	2.74	4.48	4.47	1.41
	S_y	2.23	2.47	1.49	1.03	2.46
	N_x	23	11	5	7	23
	N_y	19	39	47	48	15
	δ_f (mm)	0.50	0.50	0.50	0.51	0.50
	S_z	6.41	4.45	4.87	4.95	4.20
	L_z (mm)	1,476	713	1,495	1,318	1,499
	$\dot{m}_1$ (kg s^{-1})	8.01	8.45	13.79	8.40	6.81
F^*	ε	0.94	0.97	0.99	0.95	0.95

Table 4.3: Parameter selection and corresponding fitness for the five trials.

The fin thickness and pitch, δ_f and F_p, and tube diameter and pitches, D, P_x and P_y, together characterize the lower-scale morphology of the fin-side flow, i.e. $\langle m_1 \rangle$ and S_{w_1}, and along with the mass flow rate $\dot{m}_1$, give rise to the Reynolds number Re_1, which determines the lower-scale fin-side transport coefficients, c_{d_1} and h_1. Similarly, the tube inner diameter and pitches, D_i, P_x and P_y, characterize the lower-scale morphology of the tube-side flow, i.e. $\langle m_2 \rangle$ and S_{w_2}, and along with the mass flow rate $\dot{m}_2$, give rise to the Reynolds number Re_2, which determines the lower-scale tube-side transport coefficients, c_{d_2} and h_2. It is the morphology and transport behavior on the lower-scale that effects the design of the upper-scale variables, such as the overall exchanger body dimensions, L_x, L_y, and L_z, and the number of tube passes and rows,

N_x and N_y, see Figure 4.8. As depicted in Figure 4.8, the result of Trial 3 is an exchanger characterized by a relatively large face to the air flow, a large number of tube rows N_y, and a small number of tube passes N_x. The tube-side porosity $\langle m_2 \rangle$ and specific surface area S_{w_2} for Trial 3 are relatively low and give rise to a relatively high tube-side flow velocity and heat transfer coefficient. The exchanger resulting from Trial 4 shares very similar characteristics with that resulting from Trial 3, however the number of tube passes N_x is slightly increased and the face area to the air-flow is slightly decreased. While the exchanger resulting from Trial 2 is similar in many respects to that resulting from Trials 3 and 4, its length in the z- direction is significantly shorter, resulting in a square-shaped face to the air-flow. The exchanger resulting from Trial 5 on the other hand, unlike those resulting from Trials 2, 3, and 4, is characterized by a relatively small face to the air flow, a small number of tube rows N_y, and a large number of tube passes N_x. The tube-side porosity $\langle m_2 \rangle$ and specific surface area S_{w_2} are relatively high, and give rise to a relatively low tube-side flow velocity and heat transfer coefficient. The exchanger resulting from Trial 1 shares very similar traits with that resulting from Trial 5, however the number of tube rows N_y is slightly increased. It is interesting to note that for the five trials, despite the wide variation in tube-side morphology and transport characteristics (between Trials 2, 3, and 4 and Trials 1 and 5), the air-side did not see a wide variation in its porosity $\langle m_1 \rangle$, specific surface area S_{w_1}, flow velocity, or heat transfer coefficient.

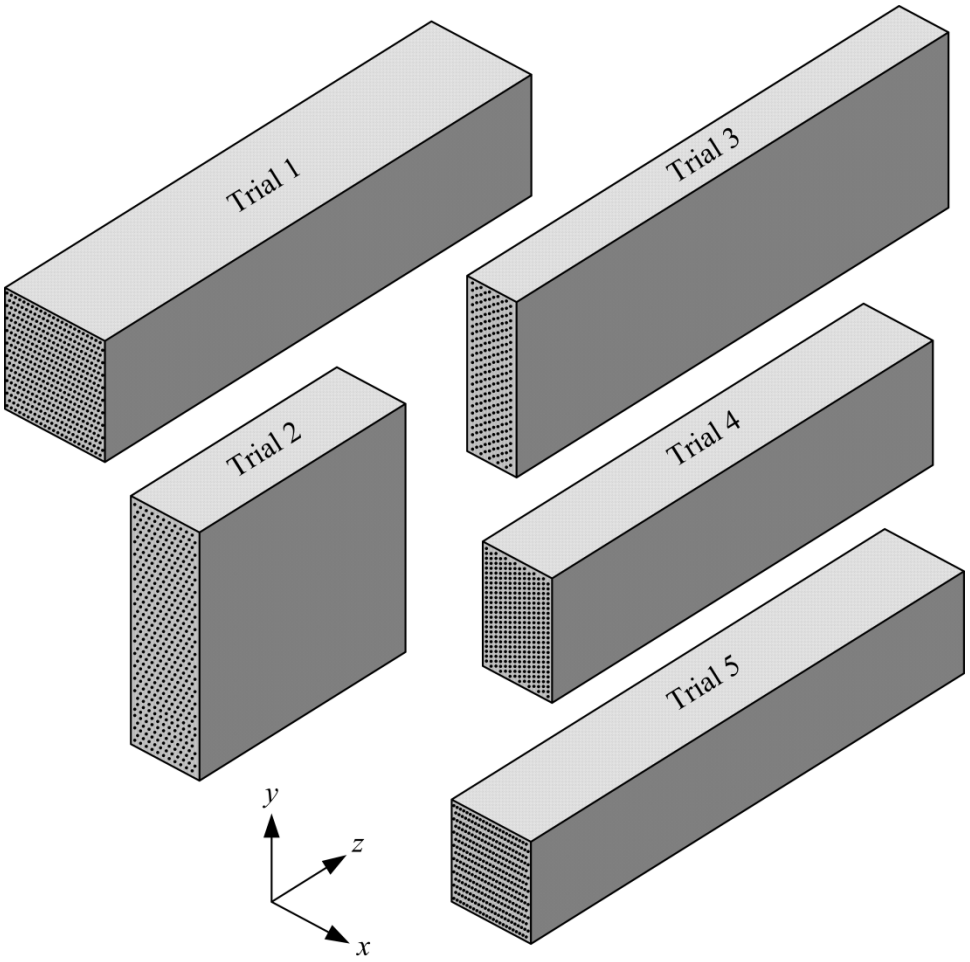

Figure 4.8: Optimum heat exchanger body dimensions, L_x, L_y, and L_z, drawn to scale with tube pass and row numbers, N_x and N_y, indicated (tube diameters not drawn to scale) for the five trials.

As was previously discussed, in the present analysis transport in each of the fluid phases is treated separately from that in the solid phase in order to account for conjugate effects, and it is the lower-scale transport coefficients on each side of the exchanger that connect the transport in the fluid phases to that in the solid phase. In the present study fin

thickness δ_f was minimized in every trial; however tube-wall thickness δ_d was significantly increased in Trials 2, 3, and 4, relative to Trials 1 and 5, indicating the role that the solid-side effects play in the exchanger design. For example, it is known that while decreasing the tube-wall thickness reduces the solid-side thermal resistance, increasing it can lead to increased fin-side surface area, thus reducing the overall thermal resistance between the fluids. Such effects must be carefully balanced with other important considerations in the exchanger design, and the present method allows such a balance to be achieved.

In any heat exchanger design process numerous constraints inevitably arise. Introducing further constraints into the optimization will reduce the size of the search domain until there may be only a single viable solution $\mathbf{x}^*$ remaining. For the successful application of the tool presented here to a specific design problem, constraints must be clearly delineated at the outset by the designer. For example, cost, certain dimensions, and manufacturability constraints all reduce the search domain of the problem. As mentioned above, heat exchanger designers typically select components of their design from a production manual or handbook and such a finite selection of parameters considerably reduces the design search space. Operational concerns also play a crucial role when specifying constraints. For example, concerns for excessive tube-wall pressure on the tube-side, and fluid elastic instability [99, 100] on the fin-side play a prominent role in some heat exchanger designs, and designing to avoid these detrimental phenomena will result in additional constraints. Table 4.4 tabulates some additional performance parameters of the optimum heat exchangers found at $\mathbf{x} = \mathbf{x}^*$ for the five

trials considered in addition to their fitness, and includes the presently constrained quantities PP_T and W. It is evident that the heat exchanger optimization procedure was bounded by the imposed constraints on these quantities and that for nearly every case these quantities were at or near the constraining values. Thus, constraints play a crucial role in the design process, decreasing the size of the search domain, and must be identified for specific design requirements.

Trial	$\dot{Q}$ [kW]	ε [-]	ε_{PP} [-]	$\varepsilon_{\Delta T}$ [°C^{-1}]	PP_1 [kW]	PP_2 [kW]	PP_T [kW]	W [kg]	V [m^3]
1	118.54	0.94	2.89	$9.62\text{x}10^{-2}$	40.99	0.07	41.06	297.23	0.1744
2	121.32	0.97	2.02	$6.75\text{x}10^{-2}$	47.51	12.41	59.92	297.93	0.1186
3	123.77	0.99	2.06	$6.88\text{x}10^{-2}$	56.92	3.04	59.96	299.79	0.1265
4	119.34	0.95	2.07	$6.89\text{x}10^{-2}$	52.03	5.74	54.77	296.87	0.1110
5	119.92	0.95	2.02	$6.75\text{x}10^{-2}$	59.03	0.22	59.25	300.00	0.1185

Table 4.4: Heat exchanger performance at $\mathbf{x} = \mathbf{x}^*$ for the five trials, $\dot{Q}_{\max} = 125.58$ kW.

As a final note, variability in convergence speed is evident in Figure 4.7. In particular, while Trial 3 converges relatively quickly, Trial 1 converges relatively slowly. Such variability in convergence speed in this study was solely the result of a different initial population and random number seed. Such effects must be carefully considered, and if, unlike the present case, the optimal fitness function value is unknown, a considerable number of function evaluations may be necessary to obtain confidence in a sufficiently near-optimal solution. Due to its computational speed, the VAT-based method presented here allows optimal heat exchangers to be found that could not be obtained with CFD. However, for specific problems the GA parameters should also be

tuned. Domanski et al. [101] presented a study recommending population size and number of generations significantly smaller than those employed here (i.e. $N_P = 40$ and $N_G = 200$). Implementing these settings or independently finding optimal settings would decrease the computational time further. It is interesting to observe the evolution of the search parameters in parallel to that of the fitness function, and to observe the wide range in convergence speed from the perspective of the search parameters. Figure 4.9 depicts the evolution of the search parameters $\mathbf{x}$, for each generation's best individual in Trial 1 and Trial 3, where the search parameters have been scaled as

$$\overline{\mathbf{x}} = \frac{\mathbf{x} - \mathbf{x}_{\min}}{\mathbf{x}_{\max} - \mathbf{x}_{\min}}, \tag{4.24}$$

and $\mathbf{x} = \mathbf{x}^*$ at the conclusion of the evolution. It is apparent that while the search parameters in Trial 3 quickly settle on a location in the domain, the search parameters in Trial 1 continue searching throughout the evolution. The difference in convergence speed observed in Figure 4.7 and Figure 4.9 highlights the need for not only careful tuning of the GA parameters, but also a fast-running computational method based on the hierarchical modeling methodology presented here.

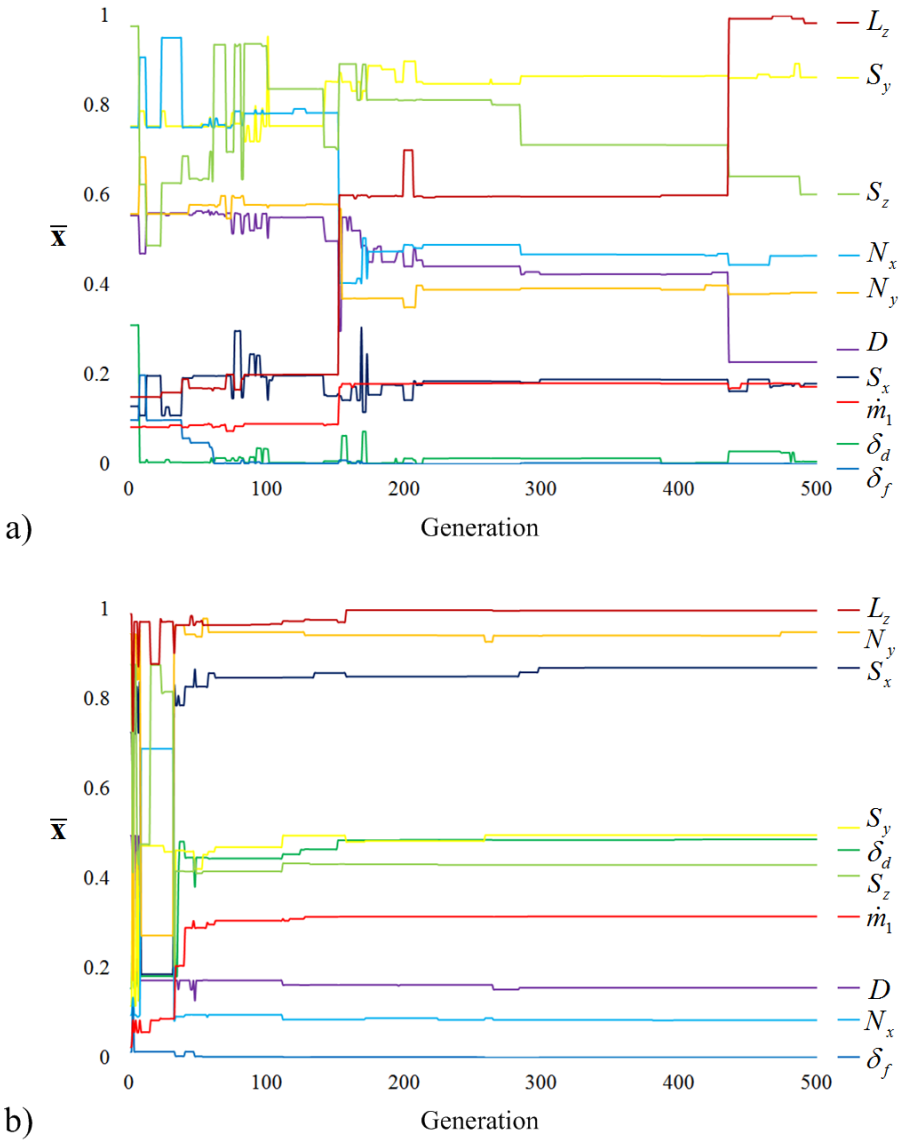

Figure 4.9: Evolution of $\bar{x}$ for the best individual in each generation for a) Trial 1 and b) Trial 3.

4.1.5. Conclusions

In this section a VAT model of a Finned-Tube Heat Exchanger is presented that provides the basis for an optimization method that enables full exploitation of the

possible parameter variations that are known to be beneficial and whose run-time significantly exceeds that of CFD. In the heat exchanger model convection effects are separated from conduction effects and a conjugate problem is solved, allowing geometric optimization to be performed. The heat exchanger modeling and optimization are based on theoretically correct governing field equations rather than the usual balance equations or ad hoc field equations. This provides a unified design approach based on simultaneous modeling of the thermal-hydraulics and thermal-structural behavior. This method is easily extended to other heat exchanger surface types. To do so, one only needs to close the VAT-based equations, which amounts to knowing the morphology and transport coefficients for the structure.

A Genetic Algorithm numerical optimizer is fully integrated with a simulation routine based on the VAT model of the Finned-Tube Heat Exchanger. Ten parameters describing the Finned-Tube Heat Exchanger are simultaneously varied to optimize the heat exchanger's effectiveness, subject to several constraints. Upon completion, the optimization yields an optimized heat exchanger, specifying the selected values of the ten parameters that were varied, and the corresponding optimal heat exchanger effectiveness. Such a computational routine provides a valuable and one-of-a-kind tool for heat exchanger designers. Future work can explore new surfaces, integrate other promising optimization methods, e.g. particle swarm optimization, simulated annealing, etc., and consider multiple-objective optimization methods, e.g. NSGA-II [102]. Moreover, tube-side phase change, fin-side wet surface conditions, and flexibility in tube circuitry architectures can be incorporated into the model.

Computer aided numerical simulation as presented here cannot yet replace the experimental work, but with the aid of computer calculations, experiments can focus on achieving optimum properties. Model calculations can be used to examine the sensitivity of heterogeneous media performance to key parameters. This minimizes developmental costs and reduces the time required for product commercialization.

4.2. Heat Sink Optimization with a Socially Inspired Algorithm

In Chapter 4.1 a two-stream heat exchanger was considered. In this section we consider a heat sink. Cooling electronic chips to satisfy the ever-increasing heat transfer demands of the electronics industry is a perpetual challenge. One approach to addressing this is through improving the heat rejection ability of air-cooled heat sinks, and nonlocal thermal-fluid-solid modeling based on Volume Averaging Thoery (VAT) has allowed for significant strides in this effort. A number of optimization methods for heat sink designers who model heat sinks with VAT can be envisioned due to VAT's singular ability to rapidly provide solutions, when compared to Direct Numerical Simulation (DNS) and Computational Fluid Dynamics (CFD) approaches. The Particle Swarm Optimization (PSO) method appears to be an attractive multi-parameter heat transfer device optimization tool, however it has received very little attention in this field compared to its older population-based optimizer cousin, the Genetic Algorithm (GA), which was considered in Chapter 4.1. The PSO method is employed in this section to

optimize smooth and scale-roughened straight-fin heat sinks modeled with VAT by minimizing heat sink thermal resistance for a specified pumping power. Optimal designs are obtained with the PSO method for both types of heat sinks, the performances of the heat sink types are compared, and the performance of the PSO method is discussed with reference to the GA method.

4.2.1. Background

Past studies have considered different methods for the optimization of heat sink designs. Much emphasis, in particular, has been placed on optimization with Genetic Algorithms (GAs). While early work on GAs for general optimization problems was performed in the 1970s and 1980s by Holland [103], Goldberg [98], and others, GAs for electronics cooling applications didn't begin to receive attention until the work of Queipo, Devarakonda, and Humphrey [104] in the mid-1990s. Since then a number of heat sink optimization studies using GAs have been reported, with various modeling approaches. Some investigators have used algebraic correlations of the heat sink performance, e.g. thermal resistance or entropy generation, as the model on which the GA operates [105-107]. Others have interfaced Direct Numerical Simulations (DNS) and Computational Fluid Dynamics (CFD) packages with GAs to perform optimization [91, 104, 108]. Further, others have coupled porous media models with GAs to optimize heat sink designs [109-111].

Less emphasis, however, has been placed on heat sink design with Particle Swarm Optimization (PSO). PSO was developed in the 1990s by Kennedy, Eberhart, and their

students [112-119], and began to receive attention for electronics cooling applications in the early 2000s. In particular, CFD heat sink simulations have been interfaced with the PSO method to optimize heat sink designs in several recent studies [120-122]. Appendix C presents an abridged survey of studies that have employed population-based optimizers to design heat sinks (and heat exchangers).

The heat sink modeling methods thus far employed with the PSO and GA optimization tools suffer from some undesirable characteristics. Although those modeling methods using algebraic performance correlations yield fast performance evaluations, allowing the PSO and GA to thoroughly explore the design/solution space, these methods' applicability are confined to the certain conditions from which they were derived and do not afford the flexibility that full simulations provide. Full simulation modeling methods using DNS and CFD can provide detailed solutions of the flow and temperature fields for different flow regimes and arbitrary channel morphologies, and at first seem ideal as a model on which to perform optimization. However, DNS and CFD solutions used for optimization typically either don't include the conjugate heat transfer effects, i.e. the solid side, or carry a large computational burden when attaining the many solutions necessary that cripples the PSO and GA's search abilities. Some porous media models show promise for certain applications, however, the models typically employed are empirically-based, often don't include conjugate effects, and don't incorporate clearly defined transport coefficients. The VAT-based hierarchical modeling methodology presented here to overcome these undesirable characteristics performs full thermal-fluid-solid simulations that account for the flow regime and arbitrary channel morphologies,

includes full conjugate heat transfer effects, is general and rigorously derived from fundamental equations, incorporates clearly defined transport coefficient expressions, and provides fast computational times that allow PSO and GA optimizations to be easily realized with even modest computing hardware. The VAT-based fluid mechanics and thermal energy equations modeling hierarchical momentum and heat transport within a heterogeneous porous medium, like a heat sink, were described in Chapter 2.

The PSO method, as employed here, was discovered by Eberhart and Kennedy [112] while performing simulations of a simple social model, and since then it has proven itself to be both fast and robust in solving a wide range of nonlinear, non-differentiable, multi-modal optimization problems. As Eberhart and Kennedy describe, it is a simple concept, can be implemented in just a few lines of computer code, requires only primitive mathematical operators, and is computationally inexpensive in terms of both memory requirements and speed. PSO is part of a long line of biologically-inspired algorithms and can be thought to lie somewhere in between Genetic Algorithms (GAs) and Artificial Neural Networks (ANNs). While evolution by natural selection (i.e. GAs) may take eons and neural processing (i.e. ANNs) may take milliseconds, social optimization (i.e. PSOs) occurs in the time frame of ordinary experience. In PSO, they explain, individuals improve through *cooperation* and *competition* among themselves in the same way individuals in a flock, school, herd, or swarm profit from the discoveries and experiences of other members of the group during their search for desirable resources that are unpredictably distributed. It is based on the premise that social sharing of information offers an evolutionary advantage. Additionally, they observed that in a similar fashion to

the way birds and fish move through three-dimensional space to seek food and mates, avoid predators, and optimize their environment, humans adjust their beliefs and attitudes to conform to their peers and societal norms in an abstract multi-dimensional space. Therefore PSO also has roots in human learning patterns.

In this study, the PSO method is implemented for optimizing heat sinks modeled with VAT. Such a modeling methodology was incorporated with a GA to optimize a two-fluid stream heat exchanger in the previous section. Here, both smooth surface and scale-roughened surface straight-fin heat sinks with tapered fins are considered, see Figure 4.10. The results from the PSO method are compared to and verified against results from a GA. The performance of these two types of heat sinks and the effectiveness of the nonlocal modeling coupled with a swarm-based design strategy are then discussed.

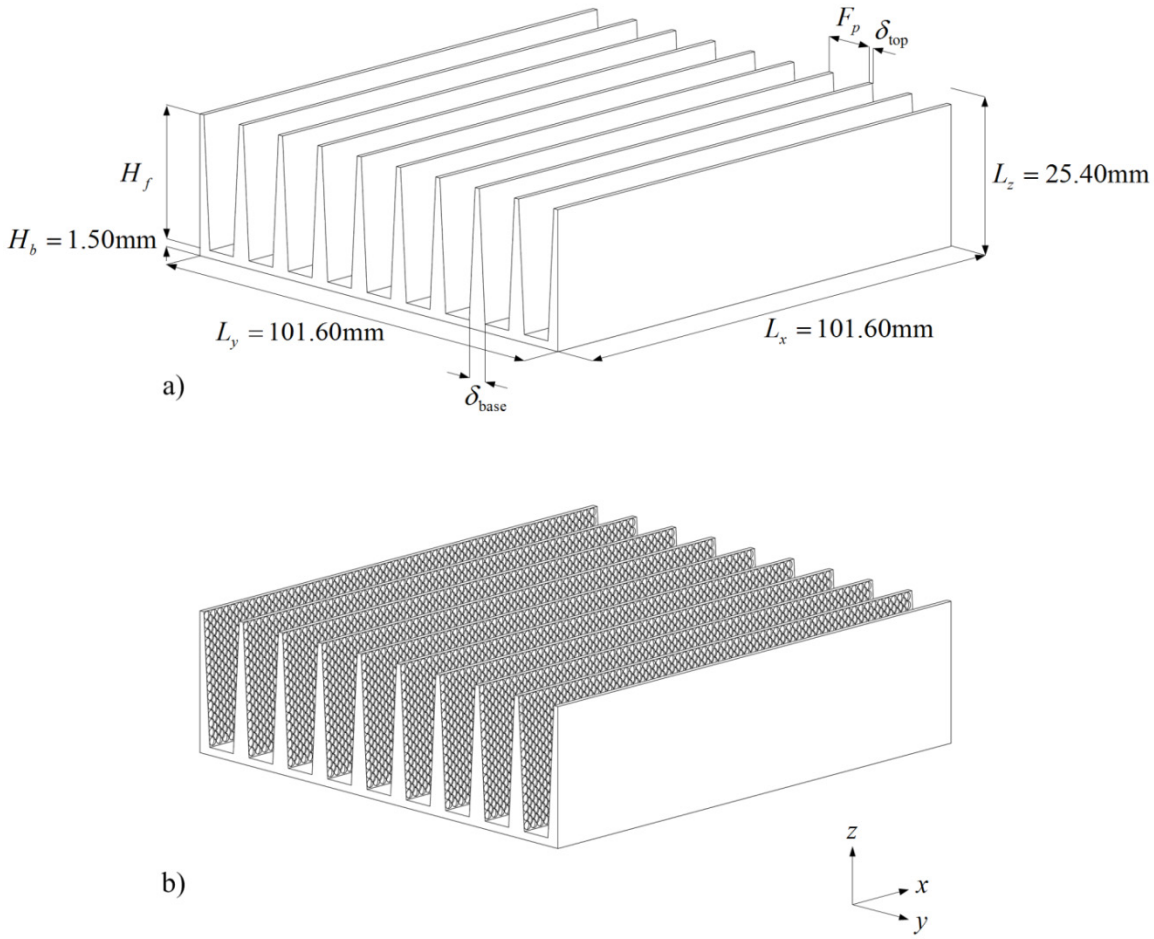

Figure 4.10: Illustration of a straight-fin heat sink with tapered, a) smooth and b) scale-roughed surface fins

4.2.2. Heat Sink Transport Model

The VAT-based steady-state, incompressible flow heat sink governing equations follow. The continuity equation is trivial, see Equation (2.6). From Equation (2.9), the

one-dimensional momentum equation is written as

$$\frac{\partial}{\partial z}\left[\left\langle m(z)\right\rangle(\nu+\nu_T)\frac{\partial\tilde{\bar{u}}(z)}{\partial z}\right]+\frac{1}{\Delta\Omega}\int_{\partial S_{wT}}\nu_T\frac{\partial\bar{u}_i}{\partial x_j}\cdot d\vec{s}$$
$$+\frac{1}{\Delta\Omega}\int_{\partial S_{wL}}\nu\frac{\partial\bar{u}_i}{\partial x_j}\cdot d\vec{s}-\frac{1}{\rho_f\Delta\Omega}\int_{\partial S_w}\bar{p}\cdot d\vec{s}=\frac{1}{\rho_f}\frac{\partial\langle\bar{p}\rangle_f}{\partial x} \tag{4.25}$$

From Equation (2.16), the two-dimensional thermal energy equation in the fluid phase is written as

$$\rho_f c_{pf}\langle m\rangle\tilde{\bar{u}}(z)\frac{\partial\tilde{\bar{T}}_f(x,z)}{\partial x}=\frac{\partial}{\partial x}\left[\langle m\rangle\left(k_T+k_f\right)\frac{\partial\tilde{\bar{T}}_f(x,z)}{\partial x}\right]$$
$$+\frac{\partial}{\partial z}\left[\langle m\rangle\left(k_T+k_f\right)\frac{\partial\tilde{\bar{T}}_f(x,z)}{\partial z}\right]+\frac{1}{\Delta\Omega}\int_{\partial S_{wL}}k_f\frac{\partial\bar{T}_f}{\partial x_i}\cdot d\vec{s}+\frac{1}{\Delta\Omega}\int_{\partial S_{wT}}k_T\frac{\partial\bar{T}_f}{\partial x_i}\cdot d\vec{s} \tag{4.26}$$

From Equation (2.17), the two-dimensional thermal energy equation in the solid phase is written as

$$\frac{\partial}{\partial x}\left[\left(1-\langle m\rangle\right)k_s\frac{\partial\tilde{T}_s(x,z)}{\partial x}\right]+\frac{\partial}{\partial z}\left[\left(1-\langle m\rangle\right)k_s\frac{\partial\tilde{T}_s(x,z)}{\partial z}\right]$$
$$+\frac{1}{\Delta\Omega}\int_{\partial S_w}k_s\frac{\partial T_s}{\partial x_i}\cdot d\vec{s}_1=0 \tag{4.27}$$

Zhou et al. [33] present correlations for c_d and h, developed from lower-scale CFD simulations, that close the VAT-based governing equations for the smooth and

scale-roughened surface straight-fin heat sinks considered here. Having found closure for the surfaces under consideration, the governing equations become simple and solutions may be readily obtained numerically, opening the door to population-based optimization efforts.

4.2.3. Computational Methods and Solution Procedure

The VAT-based momentum, turbulent kinetic energy, and thermal energy equations are solved numerically with the finite difference method over the two-dimensional x- z plane. In particular, statements for one-dimensional fully developed turbulent flow and two-dimensional, two-temperature heat transfer in a porous layer and heat transfer in a base plate are used. Uniform gridding is employed in the base plate, when it is considered, and over most of the channel, however a higher density grid in the flow (x) direction is implemented near the channel inlet and outlet regions. A flow chart of the solution algorithm is illustrated in Figure 4.11.

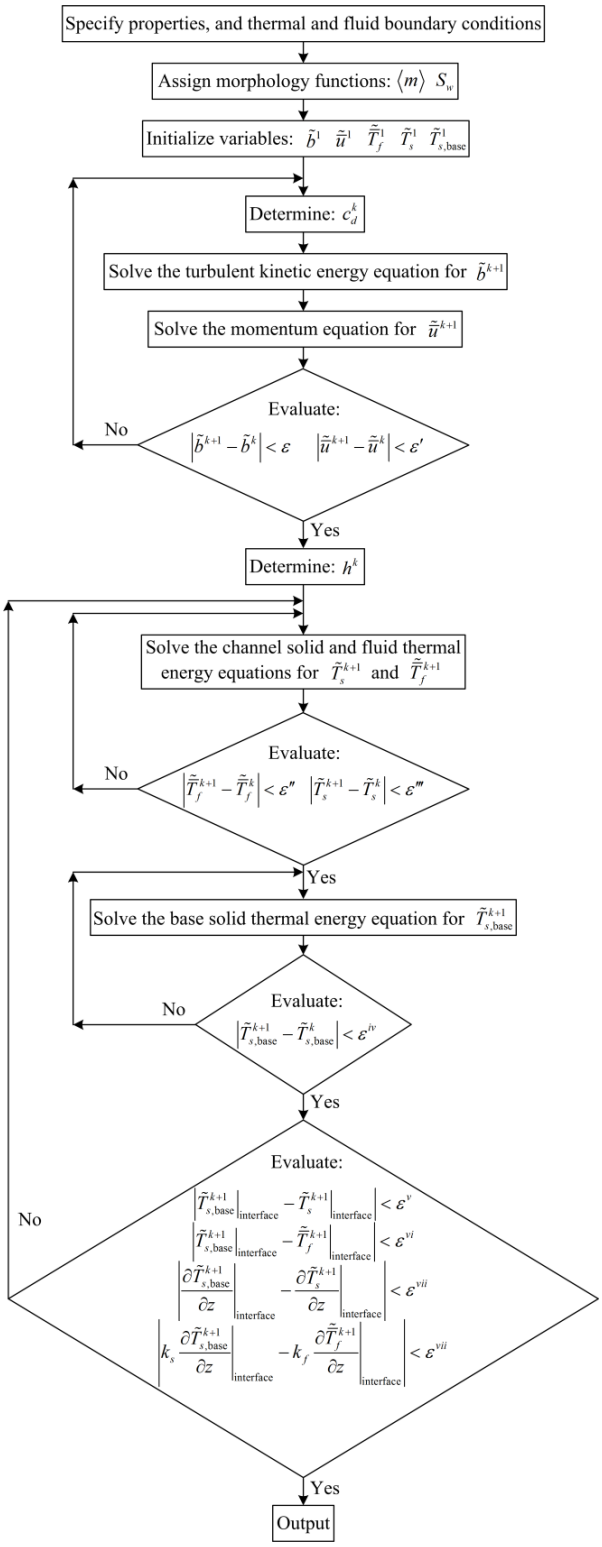

Figure 4.11: Flow chart of the VAT-based heat sink simulation routine

After the problem is formulated and the variables are initialized, the velocity distribution for turbulent channel flow in porous media is simulated for incompressible, constant property flow, i.e. it is uncoupled from the thermal routine. Subsequently, the two-dimensional, two-temperature statements modeling the turbulent heat transfer in the fluid phase and the conjugated heat transfer in the solid phase are solved using the velocity field and turbulence parameters as input. To resolve the temperature fields there are several iterative loops, as indicated in Figure 4.11. When the base plate is considered, an inner loop converges the fluid and solid channel temperatures using a form of ADI. Another inner loop converges the base temperature separately from the channel temperatures, given an interface temperature between the channel and base and a bottom base temperature or heat flux. An outer loop then matches the interface heat flux and temperature between the base and channel by varying the interface temperature. If the base plate is not considered then a simpler situation arises, and a single loop simply converges the fluid and solid channel temperatures. When the VAT-based solution routine exits, the fully-developed velocity field and two-dimensional temperature fields are obtained, along with other relevant calculated quantities, e.g. the thermal resistance.

During the optimization runs in this study the base plate is neglected, to provide quicker solution times, and a constant temperature boundary condition is imposed on the bottom of the channel. The results of the optimization are then verified by including the base plate and solving for a uniform heat flux boundary condition on the bottom of the base plate. This method stems from the assumption that the performance of a heat sink

with no base plate and a constant temperature boundary condition is related to the performance of a heat sink with a thin base plate and a uniform heat flux boundary condition.

In this study the fluid is air and the heat sink is aluminum for all cases and several geometric parameters of the heat sink are kept fixed, as indicated in Figure 4.10. Additionally, appropriate flow and thermal boundary conditions are kept fixed throughout the study. A fixed pumping power of 30W, and no-slip boundary conditions at the bottom and top of the channel fully specify the flow field through the given channel geometry. To specify the thermal fields in both the solid and fluid phases, a uniform inlet air temperature of 30°C is implemented, along with an adiabatic condition at the top of the channel, and one of two lower thermal boundary conditions. The lower thermal boundary condition is a 90°C isothermal one at the bottom of the channel during the optimization, where the base plate is neglected. After the optimization, the designs are evaluated with a uniformly distributed 1kW heat source at the bottom of the baseplate as the lower thermal boundary condition.

4.2.4. Particle Swarm Optimization

The ability to quickly obtain solutions provided by the VAT-based modeling and solution routine outlined above allows for population-based optimization to proceed. In the present study the multi-parameter, constrained optimization problem is formulated as follows. The heat sink thermal resistance, $R_{th}(X)$, is to be minimized over the bounded search domain

$$X \equiv \left(\delta_{\text{base}}, \delta_{\text{top}}, H_f, S_y\right), \tag{4.28}$$

where the parameters are bounded between minimum and maximum values $X_{\min}$ and $X_{\max}$ respectively, as shown in Table 4.5. Tapering of the fins is allowed during the search and the fin thickness varies linearly with respect to the z-coordinate. Optimization should yield X^* and $R_{th}^* = R_{th}\left(X^*\right)$, the optimal solution and its corresponding thermal resistance, respectively.

Parameter	Minimum	Maximum
Fin thickness at base, δ_{base} (mm)	1.50	5.00
Fin thickness at top, δ_{top} (mm)	1.50	5.00
Fin height, H_f (mm)	10.00	23.90
Pitch/fin thickness at base, S_y (-)	1.40	3.00

Table 4.5: Design parameter ranges for the straight-fin heat sinks

Each individual, i.e. heat sink design, in the PSO is treated as a particle, defined by its position, that flies through $D = 4$-dimensional hyperspace. In general, the i th particle is represented as $X_I = \left(x_{i1}, x_{i2}, ..., x_{iD}\right)$, its best previous position as $P_I = \left(p_{i1}, p_{i2}, ..., p_{iD}\right)$, and its velocity as $V_I = \left(v_{i1}, v_{i2}, ..., v_{iD}\right)$. The index of the best particle in the neighborhood is n. Each particle adjusts it flight according to

$$v_{id} = w \times v_{id} + c_1 \times rand(\,) \times \left(p_{id} - x_{id}\right) + c_2 \times Rand(\,) \times \left(p_{nd} - x_{id}\right), \tag{4.29}$$

$$x_{id} = x_{id} + v_{id}, \tag{4.30}$$

where c_1 and c_2 are two "learning factors", $rand(\ )$ and $Rand(\ )$ are two independently generated random numbers in the range $[0,1]$, and w is the "inertia weight" [114]. Equation (4.29) calculates the particle's new velocity according to its weighted previous velocity and stochastic functions of the distance of its current position from its own best position and that of the group. The particles then "fly" toward a new position according to Equation (4.30).

The first term on the right side of Equation (4.29) is the particle's previous velocity multiplied by an inertia weight. The inertia weight is employed to control the impact of the previous history of velocities on the current velocity, and influences the tradeoff between global and local exploration. A larger inertia weight facilitates global exploration while a smaller inertia weight facilitates local fine-tuning. The second term on the right side of Equation (4.29) is the "cognition" part, representing the private thinking of the individual particle, and contributes to a stochastic change in velocity [123]. Conceptually, p_{id} resembles autobiographical memory, as each individual remembers its own experience, and the velocity adjustment associated with this term can be viewed as "nostalgia" in that the individual tends to return to the place that most satisfied it in the past. The third term on the right side of Equation (4.29) is the "social" part, representing collaboration among the particles, and contributes to a stochastic change in velocity. Conceptually, p_{nd} resembles publicized knowledge, or a group norm

or standard, which individuals seek to attain.

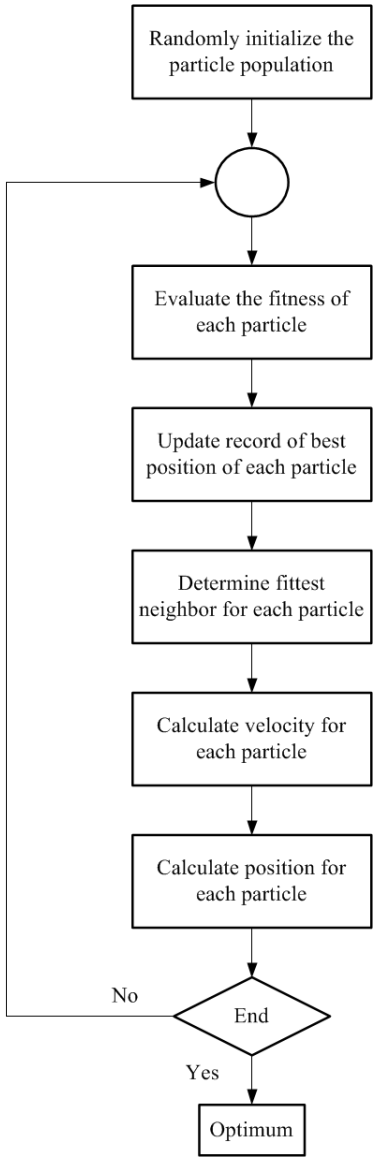

Figure 4.12: Flow chart of PSO algorithm

To implement the PSO, the particle population is initially randomized, as in the GA, and subsequently searches for optima by updating iteratively through time. In every

iteration, each particle is updated by its attraction to its own best position p_{id}, and that of its neighbors p_{nd}, through Equations (4.29) and (4.30). When a given criterion is satisfied, the iteration exits with what is taken to be the optimal solution. A flow chart of the general PSO algorithm used here is shown in Figure 4.12, [124]. The algorithm employed here randomly finds N_S neighbors for each particle at each iteration, uses a well-tested random number generator, exits after a fixed number of iterations N_G, and implements the settings tabulated in Table 4.6.

N_P	N_G	N_S	c_1	c_2	w
20	150	5	2.00	2.00	1.00

Table 4.6: PSO operation settings

4.2.5. Results and Discussion

Employing the VAT-based modeling and solution routine coupled with the PSO technique, smooth and scale-roughened straight-fin heat sinks are optimized by minimizing their thermal resistance while maintaining a constant pumping power. Boundary conditions and certain parameters are fixed as detailed above and other parameters are variable with search ranges tabulated in Table 4.5. Results from the optimization of smooth surface and then scale-roughened surface fins are first considered in this subsection, followed by a discussion on the evolution of the nonlocal flow and temperature fields and an evaluation of the performance of the PSO method in relation to the GA method.

4.2.5.1. Smooth Surface Fins

The first case considered is for a simple smooth surface straight-fin heat sink, Figure 4.10a. The PSO evolves the optimal design so that the heat sink thermal resistance favorably evolves. Ten independent PSO trials are run and the evolution of the optimal thermal resistance for the trials (thin grey lines) along with the average of the trials (thick black line) are plotted in Figure 4.13a. The inset of Figure 4.13a shows closely the first few iterations before which all ten trials converge to the optimum. By the 16th iteration, all ten trials agree on the same value for the optimal R_{th}, i.e. 0.079 °C/W without the base plate. Alternatively, from the perspective of the design space, the ten independent PSO trials evolve scaled values of H_f, S_y, δ_{base}, and δ_{top} as illustrated in Figure 4.14a. Here the search ranges of the four design parameters are scaled between 0 and 1, where 0 is the minimum value and 1 is the maximum, see Table 4.5. That is,

$$\overline{X} = \frac{X - X_{\min}}{X_{\max} - X_{\min}}, \tag{4.31}$$

where $\overline{X}$ is the scaled design space vector. While the color-coded thin lines in Figure 4.14a indicate the evolution of the optimal parameters for the ten independent trials, the color-coded thick lines indicate the average over the ten trials. Evident from Figure 4.14a is that, in addition to all ten trials converging to a single optimal value R_{th}^*, all ten trials also converge to a single optimal solution in the design space, X^*, for the ten individual PSO runs.

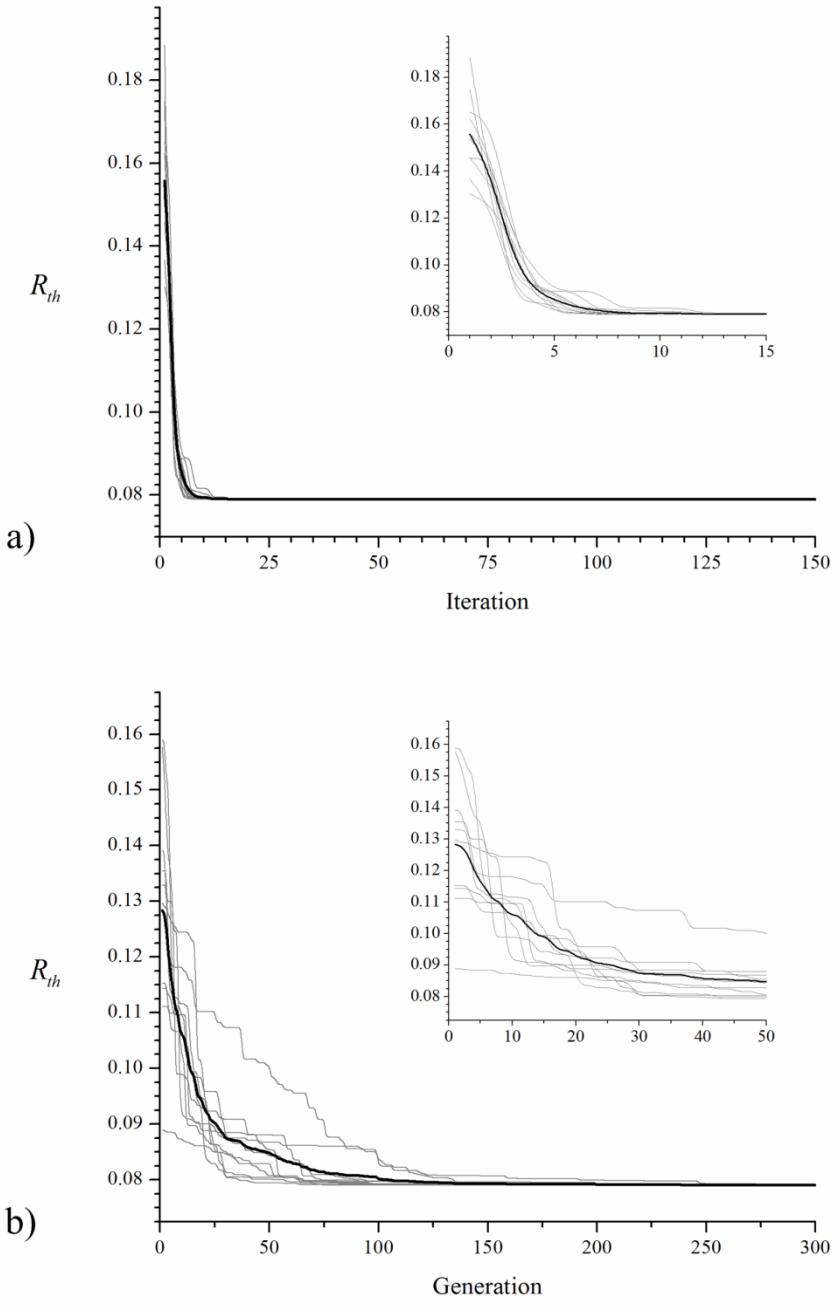

Figure 4.13: Evolution of thermal resistance during the a) PSO and b) GA optimizations of a smooth surface straight-fin heat sink. Thin, light colored lines indicate the individual trials while thick, dark colored lines indicate the average of the ten trials.

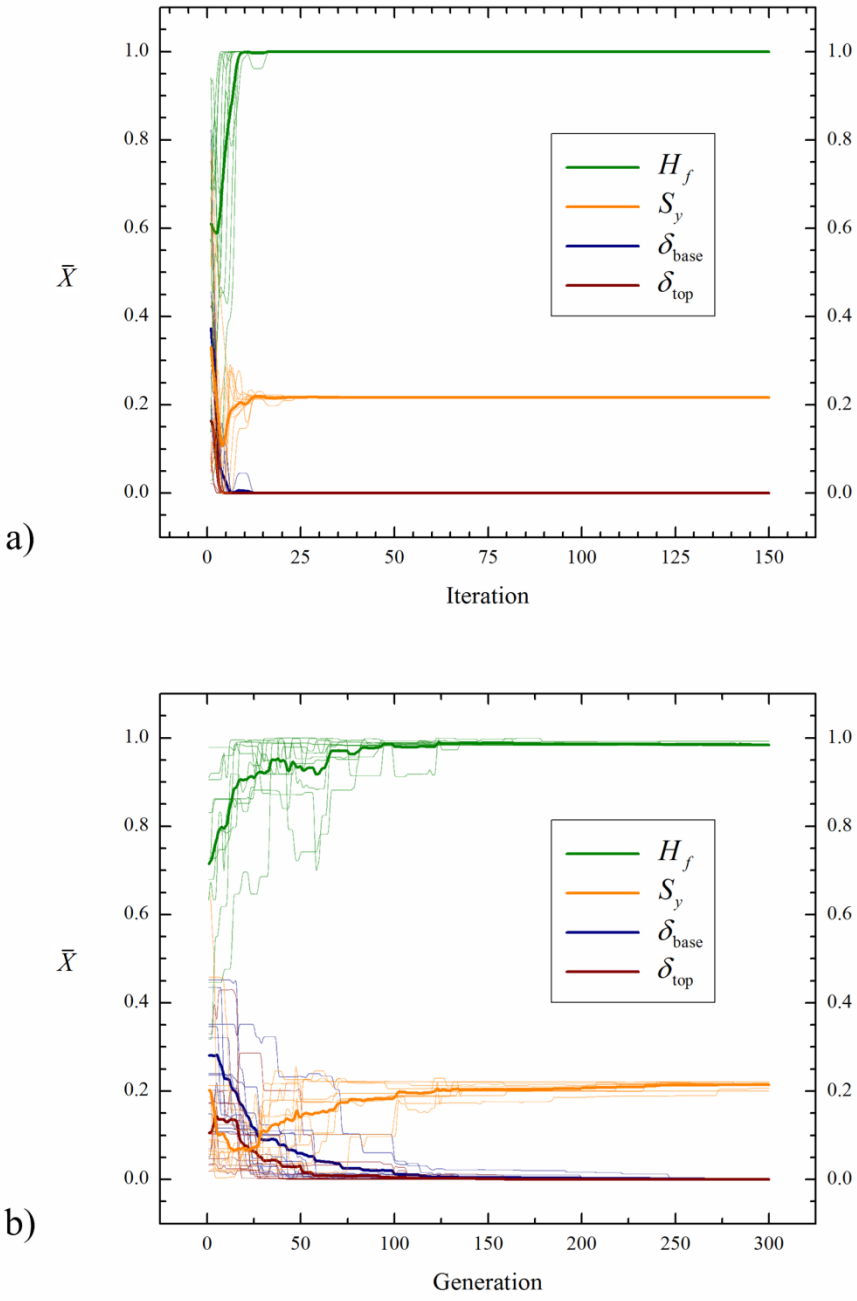

Figure 4.14: Evolution of the scaled design parameters during the a) PSO and b) GA optimizations of a smooth surface straight-fin heat sink. Thin, light colored lines indicate the individual trials while thick, dark colored lines indicate the average of the ten trials.

As a comparison to the PSO, a GA is run for the same problem. A basic single-objective GA is employed that is inspired primarily by the work of Holland [125] and Goldberg [98]. The particular details of the GA being used here were presented in Chapter 4.1, where it was applied to a two-stream heat exchanger with ten design parameters. The GA operation settings used in the present study are given in Table 4.7. The GA similarly evolves the optimal design over generations so that the heat sink thermal resistance favorably evolves, Figure 4.13b, although the GA operates based on genetic rather than social mechanisms. It is apparent from Figure 4.13b, and emphasized in its inset, that convergence is not realized as quickly as for the PSO method. Again, ten independent trials are run for the GA optimization. The optimal thermal resistance for smooth surface straight-fin heat sinks found by the GA for all ten trials is also 0.079 °C/W, and by the 247th generation, all ten individual GA trials have converged to this value. Again, from the perspective of the design space, the GA evolves scaled values of H_f, S_y, δ_{base}, and δ_{top} as shown in Figure 4.14b. Again, it is evident from this figure that all ten trials have converged to an optimal solution in the design space, X^*, for the ten individual GA runs.

N_P	N_G	P_C	P_M
20	300	0.90	0.05

Table 4.7: GA operation settings

Table 4.8 tabulates the characteristics of the optimized smooth surface straight-fin heat sinks produced by both the PSO and the GA methods. Included in this table is the

thermal resistance found by the PSO and GA without the base plate and an isothermal lower boundary condition, and that evaluated with the base plate and a uniform heat flux lower boundary condition. Evident is the 9% increase in thermal resistance resulting from considering the base plate. From Table 4.8, and from careful inspection of Figure 4.14, one can observe that while the optimal thermal resistance value R_{th}^{*} and most of the optimal design parameter values X^{*} obtained by both the PSO and GA agree, the optimal value of H_f found by the GA is slightly smaller than that obtained by the PSO. In other words, the GA's solution sacrifices side-fin surface area and fin conduction in a very small layer at the top of the channel for both a slight flow bypass and exposure of the top surface of the fins. Although it results in a new design from that produced by the PSO its performance in terms of R_{th} is equivalent.

Parameter	Selected Value	
	PSO	GA
Fin thickness at base, δ_{base} (mm)	1.50	1.50
Fin thickness at top, δ_{top} (mm)	1.50	1.50
Fin height, H_f (mm)	23.90	23.66
Pitch/fin thickness at base, S_y (-)	1.75	1.75
Thermal Resistance, R_{th}, without base plate (°C/W)	0.079	0.079
Thermal Resistance, R_{th}, with base plate (°C/W)	0.086	0.086

Table 4.8: Characteristics of optimized smooth surface straight-fin heat sink for PSO and GA methods

4.2.5.2. Scale-Roughened Surface Fins

The previous section considered smooth surface fins. It has previously been shown that augmenting the fin surface with scales enhances the heat transfer without a significant increase in pressure drop [126]. Moreover, recent advances in three-dimensional metal printing techniques [127] make such surfaces readily attainable. A small or moderate increase in the heat transfer coefficient can more than offset even a large friction factor increase because flow velocity can then be decreased and friction power varies with as much as the cube of velocity [30]. The second optimization study uses the surface scales investigated by Chang et al. [126] and more broadly correlated by Zhou et al. [33], and employs a fixed scale diameter D of 1.00mm and a fixed scale height e of 0.10mm. The parameters that are varied and their ranges are the same as for the smooth surface case, see Table 4.5. That is, everything is the same as before except now the fin surfaces are augmented with a high performance surface, Figure 4.10b.

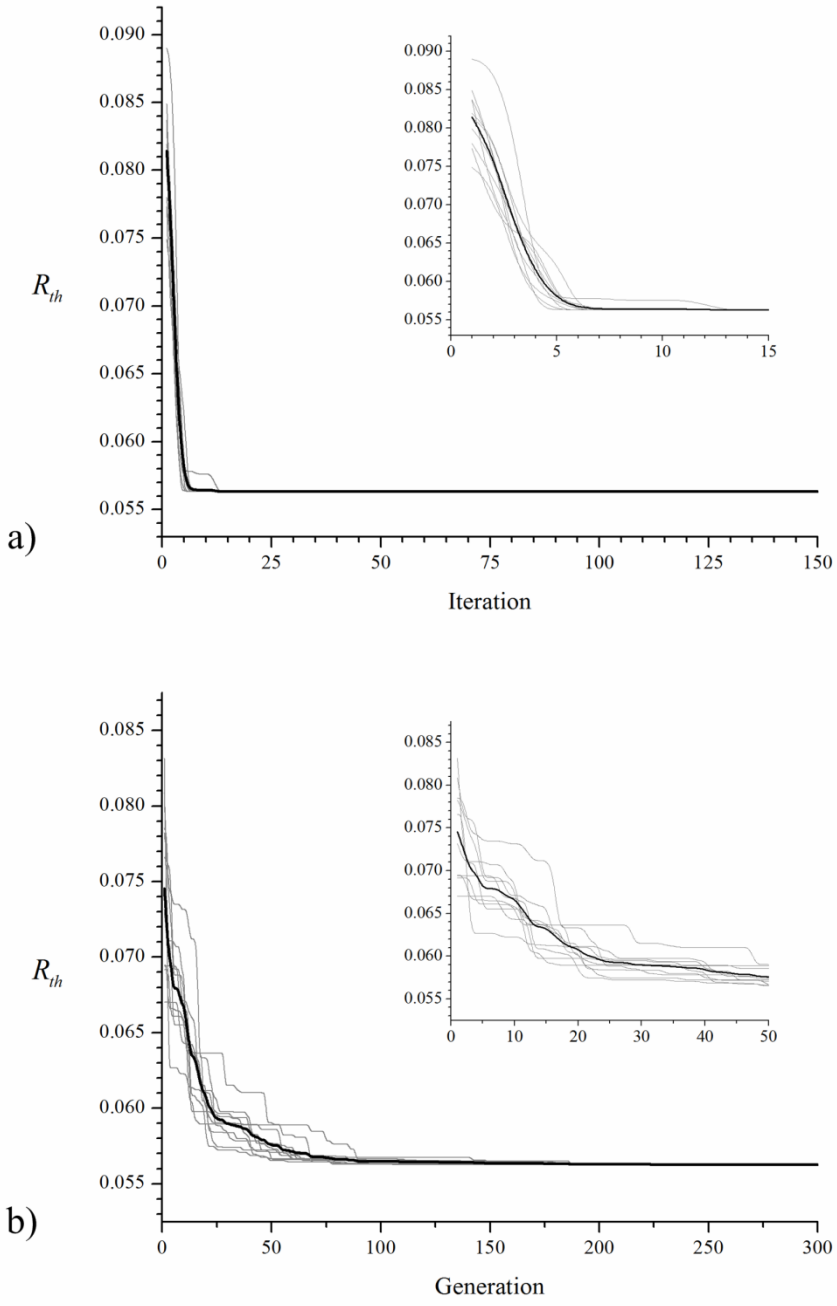

Figure 4.15: Evolution of thermal resistance during the a) PSO and b) GA optimizations of a scale-roughened straight-fin heat sink

The optimized configurations of the scale-roughened straight-fin heat sink obtained with the PSO and GA both give a thermal resistance of 0.056 °C/W when the base plate is neglected, which translates to 0.058 °C/W when the base plate is incorporated, a 4% increase. The geometric parameters are evolved again in ten independent trials by the PSO and GA and the corresponding heat sink thermal resistance evolves as shown in Figure 4.15. The ten individual PSO trials all converge to an optimum value of R_{th} within 13 iterations while the ten individual GA trials all converge within 187 generations. From the perspective of the design space, the PSO and GA evolve scaled values of H_f, S_y, δ_{base}, and δ_{top} as shown in Figure 4.16. Again, as for the case of the smooth surface straight-fin heat sink, in addition to all ten trials converging to an optimal value for R_{th}, all ten trials have also converged to a single optimal solution in the design space for both the PSO and GA methods. The primary difference in the optimal designs between the two types of heat sinks is that for the scale-roughened surface straight-fin heat sink the fins have opened up slightly compared to the smooth surface heat sink.

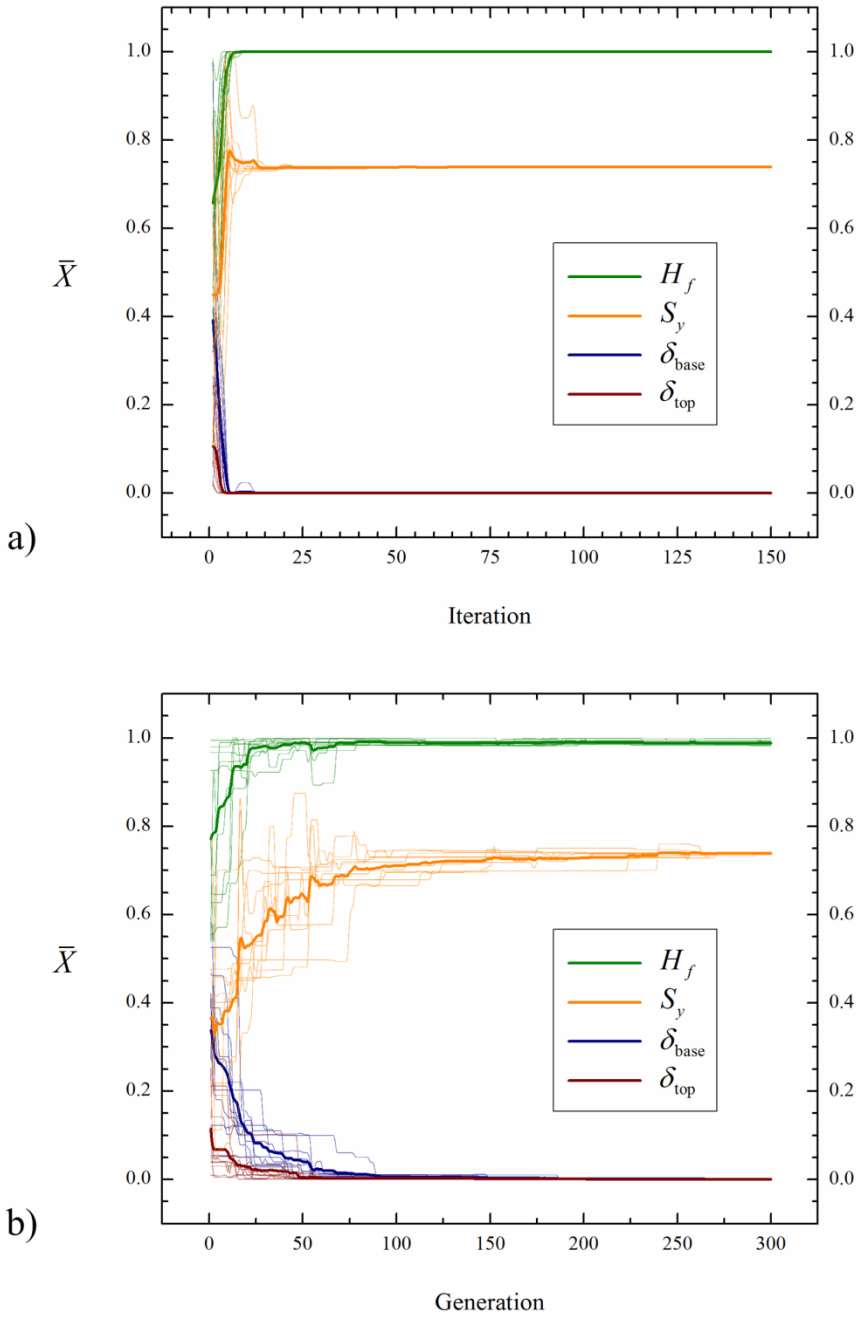

Figure 4.16: Evolution of the scaled design parameters during the a) PSO and b) GA optimizations of a scale-roughened straight-fin heat sink

The characteristics of the optimized heat sink with surface scales found by both the PSO and the GA are compared in Table 4.9. Again the GA favored a very slight by-pass flow as for the smooth surface case. By comparing Table 4.8 and Table 4.9 it is evident that the optimal scale-roughened straight-fin heat sink outperforms the optimal smooth surface heat sink in terms of thermal resistance by 33%. The higher performance of the scale-roughened surface compared to the smooth surface can be attributed to the frequent boundary layer interruption caused by the scales that precludes thickening of the boundary layer.

Parameter	Selected Value	
	PSO	GA
Fin thickness at base, δ_{base} (mm)	1.50	1.50
Fin thickness at top, δ_{top} (mm)	1.50	1.50
Fin height, H_f (mm)	23.90	23.78
Pitch/fin thickness at base, S_y (-)	2.58	2.58
Thermal Resistance, R_{th}, without base plate (°C/W)	0.056	0.056
Thermal Resistance, R_{th}, with base plate (°C/W)	0.058	0.058

Table 4.9: Characteristics of optimized scale-roughened surface straight-fin heat sinks for PSO and GA methods

4.2.5.3. Evolution of the Nonlocal Velocity and Temperature Fields

What distinguishes the present study from those in the past, as was discussed earlier, is that the population-based optimization methods employed here operate on full nonlocal simulations of turbulent flow and heat transfer within and between the fluid and solid phases of the heterogeneous and hierarchical medium. The upper-scale governing

field equations are rigorously derived from fundamental lower-scale equations, and full conjugate effects are included. Additionally, the local transport coefficients, such as the internal heat transfer coefficient that connects the fluid and solid phase thermal energy equations together, are clearly defined. It is therefore relevant to observe the evolution of the nonlocal flow field and temperature fields in both the fluid and solid phases during a PSO trial.

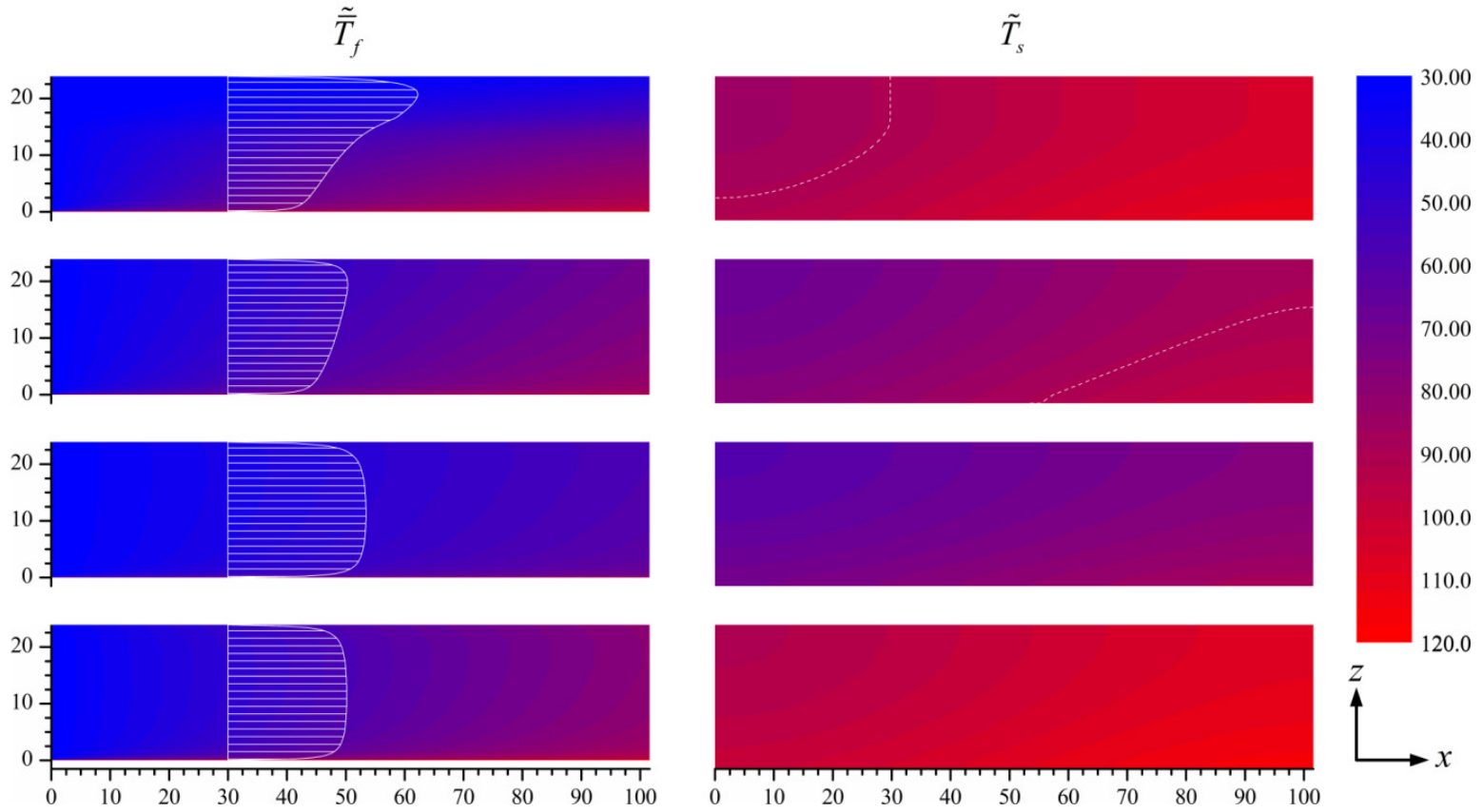

Figure 4.17: Nonlocal fluid (left) and solid (right) temperature fields for the optimal scale-roughened straight-fin heat sink found by the PSO after its a) first, b) fourth, and c) final iteration, along with those for the d) optimal smooth straight-fin heat sink. The fully-developed velocity field profiles and the 90°C contour lines are indicated superimposed on the fluid and solid temperature fields respectively.

The velocity and fluid and solid temperature fields evolve during a single trial of the PSO of a scale-roughened straight-fin heat sink as shown in Figure 4.17a-c. Figure 4.17a illustrates the best solution after the first iteration, Figure 4.17b shows the best solution after the 4th iteration, and Figure 4.17c does so for the converged solution, i.e. after the 13th iteration. Figure 4.17d displays the converged solution of the PSO for the *smooth* surface straight-fin heat sink as a comparison. The temperature fields in the figure are scaled between 30°C and 120°C and the x and z direction coordinates indicate the position in the temperature contours in mm. The velocity magnitude is indicated in m/s by the x coordinate (i.e. $x-30$) as a function of the z direction coordinate which is again indicated in mm. Note in the figure that the solid phase temperature contours include the base plate while the fluid phase temperature contours do not as the fluid phase is only defined in the channel. The details of the heat sink designs considered in Figure 4.17 are tabulated in Table 4.10 for easy reference.

	δ_{base}	δ_{top}	H_f	S_y	R_{th} with base
a)	2.43	2.00	16.46	1.67	0.081
b)	2.16	1.50	23.90	1.73	0.068
c)	1.50	1.50	23.90	2.58	0.058
d)	1.50	1.50	23.90	1.75	0.086

Table 4.10: Characteristics of the heat sinks considered in Figure 4.17.

Evident from Figure 4.17a is that the solution after the first iteration, i.e. the best among N_P randomly selected designs, is far from favorable. Table 4.10 indicates that the fins reach about 70% of the channel height, and that they are relatively thick from the

base to the top. It may be observed from the velocity profile that a significant bypass flow results from this design. Moreover, it may be observed that the fluid temperature $\tilde{\tilde{T}}_f$ becomes very hot around the fins while the flow above the fins stays very cold and is not serving to remove heat. Looking at the solid temperature field $\tilde{T}_s$ one can see that very high temperatures persist. Assuming that temperatures in the heat sink greater than 90°C are unacceptable for the electronics being cooled, and indicating the 90°C contour with a dashed white line, it is evident that this design is far from acceptable, with the maximum temperature incurred being $\tilde{T}_{s,\max} = 111.09°\text{C}$ (and occurring in the bottom of the base plate at the outlet). As a side note, one may observe that $\tilde{T}_s$ is defined throughout the channel in Figure 4.17a even where the fins do not reach. By referring back to Equations (4.26) and (4.27) this is reconciled by observing the influence of the local morphology functions, i.e. $\langle m \rangle$ and S_w, which above the fins are unity and null respectively.

It is evident from Figure 4.17b that the solution resulting from the 4$^{\text{th}}$ iteration is noticeably improved from that previously considered. In this design the fins rise to the full channel height, however the base of the fins is unnecessarily thick. The velocity profile, now without a significant bypass flow, indicates that slightly higher flow velocities occur higher in the channel due to the thinning of the fins and opening of the cross flow area. The fluid temperature does not incur very high local temperatures as was the case for the previous design. Moreover, the solid temperature field is noticeably cooler than for the previous design, with the location of the 90°C contour line indicating

that the design is approaching an acceptable one. The maximum temperature incurred for this design is $\tilde{T}_{s,\max} = 98.37°\text{C}$.

Figure 4.17c presents the solution for the optimized design. In this design the fin height was maximized, the fin thickness from the base to the top was minimized, and the fin pitch was balanced. The velocity profile is symmetric about the channel centerline and the fluid temperature stays cool throughout the domain, allowing the solid phase to remain cool while still providing sufficient heat flow. From the absence of the 90°C contour line in Figure 4.17c, it is evident that the optimal design stays sufficiently cool. The maximum temperature incurred for the optimal design, in fact, is $\tilde{T}_{s,\max} = 87.73°\text{C}$.

As a comparison to the optimized scale-roughened straight-fin heat sink solution depicted in Figure 4.17c, Figure 4.17d provides the solution to the optimized *smooth* straight-fin heat sink. The only differences between the two designs are the fin surface augmentation and the resulting fin pitch. Evident from the figure is that a similar symmetric velocity profile results, with slightly lower magnitudes as a result of the smaller fin pitch, i.e. higher number of fins on the heat sink. The fluid temperature field appears somewhat similar to that found for Figure 4.17b in terms of magnitude and distribution. However, without the surface-scale augmentation, the temperature difference between the solid and fluid must be higher to provide the same heat removal ability, and in this case the entire solid temperature domain is greater than 90°C, with the maximum temperature incurred being $\tilde{T}_{s,\max} = 116.19°\text{C}$. Together Figure 4.17c and Figure 4.17d illustrate the benefits of augmenting the fin surface with scales.

4.2.5.4. Performance of the Particle Swarm Optimization Method

Each optimization method, i.e. PSO and GA, delivers the same heat sink performance R_{th}^{*} for both heat sink types, i.e. smooth and scale-roughened fin surfaces. The time each takes to do so differs, however. In this study the PSO finds the optimum significantly quicker than the GA does, ~10^{-1} seconds quicker in fact. The performance, in particular the convergence speed, of both population-based optimization methods depends on the methods' settings for a particular problem. Since no effort was made to customize these settings in this study (rather, typically used or suggested values were employed for the settings, see Table 4.6 and Table 4.7) conclusions about which method is faster for this particular problem cannot be determined. A future study could explore this by first optimizing each method's settings for the problem and then comparing the two methods' convergence speed. Fortunately, the VAT-based nonlocal modeling method provides solutions very quickly, compared to DNS and CFD, affording designers the luxury of proceeding without fine-tuning the optimization methods' operation parameters.

As was noted above, the GA located optimal designs for both heat sink types with a very slight flow bypass arrangement that exposed the top surface of the fins. Although the optimal heat sink thermal resistances found by the GA were equivalent to those found by the PSO, the solutions – or designs – were distinct. The PSO's superior convergence speed for the problem and settings considered here is at least partly due to its inclination to explore the solution domain's boundaries relatively early in its search. Since several of the optimal designs' parameters lay on the boundary, the PSO settled on these without

much exploration of the rest of the domain. The GA on the other hand operated more methodically and slowly, more thoroughly traversing the search domain in its search for the optimal design. Although the GA ultimately selected δ_{base} and δ_{top} values at the edge of the domain, it settled on a value of H_f just short of the domain's edge, and found no motivation to move this value to the edge of the domain, where the PSO had settled.

Over the course of ten trials, on a 2.20 GHz Intel Core i7-2720QM CPU with 16.0 GB of RAM and for the settings listed in Table 4.6, the compiled Fortran PSO code runs for an average of 6 minutes and 15.2 seconds with N_G changed from 150 to 16 for the smooth surface heat sink and 5 minutes and 37.5 seconds with N_G changed to 13 for the scale-roughened heat sink. As a comparison, over the course of ten trials for the settings tabulated in Table 4.7 the compiled Fortran GA code runs for an average of 1 hour, 7 minutes and 27.5 seconds, with N_G changed from 300 to 247 for the smooth surface heat sink and 1 hour, 2 minutes and 23.3 seconds with N_G changed to 187 for the scale-roughened heat sink. It is evident that either the PSO or the GA methods with standard settings provide optimal designs in a reasonable amount of time even on modest equipment due to their reliance upon the nonlocal physical modeling provided by VAT. As a comparison, running even a single heat sink simulation, never mind any kind of optimization endeavor, with CFD on the same equipment would cost hours.

4.2.6. Conclusions

In this section a VAT-based nonlocal model of transport phenomena in a porous

channel used to simulate flow and heat transfer in a heat sink for cooling electronic devices was the basis for a population-based optimization study. The VAT-based simulation routine was coupled with a single objective PSO design tool in order to perform heat sink optimizations. Results from the PSO method were compared to and verified against those from the GA method. Two different types of straight-fin heat sinks were considered, i.e. one type with smooth surface fins and another with scale-roughened surface fins. The performance of the two types of heat sinks was discussed as was the performance of the two methods of optimization.

It was observed that both optimization methods deliver equivalent optimized heat sink designs in terms of heat sink thermal resistance, however judgment on which method performs better for this particular problem was reserved. It was found that the nonlocal modeling based on VAT allows the PSO and GA methods to obtain optimal designs within several minutes and around an hour respectively on a modest lap top without customizing the optimization methods' settings, providing more freedom in selecting computational design tools for heat sink designers. Moreover, it was observed that augmenting the fins with scales improves the heat sink performance in terms of thermal resistance by 33%. This study demonstrates that the nonlocal thermo-fluid-solid modeling provided by VAT opens the door to easily-implemented and thorough population-based optimization studies of heat sinks.

4.3. Conclusions

This chapter has demonstrated the power of modeling transport phenomena in

heterogeneous and hierarchical engineered devices with VAT. First, a VAT-based two-stream heat exchanger solution routine was coupled to a Genetic Algorithm (GA) to perform design. Subsequently, a VAT-based heat sink solution routine was paired with a Particle Swarm Optimizer (PSO) to perform design. Integrating VAT-based transport model solution routines with intelligent population-based design algorithms offers advantages to design engineers that existing tools cannot match. Such a design methodology may be readily extended to diverse engineering problems involving transport phenomena in heterogeneous and hierarchical media.

5. CONCLUSIONS

After introducing the subject of the dissertation and laying down its theoretical foundation in Chapters 1 and 2 respectively, experimental solutions to the closure problem of VAT-based modeling were provided in Chapter 3. In particular, two unique experimental techniques for evaluating the closure statements were developed, implemented, and validated, while considering several different surfaces. Subsequently, naturally-inspired optimization mechanisms coupled to closed VAT-based models were explored in Chapter 4. In particular, two unique population-based optimization routines performed design on a heat exchanger and heat sink modeled with VAT.

A consistent and important theme throughout the dissertation has been the flexibility and ready application of VAT-based modeling to problems involving hierarchical transport phenomena in heterogeneous porous media. This has been made evident by the generality of the model presented in Chapter 2, the variety of surfaces considered in Chapter 3, and the different systems considered in Chapter 4. The present chapter, Chapter 5, continues this theme by considering the potential for the application of VAT to a variety of new problems. After the discussion on the potential of applying VAT to some new and important problems, a survey of some persistent challenges in VAT-based modeling that need to be addressed is provided, followed by a discussion on the application of some new and attractive design tools to VAT-based models.

As was mentioned, VAT-based modeling readily lends itself to a wide array of problems involving hierarchical transport phenomena in heterogeneous porous media. In addition to presenting equations for nonlinear and turbulent flow and heat transfer in a

porous layer, Travkin and Catton [1] also considered micro-scale and radiative heat transport in porous media. The VAT-based equations provided by Travkin and Catton [1] are also well-suited to describe diffusive and convective transport of mass species in fixed bed catalytic reactors. Travkin later published a website [128] wherein a number of applications for VAT are discussed. For example, discussions at various degrees of depth are provided for the application of VAT-based modeling to the topics of urban air pollution, acoustics, ground water, magnetism, optics, electrodynamics, and medicine, among others [128].

Many additional potential and important applications for VAT-based modeling of hierarchical transport phenomena in heterogeneous porous media exist. Hydrogen storage systems using various adsorption materials, for use in automobiles, provide an example. Hydrogen storage systems are multi-level and hierarchical in nature, with all scales influencing the storage capability as well as the loading and unloading performance of the system. Each level must be accounted for properly, from the lowest, atomic scale, to the individual adsorbent cluster, to a bed of clusters, up to the entire container. Modeling such a system with VAT is a natural extension of the work performed in this dissertation and has yet to be performed. Once the VAT-based model for the system is formulated and implemented in a solver, a tool is at hand for the design, control, and operation of hydrogen storage technologies.

Similar to hydrogen storage systems, data centers are multi-level and hierarchical in nature, with all scales influencing the heat density, local temperature, and potential for failure. From the lowest scale, the computer chip, all the way up to the server cabinet and

room, each level must be accounted for properly. The heat sink considered in Chapter 4 is just one level in this hierarchy. Once a model and its solver are developed, numerous data center design objectives may be pursued, e.g. maximizing energy efficiency, minimizing failure rate, etc. Finding optimal data center designs is not readily possible with current technologies, despite a number of commercial data center simulators, due to time constraints and modeling insufficiencies. However modeling with VAT would provide a likely solution. A VAT-based hierarchical model can incorporate many scales into a single set of equations and yield fast simulations, thus allowing the massive number of design variables that describe the data center at all scales to be optimized with intelligent design algorithms like those presented in this dissertation. Such an application of VAT has yet to be implemented, despite the significant commercial value such a tool would possess.

Exciting and promising new applications for VAT-based modeling of hierarchical transport phenomena in heterogeneous porous media extend beyond the examples discussed above. For example, VAT-based modeling methods are well-suited for nuclear reactor and plant design. Such a modeling effort would need to incorporate, beyond the momentum, heat, and mass transport physics discussed above, additional phenomena, such as radiative transport. Moreover, recent interests, spear-headed by DARPA, have considered intra/inter-chip cooling. A VAT-based hierarchical model for two-phase heat transfer in three-dimensional stacked electronic chip sets would be an ideal basis for the design of such a system, however it has yet to be implemented. It is clear that even more potential and important applications of VAT-based modeling exist that have not been

mentioned here.

To apply VAT-based modeling to solve the important problems introduced above, among others, developments in better understanding VAT, particularly its associated closure problem, must be achieved for the variety of problems and physics encountered. Moreover, it is also important that developments are made in improving the numerical tools for solving the VAT-based equations and pursuing design. For example, improving the computational speed of the VAT equation numerical solver is a persistent desire. Currently, straight-forward finite difference methods are employed. However, numerous methods exist that possess the potential for improved computational performance. The Galerkin method solution is one such method that holds promise and should be explored.

Extending the VAT model beyond one-dimensional flow is necessary for many important problems; however this has yet to be implemented. Extending the VAT model in this way introduces new challenges that must be addressed. In addition to developing a high performance solution procedure for such a model, understanding the closure terms for such multi-dimensional flows must be achieved. Presently this has evaded a thorough understanding and treatment.

Other challenges persist as well. One such obvious challenge is extending the VAT-based model employed in this dissertation to account for new physical phenomena. As a very simple example, the VAT method has yet to even be applied to buoyant flows with variable properties. Additionally, applying new boundary conditions to the governing field equations is crucial for the extension of VAT to, and treatment of, new systems. However, the understanding of how to implement these boundary conditions is

poorly developed.

The understanding of closure theory for VAT has seen substantial gains, and tools, such as CFD and experiments, have been developed to evaluate these closure statements. However, understanding closure for new physics has yet to be developed. Moreover, Vadnjal [26] observed that the thermal boundary condition has no effect on the heat transfer coefficient. Such a claim needs to be verified, and it may be done by starting with analytical solutions, i.e. capillary flow solutions.

Beyond improvements in understanding and applying VAT-based modeling, improvements in design strategy implementation should be pursued. In particular, design for the engineering problems introduced above is often characterized by multiple objectives. Multiple-objective problems require one to seek a set of optimal solutions, i.e. Pareto-optimal solutions, rather than a single optimal solution, see Figure 5.1. In the absence of any further information, none of these solutions are superior to any of the others, thus requiring one to seek as many Pareto-optimal solutions as possible. Deb et al. [102] developed a popular constraint-handling Multi-Objective Evolutionary Algorithm (MOEA) that they labeled as the Nondominated Sorting Genetic Algorithm II (NSGA-II). NSGA-II employs a computationally fast nondominated sorting procedure, an elitist strategy, a parameterless approach, and an effective constraint-handling method to obtain a diverse Pareto-optimal set in a single run. Such a tool should be implemented with the VAT-based solution routines.

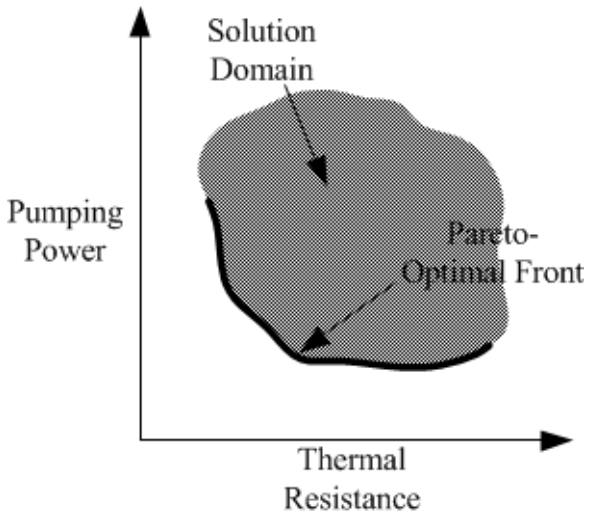

Figure 5.1: Pareto optimal front for a multiple objective optimization problem

The NSGA-II initially creates a random parent population, assigning fitness (i.e. rank and crowding) to each solution, and sorts it based on nondomination. Then, using selection, recombination, and mutation operators, an offspring population is spawned. Subsequent generations then proceed as follows. A combined parent and offspring population is formed and then sorted by nondomination. Combining the parent and offspring populations into a mating pool allows elitism to be enforced. Solutions belonging to the best nondominated sets are chosen for the new parent population, which, through selection, crossover, and mutation operators, produces a new offspring population. Selection is based on both nondomination rank and solution crowding. The new parent and offspring populations are then combined and the process is repeated. This type of design strategy is one of several that should be coupled to VAT-based solvers and explored.

Obvious from this discussion is that a significant amount of development and

work is demanded in the field of design using VAT-based modeling. It is apparent that successful development of such tools will result in significant advantages for the design engineer of such systems. This was demonstrated in Chapter 4 for two different systems, i.e. a heat exchanger and heat sink. Pursuing development of VAT-based modeling and design is crucial, and the successful accomplishment of this will yield significant engineering and societal gains.

REFERENCES

[1] Travkin, V. S., and Catton, I., 2001, "Transport phenomena in heterogeneous media based on volume averaging theory," Advances in Heat Transfer, G. G. Hari, and A. H. Charles, eds., Elsevier, pp. 1-144.

[2] Travkin, V., and Catton, I., 1992, "Models of Turbulent Thermal Diffusivity and Transfer Coefficients for a Regular Packed Bed of Spheres," ASME -PUBLICATIONS- HTD, 193, p. 15.

[3] Travkin, V., and Catton, I., 1995, "A two-temperature model for turbulent flow and heat transfer in a porous layer," Journal of Fluids Engineering, 117(1), pp. 181-188.

[4] Travkin, V. S., and Catton, I., 1998, "Porous media transport descriptions — non-local, linear and non-linear against effective thermal/fluid properties," Advances in Colloid and Interface Science, 76-77(0), pp. 389-443.

[5] Travkin, V. S., Catton, I., and Gratton, L., 1993, "Single Phase Turbulent Transport in Prescribed Non-Isotropic and Stochastic Porous Media," ASME -PUBLICATIONS- HTD, 240, p. 43.

[6] Travkin, V. S., Catton, I., Hu, K., Ponomarenko, A. T., and Shevchenko, V. G., 1999, "Transport Phenomena in Heterogeneous Media: Experimental Data Reduction and Analysis," ASME APPLIED MECHANICS DIVISION -PUBLICATIONS- AMD, 233, pp. 21-32.

[7] Catton, I., 2011, "Conjugate Heat Transfer Within a Heterogeneous Hierarchical Structure," Journal of Heat Transfer, 133(10), p. 103001.

[8] Anderson, T. B., and Jackson, R., 1967, "Fluid Mechanical Description of Fluidized Beds. Equations of Motion," Industrial & Engineering Chemistry Fundamentals, 6(4), pp. 527-539.

[9] Slattery, J. C., 1967, "Flow of viscoelastic fluids through porous media," Aiche J, 13(6), pp. 1066-1071.

[10] Marle, C. M., 1967, "Ecoulements monophasiques en milieu poreux," Rev. Inst. Francais du Petrole, 22, pp. 1471-1509.

[11] Whitaker, S., 1967, "Diffusion and dispersion in porous media," AIChE J. AIChE Journal, 13(3), pp. 420-427.

[12] Zolotarev, P. P., and Radushkevich, L. V., 1968, "An approximate analytical solution of the internal diffusion problem of dynamic absorption in the linear region of an isotherm," Russian Chemical Bulletin, 17(8), pp. 1818-1820.

[13] Slattery, J. C., 1980, Momentum, Energy and Mass Transfer in Continua, Krieger, Malabar.

[14] Kaviany, M., 1995, Principles of Heat Transfer in Porous Media, Springer-Verlag.

[15] Gray, W. G., Leijnse, A., Kolar, R. L., and Blain, C. A., 1993, Mathematical Tools for Changing Spatial Scales in the Analysis of Physical Systems, CRC Press.

[16] Whitaker, S., 1977, "Simultaneous heat, mass and momentum transfer in porous media: a theory of drying," Advances in Heat Transfer, 13, pp. 119-203.

[17] Whitaker, S., 1997, "Volume averaging of transport equations," INTERNATIONAL SERIES ON ADVANCES IN FLUID MECHANICS, 13, pp. 1-60.

[18] Kheifets, L. I., and Neimark, A. V., 1982, "Multiphase Processes in Porous Media," Khimia, Moscow.

[19] Dullien, F. A. L., 1979, Porous Media Fluid Transport and Pore Structure, Academic Press, New York.

[20] Adler, P. M., 1992, Porous Media: Geometry and Transports, Butterworth-Heinemann.

[21] Nakayama, A., Ando, K., Yang, C., Sano, Y., Kuwahara, F., and Liu, J., 2009, "A study on interstitial heat transfer in consolidated and unconsolidated porous media," Heat and Mass Transfer, 45(11), pp. 1365-1372.

[22] Nakayama, A., and Kuwahara, F., 2008, "A General Macroscopic Turbulence Model for Flows in Packed Beds, Channels, Pipes, and Rod Bundles," Journal of Fluids Engineering, 130(10), p. 101205.

[23] Nakayama, A., Kuwahara, F., and Hayashi, T., 2004, "Numerical modelling for three-dimensional heat and fluid flow through a bank of cylinders in yaw," Journal of Fluid Mechanics, 498, pp. 139-159.

[24] Nakayama, A., Kuwahara, F., and Kodama, Y., 2006, "An equation for thermal dispersion flux transport and its mathematical modelling for heat and fluid flow in a porous medium," Journal of Fluid Mechanics, 563(1), pp. 81-96.

[25] Hu, K., 2002, "Flow and heat transfer over rough surfaces in porous media."

[26] Vadnjal, A., 2009, "Modeling of a heat sink and high heat flux vapor chamber," 3401691 Ph.D., University of California, Los Angeles, United States -- California.

[27] Whitaker, S., 1999, The method of volume averaging, Kluwer Academic, Dordrecht; Boston.

[28] Rodi, W., and International Association for Hydraulic, R., 1984, Turbulence models and their application in hydraulics : a state of the art review, International Association for Hydraulic Research, The Netherlands.

[29] Zhou, F., Hansen, N. E., Geb, D. J., and Catton, I., 2011, "Obtaining Closure for Fin-and-Tube Heat Exchanger Modeling Based on Volume Averaging Theory (VAT)," Journal of Heat Transfer, 133(11), p. 111802.

[30] Kays, W. M., and London, A. L., 1984, Compact heat exchangers, McGraw-Hill, New York.

[31] Nie, X., Evitts, R., Besant, R., and Bolster, J., 2011, "A New Technique to Determine Convection Coefficients With Flow Through Particle Beds," TRANSACTIONS- AMERICAN SOCIETY OF MECHANICAL ENGINEERS JOURNAL OF HEAT TRANSFER, 133(4), p. 041601.

[32] Whitaker, S., 1972, "Forced convection heat transfer correlations for flow in pipes, past flat plates, single cylinders, single spheres, and for flow in packed beds and tube bundles," AIChE J. AIChE Journal, 18(2), pp. 361-371.

[33] Zhou, F., DeMoulin, G. W., Geb, D. J., and Catton, I., 2012, "Closure for a plane fin heat sink with scale-roughened surfaces for volume averaging theory (VAT) based modeling," International Journal of Heat and Mass Transfer, 55(25–26), pp. 7677-7685.

[34] Zhou, F., and Catton, I., 2012, "Volume Averaging Theory (VAT) based modeling and closure evaluation for fin-and-tube heat exchangers," Heat and Mass Transfer, pp. 1-11.

[35] Horvat, A., and Mavko, B., 2005, "Hierarchic modeling of heat transfer processes in heat exchangers," International Journal of Heat and Mass Transfer, 48(2), pp. 361-371.

[36] Vadnjal, A., 2009, "Modeling of a heat sink and high heat flux vapor chamber."

[37] Krishnakumar, K., John, A. K., and Venkatarathnam, G., 2011, "A review on transient test techniques for obtaining heat transfer design data of compact heat exchanger surfaces," Experimental Thermal and Fluid Science, 35(4), pp. 738-743.

[38] Bhattacharya, A., Calmidi, V. V., and Mahajan, R. L., 2002, "Thermophysical properties of high porosity metal foams," International Journal of Heat and Mass Transfer, 45(5), pp. 1017-1031.

[39] Ibrahim, M. B., Zhiguo, Z., Rong, W., Simon, T. W., and Gedeon, D., "A 2-D CFD model of oscillatory flow with jets impinging on a random wire regenerator matrix," Proc. Energy Conversion Engineering Conference, 2002. IECEC '02. 2002 37th Intersociety, pp. 511-517.

[40] Makoto, T., Iwao, Y., and Fumitake, C., 1990, "Flow and Heat Transfer Characteristics of the Stirling Engine Regenerator in an Oscillating Flow," JSME international journal. Ser. 2, Fluids engineering, heat transfer, power, combustion, thermophysical properties, 33(2), pp. 283-289.

[41] Miyabe, H., Hamaguchi, K., and Takahashi, K., 1982, An approach to the design of Stirling engine regenerator matrix using packs of wire gauzes.

[42] Gedeon, D., and Wood, J., 1992, "Oscillating-flow regenerator test rig: Woven screen and metal felt results."

[43] Gedeon, D., and Wood, J., 1996, "Oscillating-Flow Regenerator Test Rig: Hardware and Theory With Derived Correlations for Screens and Felts."

[44] Simon, T. W., and Seume, J. R., 1988, "A survey of oscillating flow in Stirling engine heat exchangers," NASA STI/Recon Technical Report N, 88, p. 22322.

[45] KNOWLES, T., 1997, "Composite Matrix Regenerator for Stirling Engines(Final Report)."

[46] Thieme, L. G., 2001, "Friction Factor Characterization for High-Porosity Random Fiber Regenerators," 2001.

[47] Tew, R., Ibrahim, M., Danila, D., Simon, T., Mantell, S., Sun, L., Gedeon, D., Kelly, K., McLean, J., and Qiu, S., 2007, "A Microfabricated Involute-Foil Regenerator for Stirling Engines."

[48] Ibrahim, M., Danila, D., Simon, T., Mantell, S., Sun, L., Gedeon, D., Qiu, S., Wood, J., Kelly, K., and McLean, J., 2007, "A Microfabricated Segmented-Involute-Foil Regenerator for Enhancing Reliability and Performance of Stirling Engines: Phase II Final Report for the Radioisotope Power Conversion Technology NRA Contract NAS3–03124," NASA Contractor Report, NASA/CR—2007-215006.

[49] Zalba, B., Marín, J. M., Cabeza, L. F., and Mehling, H., 2003, "Review on thermal energy storage with phase change: materials, heat transfer analysis and applications," Applied Thermal Engineering, 23(3), pp. 251-283.

[50] Knowels, T. R., 1997, "Composite Matrix Regenerator for Stirling Engines," NASA Contractor Report 202322.

[51] Koh, J. C. Y., and Fortini, A., 1973, "Prediction of thermal conductivity and electrical resistivity of porous metallic materials," International Journal of Heat and Mass Transfer, 16(11), pp. 2013-2022.

[52] Geb, D., Zhou, F., and Catton, I., 2012, "Internal Heat Transfer Coefficient Determination in a Packed Bed From the Transient Response Due to Solid Phase Induction Heating," Journal of Heat Transfer, 134(4), p. 042604.

[53] Anzelius, A., 1926, "Uber Erwärmung vermittels durchströmender Medien," Z. angew. Math. Mech. ZAMM - Journal of Applied Mathematics and Mechanics / Zeitschrift für Angewandte Mathematik und Mechanik, 6(4), pp. 291-294.

[54] Schumann, T. E. W., 1929, "Heat transfer: A liquid flowing through a porous prism," Journal of the Franklin Institute, 208(3), pp. 405-416.

[55] Gedeon, D., 2011, "Sage User's Guide," Gedeon Associates, Athens, OH.

[56] Jones, S., and Catton, I., 2001, "NON-INTRUSIVE HEAT TRANSFER COEFFICIENT DETERMINATION IN HIGH POROSITY RETICULATED FOAMS."

[57] Zukauskas, A., and Ulinskas, R., 1985, "Efficiency Parameters for Heat Transfer in Tube Banks," Heat Transfer Eng. Heat Transfer Engineering, 6(1), pp. 19-25.

[58] Zukauskas, A., and Ulinskas, R., 1983, "Banks of plain and finned tubes," Heat exchanger design handbook, B. A. Bodling, and M. Prescott, eds., Hemisphere Publishing Co., Washington, DC.

[59] Zukauskas, A., and Ulinskas, R., 1988, Heat transfer in tube banks in crossflow.

[60] Zukauskas, A., 1987, "Convective heat transfer in cross flow ".

[61] Incropera, F. P., DeWitt, D. P., Bergman, T. L., and Lavine, A. S., 2007, Fundamentals of heat and mass transfer, John Wiley & Sons, Danvers (MA).

[62] Rhee, S. J., 1977, "Natural convection heat transfer in beds of inductively heated particles."

[63] Somerton, C. W., 1982, "Natural convection and boiling in porous media."

[64] Cherng, J.-C., 1978, "Effect of bottom cooling on natural convection in beds of inductively heated particles."

[65] Mills, A. F., 1999, Heat transfer, Prentice Hall, Upper Saddle River, N.J.

[66] Benenati, R. F., and Brosilow, C. B., 1962, "Void fraction distribution in beds of spheres," AIChE J. AIChE Journal, 8(3), pp. 359-361.

[67] Martin, H., 1978, "Low peclet number particle-to-fluid heat and mass transfer in packed beds," Chemical Engineering Science, 33(7), pp. 913-919.

[68] Achenbach, E., 1995, "Heat and flow characteristics of packed beds," Experimental Thermal and Fluid Science, 10(1), pp. 17-27.

[69] Ziólkowska, I., and Ziólkowski, D., 1988, "Fluid flow inside packed beds," Chemical Engineering and Processing: Process Intensification Chemical Engineering and Processing: Process Intensification, 23(3), pp. 137-164.

[70] Schlunder, E. U., "Transport Phenomena in Packed Bed Reactors," Proc. Chemical Reaction Engineering Reviews-Houston, Am. Chem. Sot. Symp. Ser., D. Luss, and V. W. Weekman, eds., pp. 110-161.

[71] Fiers, B., Ferschneider, G., and Maillet, D., 2010, "Reduced model for characterization of solid wall effects for transient thermal dispersion in granular porous media," International Journal of Heat and Mass Transfer, 53(25-26), pp. 5962-5975.

[72] Scheidegger, A. E., 1957, The Physics of Flow through Porous Media, Univ. Toronto Press.

[73] Wakao, N., Kato, K., and Yokohama Natl, U., 1969, "Effective thermal conductivity of packed beds," J. Chem. Eng. Jpn., 2:1, pp. 24-33.

[74] Kar, K. K., and Dybbs, A., 1982, "Internal heat transfer coefficients of porous metals," NASA STI/Recon Technical Report A, 84, p. 13239.

[75] Rajkumar, M., 1993, "Theoretical and Experimental Studies of Heat Transfer in Transpired Porous Ceramics," M.S.M.E. , Purdue University, West Lafayette, IN.

[76] Younis, L., and Viskanta, R., 1993, "Experimental determination of the volumetric heat transfer coefficient between stream of air and ceramic foam," International Journal of Heat and Mass Transfer International Journal of Heat and Mass Transfer, 36(6), pp. 1425-1434.

[77] Galitseysky, B., and Mozhaev, A., 1993, "Heat transfer and hydraulic resistance in porous systems," Experimental Thermal and Fluid Science Experimental Thermal and Fluid Science, 7(2), pp. 168-168.

[78] Kokorev, L. S., Subbotin, V. I., Fedoseev, V. N., Kharitonov, V. V., Voskoboinikov, V. V., and Moscow Physical-Engineering Institute, U., 1987, "Relationship between fluid resistance and heat transfer in porous media," High Temp. (Engl. Transl.), 25:1, pp. 82-87.

[79] Gortyshov, Y. F., Murav'ev, G. B., Nadyrov, I. N., and A.N. Tupolev Aviation Institute, K., 1988, "Experimental study of flow and heat exchange in highly porous structures," J. Eng. Phys. (Engl. Transl.), 53:3, pp. 987-990.

[80] Spalding, D. B., Taborek, J., and Armstrong, R. C., 1983, Heat Exchanger Design Handbook, Hemisphere Puplising Corporation, New York.

[81] Ozkol, I., and Komurgoz, G., 2005, "Determination of the Optimum Geometry of the Heat Exchanger Body Via A Genetic Algorithm," Numerical Heat Transfer, Part A: Applications, 48(3), pp. 283-296.

[82] Xie, G., Wang, Q., and Sunden, B., 2008, "Application of a Genetic Algorithm for Thermal Design of Fin-and-Tube Heat Exchangers," Heat Transfer Engineering, 29(7), pp. 597-607.

[83] Domanski, P. A., 1989, "EVSIM: An Evaporator Simulation Model Accounting for Refrigerant and One Dimensional Air Distribution.," D. o. Energy, ed., NISTIR 89-4133, Washington, DC p. 142.

[84] NIST, 2003, "EVAP-COND - simulation models for finned-tube heat exchangers," N. I. o. S. a. Technologies, ed.Gaithersburg, MD, USA.

[85] Domanski, P. A., and Yashar, D., 2007, "Optimization of finned-tube condensers using an intelligent system," International Journal of Refrigeration, 30(3), pp. 482-488.

[86] Jiang, H., Aute, V., and Radermacher, R., 2006, "CoilDesigner: a general-purpose simulation and design tool for air-to-refrigerant heat exchangers," International Journal of Refrigeration, 29(4), pp. 601-610.

[87] Abdelaziz, O., Aute, V., Azarm, S., and Radermacher, R., 2010, "Approximation-Assisted Optimization for Novel Compact Heat Exchanger Designs," HVAC&R Research, 16(5), pp. 707-728.

[88] Mousavi, S. S., Hooman, K., and Mousavi, S. J., 2007, "Genetic algorithm optimization for finned channel performance," Applied Mathematics and Mechanics, 28(12), pp. 1597-1604.

[89] Mousavi, S. S., and Hooman, K., 2006, "Heat and fluid flow in entrance region of a channel with staggered baffles," Energy Conversion and Management, 47(15–16), pp. 2011-2019.

[90] Matos, R. S., Laursen, T. A., Vargas, J. V. C., and Bejan, A., 2004, "Three-dimensional optimization of staggered finned circular and elliptic tubes in forced convection," International Journal of Thermal Sciences, 43(5), pp. 477-487.

[91] Fabbri, G., 2000, "Heat transfer optimization in corrugated wall channels," International Journal of Heat and Mass Transfer, 43(23), pp. 4299-4310.

[92] Foli, K., Okabe, T., Olhofer, M., Jin, Y., and Sendhoff, B., 2006, "Optimization of micro heat exchanger: CFD, analytical approach and multi-objective evolutionary algorithms," International Journal of Heat and Mass Transfer, 49(5-6), pp. 1090-1099.

[93] Hilbert, R., Janiga, G., Baron, R., and Thévenin, D., 2006, "Multi-objective shape optimization of a heat exchanger using parallel genetic algorithms," International Journal of Heat and Mass Transfer, 49(15–16), pp. 2567-2577.

[94] Hooman, K., and Gurgenci, H., 2010, "Porous Medium Modeling of Air-Cooled Condensers," Transport in Porous Media, 84(2), pp. 257-273.

[95] Wang, C.-C., Chi, K.-Y., and Chang, C.-J., 2000, "Heat transfer and friction characteristics of plain fin-and-tube heat exchangers, part II: Correlation," International Journal of Heat and Mass Transfer, 43(15), pp. 2693-2700.

[96] Techo, R., Tickner, R. R., and James, R. E., 1965, "An accurate equation for the computation of the friction factor for smooth pipes for the Reynolds number," J. Appl. Mech., 32, p. 443.

[97] Whitaker, S., 1972, "Forced convection heat transfer correlations for flow in pipes, past flat plates, single cylinders, single spheres, and for flow in packed beds and tube bundles," AIChE Journal, 18(2), pp. 361-371.

[98] Goldberg, D. E., 1989, Genetic algorithms in search, optimization, and machine learning, Addison-Wesley Pub. Co., Reading, Mass.

[99] Chen, S. S., and Jendrzejcyk, J. A., 1981, "Experiments on fluid elastic instability in tube banks subjected to liquid cross flow," Journal of Sound and Vibration, 78(3), pp. 355-381.

[100] Weaver, D. S., and Grover, L. K., 1978, "Cross-flow induced vibrations in a tube bank—Turbulent buffeting and fluid elastic instability," Journal of Sound and Vibration, 59(2), pp. 277-294.

[101] Domanski, P. A., Yashar, D., Lee, S., and Wojtusiak, J., 2011, "Practical Aspects of Applying Evolutionary Algorithms for Optimizing Refrigerant Circuitry in Heat Exchangers," 23rd IIR International Congress of RefrigerationPrague, p. 8 pp.

[102] Deb, K., Pratap, A., Agarwal, S., and Meyarivan, T., 2002, "A fast and elitist multiobjective genetic algorithm: NSGA-II," Evolutionary Computation, IEEE Transactions on, 6(2), pp. 182-197.

[103] Holland, J. H., 1992, "Adaptation In Natural And Artificial Systems: An Introductory Analysis With Applications To Biology, Control, And Artific."

[104] Queipo, N., Devarakonda, R., and Humphrey, J. A. C., 1994, "Genetic algorithms for thermosciences research: application to the optimized cooling of electronic components," International Journal of Heat and Mass Transfer, 37(6), pp. 893-908.

[105] Manivannan, S., Devi, S. P., and Arumugam, R., "Optimization of flat plate heat sink using genetic algorithm," Proc. Electrical Energy Systems (ICEES), 2011 1st International Conference on, pp. 78-81.

[106] Mohsin, S., Maqbool, A., and Khan, W. A., 2009, "Optimization of cylindrical pin-fin heat sinks using genetic algorithms," IEEE Trans. Compon. Packag. Technol. IEEE Transactions on Components and Packaging Technologies, 32(1), pp. 44-52.

[107] Ndao, S., Peles, Y., and Jensen, M. K., 2009, "Multi-objective thermal design optimization and comparative analysis of electronics cooling technologies," International Journal of Heat and Mass Transfer, 52(19-20), pp. 4317-4326.

[108] Jian-hui, Z., Chun-xin, Y., and Li-na, Z., 2009, "Minimizing the entropy generation rate of the plate-finned heat sinks using computational fluid dynamics and combined optimization," Applied Thermal Engineering, 29(8-9), pp. 1872-1879.

[109] Wildi-Tremblay, P., and Gosselin, L., 2007, "Layered porous media architecture for maximal cooling," International Journal of Heat and Mass Transfer, 50(3–4), pp. 464-478.

[110] Tye-Gingras, M., and Gosselin, L., 2008, "Thermal Resistance Minimization of a Fin-and-Porous-Medium Heat Sink with Evolutionary Algorithms," Numerical Heat Transfer, Part A: Applications, 54(4), pp. 349-366.

[111] Leblond, G., and Gosselin, L., 2008, "Effect of non-local equilibrium on minimal thermal resistance porous layered systems," International Journal of Heat and Fluid Flow, 29(1), pp. 281-291.

[112] Kennedy, J., and Eberhart, R., "Particle swarm optimization," Proc. Neural Networks, 1995. Proceedings., IEEE International Conference on, pp. 1942-1948 vol.1944.

[113] Eberhart, R., and Kennedy, J., "A new optimizer using particle swarm theory," Proc. Micro Machine and Human Science, 1995. MHS '95., Proceedings of the Sixth International Symposium on, pp. 39-43.

[114] Eberhart, R., and Shi, Y., 1998, "Comparison between genetic algorithms and particle swarm optimization," Evolutionary Programming VII, V. Porto, N. Saravanan, D. Waagen, and A. Eiben, eds., Springer Berlin / Heidelberg, pp. 611-616.

[115] Eberhart, R. C., and Shi, Y., "Comparing inertia weights and constriction factors in particle swarm optimization," Proc. Evolutionary Computation, 2000. Proceedings of the 2000 Congress on, pp. 84-88 vol.81.

[116] Eberhart, and Yuhui, S., "Particle swarm optimization: developments, applications and resources," Proc. Evolutionary Computation, 2001. Proceedings of the 2001 Congress on, pp. 81-86 vol. 81.

[117] Shi, Y., and Eberhart, R. C., "Empirical study of particle swarm optimization," Proc. Evolutionary Computation, 1999. CEC 99. Proceedings of the 1999 Congress on, p. 1950 Vol. 1953.

[118] Xiaohui, H., and Eberhart, R., "Multiobjective optimization using dynamic neighborhood particle swarm optimization," Proc. Evolutionary Computation, 2002. CEC '02. Proceedings of the 2002 Congress on, pp. 1677-1681.

[119] Xiaohui, H., Eberhart, R. C., and Yuhui, S., "Particle swarm with extended memory for multiobjective optimization," Proc. Swarm Intelligence Symposium, 2003. SIS '03. Proceedings of the 2003 IEEE, pp. 193-197.

[120] Bureerat, S., and Srisomporn, S., 2010, "Optimum plate-fin heat sinks by using a multi-objective evolutionary algorithm," Engineering Optimization, 42(4), pp. 305-323.

[121] Kanyakam, S., and Bureerat, S., 2011, "Multiobjective evolutionary optimization of splayed pin-fin heat sink," Engineering Applications of Computational Fluid Mechanics, 5(4), pp. 553-565.

[122] Kanyakam, S., and Bureerat, S., 2012, "Multiobjective Optimization of a Pin-Fin Heat Sink Using Evolutionary Algorithms," Journal of Electronic Packaging, 134(2), pp. 021008-021008.

[123] Shi, Y., and Eberhart, R., "A modified particle swarm optimizer," Proc. Evolutionary Computation Proceedings, 1998. IEEE World Congress on Computational Intelligence., The 1998 IEEE International Conference on, pp. 69-73.

[124] Xiaohui, H., Yuhui, S., and Eberhart, R., "Recent advances in particle swarm," Proc. Evolutionary Computation, 2004. CEC2004. Congress on, pp. 90-97 Vol.91.

[125] Holland, J. H., 1992, Adaptation in natural and artificial systems: an introductory analysis with applications to biology, control, and artificial intelligence, MIT press.

[126] Chang, S. W., Liou, T.-M., and Lu, M. H., 2005, "Heat transfer of rectangular narrow channel with two opposite scale-roughened walls," International Journal of Heat and Mass Transfer, 48(19-20), pp. 3921-3931.

[127] Lyons, A., Krishnan, S., Mullins, J., Hodes, M., and Hernon, D., "Advanced heat sinks enabled by three-dimensional printing," Proc. Twentieth Annual International Solid Freeform Fabrication Symposium.

[128] Travkin, V., "HSPT - Hierarchical Scaled Physics and Technologies," Web Page, http://www.travkin-hspt.com/.

[129] Hausen, H., 1929, "Über die Theorie des Wärmeaustausches in Regeneratoren," ZAMM - Journal of Applied Mathematics and Mechanics / Zeitschrift für Angewandte Mathematik und Mechanik, 9(3), pp. 173-200.

[130] Locke, G. L., and Stanford University. Dept. of Mechanical, E., 1950, Heat transfer and flow friction characteristics of porous solids, Stanford University. Department of Mechanical Engineering, Stanford, Calif.

[131] Kohlmayr, G., 1968, "An indirect curve matching method for transient matrix heat-transfer testing in the low Ntu-range," International Journal of Heat and Mass Transfer International Journal of Heat and Mass Transfer, 11(3), pp. 567-581.

[132] Kohlmayr, G. F., 1968, "Extension of the Maximum Slope Method to Arbitrary Upstream Fluid Temperature Changes," Journal of Heat Transfer, 90(1), pp. 130-134.

[133] Rodriguez, J. I., and Mills, A. F., 1990, "Analysis of the single-blow transient testing technique for perforated plate heat exchangers," International Journal of Heat and Mass Transfer, 33, pp. 1969-1976.

[134] Liang, C. Y., and Yang, W.-J., 1975, "Modified Single-Blow Technique for Performance Evaluation on Heat Transfer Surfaces," J. Heat Transfer Journal of Heat Transfer, 97(1).

[135] Stang, J. H., and Bush, J. E., 1974, "The Periodic Method for Testing Compact Heat Exchanger Surfaces," J. Eng. Power Journal of Engineering for Power, 96(2).

[136] Gosselin, L., Tye-Gingras, M., and Mathieu-Potvin, F., 2009, "Review of utilization of genetic algorithms in heat transfer problems," International Journal of Heat and Mass Transfer, 52(9-10), pp. 2169-2188.

[137] Heymann, D., Pence, D., and Narayanan, V., 2010, "Optimization of fractal-like branching microchannel heat sinks for single-phase flows," International Journal of Thermal Sciences, 49(8), pp. 1383-1393.

[138] Pence, D., 2003, "REDUCED PUMPING POWER AND WALL TEMPERATURE IN MICROCHANNEL HEAT SINKS WITH FRACTAL-LIKE BRANCHING CHANNEL NETWORKS," Microscale Thermophysical Engineering, 6(4), pp. 319-330.

[139] Alharbi, A. Y., Pence, D. V., and Cullion, R. N., 2003, "Fluid Flow Through Microscale Fractal-Like Branching Channel Networks," Journal of Fluids Engineering, 125(6), pp. 1051-1057.

[140] Alharbi, A. Y., Pence, D. V., and Cullion, R. N., 2004, "Thermal Characteristics of Microscale Fractal-Like Branching Channels," Journal of Heat Transfer, 126(5), pp. 744-752.

[141] White, F. M., 1991, Viscous Fluid Flow, McGraw-Hill.

[142] Shah, R. K., and London, A. L., 1978, Laminar flow forced convection in ducts: a source book for compact heat exchanger analytical data, Academic Press.

[143] Rao, R. V., and Patel, V. K., 2010, "Thermodynamic optimization of cross flow plate-fin heat exchanger using a particle swarm optimization algorithm," International Journal of Thermal Sciences, 49(9), pp. 1712-1721.

[144] Bejan, A., 1977, "Concept of irreversibility in heat exchanger design: Counterflow heat exchangers for gas-to-gas applications," J. Heat Transfer;(United States), 99(3).

[145] Joshi, H. M., and Webb, R. L., 1987, "Heat transfer and friction in the offset stripfin heat exchanger," International Journal of Heat and Mass Transfer, 30(1), pp. 69-84.

[146] Mishra, M., Das, P. K., and Sarangi, S., 2009, "Second law based optimisation of crossflow plate-fin heat exchanger design using genetic algorithm," Applied Thermal Engineering, 29(14-15), pp. 2983-2989.

[147] Xie, G. N., Sunden, B., and Wang, Q. W., 2008, "Optimization of compact heat exchangers by a genetic algorithm," Applied Thermal Engineering, 28(8-9), pp. 895-906.

APPENDIX

A VAT-Based Length Scale

The following relates the discussion provided by Travkin and Catton [1] on the VAT-based length scale. They demonstrated that modeling based on volume averaging theory (VAT) provides a basis for consistency to experimental procedures and to data reduction processes. Travkin and Catton [1] suggested scaling parameters that allow a wide variety of different porous media morphologies to be normalized, which often eliminates the need for further experimental efforts [1, 7, 26, 29].

In particular, Travkin and Catton [1-7] demonstrated that globular morphologies can be described in terms of S_w, $\langle m \rangle$, and d_p and can generally be considered to be spherical particles with

$$S_w = \frac{6\left(1-\langle m \rangle\right)}{d_p} \text{ and } d_h = \frac{2}{3}\frac{\langle m \rangle}{\left(1-\langle m \rangle\right)} d_p . \tag{A.1}$$

They noted that this expression has the same dependency on equivalent pore diameter as found for a one-diameter capillary morphology, leading naturally to

$$S_w = \frac{6\left(1-\langle m \rangle\right)}{d_p} = \frac{6\left(1-\langle m \rangle\right)}{\frac{3}{2}\left(\frac{1-\langle m \rangle}{\langle m \rangle}\right) d_h} = 4\frac{\langle m \rangle}{d_h} \tag{A.2}$$

This observation then led them to define the simple VAT-based porous media length scale, given in Equation (2.25), i.e.

$$d_h = 4\frac{\langle m \rangle}{S_w}, \tag{A.3}$$

that meets the needs of both major morphologies, i.e. capillary and globular. Travkin and Catton [1] noted that this was also recognized by Whitaker [32] when he employed a very similar length scale, which only differed by a constant, to correlate heat transfer data for a wide variety of morphologies.

B An Abridged Review of Transient Test Techniques

In the literature on the subject, many transient test methods used to measure convective heat transfer characteristics are often described as "single-blow" transient test techniques. In such single-blow tests, a single fluid stream, under steady flow conditions, is subjected to an inlet fluid temperature perturbation. The temperature perturbation could be a step change or an oscillatory function, for example. The inlet and outlet stream temperatures are measured continuously over an interval of time and compared to the predictions of a model in order to determine the desired heat transfer information. This single-blow method, and its variations, along with various other transient techniques for convective heat transfer measurements have been investigated since the 1920s.

Hausen [129], Schumann [54], Locke [130], and Kohlmayr [131, 132] performed

much of the important early work on transient test methods for complicated heat transfer surfaces. Since then, transient testing methods have seen progress due to a number of investigators. The following presents an abridged review of a selection of these studies.

Rodriguez and Mills [133] adapted the single-blow transient testing technique, with a step-change in the inlet stream temperature, to analyze perforated plate heat exchangers and similar discontinuous surfaces. They formulated a set of coupled first order differential equations for the plate and fluid temperatures by applying energy balances to each of the plates in the exchanger. These equations were then solved numerically for a set of perforated plate heat exchangers containing a range of plate numbers, number of transfer units, and axial conduction parameters. Dimensionless maximum slopes were then presented in tabular form, allowing the heat transfer coefficient to be calculated from test data.

Liang and Yang [134] conducted a modified single-blow experiment to determine the convective heat transfer coefficients of surfaces. Accounting for the finite heat capacity of the heating screens used to implement the "step-change" in the inlet stream temperature, they modeled the fluid temperature jump as an exponential function. They then obtained an analytical solution using Laplace transforms and determined the heat transfer coefficient through a curve-matching technique. Their analysis unfortunately did not include axial conduction.

Stang and Bush [135] investigated heat transfer performance in a heat exchanger core by applying a periodic method. Realizing the experimental difficulty inherent in producing a step-change in the inlet fluid stream temperature, they implemented a more

experimentally convenient periodic inlet stream temperature fluctuation and measured the temperature response of the outlet flow stream. They developed a mathematical model corresponding to such an inlet stream temperature condition, obtained test results for the periodic method, and conducted a critical comparison of the periodic method with the conventional single-blow method in which a step-change in the inflow stream temperature occurs. They concluded their study by listing the advantages of the periodic method over the step-change method.

Younis and Viskanta [76] experimentally investigated heat transfer by forced convection of air through porous ceramic foams using a single-blow transient technique. Employing a two-temperature model and implementing a step-change in the inlet air stream temperature, they obtained heat transfer coefficient correlations for a variety of foam specifications.

Nie et al. [31] determined the convective heat transfer coefficient for flow through particle beds using a new technique. Applying a step change to the inlet air stream temperature, the transient experimental temperature distribution in the bed and the temperature at the outlet were obtained for the time interval during which the bed temperature distribution was essentially linear. These data were compared to a model in which the transient energy balance equations were integrated over the bed length and the specific time period in order to determine a correlation for the effective heat transfer coefficient in the bed.

C An Abridged Review of Heat Sink and Heat Exchanger Population-Based Optimization Studies

In an early article on the subject, Queipo, Devarakonda and Humphrey [104] examined the potential for GAs in "complex thermoscience problems" wherein the high dimensionality and ranges of the associated variables and parameter spaces, along with the strong non-linearities embedded in the mathematical representations of the problems (that lead to sensitivity of solutions to variations in boundary conditions and parameter values), combine to render an exhaustive search for optimal solutions practically impossible. They focused on the application of a GA to an electronics cooling problem in which they sought to simultaneously minimize the competing criteria of thermal failure rate and wiring length of eight electronic components that were convectively cooled and equally spaced along the bottom wall of a ventilated channel by searching for their optimal or nearly optimal arrangements. Information about this study and those subsequently discussed are tabulated in Table C.1. A finite-difference numerical procedure calculated the two-dimensional flow and temperature fields neglecting the solid side and determined the maximum surface temperatures of the heated components assuming steady-state conditions and constant properties. Unfortunately solution times restricted the GA's search ability, so the authors used its preliminary results as qualitative guidance for the design. As a conclusion, they observed that new applications of GA-based optimization of thermoscience problems will be "facilitated by the increasing availability of high performance computers, distributed computing environments, and

improved guidelines for the specification of the necessary GA parameters." However, they did not realize the potential impact of hierarchical physical modeling based on VAT to this field.

Gosselin, Tye-Gingras, and Mathieu-Potvin [136] provided a review in 2009 on the subject of utilizing GAs for solving heat transfer problems. Articles on this subject began to appear in the mid-1990s and the authors discussed a wide-range of studies covering thermal systems design, inverse heat transfer problems, and correlation development. GA settings (i.e. the number of objectives, type of encoding, crossover and mutation rates, population size, stopping criteria, and presence of elitism) and problem information (i.e. the objective function(s), modeling approach, and number of design variables) were reported for applicable studies. The authors noted that while GAs are robust, easy-to-use, unlikely to converge to local optima, able to explore a large portion of the design space, capable of searching over disjointed feasible domains, operable on irregular and non-differentiable functions, and easily parallelized, they can have slow convergence and imperfect repeatability. Observing that the evaluation of the fitness function is typically the most time-consuming step of the GA procedure for complex thermo-fluid systems and acknowledging that a lot of work is needed to overcome this, they pointed towards parallel computation, approximating the fitness function with methods such as artificial neural networks (ANN) and response surface methodology (RSM) (rather than perform systematic simulations to evaluate each individual's performance), and improving the GA settings (which have great influence on convergence speed and optimization success) as potential solutions. However, like

Queipo et al. [104], they did not realize the ability of hierarchical physical modeling provided by VAT for heat exchanger and heat sink design. They concluded that, as a "mature" optimization approach in the heat transfer field, an extensive description of the GA procedure is not warranted in new articles, and that more work should be done to evaluate and document the impact of different GA settings on the performance of the algorithm for heat transfer problems.

Manivannan, Devi, and Arumugam [105] optimized the geometry of a flat plate heat sink in terms of not only the thermal resistance but also the electromagnetic emitted radiation of the heat sink. Due to the proximity of the heat sink to the integrated circuits (ICs), radiofrequency (RF) fields can couple to the heat sinks and the heat sink fin can effectively behave as a monopole at high frequency, causing emitted radiation that can disturb nearby electronic devices and result in the device being out of compliance with regulations. A regression model yielded algebraic equations predicting the thermal resistance and electromagnetic emitted radiation in terms of the heat sink length, width, base thickness, fin height, fin pitch, and fin thickness. A single fitness function combined the two objectives and the optimization was carried out using the MATLAB GA.

Mohsin, Maqbool, and Khan [106] used a GA to optimize cylindrical pin fin heat sinks with a uniform heat flux at the base by minimizing the entropy generation rate associated with heat transfer and frictional effects. An expression for the dimensionless entropy generation rate was formulated using known correlations for Nusselt number and friction factor, and minimized by varying the pin height, diameter, and approach velocity, while imposing several constraints (such as fixing the heat sink volume) for different heat

sink configurations (i.e. inline or staggered), materials (i.e. enhanced plastic composites or aluminum), and pin fin densities. They made several observations on the behavior of the minimum entropy generation rate as the search variables and settings changed, pointing to several trends.

Ndao, Peles, and Jensen [107] undertook a multi-objective optimization and comparative study of several electronic cooling systems, considering, in particular, continuous parallel micro-channel heat sinks, inline and staggered pin-fin heat sinks, offset strip fin heat sinks, and single and multiple submerged impinging jets. For each system they simultaneously minimized the total thermal resistance and pumping power consumption under constant pressure drop and heat source base area, and subsequently compared the optimum designs of each system. Their physical model consisted of referenced, and their own developed, correlations for thermal resistance, heat transfer coefficient, and friction factor. The tradeoff between thermal resistance and pumping power consumption was noted, and they observed that the offset strip fin heat sink outperformed the other systems.

Optimization of fractal-like branching flow networks in disk-shaped heat sinks was considered by Heymann, Pence, and Narayanan [137]. Inspired by the efficient transport characteristics of biological systems (e.g. circulatory systems), and assuming an analogy exists between metabolic and thermal transport processes, they indicated that channel wall temperature and pressure drop can be reduced by using multi-scaled branching flow networks. For a series of heat fluxes, disk radii, and maximum wall temperatures, the length and width ratios between consecutive branch levels and the

terminal channel width that yielded minimal flow power or pressure drop were determined for specified numbers of branch levels and channels emanating from the inlet plenum. The inlet fluid temperature and channel depth were fixed and fabrication constraints were imposed on the channel width and spacing and the inlet plenum radius. A one-dimensional model [138] that was previously validated [139, 140] was used for predicting pressure and wall temperature distributions. The pressure distribution was found from the correlation and friction coefficient data provided by White [141], and the wall temperature distribution was obtained from Newton's law of cooling with heat transfer coefficients found in [142]. Moreover, it was assumed that both hydrodynamic and thermal boundary layers reinitiate following each channel bifurcation and that a constant heat flux was applied on one wall with uniform temperature on the remaining walls (i.e. highly conductive solid). Although they primarily used the gradient-based optimization method, a GA (in addition to a direct search) was employed for the heat sink optimization.

Wildi-Tremblay and Gosselin [109] considered a heat sink composed of a stack of porous layers through which a coolant flows. The thermal resistance (or hot spot temperature) was minimized by selecting the optimal porosity and material of each layer subject to global mass and cost constraints. The porous layers were assumed to each have uniform characteristics (i.e. porosity, effective thermal conductivity, and permeability), and to be composed of bundles of small pores of fixed diameter parallel to the flow. A pressure drop across the heat sink was specified, and Darcy's law was used to calculate the one-dimensional velocity in each layer. Assuming negligible thermal

diffusion in the flow direction and thermal equilibrium conditions, a single-temperature thermal energy model was employed to calculate the thermal resistance (with a specified heat flux at the base, adiabatic conditions at the top, and a uniform fluid inlet temperature) using a finite volume approach (without the need for iteration). The finite volume code was then coupled to MATLAB's GA tool to determine the optimal porosity and material of each of the ten layers composing the heat sink of a specified height and length. It was observed that a lower porosity near the hot plate and a higher porosity away from the plate is favorable, and several optimal configurations were found in the design space.

Kanyakam and Bureerat [122] considered the geometrical design of a square-pin-fin heat sink subjected to a uniform heat load applied to the bottom of the base plate and a uniform vertical flow impinging from above the fins. Using several MOEAs, including Population-Based Incremental Learning (PBIL), Strength Pareto Evolutionary Algorithm (SPEA), Particle Swarm Optimization (PSO), and Archived Multiobjective Simulated Annealing (AMOSA), they simultaneously minimized the heat sink junction temperature and the fan pumping power by varying the fin width and individual heights, inlet air velocity, base thickness, and number of fins in each array. A CFD code evaluated the heat sink using a finite volume analysis assuming steady state, laminar, forced convection of a constant property, Newtonian fluid. It was found that the PBIL yielded the best performance among the MOEAs considered and that allowing the individual pin-fin heights to be varied improves the heat sink's performance.

Jian-hui, Chun-xin, and Li-na [108] sought to design a plate-finned heat sink with

side and top bypass flow for minimum entropy generation rate by employing a multi-parameter constrained optimization procedure that integrates Design of Experiment (DOE), Genetic Algorithm (GA), Response Surface Model (RSM), and Mixed Integer Optimization (MOST). The heat sink is evaluated with a CFD code wherein the flow is three-dimensional, steady, turbulent ($k-\varepsilon$ model), and incompressible with constant properties and negligible radiation heat transfer effects. The blended or hybridized or combined optimization proceeds as follows. First, the DOE selects a number of design candidates for the CFD code to evaluate, identifying significant design variables and their interactions, and reducing the search space. Then, the GA, based on CFD evaluations, proceeds to facilitate the optimization and ensure a global optimization perspective. Next, the RSM is constructed from the results produced by the DOE and GA. Finally, the MOST proceeds to optimize the design based on the surrogate model produced by the RSM. Once the RSM model cannot be further improved a CFD simulation is performed. The RSM model is then updated with the new point and an optimization is performed again based on the updated RSM model. This is repeated until convergence. Additionally, from the results of the CFD simulations performed during the optimization, correlations for the Nusselt number and friction factor in terms of geometrical and operational parameters are established.

Rao and Patel [143] considered the geometrical optimization of a cross flow plate-fin heat exchanger using Particle Swarm Optimization (PSO), minimizing the entropy generation rate for a specific heat duty requirement and space restrictions (total volume and total annual cost were also minimized independently). The expression for entropy

generation rate was taken from Bejan [144] and was evaluated using the ε-NTU expression from Incropera and Dewitt [61] with heat transfer and friction factor relations adopted from Joshi and Webb [145]. Two application examples were considered, one taken from Mishra et al. [146] and the other from Xie et al. [147], both of which originally used a GA for the optimization. The PSO results were validated by the previous GA results and the authors found that the PSO technique outperforms the GA technique, converging noticeable quicker. Moreover, it was observed that by allowing the inertia weight to be variable in the PSO algorithm even faster convergence is realized.

Leblond and Gosselin [111] employed a two-temperature, non – Local Thermal Equilibrium (non – LTE) model to optimize a heat sink composed of a stack of porous media layers in what was a sequel to the work of Wildi-Tremblay and Gosselin [109] who approached a very similar problem assuming LTE. In [111] a hybridized GA, which implemented local search and database strategies, minimized the hot spot temperature with respect to the porosity, pore diameter, and material of each layer subject to global mass and cost constraints. The porous media-layered heat sink was subjected to a constant heat flux at the base, and each layer was composed of a pile of uniformly aligned pores of equal diameter. The unidirectional flow through the capillaries, imposed by a pressure drop across the heat sink, is laminar and governed by Darcy's law. It was assumed that thermal conductivity in the flow direction and viscous dissipation in the pores are negligible, the physical properties are constant, and the flow is thermally fully developed within each tube and subjected to a constant temperature boundary condition so that the Nusselt number can be set to about 4. It was found that the optimal designs do

not operate in LTE and that assuming LTE may result in an underestimation of the hot spot temperature and in different final designs as well. Moreover, it was observed that in the optimal designs porosity increases in layers found further away from the heat source, and that local search and the use of a database in the GA promoted faster convergence.

Tye-Gingras and Gosselin [110] considered a heat sink composed of porous media layers, a fin, and massless deflectors that served to direct the flow and reduce the size of the inlets and outlets, assuming Local Thermal Equilibrium (LTE) as described in [109]. A GA was used to minimize the heat sink thermal resistance (or maximum temperature), subject to mass constraints, with respect to geometric design variables, i.e. the porosity of each layer, the materials (4 types) composing each layer and the fin, and the fin, deflector, and heat sink geometry. The heat sink's porous layers are assumed to be composed of randomly distributed pores, it is subjected to a uniform heat flux at the base, and a vertical flow into the top of the heat sink exits through the sides, driven by a fixed pressure drop and guided by the adiabatic deflectors. They observed that as the mass constraint became stricter the GA selected a smaller fin and heat sink height, a larger deflector, and aluminum rather than copper for the material. Additionally, they found it was more beneficial to remove mass by enlarging the massless deflector than by changing the material, and surprisingly, that the optimal thermal resistance was actually rather insensitive to the mass constraint. Again, as in [109, 111], they found that the GA selected a higher porosity in layers further away from the hot plate.

Investigator	Year	Device	System Model	Conjugate Analysis	Optimization Method	Population /Generations	Search parameters	Independent Objectives
Queipo et al. [104]	1994	Electronic components convectively cooled in a channel	CFD, 2-D, steady, constant properties	No	MSGA	7/7	N/A	1
Hilbert et al. [93]	2006	Tube bank heat exchanger with tube shape varied	Commercial CFD, 2-D, steady, laminar	-	Multi-objective GA	30/20	4	2
Manivannan et al. [105]	2011	Flat plate-fin heat sink	Regression equations for thermal resistance and emitted radiation	-	MATLAB GA	30/200	6	1
Mohsin et al. [106]	2009	Cylindrical pin fin heat sink	Correlations for heat transfer and pressure drop in an expression for entropy generation rate	-	GA	21/2,000	3	1
Matos et al. [90]	2004	Staggered circular and elliptical finned tubes	FEM, 3-D, incompressible, steady state, laminar, constant properties, and experiments	-	Parametric	N/A	3	1
Foli et al. [92]	2006	Micro-heat exchanger, channel shapes defined by NURBS	Commercial CFD, 3-D, ideal gas	Yes	Multi-objective GA (NSGA-II)	100/500	10	2
Mousavi et al. [88]	2007	Finned/baffled channel	FVM, 2-D, laminar, steady, constant properties	No	GA	32/1000	2	1
Fabbri [91]	2000	Corrugated wall channel	FEM, 2-D, laminar, steady-state, fully developed, incompressible, uniform properties	Yes	GA	N/A	4	1
Xie et al. [82]	2008	Finned-tube heat exchanger	LMTD, experimental correlations	No	GA	50/1,000	7	1
Ozkol and Komurgoz [81]	2005	Air-cooled exchangers	ε-NTU	No	GA	250/400	3	1
Ndao et al. [107]	2009	Heat sinks and impinging jets	Correlations for thermal resistance, heat transfer coefficient, and friction factor	-	MATLAB MOGA	N/A	3-4	2
Heymann et al. [137]	2010	Fractal-like branching	(1-D, constant properties,	-	GA (gradient-	50/N/A	3	1

		disk-shaped heat sink	laminar, developing flow)?		based, and direct)			
Wildi-Tremblay and Gosselin [109]	2007	Layered porous media heat sink	FVM, laminar Darcy 1-D flow, 2-D single temperature heat transfer	No	MATLAB GA	30/N/A	N/A	1
Kanyakam and Bureerat [122]	2012	Pin-fin heat sink with vertical flow	CFD, steady, laminar, constant properties	Yes	4 different MOEAs	25/35	21	2
Jian-hui et al. [108]	2009	Plate-finned heat sink with bypass flows	CFD, 3-D, steady, turbulent ($k-\varepsilon$), incompressible, constant properties	Yes	Combined DOE-GA-RSM-MOST	9/10	3	1
Rao and Patel [143]	2010	Cross flow plate-finned heat exchanger	ε-NTU relation and experimental correlations	-	PSO	50/100	7/3	1
Leblond and Gosselin [111]	2008	Layered porous media heat sink	FVM, laminar Darcy 1-D flow, 2-D and two temperature heat transfer	Yes	Hybridized GA	20/N/A	9	1
Tye-Gingras and Gosselin [110]	2008	Layered porous media heat sink with a solid fin and flow deflectors	FVM, laminar Darcy 2-D flow, 2-D single temperature heat transfer	No	GA	30/N/A	14	1

Table C.1: Tabulation of the relevant characteristics of the population-based heat exchanger and heat sink optimization studies referenced in this dissertation.

D Experimental Closure Source Code

Main Body

```
%%%%%%%%%%%%%%%%%%%%%%%%%%%%%%%%%%%%%%%%%%%%%%%%%%%%%%%%%%%%%%%%%%%%%%%%%%
% From knowledge of physical properties, geometry, flow condition,
% experimental data, a speficied error criteria, and two initial guesses
% of the pore Nusselt number this code can estimate the actual pore Nusselt
% number.  Accompanying the estimate for the actual pore Nusselt number is
% its associated error, along with the corresponding heat transfer
```

```
% coefficient, pore Reynolds number, and solid phase heat generation rate.
% A plot showing the experimental data juxtaposed with the iterated
% simulations is given, along with a plot showing the experimental data
% together with the final simulation corresponding to the estimated actual
% pore Nusselt number.  Additionally, the fluid and solid phase temperature
% spatial distributions are optionally available.


% eps                       -- volumetric porosity [1]
% L                         -- length of heated test section [m]
% rho_f                     -- density of fluid [kg/m^3]
% rho_s                     -- density of solid [kg/m^3]
% mu_f                      -- dynamic viscosity of fluid [kg/m*s]
% C_p_f                     -- specific heat of fluid [J/kg*K]
% C_p_s                     -- specific heat of solid [J/kg*K]
% k_f                       -- thermal conductivity of fluid [W/m*K]
% k_eff                     -- effective thermal conductivity [W/m*K]
% D                         -- cross section diameter [m]
% d                         -- diameter of beads [m]
% A_c                       -- cross section area [m^2]
% V_dot                     -- volumetric flow rate [m^3/s]
% U_sup_vel                 -- superficial velocity [m/s]
% tau                       -- non-dimensional time constant [1]
% alpha_divided_by_Nu_p     -- governing equation parameter divided by the pore
Nusselt number [1]
% beta                      -- governing equation parameter [1]
% gamma_assumed             -- governing equation parameter assuming effective
thermal conductivity is known [1]
% time                      -- raw time data [s]
% inlet_temp                -- raw inlet temperature data [C]
% outlet_temp               -- raw outlet temperature data [C]
% theta_exp                 -- experimental non-dimensional gas temperature
response at integer values of the non-dimensional time [1]
% Nu_p                      -- pore Nusselt number [1]
```

```
% theta_sim                  -- simulated non-dimensional gas temperature response
at integer values of the non-dimensional time [1]

% error                      -- mean squared error between the two data sets [1]

% size_of_theta              -- the vector size of theta_exp and theta_sim

% E                          -- error criteria

% Final_Nu_p                 -- the correct pore Nusselt number [1]

% h                          -- heat transfer coefficient

% char_temp_diff             -- characteristic temperature difference, the
temperature increase, at steady-state, of the fluid [K]

% Q_per_unit_solid_volume    -- the volumetric heat generation rate in the solid
phase porous medium [J/s/m^3]

% Q                          -- the heat generation rate in the solid phase porous
medium [J/s]

% V_s                        -- volume of solid phase

% bb                         -- a logic variable that determines whether or not a
solution for the pore Nusselt number has been found.  If a solution has not been
found, this logic variable allows us to skip the step of calculating the heat
tranfer coefficient h.  Also, it allows us to skip the step of making a final plot
of the correct simulation with the experimental data.

% kk                         -- index used to accumulate attempted pore Nusselt
numbers and there corresponding errors

% xx                         -- a logic variable used to stop the pore Nusselt
number-determining iteration once either a satisfactory value has been found, or
the iteration has gone on for too long

% Re_p                       -- the pore Reynolds number [1]

% S                          -- the specific surface area [1/m]

% figure(1)                  -- plots theta_exp on the same graph as theta_sim for
every pore Nusselt number attempted

% figure(2)                  -- plots theta_exp on the same graph as theta_sim for
the finally determined pore Nusselt number

% figure(3)                  -- steady-state non-dimensional fluid temperature
spatial distribution

% figure(4)                  -- steady-state non-dimensional solid temperature
spatial distribution



clear

clc



% Physical Properties
```

```
%%%%%%%%%%%%%%%%%%%%%%%%%%%%%%%%%%%%%%%%%%%%%%%%%%%%%%%%%%%%%%%%%%%%%%%%%%%%%%%%%%%%
%%%%%%%%%%%%%%%%%%%%%%%%%%%%%%%

rho_f = 1.0877; % kg/m^3, at 45C, 1 atm

rho_s = 7830; % kg/m^3, at 300K,  Low Carbon Steel AISI 1010

mu_f = 19.38*10^-6; % kg/m*s, at 45C, 1 atm

C_p_f = 1006.8; % J/kg*K, at 45C, 1 atm

C_p_s = 450; % J/kg*K,  at 300K,  Low Carbon Steel AISI 1010

k_f = 0.0281; % W/m*K, at 45C, 1 atm

k_eff = 1; %%%%%%%%%%%%%%%%%%%%GUESSED VALUE

%%%%%%%%%%%%%%%%%%%%%%%%%%%%%%%%%%%%%%%%%%%%%%%%%%%%%%%%%%%%%%%%%%%%%%%%%%%%%%%%%%%%
%%%%%%%%%%%%%%%%%%%%%%%%%%%%%%%



% Flow Condition and Geometry

%%%%%%%%%%%%%%%%%%%%%%%%%%%%%%%%%%%%%%%%%%%%%%%%%%%%%%%%%%%%%%%%%%%%%%%%%%%%%%%%%%%%
%%%%%%%%%%%%%%%%%%%%%%%%%%%%%%%

V_dot = 0.005168; % m^3/s,        (10.95 cubic foot/minute = 0.005168 cubic
meter/second)

eps = 0.4;  % see Adnani pg 9

L = 0.04826; % m             (1.9 inch = 0.04826 meter)

d = 0.004763; % m,           (0.1875 inch = 0.0047625 meter)

D = 0.06604; % m,             (2.6 inch = 0.06604 meter)

A_c = (pi*D^2)/4; % m^2

U_sup_vel = V_dot/A_c; % m/s

V_s = A_c * L * (1 - eps); % m^3

%%%%%%%%%%%%%%%%%%%%%%%%%%%%%%%%%%%%%%%%%%%%%%%%%%%%%%%%%%%%%%%%%%%%%%%%%%%%%%%%%%%%
%%%%%%%%%%%%%%%%%%%%%%%%%%%%%%%



[alpha_divided_by_Nu_p, beta, gamma_assumed, tau, Re_p, S] =
Physical_Properties_and_Flow_Condition (eps, L, rho_f, rho_s, mu_f, C_p_f, C_p_s,
k_f, k_eff, U_sup_vel, d);



[time, inlet_temp, outlet_temp] = textread ('10.95_for_code.txt', '%f %f %f');



[theta_exp, size_of_theta, char_temp_diff] = Experimental_Data_Processing (time,
inlet_temp, outlet_temp, tau);
```

```
figure(1)

plot(theta_exp)

hold on


E = input('Enter your error criteria: ');


Nu_p(1) = input('Enter your first guess for the pore Nusselt number: ');


theta_sim = Equation_Solver(alpha_divided_by_Nu_p, beta, gamma_assumed, Nu_p(1),
size_of_theta);


error(1) = Mean_Squared_Error(theta_exp, theta_sim, size_of_theta)


plot(theta_sim)


if error(1) >= E


    Nu_p(2) = input('Enter your second guess for the pore Nusselt number: ');


    theta_sim = Equation_Solver(alpha_divided_by_Nu_p, beta, gamma_assumed,
Nu_p(2), size_of_theta);


    error(2) = Mean_Squared_Error(theta_exp, theta_sim, size_of_theta)


    plot(theta_sim)


end


bb = 1;


if error(1) < E


    Final_Nu_p = Nu_p(1);
```

```
    fprintf('The first guess for the pore Nusselt number is correct, Nu_p = %f \n',
Final_Nu_p)


elseif error(2) < E


    Final_Nu_p = Nu_p(2);


 fprintf('The second guess for the pore Nusselt number is correct, Nu_p = %f \n',
Final_Nu_p)


else


 kk = 2;

 xx = 1;


 while xx == 1;


         Nu_p(kk+1) = Nu_p(kk) - error(kk)*(Nu_p(kk-1) - Nu_p(kk))/(error(kk-1) -
error(kk))


         theta_sim = Equation_Solver(alpha_divided_by_Nu_p, beta, gamma_assumed,
Nu_p(kk+1), size_of_theta);


         error(kk+1) = Mean_Squared_Error (theta_exp, theta_sim, size_of_theta)


        plot(theta_sim)


         if error(kk+1) < E


                Final_Nu_p = Nu_p(kk+1);


            fprintf('The pore Nusselt number Nu_p is, %f \n', Final_Nu_p)
```

```
            xx = 0;

        elseif kk+1 == 20

            disp('Cannot converge to a solution for the pore Nusselt number')

            xx = 0;

           bb = 0;

        end

        kk = kk + 1;

 end

end

if bb == 1  % if bb == 1 a solution has been found, if bb == 0 a solution was not
obtained

    h = (S * k_f * Final_Nu_p)/(4 * eps);

    fprintf('The heat transfer coefficient is h = %f \n', h)

    figure(2)
    plot(theta_exp)
    hold on
    plot(theta_sim)

end
```

```
Q_per_unit_solid_volume = (char_temp_diff * U_sup_vel * rho_f * C_p_f)/(L * (1 -
eps));


Q = V_s * Q_per_unit_solid_volume;


fprintf('The pore Reynolds number is Re_p = %f \n', Re_p)


fprintf('The heat generation rate [Watts] in the solid phase porous medium is
determined from experimental data to be, %f \n', Q)


%%%%%%%%%%%%%%%%%%%%%%%% Steady-State Spatial Temperature Distribution
%%%%%%%%%%%%%%%%%%%%%%%%


if bb == 1  % a solution has been found, if bb == 0 a solution was not obtained


    hh = input('Would you like to see the steady-state spatial distribution of
solid and fluid temperature? (1 = yes, 0 = no) ');


    if hh == 1


        [solid_temp_distribution, fluid_temp_distribution,
non_dimensional_spatial_coordinate] =
Steady_State_Temperature_Distribution(alpha_divided_by_Nu_p, beta, gamma_assumed,
Final_Nu_p, size_of_theta);


        figure(3)


        plot(non_dimensional_spatial_coordinate, fluid_temp_distribution)


        figure(4)


        plot(non_dimensional_spatial_coordinate, solid_temp_distribution)


    end
```

```
end


%%%%%%%%%%%%%%%%%%%%%%%%%%%%%%%%%%%%%%%%%%%%%%%%%%%%%%%%%%%%%%%%%%%%%%%%%%%%%%%%%%%
%%%%%%%%%%%%%%%
```

Equation Solver

```
function [theta_sim] = Equation_Solver(alpha_divided_by_Nu_p, beta, gamma_assumed,
Nu_p, size_of_theta)



% Equation_Solver calculates theta_sim from knowledge of alpha, beta, and

% gamma_assmumed.  Alpha is determined from a user inputted Nu_p and

% alpha_divided_by_Nu_p.  The size of theta_sim is determined from

% size_of_theta.



% Define variables:

% theta_sim                  -- simulated non-dimensional gas temperature response
at integer values of the non-dimensional time [1]

% alpha_divided_by_Nu_p      -- governing equation parameter divided by the pore
Nusselt number [1]

% alpha                      -- governing equation parameter [1]

% beta                       -- governing equation parameter [1]

% gamma_assumed              -- governing equation parameter assuming effective
thermal conductivity is known [1]

% Nu_p                       -- pore Nusselt number [1]

% size_of_theta              -- the vector size of theta_exp and theta_sim

% delta_x                    -- non-dimensional spatial-coordinate step used in
numerical simulation

% delta_t                    -- non-dimensional temporal-coordinate step used in
numerical simulation

% G1                         -- convenientaly gathered group of constant terms in
the gas phase finite difference equation

% G2                         -- convenientaly gathered group of constant terms in
the gas phase finite difference equation

% G3                         -- convenientaly gathered group of constant terms in
the gas phase finite difference equation

% S1                         -- convenientaly gathered group of constant terms in
the solid phase finite difference equation
```

```
% S2                         -- convenientaly gathered group of constant terms in
the solid phase finite difference equation

% S3                         -- convenientaly gathered group of constant terms in
the solid phase finite difference equation

% S4                         -- convenientaly gathered group of constant terms in
the solid phase finite difference equation

% MATRIX                     -- solution matrix

% inverse_MATRIX             -- inverse of solution matrix

% solution                   -- gives the spatial non-dimensional temperature
distribution of both the gas and solid phase at

%                               a certain point in time.  solution(1:40) gives the
gas phase distribution at a certain point

%                               in time, where solution(1) is the gas phase non-
dimensional temperature at the first nodal point

%                               from the entrance nodal point, and solution(40) is
the gas phase non-dimensional temperature at

%                               the exit nodal point.  solution(41:81) gives the
solid phase distribution at a certain point in

%                               time, where solution(41) is the solid phase non-
dimensional temperature at the entrance nodal

%                               point and solution(81) is the solid phase non-
dimensional temperature at the exit nodal point.

% new_solution               -- essentially the same as "solution."  it's purpose
is to facilitate the time iteration.


alpha = Nu_p * alpha_divided_by_Nu_p;



delta_x = 1/40;  %% delta_x = 1/40 corresponds to L/40 meters



delta_t = 1;  %% delta_t = 1 corresponds to tau seconds



% gas phase finite difference equation constants

%%%%%%%%%%%%%%%%%%%%%%%%%%%%%%%%%%%%%%%%%%%%%%%%%%%%%%%%%%%%%%%%%%%%%%%%%%%%%%%%
%%%%%%%%%%%%%%%%%%%%%%%%%%%%%%

G1 = delta_t;



G2 = -(delta_x + delta_t + (delta_x * delta_t) * alpha);
```

```
G3 = delta_x * delta_t * alpha;

%%%%%%%%%%%%%%%%%%%%%%%%%%%%%%%%%%%%%%%%%%%%%%%%%%%%%%%%%%%%%%%%%%%%%%%%%%%%%%%%%%%
%%%%%%%%%%%%%%%%%%%%%%%%%%%%%%%




% solid phase finite difference equation constants

%%%%%%%%%%%%%%%%%%%%%%%%%%%%%%%%%%%%%%%%%%%%%%%%%%%%%%%%%%%%%%%%%%%%%%%%%%%%%%%%%%%
%%%%%%%%%%%%%%%%%%%%%%%%%%%%%%%

S1 = beta * gamma_assumed * delta_t / (delta_x)^2;


S2 = - (1 + alpha * beta * (delta_t) + 2 * beta * gamma_assumed *delta_t /
(delta_x)^2);


S3 = S1;


S4 = alpha * beta * delta_t;

%%%%%%%%%%%%%%%%%%%%%%%%%%%%%%%%%%%%%%%%%%%%%%%%%%%%%%%%%%%%%%%%%%%%%%%%%%%%%%%%%%%
%%%%%%%%%%%%%%%%%%%%%%%%%%%%%%%



MATRIX = [ ];


inverse_MATRIX = inv(MATRIX);


solution = zeros(81,1); %%% initial solution


theta_sim = zeros(size_of_theta,1);

theta_sim(1) = solution(40);


for ii = 1:(size_of_theta - 1)


    new_solution = inverse_MATRIX * [-delta_x * solution(1) ; -delta_x *
solution(2) ; -delta_x * solution(3) ; -delta_x * solution(4) ;...

                                     -delta_x * solution(5) ; -delta_x *
solution(6) ; -delta_x * solution(7) ; -delta_x * solution(8) ;...

                                     -delta_x * solution(9) ; -delta_x *
solution(10) ; -delta_x * solution(11) ; -delta_x * solution(12) ;...
```

```
                                    -delta_x * solution(13) ; -delta_x *
solution(14) ; -delta_x * solution(15) ; -delta_x * solution(16) ;...

                                    -delta_x * solution(17) ; -delta_x *
solution(18) ; -delta_x * solution(19) ; -delta_x * solution(20) ;...

                                    -delta_x * solution(21) ; -delta_x *
solution(22) ; -delta_x * solution(23) ; -delta_x * solution(24) ;...

                                    -delta_x * solution(25) ; -delta_x *
solution(26) ; -delta_x * solution(27) ; -delta_x * solution(28) ;...

                                    -delta_x * solution(29) ; -delta_x *
solution(30) ; -delta_x * solution(31) ; -delta_x * solution(32) ;...

                                    -delta_x * solution(33) ; -delta_x *
solution(34) ; -delta_x * solution(35) ; -delta_x * solution(36) ;...

                                    -delta_x * solution(37) ; -delta_x *
solution(38) ; -delta_x * solution(39) ; -delta_x * solution(40) ;...

                                    -solution(41) - beta*delta_t ; -solution(42) -
beta*delta_t ; -solution(43) - beta*delta_t ; -solution(44) - beta*delta_t ;...

                                    -solution(45) - beta*delta_t ; -solution(46) -
beta*delta_t ; -solution(47) - beta*delta_t ; -solution(48) - beta*delta_t ;...

                                    -solution(49) - beta*delta_t ; -solution(50) -
beta*delta_t ; -solution(51) - beta*delta_t ; -solution(52) - beta*delta_t ;...

                                    -solution(53) - beta*delta_t ; -solution(54) -
beta*delta_t ; -solution(55) - beta*delta_t ; -solution(56) - beta*delta_t ;...

                                    -solution(57) - beta*delta_t ; -solution(58) -
beta*delta_t ; -solution(59) - beta*delta_t ; -solution(60) - beta*delta_t ;...

                                    -solution(61) - beta*delta_t ; -solution(62) -
beta*delta_t ; -solution(63) - beta*delta_t ; -solution(64) - beta*delta_t ;...

                                    -solution(65) - beta*delta_t ; -solution(66) -
beta*delta_t ; -solution(67) - beta*delta_t ; -solution(68) - beta*delta_t ;...

                                    -solution(69) - beta*delta_t ; -solution(70) -
beta*delta_t ; -solution(71) - beta*delta_t ; -solution(72) - beta*delta_t ;...

                                    -solution(73) - beta*delta_t ; -solution(74) -
beta*delta_t ; -solution(75) - beta*delta_t ; -solution(76) - beta*delta_t ;...

                                    -solution(77) - beta*delta_t ; -solution(78) -
beta*delta_t ; -solution(79) - beta*delta_t ; -solution(80) - beta*delta_t ;...

                                    -solution(81) - beta*delta_t];


    solution = new_solution;


    theta_sim(ii+1) = solution(40);


end
```

```
end
```

Experimental Data Processing

```
function [theta_exp, size_of_theta, char_temp_diff] =
Experimental_Data_Processing(time, inlet_temp, outlet_temp, tau)


% Experimental_Data_Processing takes the raw experimental data (time,

% inlet-temp, and outlet_temp) and non-dimensionalizes the gas temperature

% response.  The appropriate size of the non-dimensional gas temperature

% response vector is then determined.  With this information and knowledge

% of tau, the previously determined non-dimensional gas temperature

% response is then converted into theta_exp, which gives the

% non-dimensional gas temperature response at integer values of the

% non-dimensional time.  The characteristic temperature difference is also

% obtained from the experimental data.


% Define variables:


% theta_exp                  -- experimental non-dimensional gas temperature
response at integer values of the non-dimensional time [1]

% size_of_theta              -- the vector size of theta_exp and theta_sim

% char_temp_diff             -- the characteristic temperature difference; defined
as the temperature increase, at steady state, of the fluid [C]

% time                       -- raw time data [s]

% inlet_temp                 -- raw inlet temperature data [C]

% outlet_temp                -- raw outlet temperature data [C]

% tau                        -- non-dimensional time constant [1]

% delta_t                    -- time interval between measurements [s]

% max_temp                   -- maximum outlet temperature [c]

% min_temp                   -- minimum outlet temperature [c]

% N                          -- size of the outlet_temp, inlet_temp, or time
vector; number of raw temperature data points or time data points [1]

% nd_temp                    -- full set of non-dimensional temperatures [1]
```

```
% theta_exp                  -- reduced set of non-dimensional temperatures [1]
% jj                         -- index
% kk                         -- index

%%%%%%% obtain initial information to perform non-dimensionalization

delta_t = time(2) - time(1);

max_temp = max(outlet_temp);

min_temp = min(outlet_temp);

NN = size(outlet_temp);
N= NN(1);    %%%%%%%%%%%%% gives the size of the vector

nd_temp = zeros(N,1);

%%%%%%% non-dimensionalize the full set of temperature data

for jj = 1:N

    nd_temp(jj) = (outlet_temp(jj) - min_temp) / (max_temp - min_temp);

end

% determine the size of theta_exp and theta_sim
%%%%%%%%%%%%%%%%%%%%%%%%%%%%%%%%%%%%%%%%%%%%%%%%%%%%%%%%%%%%%%%%%%%%%%%%%%%

mm = time(N)/tau;

mmm = floor(mm);
```

```
size_of_theta = mmm + 1;

%%%%%%%%%%%%%%%%%%%%%%%%%%%%%%%%%%%%%%%%%%%%%%%%%%%%%%%%%%%%%%%%%%%%%%%%

theta_exp = zeros(size_of_theta,1);

%%%%%%% reduce the full set of non-dimensional temperature data to a set of non-
dimensional
%%%%%%% temperatures at integer values of the non-dimensional time (0,1,2,3,...).

for kk = 1:size_of_theta

    F = (kk-1) * tau / delta_t;

    a = floor(F);

    b = F - a;

    theta_exp(kk) = nd_temp(a+1) + b*(nd_temp(a+2) - nd_temp(a+1));

end

char_temp_diff = outlet_temp(N) - outlet_temp(1);

end
```

Mean Squared Error

```
function [error] = Mean_Squared_Error(theta_exp, theta_sim, size_of_theta)

% Mean_Squared_Error calculates the the mean squared error between
% the experimental (theta_exp) and simulated (theta_sim) non-dimensional
% temperature responses.
```

```
% Define variables:


% theta_exp          -- experimental non-dimensional temperature response at
integer values of the non-dimensional time

% theta_sim          -- simulated non-dimensional temperature response at integer
values of the non-dimensional time

% error              -- mean squared error between the two data sets


error = 0;


for jj = 1:size_of_theta


    error = error + (theta_exp(jj) - theta_sim(jj))^2;


end
```

Physical Properties and Flow Condition

```
function [alpha_divided_by_Nu_p, beta, gamma_assumed, tau, Re_p, S] =
Physical_Properties_and_Flow_Condition (eps, L, rho_f, rho_s, mu_f, C_p_f, C_p_s,
k_f, k_eff, U_sup_vel, d)


% Physical_Properties_and_Flow_Condition obtains the governing equation

% parameters alpha_divided_by_Nu_p, beta, and gamma_assumed, the

% characteristic time scale tau, the pore Reynolds number Re_p, and the

% specific surface area S from the physical properties, geometry, and flow

% condition.


% Define variables:


% alpha_divided_by_Nu_p      -- governing equation parameter divided by the pore
Nusselt number [1]

% beta                       -- governing equation parameter [1]

% gamma_assumed              -- governing equation parameter assuming effective
thermal conductivity is known [1]
```

```
% tau                          -- non-dimensional time constant [1]

% Re_p                         -- the pore Reynolds number [1]

% S                            -- the specific surface area [1/m]

% eps                          -- volumetric porosity [1]

% L                            -- length of heated test section [m]

% rho_f                        -- density of fluid [kg/m^3]

% rho_s                        -- density of solid [kg/m^3]

% mu_f                         -- dynamic viscosity of fluid [kg/m*s]

% C_p_f                        -- specific heat of fluid [J/kg*K]

% C_p_s                        -- specific heat of solid [J/kg*K]

% k_f                          -- thermal conductivity of fluid [W/m*K]

% k_eff                        -- effective thermal conductivity [W/m*K]

% U_sup_vel                    -- superficial velocity [m/s]

% d                            -- diameter of beads [m]


% d_h                          -- hydraulic diameter [m]

% chi                          -- hydraulic diameter to length ratio [1]

% Pr                           -- Prandtl number [1]


S = 6*(1-eps)/d;  % see David's personal notes for this relation.  it was derived
from geometric considerations


d_h = 4*eps/S; % [1]/[1/m] = [m]


Re_p = (4 * rho_f * U_sup_vel)/(mu_f * S);  %[kg/m^3][m/s]/([kg/m*s][1/m] = [1]


Pr = (C_p_f * mu_f) / (k_f); % [J/kg*K][kg/m*s]/[J/s*m*K] = [1]


tau = eps * L / U_sup_vel; % [m]/[m/s] = [s]


chi = d_h / L; % [m]/[m] = [1]
```

```
alpha_divided_by_Nu_p = 4 / (chi * Re_p * Pr); %[1]


beta = (eps * rho_f * C_p_f) / ((1-eps) * rho_s * C_p_s); % [1]


gamma_assumed = (k_eff * chi) / (k_f * eps * Re_p * Pr); % [1]


end
```

Steady State Temperature Distribution

```
function [solid_temp_distribution, fluid_temp_distribution,
non_dimensional_spatial_coordinate] =
Steady_State_Temperature_Distribution(alpha_divided_by_Nu_p, beta, gamma_assumed,
Final_Nu_p, size_of_theta)


% Steady_State_Temperature_Distribution calculates the steady state

% non-dimensional solid and fluid temperature spatial distributions from

% knowledge of alpha, beta, and gamma_assmumed.  Alpha is determined from

% the actual estimated pore Nusselt number and alpha_divided_by_Nu_p.  The

% non-dimensional spatial coordinate nodal locations are also obtained.


% alpha_divided_by_Nu_p                -- governing equation parameter divided by
the pore Nusselt number [1]

% beta                                 -- governing equation parameter [1]

% gamma_assumed                        -- governing equation parameter assuming
effective thermal conductivity is known [1]

% Final_Nu_p                           -- actual estimated pore Nusselt number
used in this simulation

% size_of_theta                        -- the vector size of theta_exp and
theta_sim

% solid_temp_distribution              -- solid phase steady-state temperature
spatial distribution

% fluid_temp_distribution              -- fluid phase steady-state temperature
spatial distribution

% non_dimensional_spatial_coordinate   -- non-dimensional spatial coordinate nodal
locations [1]

% alpha                                -- governing equation parameter [1]

% delta_x                              -- non-dimensional spatial-coordinate step
used in numerical simulation
```

```
% delta_t                                -- non-dimensional temporal-coordinate step
used in numerical simulation

% G1                                     -- convenientaly gathered group of constant
terms in the gas phase finite difference equation

% G2                                     -- convenientaly gathered group of constant
terms in the gas phase finite difference equation

% G3                                     -- convenientaly gathered group of constant
terms in the gas phase finite difference equation

% S1                                     -- convenientaly gathered group of constant
terms in the solid phase finite difference equation

% S2                                     -- convenientaly gathered group of constant
terms in the solid phase finite difference equation

% S3                                     -- convenientaly gathered group of constant
terms in the solid phase finite difference equation

% S4                                     -- convenientaly gathered group of constant
terms in the solid phase finite difference equation

% MATRIX                                 -- solution matrix

% inverse_MATRIX                         -- inverse of solution matrix

% solution                               -- gives the spatial non-dimensional
temperature distribution of both the gas and solid phase at

%                                        a certain point in time.  solution(1:40)
gives the gas phase distribution at a certain point

%                                        in time, where solution(1) is the gas phase
non-dimensional temperature at the first nodal point

%                                        from the entrance nodal point, and
solution(40) is the gas phase non-dimensional temperature at

%                                        the exit nodal point.  solution(41:81)
gives the solid phase distribution at a certain point in

%                                        time, where solution(41) is the solid phase
non-dimensional temperature at the entrance nodal

%                                        point and solution(81) is the solid phase
non-dimensional temperature at the exit nodal point.

% new_solution                           -- essentially the same as "solution."
it's purpose is to facilitate the time iteration.

% fluid_temp_distribution                -- steady state non-dimensional fluid
temperature distribution

% solid_temp_distribution                -- steady state non-dimensional solid
temperature distribution



non_dimensional_spatial_coordinate = transpose(0:0.0250:1);  %% spatial coordinate
nodal locations separated a distance L/40 meters apart
```

```
alpha = Final_Nu_p * alpha_divided_by_Nu_p;


delta_x = 1/40;


delta_t = 1;


G1 = delta_t;


G2 = -(delta_x + delta_t + (delta_x * delta_t) * alpha);


G3 = delta_x * delta_t * alpha;


S1 = beta * gamma_assumed * delta_t / (delta_x)^2;


S2 = - (1 + alpha * beta * (delta_t) + 2 * beta * gamma_assumed *delta_t /
(delta_x)^2);


S3 = S1;


S4 = alpha * beta * delta_t;


MATRIX = [ ];


inverse_MATRIX = inv(MATRIX);


solution = zeros(81,1); %%% initial solution


for ii = 1:(size_of_theta - 1)


    new_solution = inverse_MATRIX * [-delta_x * solution(1) ; -delta_x *
solution(2) ; -delta_x * solution(3) ; -delta_x * solution(4) ;...

                                     -delta_x * solution(5) ; -delta_x *
solution(6) ; -delta_x * solution(7) ; -delta_x * solution(8) ;...
```

```
                                    -delta_x * solution(9) ; -delta_x *
solution(10) ; -delta_x * solution(11) ; -delta_x * solution(12) ;...

                                    -delta_x * solution(13) ; -delta_x *
solution(14) ; -delta_x * solution(15) ; -delta_x * solution(16) ;...

                                    -delta_x * solution(17) ; -delta_x *
solution(18) ; -delta_x * solution(19) ; -delta_x * solution(20) ;...

                                    -delta_x * solution(21) ; -delta_x *
solution(22) ; -delta_x * solution(23) ; -delta_x * solution(24) ;...

                                    -delta_x * solution(25) ; -delta_x *
solution(26) ; -delta_x * solution(27) ; -delta_x * solution(28) ;...

                                    -delta_x * solution(29) ; -delta_x *
solution(30) ; -delta_x * solution(31) ; -delta_x * solution(32) ;...

                                    -delta_x * solution(33) ; -delta_x *
solution(34) ; -delta_x * solution(35) ; -delta_x * solution(36) ;...

                                    -delta_x * solution(37) ; -delta_x *
solution(38) ; -delta_x * solution(39) ; -delta_x * solution(40) ;...

                                    -solution(41) - beta*delta_t ; -solution(42) -
beta*delta_t ; -solution(43) - beta*delta_t ; -solution(44) - beta*delta_t ;...

                                    -solution(45) - beta*delta_t ; -solution(46) -
beta*delta_t ; -solution(47) - beta*delta_t ; -solution(48) - beta*delta_t ;...

                                    -solution(49) - beta*delta_t ; -solution(50) -
beta*delta_t ; -solution(51) - beta*delta_t ; -solution(52) - beta*delta_t ;...

                                    -solution(53) - beta*delta_t ; -solution(54) -
beta*delta_t ; -solution(55) - beta*delta_t ; -solution(56) - beta*delta_t ;...

                                    -solution(57) - beta*delta_t ; -solution(58) -
beta*delta_t ; -solution(59) - beta*delta_t ; -solution(60) - beta*delta_t ;...

                                    -solution(61) - beta*delta_t ; -solution(62) -
beta*delta_t ; -solution(63) - beta*delta_t ; -solution(64) - beta*delta_t ;...

                                    -solution(65) - beta*delta_t ; -solution(66) -
beta*delta_t ; -solution(67) - beta*delta_t ; -solution(68) - beta*delta_t ;...

                                    -solution(69) - beta*delta_t ; -solution(70) -
beta*delta_t ; -solution(71) - beta*delta_t ; -solution(72) - beta*delta_t ;...

                                    -solution(73) - beta*delta_t ; -solution(74) -
beta*delta_t ; -solution(75) - beta*delta_t ; -solution(76) - beta*delta_t ;...

                                    -solution(77) - beta*delta_t ; -solution(78) -
beta*delta_t ; -solution(79) - beta*delta_t ; -solution(80) - beta*delta_t ;...

                                    -solution(81) - beta*delta_t];


    solution = new_solution;


end
```

```
fluid_temp_distribution = [0 ; solution(1:40)];


solid_temp_distribution = solution(41:81);


end
```

E Finned-Tube Heat Exchanger Subroutine

```
SUBROUTINE FTHX(TEST,KSOLID,KFLUID,XMDOT,TF2IN,TF1IN,XINPUT,XOUTPUT,KP)

! GEOMETRY

! using method of designating a cross fin coil from "HeatCraft, Worldwide
Refrigeration

! Type K copper tube diameter                                    6061-T6 Aluminum

!   1/4"  = 9.525 mm,  wall thickness = 0.035 = 0.889  mm    1/4"  = 6.35 mm,  wall
thickness = 0.035" = 0.889  mm

!   5/16" = 7.94 mm,   wall thickness = 0.049 = 1.2446 mm    5/16" = 7.94 mm,  wall
thickness = 0.058  = 1.4732  mm

!   3/8"  = 12.7   mm, wall thickness = 0.049 = 1.2446 mm    3/8"  = 9.525mm,  wall
thickness = 0.058  = 1.4732 mm

!   1/2"  = 15.875 mm  wall thickness = 0.049 = 1.2446 mm    1/2"  = 12.7 mm,  wall
thickness = 0.065  = 1.651  mm

!   5/8"  = 19.05 mm   wall thickness = 0.049 = 1.2446 mm    5/8"  = 15.875 mm wall
thickness = 0.065  = 1.651 mm

!   3/4"  = 22.22 mm   wall thickness = 0.065 = 1.651  mm    3/4"  = 19.05 mm  wall
thickness = 0.065  = 1.651 mm

!   1"    = 28.575 mm  wall thickness = 0.065 = 1.651  mm     1"   = 25.4 mm   wall
thickness = 0.065  = 1.651 mm

!   1-1/2"= 41.275 mm  wall thickness = 0.072 = 1.8288 mm   1-1/2" = 38.1 mm   wall
thickness = 0.065  = 1.651 mm

!   Tubes can be 1) Smooth bore, 2) Rifle Bore or 3) Cross-Hatch: at this time only
smooth bore tubes

!

!Fin length LZ is in the tube flow direction, the Z dimension

!Fin widthe LY is the Y direction dimension

!Fin height LX is the X direction lentgth
```

```
!Mounting position; Vertical; Air flow into YZ face

!               or Horizontal; Airflow into  XZ face

!

! Number of tubes in X direction from (PX+1)*NTX =LX

! Number of rows  in Y direction from (PY+1)*NTY =LY

!

! Fin pitch     12.5 mm = 2F/inch

!                8.33mm = 3F/inch

!                6.25mm = 4F/inch

! Number of fins from  FP*(NFZ+1) = LZ

!Need to allow for fin augmentation: 1) smooth, 2) louvered, 3) lanced, 4) Scales
or 5)!Overall length

! PD      PT      PXOPD   PYOPD  NTX      NTY     FT      FPOFT  LZ      RATIO

! THIS PROGRAM WILL PRODUCE RESULTS FOR WHAT IS CALLED A VERTICAL FTHX BECAUSE ITS
A TWO DIMENSIONAL PROBLEM AND CAN BE

! ADDRESSED WITH THE PRESENT CODE. cOLUMNS OF TUBES IN THE AIR FLOW DIRECTION FORM
ROWS. eACH ROW IS A SINGLE TUBE

! WOUND UP AND DOWN FROM ONE END TO THE OTHER. SUCH DEVICES ARE MANUFACTURED WITH
AS MANY AS 40 PASSES IN A ROW AND 10

! OR SO ROWS. tHE ANALYSIS ONLY NEED TO TREAT ONE ROW AS SYMMETRY WILL ALLOW hx
CAPABILITY TO BE INCREASED BY INCREASING

! THE NUMBER OF TUBE ROWS. fOR A GIVE MASS FLOW, THERE IS SOME OPTIMIZATION HERE AS
INCREASING THE NUMBER OF ROWS REDUCES

! THE FLOW IN A TUBE ( A SET OF COLUMNS)AND COULD LEAD TO REDUCED PUMPING POWER.

!

! AT SOME POINT WE WILL HAVE TO CONSIDER THE OTHER ORIENTATION. IT IS THREE
DIMENSIONAL AND IS IN CROSS FLOW. WILL BE MORE

! COMPLICATED LEADING TO HAVE TUSE SOMETHING OTHER THAN GUASS SEIDEL.



! THESE ARE THE PARAMETERS NEEDED TO DESCRIBE THE A VERTICAL FTHX.

! FLOW PARAMTERS THAT CAN BE VARIED WILL BE ASSOCIATED WIT THE FLUID ACCOMPLISHING
A GIVEN TASK; IN THIS CASE THE AIR FLOW

! AND ITS TEMPRATURE. iT IS NOT CLEAR WHAT SHOULD BE OPPTIMIZED BUT WE WILL CHOOSE
TO GET THE MOST HEAT TRANSFER FOR THE

! LEAST PUMPING POWER. VOLUME AND WEIGHT COULD ALSO BE A CONSIDERATION.

!  Read in variables, ALL LENGTHS IN MM
```

```
! XINPUT( 1) = PD     XOUTPUT( 1) = XINPUT( 1)    TUBE DAIMETER [mm]

! XINPUT( 2) = PT     XOUTPUT( 2) = XINPUT( 2)    TUBE WALL THICKNESS [mm]

! XINPUT( 3) = PXOD   XOUTPUT( 3) = XINPUT( 3)    PITCH IN FLOW DIRECTION DIVIDED
BY TUBE DIAMETER

! XINPUT( 4) = PYOD   XOUTPUT( 4) = XINPUT( 4)    PITCH IN CROSS FLOW DIRECTION
DIVIDED BY TUBE DIAMETER

! XINPUT( 5) = NTX    XOUTPUT( 6) = XINPUT( 6)    COLUMNS OF TUBES. NX IS THE
NUMBER OF NODES AND MUST BE A MULTIPLE OF NTX, CHOSE NX = NTX*20

! XINPUT( 7) = FT     XOUTPUT( 7) = XINPUT( 7)    FT IS THE FIN THICKNESS

! XINPUT( 8) = FPOFT  XOUTPUT( 8) = XINPUT( 8)    FPOFT IS THE FIN PITCH OVER THE
FIN THICKNESS

! XINPUT( 9) = LZ     XOUTPUT( 9) = XINPUT( 9)    THE HEAT EXCHANGER HEIGHT

! XINPUT(10) = RATIO  XOUTPUT(10) = XINPUT(10)    RATIO OF FIN SIDE MASS FLOW TO
TUBE SIDE MASS FLOW

! XINPUT(11) = MDOTH  XOUTPUT(11) = XINPUT(11)    HOT SIDE MASS FLOW [Kg/S]

! XINPUT(12) = TF1IN  XOUTPUT(12) = XINPUT(12)    TF1IN IS FIN SIDE INLET
TEMPRATURE [C]

! XINPUT(13) = TF2IN  XOUTPUT(13) = XINPUT(13)    TF2IN IS HOT SIDE INLET
TEMPERATURE

!                     XOUTPUT(14) = PP1           FIN SIDE PUMPING POWER

!                     XOUTPUT(15) = PP2           TUBE SIDE PUMPING POWER

!                     XOUTPUT(16) = QX2           FIN SIDE TOTAL HEAT TRANSFER

!                     XOUTPUT(17) = QZ2           TUBE SIDE TOTAL HEAT TRANSFER

!                     XOUTPUT(18) = QMAX          QMAX = XMDOTH*WCPF*(TF2IN -
TF1IN)

!                     XOUTPUT(19) = HTEFF         HTEFF  = QX2/QMAX

!                     XOUTPUT(20) = EFFECTIVENESS EFFECTIVENESS = QX2/PPT, PPT IS
TOTAL PUMPING POWER

!                     XOUTPUT(21) = EFFECTIVENESS/(T2FIN-TF1IN)

!                     XOUTPUT(22) = VOLUME

!                     XOUTPUT(23) = WEIGHT


        IMPLICIT REAL*8 (A-H,O-Z)

        PARAMETER (NZ=100)  ! NOTE THAT NX MUST BE A MULTIPLE OF THE NUMBER OF
TUBES IN THE COLUMN

        REAL*8 KS, LX, LZ, IPD, LY, NUT1,NUT2
```

```
        DIMENSION
U1(1000,NZ),U2(1000,NZ),T1(1000,NZ),T2(1000,NZ),TS(1000,NZ),XOUTPUT(30),XINPUT(13),
&


F(NZ),CD(1000,NZ),H1(1000,NZ),H2(1000,NZ),X(1000),Z(NZ),HH1(1000,NZ),HH2(1000,NZ),C
T1(1000,NZ),&


CT2(1000,NZ),AJTS(1000,NZ),BJTS(1000,NZ),CJTS(1000,NZ),AITS(1000,NZ),BITS(1000,NZ),
CITS(1000,NZ),&


 FJTS(1000,NZ),FITS(1000,NZ),CJTSS(1000,NZ),FJTSS(1000,NZ),CONV1(1000,NZ),CONV2(100
0,NZ),SW1(1000,NZ),&


 SW2(1000,NZ),DH1(1000,NZ),DH2(1000,NZ),COEF(1000,NZ),CT2S(1000,NZ),CT1S(1000,NZ),X
M1(1000,NZ),XM2(1000,NZ),HX(1000),&

         HZ(NZ),
REP1(1000,NZ),REP2(1000,NZ),CD1(1000,NZ),CD2(1000,NZ),Y1(1000,NZ),Y2(1000,NZ),Y3(10
00,NZ),&


FJT1(1000,NZ),FJT2(1000,NZ),FIT1(1000,NZ),FIT2(1000,NZ),FITSS(1000,NZ),CITSS(1000,N
Z)

        CHARACTER TEST

        PI = 3.14159265358979323846264338327950288419716939937510


!-----------------------------------------------------------------------

!------------------ MATERIAL PROPERTIES ----------------------------------

!-----------------------------------------------------------------------

            ANU=20.92E-06           ! Air at 300K kiN ematic viscosity,[m**2/s]

            ACPF=1009               ! Air at 300K specific heat [J/Kg.K]

            AROF=.9950              ! Air at 300K deN sity [Kg/m**3]

            AKF=30.0E-03            ! Air at 300K thermal conductivity [W/mK]

            AAF=AKF/(ACPF*AROF)     ! THERMAL DIFFUSIVITY OF AIR

            IF(KFLUID.EQ.1) GOTO 10

            IF(KFLUID.EQ.2) GOTO 20

    !   Fluid--Water

       10   WNU=1.10E-6             !Water kinematic viscosity,[m**2/s]

            WCPF=4186               !Water specific heat @290K [J/Kg.K]

            WROF=999                !Water deN sity @290K [Kg/m**3]

            WKF=0.57                !Water thermal coN ductivity [W/mK]
```

```
      WAF=WKF/(WCPF*WROF)     ! THERMAL DIFFUSIVITY of water
      GOTO 40
   20 CONTINUE
  !   Freon at 300k
   30 CONTINUE
      WNU=0.195E-06
      WCPF=9781
      WROF=1305.8
      WKF=72
      WAF=WKF/(WCPF*WROF)
      GOTO 40
   40 CONTINUE
      IF(KSOLID.EQ.1) GOTO 110
      IF(KSOLID.EQ.2) GOTO 120
      IF(KSOLID.EQ.3) GOTO 130
      IF(KSOLID.EQ.4) GOTO 135
      IF(KSOLID.EQ.5) GOTO 138
      GOTO 140
!   Solid--Steel
  110 CONTINUE
      CPS=480.0           !Solid specific heat, steel [J/kg/K]
      ROS=8055.0          !Solid density, steel [kg/m**3]
      KS=15.0             !Solid thermal conductivity [W/mK], steel
      GOTO 140
  120 CONTINUE
! SOLID--COPPER
      CPS=385
      ROS=8933
      KS=401
      GOTO 140
  130 CONTINUE
! SOLID ALUMINUM
```

```
            CPS=903
            ROS=2702
            KS=237
            GOTO 140
    ! VERY HIGH CONDUCTIVITY SOLID
      135   CONTINUE
            CPS=50
            ROS=19300
            KS=100000
            GO TO 140
     ! SILICON
       138  CONTINUE
            CPS=712.0         !Solid specific heat, Silicon [J/kg/K]
            ROS=2330.0        !Solid density, Silicon [kg/m**3]
            KS=148.0          !Solid thermal conductivity [W/mK], Silicon
      140   CONTINUE
            AS=KS/ROS/CPS

!-------------------------------------------------------------------------
!-------------------------------------------------------------------------
!-------------------------------------------------------------------------

!-------------------------------------------------------------------------
!--------------------OPEN OUTPUT FILES------------------------------------
!-------------------------------------------------------------------------

            OPEN (32, FILE = 'OUTPUT.TXT')
            OPEN (71, FILE = 'PARAMETERS.TXT')
            OPEN (81, FILE = 'RESPONSE.TXT')

!            OPEN (1801, FILE = 'TF1.DAT')
!            OPEN (1802, FILE = 'TF2.DAT')
```

```
!             OPEN (1803, FILE = 'TS.DAT')
!             OPEN (1804, FILE = 'U1.DAT')
!             OPEN (1805, FILE = 'U2.DAT')

!-----------------------------------------------------------------------
!-----------------------------------------------------------------------
!-----------------------------------------------------------------------

!-----------------------------------------------------------------------
!----------------------PROGRAM INPUTS-----------------------------------
!-----------------------------------------------------------------------

            NCASE = 1
            NTEST = 0

            IF (TEST.EQ.'Y'.OR.TEST.EQ.'y') NTEST=1
            CONTINUE

            IF(NTEST.EQ.1) THEN
 !************************TEST CASE INPUT VALUES ***************************
                PD    =    12.70             !OUTER TUBE DIAMETER [mm]
                XOUTPUT(1)  = PD
                PT    = 1.65                 !TUBE WALL THICKNESS [mm]
                XOUTPUT(2)  = PT
                IPD   = PD - 2*PT            !inside pin  diameter [mm]
                PXOPD = 2.50                 !THIS IS THE PITCH/DIAMETER OF THE
SERPENTINE THAT MAKES UP THE COLUMNS [-]
                XOUTPUT(3) = PXOPD
                PYOPD = 2.16                 !THIS IS THE SPACING/DIAMETER OF THE
ROWS OF SINGLE TUBES [-]
                XOUTPUT(4) = PYOPD
                PX    = PXOPD*PD             !tube  pitch in  X direction [mm]
                PY    = PYOPD*PD             !tube  pitch in  Y direction [mm]
```

```
                NTX   = 50                  ! Columns of tubes [-]
                XOUTPUT(5) = NTX
                NX = 20*NTX
                LX    = PX*NTX              ! Length of air flow passage [mm]
                NTY   = 8                   ! Rows of tubes [-]
                XOUTPUT(6) = NTY
                LY    = PY*NTY              ! Width [mm]


                FT    = 2.00                !fin
thickness;1.0/1.2/1.6/2.0/2.5/3.0 [mm]
                XOUTPUT(7) = FT
                FPOFT = 4.00                !FIN PITCH TO THICKNESS RATIO [-]
                XOUTPUT(8) = FPOFT
                FP    = FPOFT*FT            !fin  pitch [mm]
                FPI   = (1.0/FP)*25.4       !fins per INCH
                LZ    = 1000.00             !HEIGHT OF UNIT [mm]
                XOUTPUT(9) = LZ
                XMDOTH = 1.00               !HOT SIDE MASS FLOW [KG/S]
                RATIO = 1.00                !XMDOTH*CPH/XMDOTC*CPC [-]
                XOUTPUT(10) = RATIO
                XOUTPUT(11) = XMDOTH
                TF1IN = 30.00               !COLD INLET TEMPERATURE [C]
                TF2IN = 60.00               !HOT SIDE INLET [C]
                XOUTPUT(12) = TF1IN
                XOUTPUT(13) = TF2IN
                CONTINUE
 !***********************END TEST CASE INPUT VALUES ************************
                GO TO 25


            ELSE
 !*********************USER-SELECTED INPUT VALUES (MM)***********************
                XOUTPUT( 1) = XINPUT( 1)         !PD
```

```
      PD      = XINPUT( 1)
XOUTPUT( 2) = XINPUT( 2)         !PT
      PT      = XINPUT( 2)
      IPD     = PD - 2*PT
XOUTPUT( 3) = XINPUT( 3)         !PXOPD
      PXOPD   = XINPUT( 3)
XOUTPUT( 4) = XINPUT( 4)         !PYOPD
      PYOPD   = XINPUT( 4)
      PX      = PXOPD*PD
      PY      = PYOPD*PD
XOUTPUT( 5) = XINPUT( 5)         !NTX
      NTX     = XINPUT( 5)
      NX      = 20*NTX
XOUTPUT( 6) = XINPUT( 6)         !NTY
      NTY     = XINPUT( 6)
      LX      = PX*NTX
      LY      = PY*NTY
XOUTPUT( 7) = XINPUT( 7)         !FT
      FT      = XINPUT( 7)
XOUTPUT( 8) = XINPUT( 8)         !FPOFT
      FP      = FPOFT*FT
XOUTPUT( 9) = XINPUT( 9)         !LZ
      LZ      = XINPUT( 9)
XOUTPUT(10) = XINPUT( 10)        !RATIO
      RATIO   = XINPUT( 10)
XOUTPUT(11) = XINPUT( 11)        !XMDOTH
      XMDOTH  = XINPUT( 11)
XOUTPUT(12) = XINPUT(12)
      TF1IN   = XINPUT(12)
XOUTPUT(13) = XINPUT(13)
      TF2IN   = XINPUT(13)
!**********************END USER-SELECTED INPUT VALUES (MM)*******************
```

```
            END IF

25      CONTINUE


!******************WRITE OUT TO FILE = 71, "PARAMETERS.TXT"******************

    IF(NCASE.EQ.1)WRITE(71,*)'NCASE    PD       PT       PXOPD    PYOPD  NTX       NTY
FT       FPOFT  LZ       RATIO    XMDOTH TF1IN    TF2IN'

    WRITE(71,72)NCASE,(XOUTPUT(KK),KK=1,13)

72          FORMAT(1X,I4,13F8.2)

!*****************END WRITE OUT TO FILE = 71, "PARAMETERS.TXT"***************


!******************* CONVERT GEOMETRY INPUTS FROM MM TO M *******************

    SC     =  0.001

    PD     =  XOUTPUT(1)*SC          !TUBE DIAMETER [m]

    PT     =  XOUTPUT(2) *SC         !TUBE WALL THICKNESS [m]

    IPD    =  PD - 2*PT              !inside pin  diameter [m]

    PXOPD  =  XOUTPUT(3)             !THIS IS THE PITCH/DIAMETER OF THE SERPENTINE
THAT MAKES UP THE COLUMNS [-]

    PYOPD  =  XOUTPUT(4)             !THIS IS THE SPACING/DIAMETER OF THE ROWS OF
SINGLE TUBES [-]

    PX     =  PXOPD*PD               !tube  pitch in  X direction[m]

    PY     =  PYOPD*PD               !tube  pitch in  Y direction[m]

    NTX    =  XOUTPUT(5)             !Columns of tubes [-]

    LX     =  PX*NTX                 !Length of air flow passage [m]

    NTY    =  XOUTPUT(6)             !Rows of tubes [-]

    LY     =  PY*NTY                 !Width [m]

    FT     =  XOUTPUT(7)*SC          !fin  thickness [m]

    FPOFT  =  XOUTPUT(8)             !FIN PITCH TO THICKNESS RATIO [-]

    FP     =  FPOFT*FT               !fin  pitch [m]

    FPI    = (1.0/FP)*(25.4*SC)      !fins per INCH

    LZ     =  XOUTPUT(9)*SC          !HEIGHT OF UNIT [m]

    RATIO  =  XOUTPUT(10)            !RATIO OF XMDOTH*CPH/XMDOTC*CPC

    XMDOTH=  XOUTPUT(11)             ![KG/S]

    CONTINUE

!****************************** END ************************************
```

```
!------------------------------------------------------------------------

!------------------------------------------------------------------------

!------------------------------------------------------------------------




!------------------------------------------------------------------------

!------------------- POROSITY AND WETTED SURFACE AREA ---------------------

!------------------------------------------------------------------------


!WILL EVENTUALLY BE A FUNCTION  OF X,Z.

!Current correlations from Zhou, F., et al. (2011). "Obtaining Closure for Fin-and-
Tube

!Heat Exchanger Modeling Based on Volume Averaging Theory (VAT)." Journal of Heat
Transfer 133(11): 111802.

       DO I = 1,NX

           DO J = 1,NZ

                XM1(I,J)  = 1-FT/FP-(PI*PD*PD*(FP-FT)/(4.0*PX*PY*FP))
! Porosity fluid 1 [-]

                XM2(I,J)  = PI*IPD*IPD/(4.0*PX*PY)
! Porosity fluid 2 [-]

                SW1(I,J)  = (2*PX*PY-2*PI*(PD/2)**2+PI*PD*(FP-FT))/(PX*PY*FP)
! Surface wetted fluid 1 [1/m]

                SW2(I,J)  = PI*IPD/(PX*PY)
! Surface wetted fluid 2 [1/m]

                DH1(I,J)   = 4.0*XM1(I,J)/SW1(I,J)
! Hydraulic diameter of airside [m]

                DH2(I,J)   = 4.0*XM2(I,J)/SW2(I,J)
! Hydraulic diameter of WATER side [m]

                COEF(I,J) = 1.0 - XM1(I,J) - XM2(I,J)

           END DO

       END DO

       CONTINUE



!------------------------------------------------------------------------

!------------------------------------------------------------------------
```

```
!------------------------------------------------------------------------

!------------------------------------------------------------------------
!------------------------------GRIDDING----------------------------------
!------------------------------------------------------------------------

!WANT TO BE ABLE TO USE VARIABLE GRIDDING AND WILL PUT THIS IN TO A SUBROUTINE.
            X(1) = 0.0
        DO I=2,NX
            X(I)=(LX/(NX-1))*(I-1)  ! spacing in the x direction [m]
            HX(I-1) = X(I)-X(I-1)   ! [m]
        END DO
            HX(NX) = HX(NX-1)

            Z(1) = 0
        DO J=2,NZ
            Z(J)=(LZ/(NZ-1))*(J-1)  ! spacing in the z direction [m]
            HZ(J-1) = Z(J)-Z(J-1)   ! [m]
        END DO
            HZ(NZ) = HZ(NZ-1)

!------------------------------------------------------------------------
!------------------------------------------------------------------------
!------------------------------------------------------------------------

!------------------------------------------------------------------------
!---------------------- FLOW CONDITIONS ---------------------------------
!------------------------------------------------------------------------

! If a balanced heat exchanger, Cc = Ch
```

```
! Input flow conditions

! THIS WILL NEED TO BE A SUBROUTINE SO THAT FRICTION FACTOR AND FLOW RATES CAN BE
RELATED.

    XMDOTC = (XMDOTH/RATIO)*(WCPF/ACPF)     ![-]

! CALCULATE INLET VELOCITIES OF HOT LIQUID

    XNP = NTX           ! # OF PASSES OR # OF COLUMNS OF TUBES [-]


!*****************TUBE SIDE INLET VELOCITIES**************

            U2AVG = 0.

        DO I = 1 , NX

            U2(I,1) = (XMDOTH/(LX*LY)/XM2(I,1)/WROF)*XNP        ! HOT FLUID INLET
VELOCITIES [m/s]

            U2AVG   = U2AVG + U2(I,1)*HX(I)                  ![m/s]

            REP2(I,1) = ABS(U2(I,1)*DH2(I,1)/WNU)

        END DO

!           U2AVG   = (U2AVG/LX)*XNP ! THIS IS PROF. CATTON'S ORIGINAL FORMULA -
HOT FLUID AVERAGE VELOCITY

            U2AVG   = (U2AVG/LX) !

!************************END*****************************


!*****************FIN SIDE INLET VELOCITIES***************

            U1AVG = 0.

        DO J = 1, NZ

            U1(1,J) = XMDOTC/(LZ*LY)/XM1(1,J)/AROF ! [m/s]

            U1AVG   = U1AVG + U1(1,J)*HZ(J)

            REP1(1,J) = ABS(U1(1,J)*DH1(1,J)/ANU)

        END DO

            U1AVG   = U1AVG/LZ

!************************END*****************************


!************************FLOW FIELD***********************

        DO I = 1, NX

            DO J = 1, NZ
```

```
                U1(I,J)    = U1(1,J)                    ![m/s] FLOW FIELD IS
UNIFORM

                U2(I,J)    = U2(I,1)                    ![m/s] FLOW FIELD IS
UNIFORM

                REP1(I,J)  = REP1(1,J)                  ![-]

                REP2(I,J)  = REP2(I,1)                  ![-]

                !FIN SIDE DRAG COEFFICIENT

!                CD1(I,J)   = 13.9/REP1(I,J)+0.015 ! ORIGINAL; Drag on  Airside for
Staggered tubes

                CD1(I,J) = 112.4/REP1(I,J)+0.252 !FENG'S CORRELATION FOR THE AIR
SIDE, FROM WANG'S CORRELATIONS

                !TUBE SIDE DRAG COEFFICIENT

                IF(REP2(I,J).LT.2300)THEN

                       CD2(I,J)   = 64.0/REP2(I,J) ! REP2.LT.2300

                END IF

                IF(REP2(I,J).GT.10000) THEN     ! 10,000<RE<2.5XE08

!                        FF         = 1.7372*LOG(REP2(I,J))/(1.964*LOG(REP2(I,J))-
3.8215) !ORIGINAL

                        FF         = 1.7372*LOG(REP2(I,J)/(1.964*LOG(REP2(I,J))-
3.8215)) ! TECHO ET AL.

                       CD2(I,J)   = 1/FF**2

                END IF

                IF(REP2(I,J).GT.2300.AND.REP2(I,J).LT.10000) THEN

!                         FF         = 1.7372*LOG(REP2(I,J))/(1.964*LOG(REP2(I,J))-
3.8215)

!                         FF        =   1.7372*LOG(REP2(I,J)/(1.964*LOG(REP2(I,J))-
3.8215)) !

!                         CH        = 1/FF**2

                        AA        = 64.0/2300

                        BB        = 1.0/(1.7372*LOG(10000.0/(1.964*LOG(10000.0)-
3.8215)))**2 !

!                         CD2(I,J)  = AA + (BB-AA)*REP2(I,J)/10000.0 !ORIGINAL
FORMULA

                        CD2(I,J)  = AA + (BB-AA)*(REP2(I,J)-2300)/(10000-2300) !,
SIMPLE INTERPOLATION

                END IF


                CONV1(I,J) = AROF*ACPF*U1(I,J)*XM1(I,J)/HX(I)
```

```
                CONV2(I,J) = WROF*WCPF*U2(I,J)*XM2(I,J)/HZ(J)
            END DO
        END DO
!************************END*****************************

!********************FLOW PARAMETERS**********************
! CALCULATE PRESSURE DROP AND PUMPING POWER
            DP1 = CD1(1,1)*AROF*U1(1,1)**2*LX/DH1(1,1)/2.0  ! [N/m**2],[Pa]
            !            F1  = DP1*LY*LZ
            ETA1 = 1.0 !AIR SIDE BLOWER EFFICIENCY [-]
            F1 = DP1*LY*LZ*XM1(1,1) ![N; Newtons]
            PP1 = F1*U1(1,1)/ETA1    ! [W]

!            ROD = PX/IPD
!            XK  = 20.0/ROD + 2.5*(ROD-1.0)
!            XK  = XK*CD2(1,1)
!            CDB = 0.25*PI*CD2(1,1)*ROD + 1.5*XK    !something for tube bends
separately.

            DPB=0.

            DP2 = CD2(1,1)*WROF*U2(1,1)**2*((LZ+.05)*NTX)/DH2(1,1)/2.0 + DPB*(NTX-
1) ! [Pa]
            ETA2 = 1.0 !LIQUID SIDE PUMP EFFICIENCY [-]
            F2  = DP2*XM2(1,1)*LY*LX/XNP    ! [N]
            PP2 = F2*U2(1,1)/ETA2           ! [W]

            PPT = PP1 + PP2 ![W]

            XOUTPUT(14)=PP1
            XOUTPUT(15)=PP2
        CONTINUE
!************************END*****************************
```

```
!------------------------------------------------------------------------

!------------------------------------------------------------------------

!------------------------------------------------------------------------




!------------------------------------------------------------------------

!-------------------------THERMAL CONDITIONS-------------------------------

!------------------------------------------------------------------------


                PR1 = ANU*ACPF*AROF/AKF ! PRANDTL NUMBER OF FLUID 1

                PR2 = WNU*WCPF*WROF/WKF ! PRANDTL NUMBER OF FLUID 2

        DO i=1,NX

            DO j=1,NZ

                T1(i,j)  =  TF1IN !temperature of fluid 1 [c] THIS IS THE FLOW
THROUGH THE TUBE BANKS BETWEEN  THE FINS

                T2(i,j)  =  TF2IN !temperature of fluid 2 [c] THIS IS THE TUBE FLOW

                TS(i,j)  =  (TF2IN+TF1IN)/2.0 !temperature of solid [c]   THE SOLID


                Y1(i,j)  =  TF2IN

                Y2(i,j)  =  TF2IN

                Y3(i,j)  =  TF2IN


!                NUT1     =  (-
.171*(REP1(i,j)**.71)+.232*(REP1(i,j)**.72))*PR1**(1./3.) ! Nusselt Number of fluid
1

                NUT1     =  0.24*(REP1(i,j)**0.6)*PR1**(1./3.) !FENG'S CORRELATION


                IF(REP2(i,j).LT.2100) THEN

                      NUT2     =  4.36; ! Nusselt Number of fluid 2, cappilary flow

                ELSE

                      NUT2     = 0.023*REP2(i,j)**0.8*PR2**0.3  ! DITTUS BOELTER

                END IF
```

```
                HH1(i,j) =  NUT1*AKF/DH1(i,j)    ! heat transfer coefficient, fluid
1 [W/m**2/K]

                HH2(i,j) =  NUT2*WKF/DH2(i,j)        ! heat transfer coefficient,
fluid 2 [W/m**2/K]

                CT1S(i,j)=  HH1(i,j)*SW1(i,j)

                CT2S(i,j)=  HH2(i,j)*SW2(i,j)

             END DO

          END DO


!-------------------------------------------------------------------------

!-------------------------------------------------------------------------

!-------------------------------------------------------------------------



!-------------------------------------------------------------------------

!-----------------------COEFFICIENTS--------------------------------------

!-------------------------------------------------------------------------


     DO I = 1,NX

         DO J = 1,NZ


                ZKS       = KS  ![W/mK]

            IF(J.EQ.1)THEN

                HBZ2  = HZ(1)**2

                HBZ2M = HBZ2

            ELSE

                HBZ2M = HZ(J-1)*(HZ(J-1)+HZ(J))/2.0     ! [m**2]

                HBZ2  = HZ(J)*(HZ(J-1)+HZ(J))/2.0       ! [m**2]

            END IF


                XKS       = KS  ![W/mK]

            IF(I.EQ.1) THEN

                HBX2  = HX(1)**2
```

```
            HBX2M = HBX2
        ELSE
            HBX2M = HX(I-1)*(HX(I-1)+HX(I))/2.0     ! [m**2]
            HBX2  = HX(I)*(HX(I-1)+HX(I))/2.0       ! [m**2]
        END IF
            AJTS(I,J) = COEF(I,J)*ZKS/HBZ2M         ! [W/m**3/K]
            BJTS(I,J) = COEF(I,J)*ZKS/HBZ2          ! [W/m**3/K]
            CJTS(I,J) = AJTS(I,J) + BJTS(I,J)       ! [W/m**3/K]
            AITS(I,J) = COEF(I,J)*XKS/HBX2M         ! [W/m**3/K]
            BITS(I,J) = COEF(I,J)*XKS/HBX2          ! [W/m**3/K]
            CITS(I,J) = AITS(I,J) + BITS(I,J)       ! [W/m**3/K]
            !  FLUID NUMBER 1   ****************************
            CT1(I,J)  = CONV1(I,J) + CT1S(I,J)      ! [W/m**3/K]
            ! FLUID NUMBER 2 ******************************
            CT2(I,J)   = CONV2(I,J)+ CT2S(I,J)      ! [W/m**3/K]

            CJTSS(I,J) = CJTS(I,J) + CITS(I,J) +CT1S(I,J) + CT2S(I,J)   !
[W/m**3/K]
         END DO
     END DO
     CONTINUE

!-------------------------------------------------------------------------
!-------------------------------------------------------------------------
!-------------------------------------------------------------------------



!-------------------------------------------------------------------------
!----------------------------COMPUTATIONS---------------------------------
!-------------------------------------------------------------------------

DO 1000     K = 1, 10000
```

```
! SOLID SIDE TEMPERATURE
DO I = 1, NX
    DO J = 1, NZ

        IF(I.EQ.NX)THEN
            TSP = TS(I,J)
        ELSE
            TSP = TS(I+1,J)     ![C]
        END IF

        IF(I.EQ.1)THEN
            TSM = TS(I,J)
        ELSE
            TSM = TS(I-1,J)     ![C]
        END IF

        IF(J.EQ.NZ) THEN
            TSJP = TS(I,J)
        ELSE
            TSJP = TS(I,J+1)    ![C]
        END IF

        IF(J.EQ.1)THEN
            TSJM = TS(I,J)
        ELSE
            TSJM = TS(I,J-1)    ![C]
        END IF

        Y2(I,J) =
(AJTS(I,J)*TSJM+BJTS(I,J)*TSJP+AITS(I,J)*TSM+BITS(I,J)*TSP)/CJTSS(I,J) &      ![C]
             + CT1S(I,J)*T1(I,J)/CJTSS(I,J) + CT2S(I,J)*T2(I,J)/CJTSS(I,J)
```

```
        END DO
    END DO
!             DO J = 1,NZ
!             Y2(NX,J) = Y2(NX-1,J)
!             END DO
!
    CONTINUE


! AIR SIDE TEMPERATURE


    DO J = 1, NZ
        DO I = 1, NX


            IF(I.EQ.1) THEN
                Y1(1,J) = TF1IN     ![C]
            ELSE
                Y1(I,J) = (CT1S(I,J)*Y2(I,J)/CONV1(I,J)+Y1(I-
1,J))/(1.0+CT1S(I,J)/CONV1(I,J))   ![C]
            END IF


        END DO
    END DO
    CONTINUE


! LIQUID SIDE TEMPERATURE. HERE MUST DO SOMETHING WITH BOUNDARY CONDITIONS.  HERE
IS WHERE GAMES ARE PLAYED TO GET MULTIPLE PASSES
! FIRST SOME BOUNDARIES FOR THE PASSES:


    NTR = NX/NTX    !NTR = 20


    DO   NTC = NX,1,-NTR    !Move from right to left, delineate individual
"serpentine pass" regions
        IU = NTC
```

```
        IL = IU-NTR+1

        DO I = IU,IL,-1     !Move from right to left within a single "serpentine
pass"

            LOGIC = NTC/NTR

            IF((LOGIC/2)*2.EQ.LOGIC) THEN   !Even # of tube passes

                ! UPWARD PASS
*****************************************************

                DO J = 1, NZ

                    IF(J.EQ.1) THEN

                        IF(NTC.EQ.NX)   Y3(I,1) = TF2IN     ![C]

                        IF(NTC.LT.NX)   Y3(I,1) = Y3(I+NTR,1)   !

                    ELSE

                       Y3(I,J) = (CT2S(I,J)*Y2(I,J)/CONV2(I,J)+Y3(I,J-
1))/(1.0+CT2S(I,J)/CONV2(I,J))

                    END IF

                END DO

!                               write(*,*)LOGIC,NTC,i,1,i+ntr,1

                 CONTINUE

            ELSE    !Odd # of tube passes

                ! DOWNWARD PASS REVERSE DIRECTION  ***************

!                         write(*,*)LOGIC,NTC,i,nz,i+ntr,nz

                DO J = NZ,1,-1

                    IF(J.EQ.NZ)THEN

                        IF(NTC.EQ.NX)   Y3(I,NZ) = TF2IN        !

                        IF(NTC.LT.NX)   Y3(I,NZ) = Y3(I+NTR,NZ)

                    ELSE

                        Y3(I,J)  =
(CT2S(I,J)*Y2(I,J)/CONV2(I,J)+Y3(I,J+1))/(1.0+CT2S(I,J)/CONV2(I,J))

                    END IF

                END DO   ! J

            END IF

        END DO ! I

    END DO    ! NTC

    CONTINUE
```

```
900 CONTINUE



!    IF(K.EQ.(K/10)*10)THEN
!    CONTINUE
!    END IF
    EPS = 0
    DO I = 2, NX-1
        DO J = 2, NZ-1
            EPSTF1 = ABS( (T1(I,J)-Y1(I,J))/T1(I,J))
            EPSTS  = ABS( (TS(I,J)-Y2(I,J))/TS(I,J))
            EPSTF2 = ABS( (T2(I,J)-Y3(I,J))/T2(I,J))
            IF (EPS.LT.EPSTF1)THEN
                EPS = EPSTF1
            END IF
            IF (EPS.LT.EPSTS)THEN
                EPS = EPSTS
            END IF
            IF (EPS.LT.EPSTF2)THEN
                EPS = EPSTF2
            END IF
        END DO
    END DO
    CONTINUE



    DO I = 1, NX
        DO J = 1, NZ
            T1(I,J)  = Y1(I,J)  ![C]
            TS(I,J)  = Y2(I,J)  ![C]
            T2(I,J)  = Y3(I,J)  ![C]
        END DO
```

```
    END DO



    IF(K.EQ.(K/10)*10)THEN  ! REPORT EVERY 10 ITERATIONS


        QX2 = 0.0
        DO J = 1, NZ
            QX2 = QX2 + AROF*ACPF*U1(NX,J)*XM1(NX,J)*(T1(NX,J)-TF1IN)*HZ(J)
        END DO
        QX2 = QX2*LY    ![W]
        XOUTPUT(16)= QX2


        QZ2 = 0.0
        DO I = 1,NTR  !GOES ACROSS THE OUTLET SECTION OF THE TUBE FLOW ON THE LEFT
END
            QZ2 = QZ2 +  WROF*WCPF*U2(I,1)*XM2(I,1)*(TF2IN-T2(I,1))*HX(I)
        END DO
        QZ2 = QZ2*LY    ![W]
        XOUTPUT(17) = QZ2


        T1AVG=0
        DO KK=1,NZ
            T1AVG = T1AVG+T1(NX,KK)
        END DO
        T1AVG = T1AVG/NZ
!        TAVG = (T2(1,1)+T2(2,1)+T2(3,1)+T2(4,1))/4.0
        QX3 = XMDOTC*ACPF*(T1AVG-TF1IN) ![W]


        T2AVG=0
        DO KK=1,NTR
            T2AVG = T2AVG+T2(KK,1)
        END DO
```

```
        T2AVG = T2AVG/NTR

!        TAVG = (T2(1,1)+T2(2,1)+T2(3,1)+T2(4,1))/4.0

        QZ3 = XMDOTH*WCPF*(TF2IN-T2AVG) ![W]




    !****************REAL-TIME USER UPDATES*******************

        WRITE(*,1550)NCASE,K,EPSTF1,EPSTS,EPSTF2

        WRITE(*,1551)   QX2,QZ2,QX3,QZ3

        WRITE(*,*)'AT TOP OF HX - J = ',NZ-1

        WRITE(*,1552) X(1)*1000, X(NX/6)*1000, X(NX/3)*1000,     X(NX/2)*1000,
X(2*NX/3)*1000,  X(5*NX/6)*1000,   X(NX)*1000

        WRITE(*,*)

        WRITE(*,1552) T1(1,NZ-1),T1(NX/6,NZ-1),T1(1.0*NX/3,NZ-1),T1(NX/2,NZ-
1),T1(2.0*NX/3,NZ-1),T1(5.0*NX/6,NZ-1),T1(NX,NZ-1)

        WRITE(*,1552) TS(1,NZ-1),TS(NX/6,NZ-1),TS(1.0*NX/3,NZ-1),TS(NX/2,NZ-
1),TS(2.0*NX/3,NZ-1),TS(5.0*NX/6,NZ-1),TS(NX,NZ-1)

        WRITE(*,1552) T2(1,NZ-1),T2(NX/6,NZ-1),T2(1.0*NX/3,NZ-1),T2(NX/2,NZ-
1),T2(2.0*NX/3,NZ-1),T2(5.0*NX/6,NZ-1),T2(NX,NZ-1)

        WRITE(*,*)

        WRITE(*,*)'AT CENTER OF HX - J = ',NZ/2

        WRITE(*,1552) X(1)*1000, X(NX/6)*1000, X(NX/3)*1000,     X(NX/2)*1000,
X(2*NX/3)*1000,   X(5*NX/6)*1000,  X(NX)*1000

        WRITE(*,*)

        WRITE(*,1552)
T1(1,NZ/2),T1(NX/6,NZ/2),T1(1.0*NX/3,NZ/2),T1(NX/2,NZ/2),T1(2.0*NX/3,NZ/2),T1(5.0*N
X/6,NZ/2),T1(NX,NZ/2)

        WRITE(*,1552)
TS(1,NZ/2),TS(NX/6,NZ/2),TS(1.0*NX/3,NZ/2),TS(NX/2,NZ/2),TS(2.0*NX/3,NZ/2),TS(5.0*N
X/6,NZ/2),TS(NX,NZ/2)

        WRITE(*,1552)
T2(1,NZ/2),T2(NX/6,NZ/2),T2(1.0*NX/3,NZ/2),T2(NX/2,NZ/2),T2(2.0*NX/3,NZ/2),T2(5.0*N
X/6,NZ/2),T2(NX,NZ/2)

        WRITE(*,*)

        WRITE(*,*)'AT BOTTOM OF HX - J = ',2

        WRITE(*,1552) X(1)*1000, X(NX/6)*1000, X(NX/3)*1000,X(NX/2)*1000,
X(2*NX/3)*1000,   X(5*NX/6)*1000,   X(NX)*1000

        WRITE(*,*)
```

```
        WRITE(*,1552)
T1(1,2),T1(NX/6,2),T1(1.0*NX/3,2),T1(NX/2,2),T1(2.0*NX/3,2),T1(5.0*NX/6,2),T1(NX,2)

        WRITE(*,1552)
TS(1,2),TS(NX/6,2),TS(1.0*NX/3,2),TS(NX/2,2),TS(2.0*NX/3,2),TS(5.0*NX/6,2),TS(NX,2)

        WRITE(*,1552)
T2(1,2),T2(NX/6,2),T2(1.0*NX/3,2),T2(NX/2,2),T2(2.0*NX/3,2),T2(5.0*NX/6,2),T2(NX,2)

        WRITE(*,*)

        !*************************END****************************

    END IF




    CONTINUE

    IF(K.GT.10.AND.EPS.LT.0.1E-05)THEN

        GO TO 1500  ! EXIT CLAUSE

    ELSE

        GO TO 1000

    END IF

1000 CONTINUE  ! END OF ITERATIVE LOOP. CONTROLLED BY SETTING THE NUMBER OF
ITERATIONS



1500 CONTINUE

! CALCULATE HEAT EXCHANGER EFFECTIVENESS




     QMAX = XMDOTH*WCPF*(TF2IN - TF1IN)


!    C1=XMDOTC*ACPF  ![W/K] AIR FLOW THERMAL CAPACITY

!    C2=XMDOTH*WCPF  ![W/M] WATER FLOW THERMAL CAPACITY

!

!    IF (C1.LT.C2) THEN      !

!        CMIN=C1

!        CMAX=C2

!        ELSE

!        CMIN=C2
```

```
!        CMAX=C1
!    END IF



     XOUTPUT(18) = QMAX
     HTEFF  = QX2/QMAX
     XOUTPUT(19) = HTEFF
     EFFECTIVENESS = QX2/PPT
     XOUTPUT(20) = EFFECTIVENESS
     EFFODT = EFFECTIVENESS/(T2FIN-TF1IN)
     XOUTPUT(21) = EFFODT

     WRITE(*,*) ' QX2/QMAX HEAT EXCHANGER EFFECTIVENESS = ',HTEFF
     WRITE(*,*) '   QX2/PPT, EFFECTIVENESS              = ',EFFECTIVENESS
     WRITE(*,*) '   QX2/PPT/DTMAX EFFECTIVENESS         = ',EFFODT

1550 FORMAT(1X,'NCASE = ',I4,'   K =',I6,3E10.3)
1551 FORMAT( 4X,'QX2 = ',E10.3,'  QZ2 = ',E10.3,'  QX3 = ',E10.3,' QZ3 = ',E10.3)
1552 FORMAT(2x,7F11.2)
1553 FORMAT(1X,'QX1 = ',E10.3,'  QZ1 = ',E10.3)
     CONTINUE
     VOLUME = LX*LY*LZ
  XOUTPUT(22) = VOLUME
!     WEIGHT = VOLUME*ROS*XM1(1,1)*XM2(1,1)
        WEIGHT = VOLUME*ROS*(1-XM1(1,1)-XM2(1,1))   !
  XOUTPUT(23) = WEIGHT

!-------------------------------------------------------------------------
!-------------------------------------------------------------------------
!-------------------------------------------------------------------------
```

```
!-------------------------------------------------------------------------

!---------------------------------OUTPUT----------------------------------

!-------------------------------------------------------------------------



     !*****************WRITE OUT TO FILE = 81, "RESPONSE.TXT"*******************

     IF(NCASE.EQ.1) WRITE(81, * )'NCASE  PPT       QX2              QZ2
QMAX            HTEFF             EFFODT      VOL               WEIGHT'

     WRITE(81,82)NCASE,PPT,QX2,QZ2,QMAX,HTEFF,EFFECTIVENESS/(TF2IN-
TF1IN),VOLUME,WEIGHT

82   FORMAT(I4,12E12.4)

     !****************************END*************************************



     !*****************WRITE OUT TO FILE = 32, "OUTPUT.TXT"*********************


WRITE(32,*)'************************************************************************
********'

     WRITE(32,*)' NCASE = ', NCASE

     WRITE(32,*)'               FIN-TUBE HEAT EXCHANGER MORPHOLOGY   '

     WRITE(32,*)' TUBE OUTER DIAMETER    PD      [mm]    = ',PD*1000
!

     WRITE(32,*)' TUBE WALL THICKNESS    PT      [mm]    = ',PT*1000

     WRITE(32,*)' TUBE INNER DIAMETER    IPD     [mm]    = ',(PD - 2*PT)*1000

     WRITE(32,*)' TUBE PITCH(X)/DIAMETER PXOPD   [-]     = ',PXOPD
!THIS IS THE PITCH/DIAMETER OF THE SERPENTINE THAT MAKES UP THE COLUMNS

     WRITE(32,*)' TUBE PITCH(Y)/DIAMETER PYOPD   [-]     = ',PYOPD
!THIS IS THE SPACING/DIAMETER OF THE ROWS OF SINGLE TUBES

     WRITE(32,*)' TUBE PITCH(X)          PX      [mm]    = ',PX*1000
!tube  pitch in  X direction[m]

     WRITE(32,*)' TUBE PITCH(Y)          PY      [mm]    = ',PY*1000
!tube  pitch in  Y direction[m]

     WRITE(32,*)' COLUMNS OF TUBES(X)    NTX     [-]     = ',NTX

     WRITE(32,*)' LENGTH(X)              LX      [mm]    = ',LX*1000

     WRITE(32,*)' ROWS OF TUBES(Y)       NTY     [-]     = ',NTY

     WRITE(32,*)' WIDTH(Y)               LY      [mm]    = ',LY*1000

     WRITE(32,*)' FIN THICKNESS          FT      [mm]    = ',FT*1000

     WRITE(32,*)' FIN PITCH(Z)/THICK     FPOFT   [-]     = ',FPOFT
```

```
      WRITE(32,*)' FIN PITCH              FP      [mm]    = ',FP*1000

      WRITE(32,*)' FINS PER INCH          FPI             = ',(1.0/FP)*0.0254

      WRITE(32,*)' HEIGHT(Z)              LZ      [mm]    = ',LZ*1000

      WRITE(32,*)' HX VOLUME                      [m**3]  = ',VOLUME

      WRITE(32,*)' HX WEIGHT                      [kg]    = ',WEIGHT

          IF(KSOLID.EQ.1)WRITE(32,*)'           NATERIAL IS STEEL'

          IF(KSOLID.EQ.2)WRITE(32,*)'           MATERIAL IS COPPER'

          IF(KSOLID.EQ.3)WRITE(32,*)'           MATERIAL IS ALUMINUM'

          IF(KSOLID.EQ.4)WRITE(32,*)'           MATERIAL IS VERY HIGH THERMAL
CONDUCTIVITY'

          IF(KSOLID.EQ.5)WRITE(32,*)'           MATERIAL IS SILICON'


      WRITE(32,*)'*****************************************************************'

      WRITE(32,*)'HOT FLUID MASS FLOW RATE          XMDOTH  [kg/s]  = ', XMDOTH

      WRITE(32,*)'COLD FLUID MASS FLOW RATE         XMDOTC  [kg/s]  = ', XMDOTC
!XMDOTH*WCPF/ACPF  BALANCED FLOW

      WRITE(32,*)'HOT FLUID INLET TEMPERATURE       TF2IN   [C]     = ', TF2IN

      WRITE(32,*)'COLD FLUID INLET TEMPERATURE      TF1IN   [C]     = ', TF1IN

      WRITE(32,*)'FLOW THERMAL CAPACITY RATIO       RATIO   [-]     = ', RATIO



      WRITE(32,*)'******************   FLOW PARAMETERS   ******************'

      WRITE(32,*)'   TUBE SIDE VELOCITY         U2AVG [m/s] = ',U2AVG

      WRITE(32,*)'   TUBE SIDE REYNOLDS NUMBER  REP2    [-] = ',REP2(1,1)

      WRITE(32,*)'   TUBE SIDE PUMPING POWER    PP2     [W] = ',PP2             !
NOT SURE OF UNITS

      WRITE(32,*)'   FIN SIDE VELOCITY          U1AVG [m/s] = ',U1AVG

      WRITE(32,*)'   FIN SIDE REYNOLDS NUMBER   REP1    [-] = ',REP1(1,1)

      WRITE(32,*)'   FIN SIDE PUMPING POWER     PP1     [W] = ',PP1

      WRITE(32,*)'**********************   THERMAL   **********************'

      WRITE(32,*)' MAXIMUM POSSIBLE HEAT TRANSFER   QMAX    [W]     = ',QMAX

      WRITE(32,*)' HEAT LOSS FROM HOT FLUID         QX2     [W]     = ',QX2

      WRITE(32,*)' HEAT GAIN TO COLD FLUID          QZ2     [W]     = ',QZ2

      WRITE(32,*)' HEAT LOSS FROM HOT FLUID         QX3     [W]     = ',QX3
```

```
     WRITE(32,*)' HEAT GAIN TO COLD FLUID           QZ3     [W]     = ',QZ3

     WRITE(32,*)' QX2/QMAX EFFECTIVENESS,           HTEFF   [-]     = ',HTEFF

     WRITE(32,*)' QX2/PPT EFFECTIVENESS,    EFFECTIVENESS   [-]     =
',EFFECTIVENESS

     WRITE(32,*)' QX2/PPT/DTMAX EFFECTIVENESS,      EFFODT  [1/C]   =
',EFFECTIVENESS/(TF2IN-TF1IN)

     WRITE(32,*)' ******************************************************'



     WRITE(32,1552) X(1)*1000, X(NX/6)*1000, X(NX/3)*1000,     X(NX/2)*1000,
X(2*NX/3)*1000,  X(5*NX/6)*1000,   X(NX)*1000

     DO J = NZ,1,-10

         WRITE(32,*)'ELEVATION = ',Z(J)*1000

         WRITE(32,1552)
T1(1,J),T1(NX/6,J),T1(1.0*NX/3,J),T1(NX/2,J),T1(2.0*NX/3,J),T1(5.0*NX/6,J),T1(NX,J)

         WRITE(32,1552)
TS(1,J),TS(NX/6,J),TS(1.0*NX/3,J),TS(NX/2,J),TS(2.0*NX/3,J),TS(5.0*NX/6,J),TS(NX,J)

         WRITE(32,1552)
T2(1,J),T2(NX/6,J),T2(1.0*NX/3,J),T2(NX/2,J),T2(2.0*NX/3,J),T2(5.0*NX/6,J),T2(NX,J)

         WRITE(32,*)

     END DO

         J = 1

         WRITE(32,*)'ELEVATION = ',Z(J)*1000

         WRITE(32,1552)
T1(1,J),T1(NX/6,J),T1(1.0*NX/3,J),T1(NX/2,J),T1(2.0*NX/3,J),T1(5.0*NX/6,J),T1(NX,J)

         WRITE(32,1552)
TS(1,J),TS(NX/6,J),TS(1.0*NX/3,J),TS(NX/2,J),TS(2.0*NX/3,J),TS(5.0*NX/6,J),TS(NX,J)

         WRITE(32,1552)
T2(1,J),T2(NX/6,J),T2(1.0*NX/3,J),T2(NX/2,J),T2(2.0*NX/3,J),T2(5.0*NX/6,J),T2(NX,J)

         WRITE(32,*)


     ! WRITE OUT FIELD TEMPERATURE AND VELOCITY VALUES


!     DO J=1,NZ

!         WRITE(1801,111) (T1(KK,J),KK=1,1000)

!         WRITE(1802,111) (T2(KK,J),KK=1,1000)

!         WRITE(1803,111) (TS(KK,J),KK=1,1000)

!         WRITE(1804,111) (U1(KK,J),KK=1,1000)
```

```
!          WRITE(1805,111) (U2(KK,J),KK=1,1000)
!      END DO
!111   FORMAT(1x,1000ES15.6)


    CONTINUE
 RETURN
    END
```